IMPROVEMENT OF CORONARY ANGIOGRAPHY FOR QUANTITATIVE CORONARY ANALYSIS BY USING A COMPUTER VISION TECHNIQUE

Kodikara Arachchillaya Saneera Hemantha Kulathilake

(128011R)

Degree of Master of Philosophy

Department of Information Technology

University of Moratuwa

Sri Lanka

May 2017

IMPROVEMENT OF CORONARY ANGIOGRAPHY FOR QUANTITATIVE CORONARY ANALYSIS BY USING A COMPUTER VISION TECHNIQUE

Kodikara Arachchillaya Saneera Hemantha Kulathilake

(128011R)

Thesis submitted in partial fulfillment of the requirements for the degree Master of Philosophy

Department of Information Technology

University of Moratuwa

Sri Lanka

May 2017

DECLARATION

I declare that this is my own work and this thesis does not incorporate without acknowledgement any material previously submitted for a Degree or Diploma in any other University or institute of higher learning and to the best of my knowledge and belief it does not contain any material previously published or written by another person except where the acknowledgement is made in the text.

Also, I hereby grant to University of Moratuwa the non-exclusive right to reproduce and distribute my thesis, in whole or in part in print, electronic or other medium. I retain the right to use this content in whole or part in future works (such as articles or books).

Signature: Date:

The above candidate has carried out research for the MPhil thesis under my supervision.

Name of the supervisor I: Dr. Lochandaka Ranathunga

Signature of the supervisor I: Date:

Name of the supervisor II: Dr. Godvin Roger Constantine

Signature of the supervisor II: Date:

Name of the supervisor III: Associate Professor Dr. Nor Aniza Abdullah

Signature of the supervisor III: Date:

ACKNOWLEDGEMENT

First and foremost I consider it is my bounden duty to record here my sincerest gratitude and appreciation to my supervisor, Dr. Lochandaka Ranathunga for his kind cooperation, guidance, and supervision extended throughout this research project. If not for his encouragement and support this project would never have been a reality. I would like to unreservedly thank my co-supervisors Dr. G.R. Constantine from University of Colombo and Associate Professor Dr. N.A. Abdullah from University of Malaya- Malaysia for guiding me to achieve success in this endeavor.

I would like to express my heartfelt thanks to the Vice Chancellor of the University of Moratuwa, the Dean of the Faculty of Information Technology and the Head of the Department of Information Technology, University of Moratuwa for granting me the opportunity to commence my research work at the University of Moratuwa and facilitating me to carry out same successfully. Further, I would be failing in my duty if I do not extend my sincere gratefulness to the Vice Chancellor of the Rajarata University of Sri Lanka, the Dean of the Faculty of Applied Sciences and the Head of the Department of Physical Sciences, Rajarata University of Sri Lanka for granting me two years paid study leave and releasing me from all academic duties in the University, thus allowing me to concentrate fully on my research work during the said two years. Thanks are also due to the Director and staff of the National Science Foundation, Sri Lanka for granting a research scholarship under the grant number NSF/SCH/2013/06 to financially support this effort. Furthermore, I would like to express my indebtedness to the CEO of LK Domain Registry for granting me the Prof. V.K. Samaranayake Research Grant in order to continue my research studies in the University of Malaya, Malaysia.

A special word of thanks should also be extended to the Chairperson of the Ethics Review Committee of the Faculty of Medicine, University of Colombo for issuing the ethical clearance for extracting clinical data needed for validating the results of this study. It is an honor for me to express my sincere gratitude to Mr. V.G. Vimalasena who is the Principal of School of Radiography, National Hospital of Sri

Lanka for facilitating the domain knowledge to make this effort a success. I would like to convey my heartfelt appreciation to Radiographer Mr. R.M. Janaka Thushara Rathnayaka who is attached to the Cath Lab of the Cardiology Unit, National Hospital of Sri Lanka for facilitating me to obtain the necessary resources, conveying domain knowledge and providing valuable clinical experience. His motivation, prompt support and positive response directed the research work towards its success. Moreover, I acknowledge all Radiographers and Cath Lab staff members in the Cardiology Unit of National Hospital of Sri Lanka for providing necessary resources, data and training on clinical procedures. It is also important to highly appreciate Mr. Riyas Mohomed, Radiographer in Durdans Hospital PLC and Cath Lab staff members of Asiri Surgical Hospital PLC for providing the necessary knowledge and data for the experiments. I declare my salutation and admiration for all the esteemed authors, researchers and philosophers for their great theories, researches, publications and ideas, which have helped to enrich this research work.

I would like to thank all the staff members of the University of Moratuwa for their cooperation and commitment extended in various ways in order to make this project a success. The support and motivation provided by my post graduate friends, Mr. A.M.R.R. Bandara, Mr. V. Senthooran and Mrs. N.M. Wagarachchi who are attached to the Faculty of Information Technology, University of Moratuwa too deserves mentioning with a debt of gratitude.

The members of the testing team Mr. K.A.S.N Wijerathna, Mr. D.D. Hewage, Mr. I.K. Sirirathna and Mr. H.A. Haputhanthri too should be acknowledged for the continuous assistance offered to me for data analysis, testing and component integration. I would like to express my appreciation to Mr. S.S. Ratnajeewa for his immense support and contribution to make this thesis a success.

Last but not least, I offer a debt of gratitude to my parents and my sister for all their encouragement and support extended right through this endeavor. Finally, I am grateful to all those who assisted me in numerous ways during the course of this research.

Abstract

Coronary cine-angiography is an invasive medical image modality, which is widely used in Interventional Cardiology for the detection of stenosis in Coronary arteries. Quantitative coronary analysis is one of the demanding areas in medical imaging and in this study a semi automated quantitative coronary analysis method has been proposed. Direct coronary cine-angiogram frames are processed in order to obtain the features of lumen such as, vessel boundary, skeleton and luminal diameter along the vessels' skeleton as the results. The proposed method consists of four main implementation phases namely, pre-processing, segmentation, vessel path tracking and quantitative analysis. The visual quality of the input frames is enhanced within the pre-processing phase. The proposed segmentation phase is implemented based on a spatial filtering and region growing approach. A clinically important vessel region is processed to detect the vessel boundary and skeleton, which is required as prior knowledge for quantitative analysis. Moreover, the vessel diameter is computed while tracking the vessel skeleton path starting from a given seed. The proposed segmentation method possesses 93.73% mean segmentation accuracy and 0.053 mean fallout rate. Moreover, the proposed quantitative analysis method has been validated for assessing its' technical supportability using a clinically approved data set. As a result of that, this proposed method computes the vessel diameter along the vessel skeleton in single pixel gap and develops the ability to determine the diameter stenosis as the quantitative analysis results. Additionally, the clinical feasibility of the proposed method has been validated to emphasize the clinical usability. Moreover, this study can be further extended to make clinical decisions on stenosis through the functional significance of the vasculature by using proper medical image modality like biplane angiography.

Key words: motion stabilization, vessel segmentation, vessel tracking, quantitative coronary analysis

TABLE OF CONTENTS

LIST OF FIGURES

LIST OF TABLES

LIST OF ABBREVIATIONS

Abbreviation	Description
AMB	Acute Marginal Branch
AP	Anterior-Posterior
CA	Coronary Artery
CC	Correlation Coefficient
CCA	Coronary Cine-angiogram
CLAHE	Contrast Limited Adaptive Histogram Equalization
CMRI	Cardiac Magnetic Resonance Imaging
CX	Circumflex Artery
DFT	Discrete Fourier Transform
FFR	Fractional Flow Reserve
GMV	Global Motion Vector
HOG	Histogram based Oriented Gradient
IVUS	Intra-vascular Ultrasound
LAD	Left Anterior Descending Artery
LAO	Left Anterior Oblique
LCA	Left Coronary Artery
LMCA	Left Main Coronary Artery
MR	Median Ramus
MSCT	Multi Slice Computer Tomography

NIR	Near-Infrared
OCT	Optical Coherent Tomography
OMB	Obtuse Marginal Branch
PCI	Percutaneous Coronary Intervention
PDA	Posterior Descending Artery
PET	Positron Emission Tomography
PLV	Posterior Left Ventricular
RAO	Right Anterior Oblique
RCA	Right Coronary Artery
SIFT	Scale Invariant Feature Transform
SP	Septal Perforators
SPECT	Single Photon Emission Computed Tomography
SPT	Skeleton Path Tracker
VDC	Vessel Diameter Calculation

LIST OF APPENDICES

CHAPTER 1
INTRODUCTION

Coronary Cine-angiogram (CCA) is one of the invasive medical image modalities used in interventional cardiology for the detection of luminal obstructions or stenosis in Coronary Artery (CA) vasculature. It provides excellent visualizations of the CA lumen and the clinical judgments based on angiography are subjective. Hence, it leads to overestimation and underestimation of the detected stenosis and causes negative effects to the patients' quality of life. Angiography based quantitative coronary analysis is known as the way of assessing the detected stenosis in an objective manner and this research study is done for devising a novel method to objectively assess the severity of stenosis recorded in CCAs. This thesis has been elaborated the introduction to the problem, research background, methodology, experimental methods, results and discussion of the study comprehensively in the following chapters. Moreover, the objective of this chapter is to discuss about the biological and medical background of the domain of this research study, which is the CA vasculature.

The CAs are the blood vessels that supply Oxygen and nutrients to the heart muscles. Therefore, at the very outset, it is important to discuss about the anatomy of the human heart and the blood vessels to recognize the organization and interrelation ship among them. Hence, the first section of this chapter is allocated to discuss about the anatomy of human heart and the blood vessels broadly. Since this study is based on CAs, it is important to emphasize the anatomy of the CA vasculature comprehensively. Thus, the structure and localization of the main CAs on heart are discussed as the second section of this chapter. Further, the images of heart, CAs and arterial diseases are illustrated. A discussion about the common CA diseases is included in the next section of this chapter. Subsequently, the clinically relevant medical image modalities that are widely used in diagnosing the CA diseases have been elaborated with possible illustrations. The treatment options for the clinically diagnosed CA diseases are also in the fifth section of the chapter. The next section of this chapter briefly emphasizes the problems in coronary angiography. Moreover, the

objectives of this research study have been elaborated consequently. Finally, the chapter organization of this thesis is elaborated based on the chapter objectives and it makes easy for navigation to the interesting topics of this research study promptly.

1.1 Heart anatomy and blood supply to the heart

This section emphasizes the anatomy of the heart and the blood vessels to realize the organization and the functional relationship among them.

1.1.1 Anatomy of human heart

The heart is a hollow muscular organ, which placed in thoracic cavity in the mediastinum between the lungs [1]. It is about 10cm long and weights about 225g in women and about 310g in men. It lies towards the left side in human body. The base of the heart lays above and to the right and the apex lays below and to the left.

There are various organs and vessels placed around the human heart. The apex of the heart positioned inferiorly on the central tendon of the diaphragm and the great blood vessels i.e. the aorta, superior vena cava, pulmonary artery and pulmonary veins are placed superiorly. The esophagus, trachea, left and right bronchus, descending aorta, inferior vena cava and thoracic vertebrae are positioned posteriorly to the human heart and the lungs are placed laterally. Further, left lung overlaps the left side of the heart. The sternum and ribs are positioned anteriorly to the heart. Figure 1.1 depicts the organs and vessels associated with heart clearly.

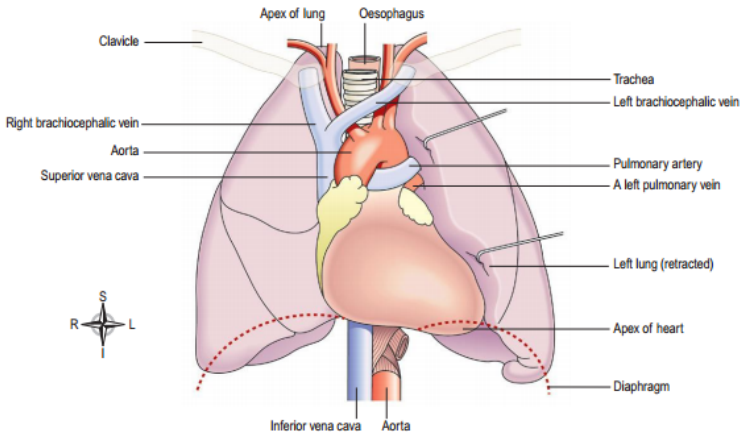

Figure 1.1: Organs and vessels associated with heart [1].

The heart is composed of three layers of tissues namely pericardium, myocardium and endocardium. Further, the heart consists of four chambers. Top left and right side chambers are known as left and right atrium respectively and bottom left and right chambers are known as left and right ventricle. The wall between the right and left side atrium and ventricle is known as septum. The atrium and the ventricle of the same side are separated by an atrio-ventricular valve. These valves are made of cusps. The left atrio-ventricular valve has two cusps and it is called the mitral valves, while the right atrio-ventricular valve has three cusps and it is called the tri-cuspid valve. Figure 1.2 depicts the interior of the heart.

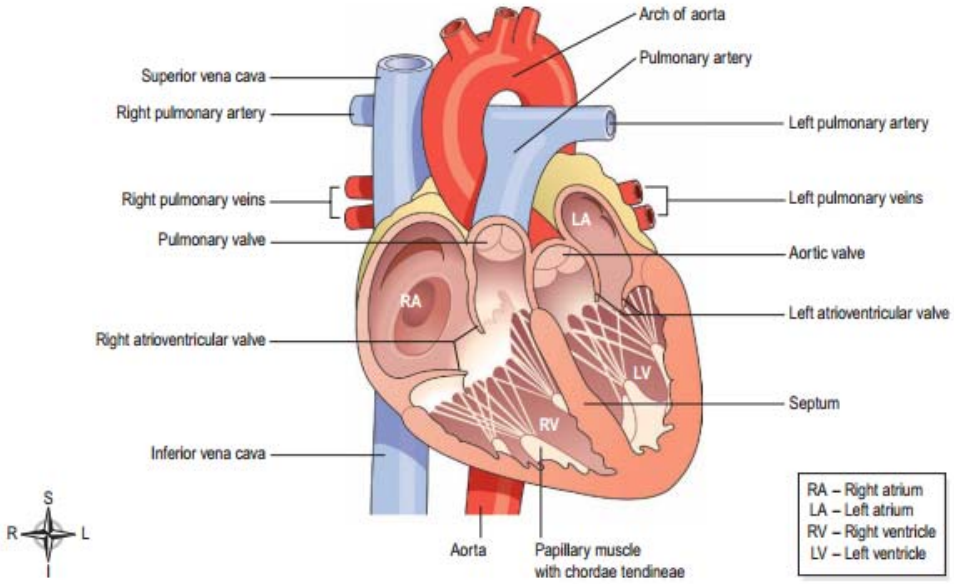

Figure 1.2: Interior of the heart [1].

The main function of the heart is to maintain circulation of blood throughout the body. Deoxygenated blood (represents in blue color) from the body returns to the right atrium through superior and inferior vena cava. After the right atrium is filled with this deoxygenated blood, it contracts and tri-cuspid valve opens and blood is pumped in to the right ventricle in the heart. When the right ventricle is filled with blood, the tri-cuspid valve is closed so as to prevent blood from flowing back in to the atrium. Then, the right ventricle contracts and pulmonary valves, which are known as semilunar value opens and blood is pumped into the pulmonary artery and

flows into the lungs. Afterwards, the semilunar valves are closed to prevent the blood from flowing back in to the ventricle. Oxygenated blood (represents in red color) from lungs returns to the left atrium of the heart via the pulmonary veins. After the left atrium is filled with oxygenated blood it contracts. Then the mitral valves open and blood is pumped in to the left ventricle. This occurs simultaneously as the right atrium pumps blood in to the right ventricle on the other side of the heart. After the left ventricle is filled with blood, the mitral valves close and aortic valves placed between the ventricle and the aorta are opened. The left ventricle contracts and oxygenated blood is pumped in to the aorta to be supplied to all parts of the body. This happens simultaneously as the right ventricle pumps blood in to the pulmonary artery on the other side of the heart. The aortic valves quickly close to prevent blood from flowing back to the heart. In the meantime, the atria are filled with blood and the cycle repeats itself. Figure 1.3 represents the directions of the blood flow through the heart.

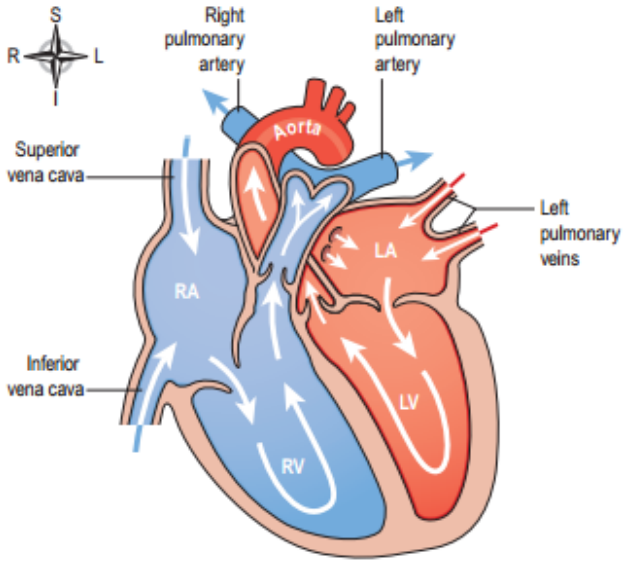

Figure 1.3: Blood flow through the heart [1].

The cardiac cycle repeats itself to maintain the constant circulation of blood throughout the body. During a cardiac cycle the heart contracts (systole) and relaxes (diastole), at 60 to 80 times per minute. Moreover, it consists of three functions

namely; atrial systole (contraction of the atria), ventricular systole (contractions of the ventricles) and complete cardiac diastole (relaxation of the atria and ventricles) per cardiac cycle.

1.1.2 Anatomy of blood vessels

This section emphasizes some important facts about blood vessel anatomy and the different types of blood vessels that carry blood throughout the body. The heart pumps blood through vessels, which vary in size, structure and function. Thus, different types of vessels can be identified in the human vascular system namely; arteries, arterioles, capillaries, venules and veins. The formation of different types of blood vessels is clearly depicted in Figure 1.4 and in accordance with that figure, the blood vessels (artery and veins) have three layers of tissues namely inner layer (tunica intima), middle layer (tunica media) and outer layer (tunica adventitia). The middle layer also known as tunica media gradually smoothen when the artery branches off and reach capillary level and gradually congeal when it forms venules and veins.

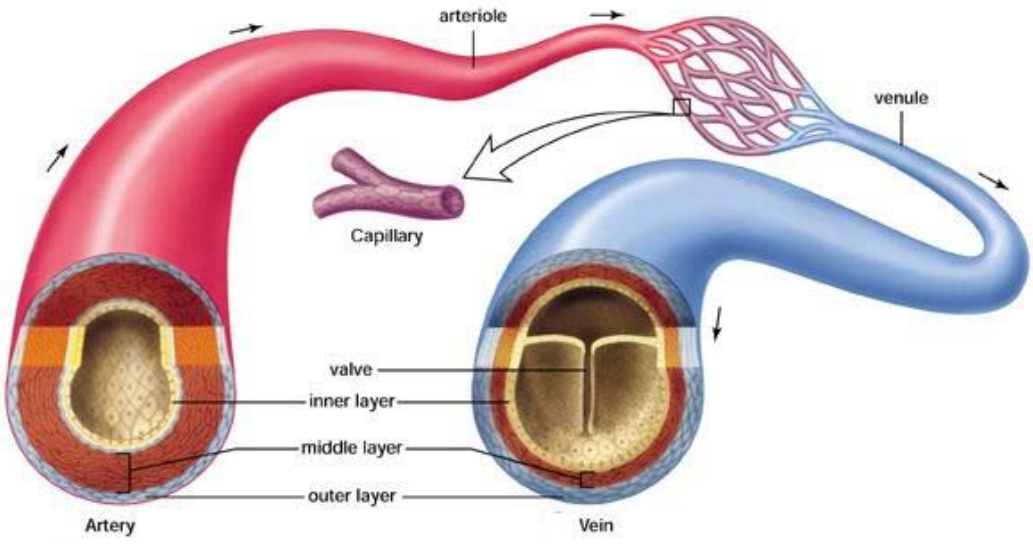

Figure 1.4: Different types of blood vessels [1].

Arteries transport oxygenated blood away from the heart (except pulmonary artery) under high pressure. Arterioles are tiny branches of arteries that lead to capillaries and transport blood from arteries to capillaries. Capillaries are tiny blood vessels and formed as a network of capillaries in most of the organs and tissues of the body. Capillary walls are made out of single cell layer and permit the exchange of Oxygen and other substances between the tissues and blood. Oxygen and water are mainly absorbed by the tissues from blood and Carbon Dioxide and waste substances are released back into the blood. As the next step, venules are formed and drains blood from capillaries into veins. Finally, the veins are formed to complete the returning of deoxygenated blood (except pulmonary vein) to the heart. The walls (outer structure) of veins consist of three layers of tissues that are thinner and less elastic than the corresponding layers of arteries and include valves that aid the return of blood to the heart by preventing blood from flowing in the reverse direction. .

1.2 Blood supply to the heart

The blood supply to the heart is known as coronary circulation. CAs are branched from the aorta immediately distal to the aortic valve. There are two main CAs formed from aorta namely; Left Coronary Artery (LCA) and Right Coronary Artery (RCA). Moreover, it has been reported that 4% of people have a third, the Posterior CA [2]. LCA supplies blood mainly to the left side of the myocardium (muscular tissues of the heart) and is divided into two branches, Left Anterior Descending Artery (LAD) and Circumflex Artery (CX). The LAD travels in the anterior inter-ventricular groove that separates the right and the left ventricles, in the front of the heart and the CX travels in the left atrio-ventricular groove that separates the left atrium from the left ventricle. Further, the CX moves away from the LAD and wraps around to the back of the heart. The RCA travels in the right atrio-ventricular groove between the right atrium and right ventricle, as it wraps around to the bottom or inferior portion of the heart. Figure 1.5 depicts the main CAs for further clarification of its positioning on the heart. These CAs receives about 5% of blood pumped from the heart and it flows through these main arteries [3]. Further, these main CAs send smaller branch arteries into the myocardium that are known as myocardial arteries

and these myocardial arteries further divide into arterioles and capillaries to supply the blood to the myocardium. This process is known as perfusion.

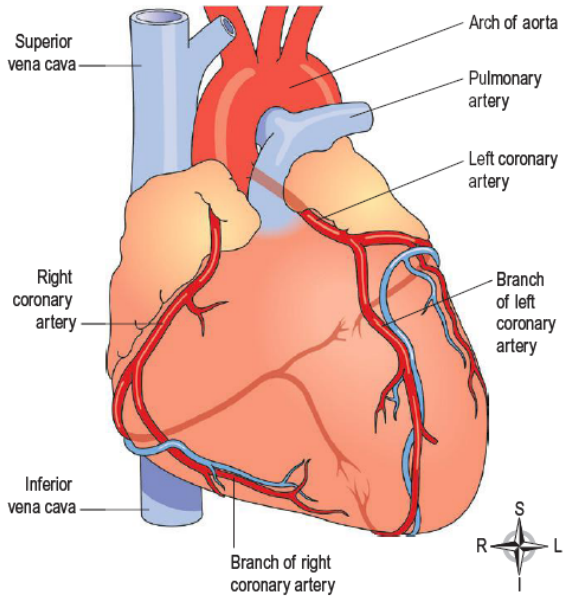

Figure 1.5: CA vasculature [1].

Changes in aortic pressure and compression of myocardial vessels during systole and changes in Oxygen demand are considered as the most important factors that can be affected to myocardial blood flow. During the cardiac cycle, contracting and relaxing heart muscles influences its own blood supply by changing the pressure in the aorta, which affects the flow of blood in to CAs and alternately compressing and releasing the blood vessels in myocardium. During the systolic phase the pressure of the contracting cardiac muscle compresses the intra myocardial vessels. In addition, the increase pressure in the ventricles causes further compression of the coronary vessels thus reducing myocardial blood flow. The heart myocardium needs significant amount of Oxygen to do its' work. The heart myocardium has auto regulatory mechanism that affects blood flow based on the amount that is needed. During periods of increased activity or stress the cardiac arteries are dilated and increase their flow of blood.

Next section contains the information about the anatomy of CAs because, this knowledge is important to understand this research study. As mentioned above in this section, LAD and CX arteries of LCA and RCA are considered as main CAs. The CA segments and nomenclature published by J. T. Dodge, B. G. Brown, E. L. Bolson, and H. T. Dodge is used in this study to characterize the anatomy of the three main CAs [4]. Figure 1.6 depicts Dodge's nomenclature of CA segments for further clarifications.

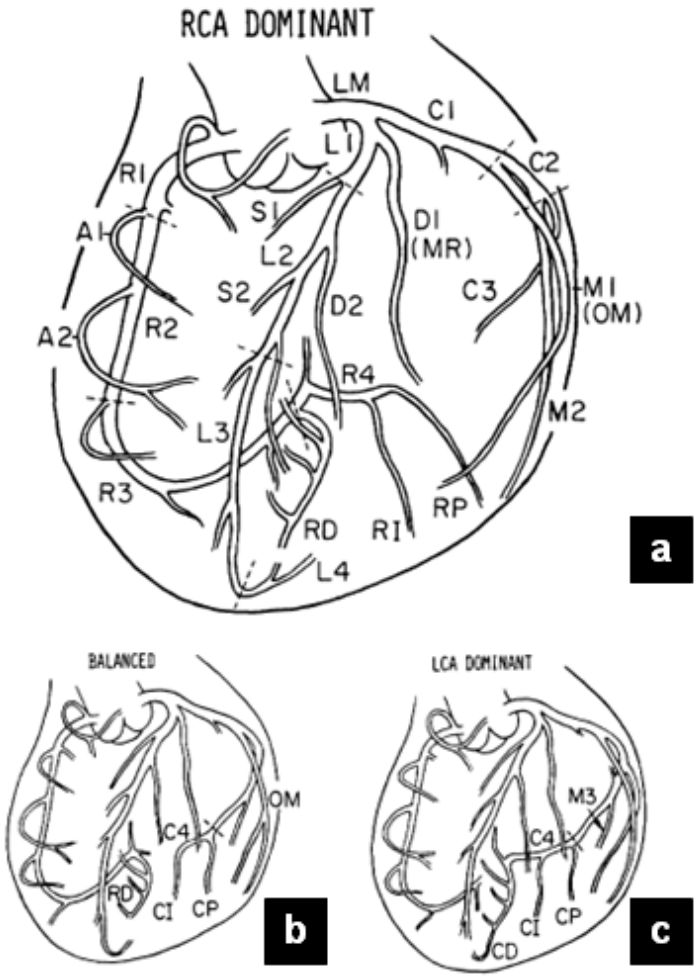

Figure 1.6: CA segments and branch nomenclature. (a) RCA dominant; (b) balanced system; (c) LCA dominant [4]. (CD -Posterior Descending Artery (PDA), CP - Posterior wall branch, CI – Inferior wall branch, C4 – Fourth segment, A1 – First Acute Marginal Branch , A2 – Second Acute Marginal Branch)

1.2.1 Left Anterior Descending Artery (LAD)

According to the Figure 1.6(a), the LAD artery appears to be a direct continuation of the LCA. As described in [4], the LAD artery is separated into four segments defined by its origin from the LCA, the first septal perforator (S1), the third septal perforator (S3), the cardiac apex, and its terminal point on the inferior wall. S3 was not marked in Figure 1.6(a) and is commonly arises near the bend of the LAD in Right Anterior Oblique (RAO) views and often is near the origin of the second diagonal branch. LAD consists of three largest septal branches (S1-S3) and the three largest diagonal branches (D1-D3). As mentioned in [4], a Median Ramus (MR) branch was present in some cases as an anatomic variant arising at the trifurcation of the LCA.

The first diagonal branch of the LAD runs diagonally away from the anterior inter-ventricular groove and towards the anterior-lateral portion of the heart. Moreover the Septal Perforators (SP) run into the septum and provide blood to septum. Figure 1.7 depicts the anatomy of the LCA for further clarifications.

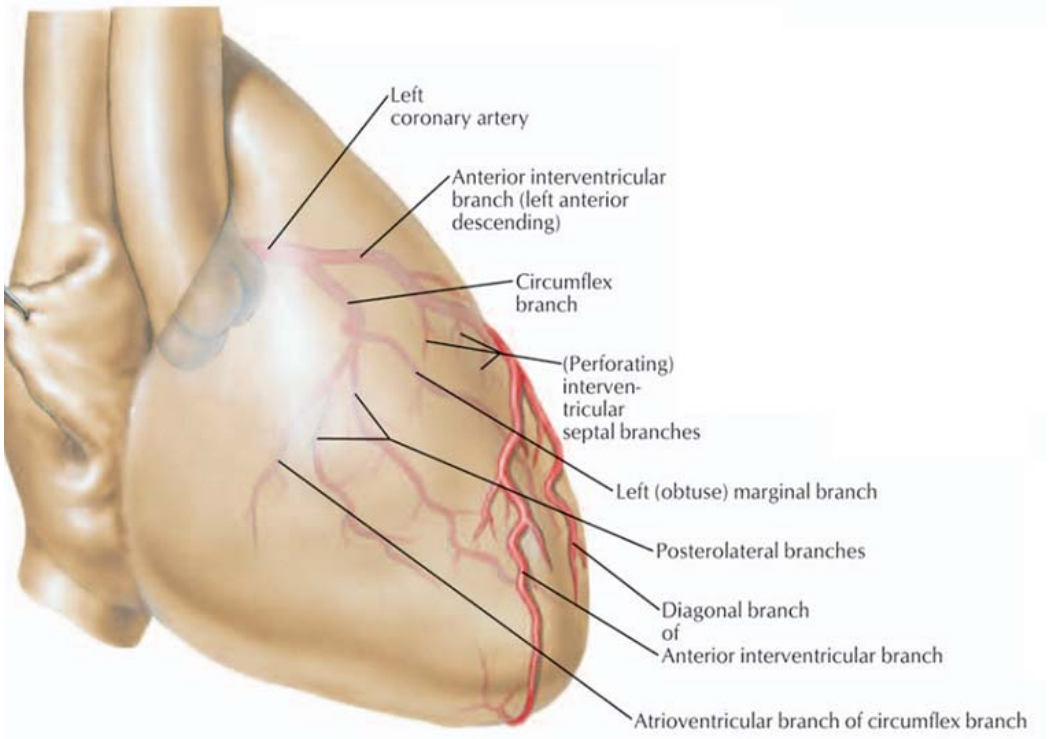

Figure 1.7: Anatomy of LCA [1].

1.2.2 Circumflex Artery (CX)

As shown in Figure 1.7, the CX travels in the left atrio-ventricular groove that separates the left atrium from the left ventricle. Hence, the CX artery moves away from the LAD and wraps around to the back of the heart. The Obtuse Marginal Branch (OMB) is the major branch that the CX artery has possessed. Rarely, the Posterior Descending Artery (PDA) can be branched from the distal part of the CX artery. However, it is reported that in 85% of cases, PDA branches in the distal part of the RCA [5]. Hence in most of the cases, CX terminates without having PDA branches in the distal location of it. This feature is known as a non-dominant LCA system. Further, it is also named as balanced system or right dominant system. Figure 1.6 (b) depicts this right dominant system and Figure 1.6 (c) depicts the left dominant LCA system to indicate the difference between the two views. Moreover, CX artery in non-dominant system can be divided into three parts (C1-C3) by the OMB and the second marginal branches.

1.2.3 Right Coronary Artery (RCA)

The RCA originates from the right coronary cusp in aorta and travels in the right atrio-ventricular groove, between the right atrium and the right ventricle. As shown in Figure 1.8, the conus and the sino-atrial node branch are given off by the proximal part of the RCA. Moreover, RCA gives rise to the Acute Marginal Branch (AMB) that travels along the anterior portion of the right ventricle. Afterwards, the RCA continues to travel in the right atrio-ventricular groove. About 85% of cases, the RCA is a dominant vessel and give rise to the PDA branch. According to the vessel segment nomenclature described in [4] and [5], the RCA, with a right dominant anatomy, is divided into four parts between its origin, the first AMB, the third AMB and the PDA.

Over the time, the waxy substance called plaque builds up inside the CAs and cause some negative consequences to the coronary circulation. These plaques are also known as atheroma and are considered as the major source for the CA disease. Generally, 50% of all cardiac deaths result from CA diseases [6]. The subject of the

next section of this chapter is about the atheroma, which is the main pathology of the coronary vasculature.

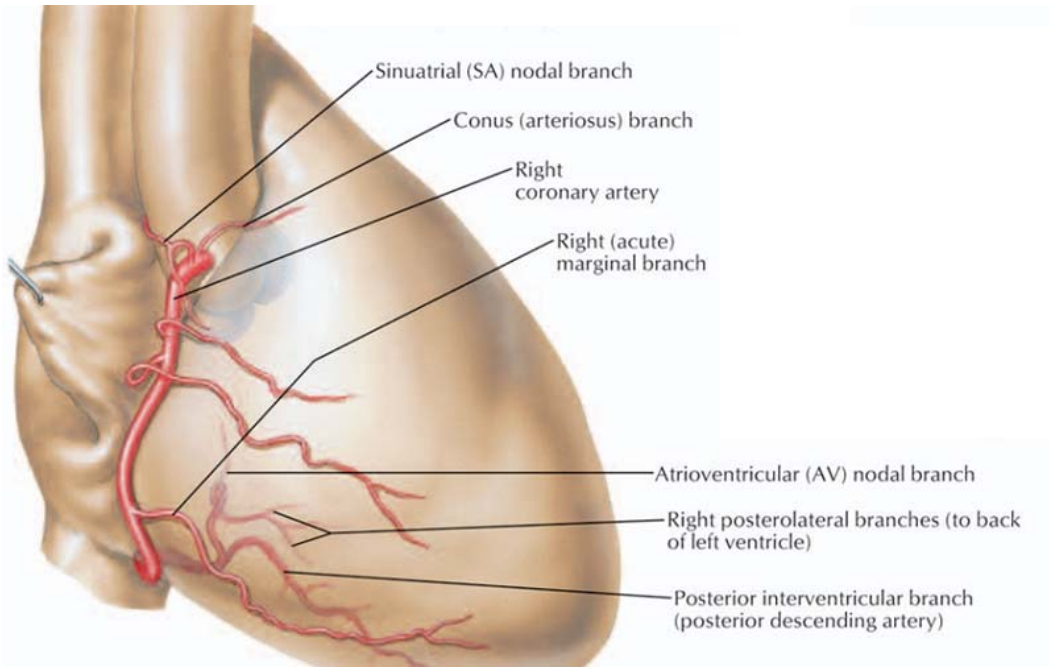

Figure 1.8: Anatomy of RCA [1].

1.3 Atheroma and its consequences

According to the WHO, CA disease is a major life-threatening disease in Europe and America and the rates of it increasing in African and Asian countries annually almost proportional to the rate of development of these countries [7]. Moreover, the deposit of atheroma within arteries is the main reason for incident of CA disease. This section contains the information about the formation of atheroma in the CAs and its consequences with visual illustrations to elaborate the severity of the disease.

1.3.1 Development of plaque

Atheroma is the deposit of fatty material within the artery wall. It develops under the tunica intima of large and medium-sized arteries (Figure 1.9(a)). As shown in Figure 1.9(b), the initial changes of atheroma show a fatty streak in the artery wall. Mature

plaque accumulates cholesterol and other lipids, excess smooth muscle and fat-filled monocytes (foam cells) as shown in Figure 1.9(c) [1]. Matured plaque is covered with a rough fibrous cap and spread further along the artery wall and protrudes into the lumen when it is grown and is thick. As a result, the vessel lumen narrows and restricts the blood flow to a certain extent. Moreover, the plaque may rupture as depicted in Figure 1.9 (d) and expose sub intimal materials to the blood. This may cause clotting of the blood in a part of the circulatory system (also known as thrombosis) and narrowing of blood vessels (also known as vasospasm) to restrict the blood flow within the vessels further.

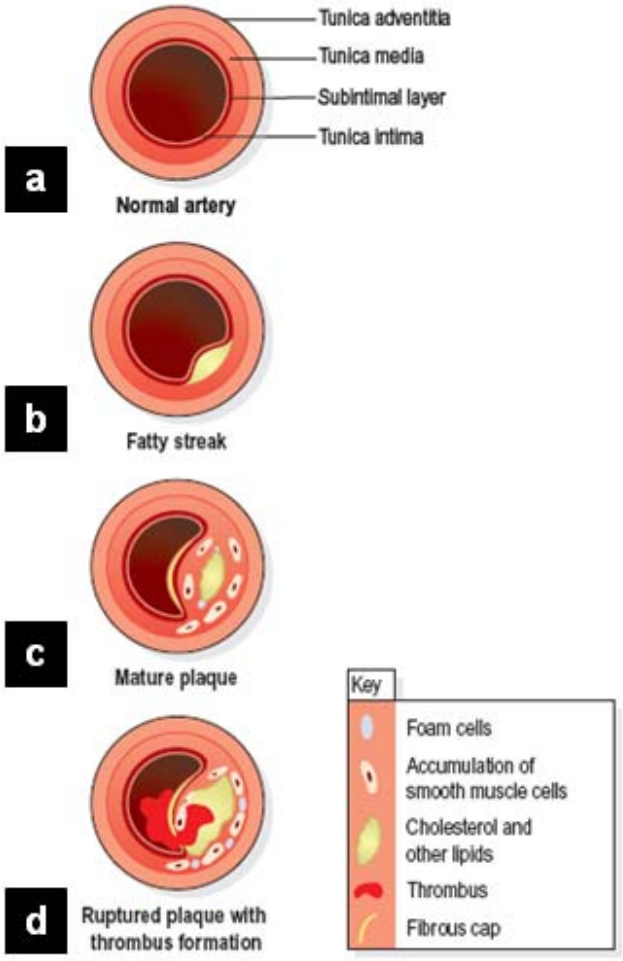

Figure 1.9: Stages in the development of atheromatous plaque [1].

1.3.2 Consequences of atheroma

Atheromatous plaque may cause partial or complete obstruction of an artery. Atheroma causes ischaemia due to the luminal narrowing. Further, it results in the reduction of blood flow to the heart muscles, which obtain the blood from the narrowed artery. As a result, these effected myocardial tissues may die due to reduction in the supply of Oxygen and nutrients required for its normal functioning. Chest pain, which is known as angina is the main symptom of the ischemia.

The complete obstruction of a CA is considered as occlusion that causes through atherosclerosis. As depicted in Figure 1.10, atherosclerosis is a process in which blood, fats such as cholesterol, and other substances build up within the artery walls, this forming plaque over a period of time. Finally, this plaque blocks the arteries completely and later it could be ruptured. These ruptured plaque causes blood to clot within the artery. As a consequence, the myocardial infarction occurs, which is considered as a serious consequence that causes death.

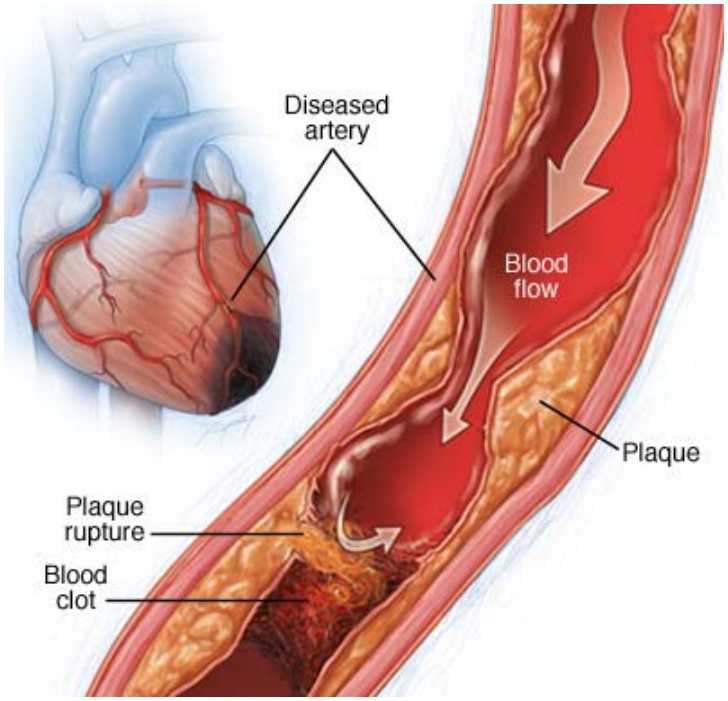

Figure 1.10: The effect of atheromatous plaques [1].

WHO has reported that 7.2 million global deaths occurred in 2008 due to ischaemic heart disease and it was the highest number of deaths reported out of all deaths under various disease categories [7]. As CA disease is one of the major life threatening conditions all over the globe, it is better to discuss about the available diagnosis methods used to detect and measure the severity level of ischaemia. The next section of this chapter will elaborate some of the available diagnosis methods widely used by the clinicians.

1.4 Diagnosing CA disease

The diagnosis method in CA disease can be divided into two categories namely invasive techniques and non-invasive techniques [8]. The main difference between these two techniques is that the invasive techniques are all catheter-based imaging techniques, which use contrast agents or imaging sensors carried to the desired location inside the vessel by a catheter and non-invasive techniques are not based on catheters[8]. X-ray angiography, Intra-vascular ultrasound (IVUS), Optical Coherent Tomography (OCT) and Fractional Flow Reserve (FFR) can be listed as invasive diagnosis methods. Moreover, stress echo-cardiography, Single Photon Emission Computed Tomography (SPECT), Positron Emission Tomography(PET), Cardiac Magnetic Resonance Imaging (CMRI), Multi Slice Computer Tomography (MSCT) are considered as non-invasive diagnostic techniques [9]. Following sub sections briefly explain about each of these diagnostic modalities under the aforementioned two categories for further clarifications.

1.4.1 Non- invasive diagnostic methods

This section briefly describes the non-invasive diagnostic techniques used in the cardiac clinical procedures namely Stress echo-cardiography, SPECT, PET, CMRI and MSCT.

Stress echo-cardiography

Stress echo-cardiography uses ultrasound imaging to determine how well the heart muscles are working to pump blood to the body [10]. During the test, a resting echo-cardiogram (a test uses ultra sound waves to create moving pictures of the heart) is

done first. Afterwards, the patient is asked to exercise on a treadmill or stationary bike and while the patient is exercising the doctor monitors the blood pressure and heart rhythm. When the patients' heart rate reaches peak levels, the doctor will take ultrasound images of the heart to determine whether the heart muscles are getting enough blood and Oxygen while exercising. These images represent the heart muscles, which do not work well when the heart rate is increasing. Moreover, it indicates that part of the heart may not be getting enough blood or Oxygen because of narrowed or blocked arteries [11]. Figure 1.11 depicts the different views of the stress echo-cardiography. The ventricles and atria are marked in each view depicted in this image to recognize the placement of them.

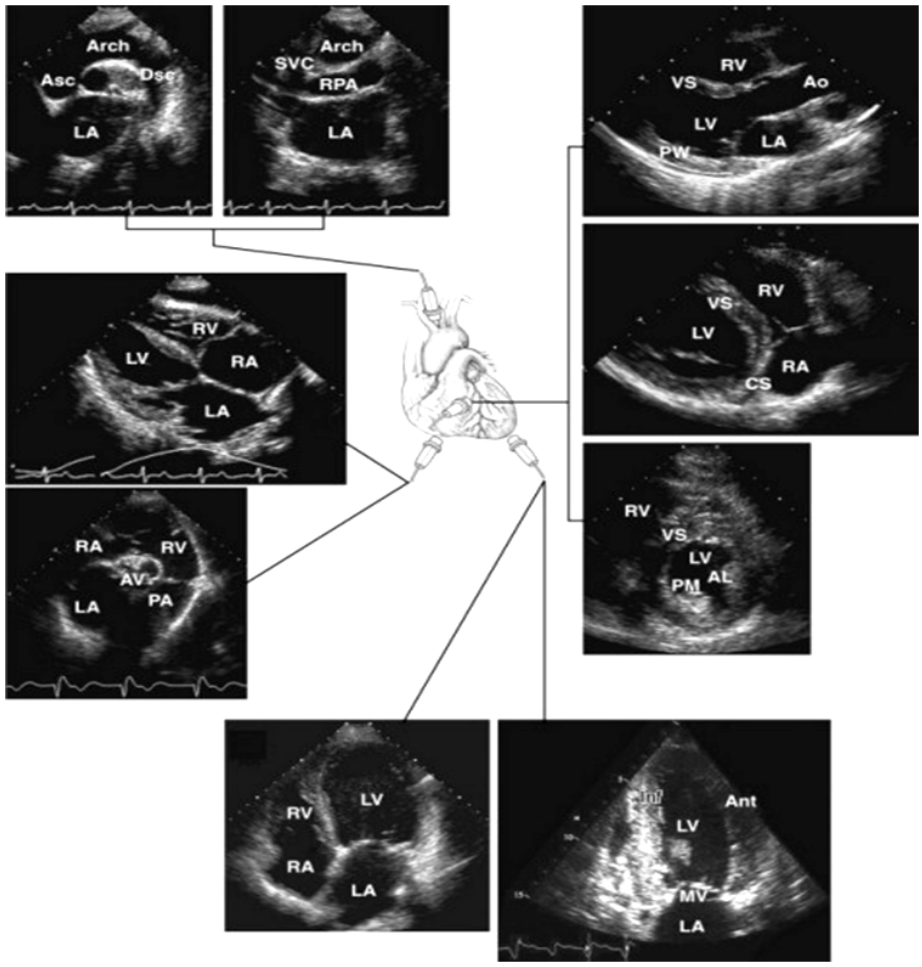

Figure 1.11: Views of stress echo-cardiography. (RA- right atrium, RV- right ventricle, LA- left atrium, LV – left ventricle)

SPECT

SPECT uses gamma rays for imaging and it is considered as a nuclear medicine topographic imaging technique. It produces three-dimension planar images using gamma cameras [12]. SPECT scans use radioactive material called tracers. These tracers are injected in to the blood circulation, which is taken up by living heart muscle. Then the gamma camera captures the signals from the tracer as it moves around the chest and these signals are converted into images by a computer [13]. The underlying principle of SPECT is that under conditions of stress, the diseased myocardium receives less blood flow than normal myocardium. As shown in Figure 1.12, this method was developed to evaluate myocardial perfusion and viability. It is applied both at rest and after exercise or pharmacologic stress to assess ischeamia [12].

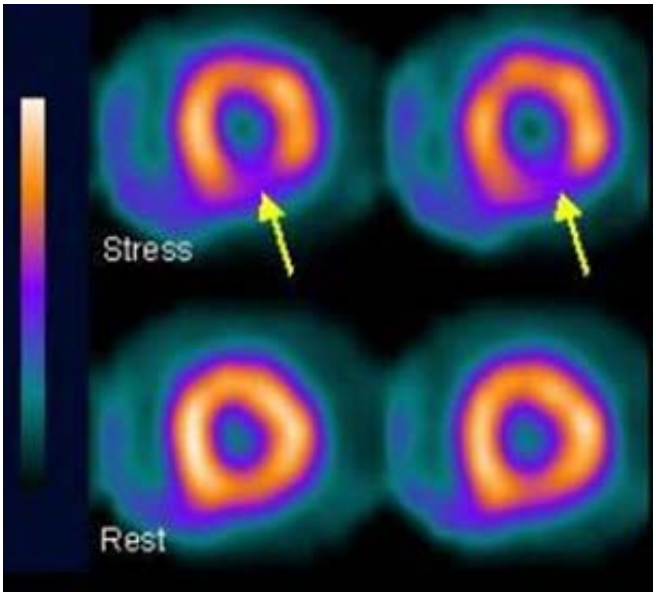

Figure 1.12: SPECT imaging [12]. (The upper row shows short-axis slices after stress condition and the lower row shows the same slices when the body is at rest. Arrows indicate an ischeamic region of the heart wall).

PET

PET is also considered as a nuclear medicine topographic imaging technique and produces three-dimension image of functional processes in the body. In cardiac PET imaging, three positron-emitting radiotracers are used for assessing myocardial perfusion and evaluating myocardial glucose metabolism and viability [11]. These tracers are injected in to the blood circulation to take it up to living heart muscle. The tracer is chemically incorporated in to a biologically active molecule and has a waiting period while the active molecule becomes concentrated in tissues of interest. Afterwards, these injected radiotracers undergo positron emission decay and emits a positron. Encountering of positron with electron annihilates them both and produces gamma rays as a result. These gamma rays are detected by the gamma camera and converted them in to the images by a computer.

Cardiac MRI (CMRI)

The MRI uses radiofrequency and high intensity magnetic fields to generate three-dimension tomographic images. CMRI images have high resolution and excellent tissue contrast [11]. MRI techniques were developed to localize the small amount of radio frequency energy generated from spinning hydrogen protons when a patient is placed in a strong magnetic field. The CMRI technique is as follows; the human body is mainly composed of water molecules, which each contain two hydrogen nuclei or protons and these protons align with the direction of the field when a patient goes inside the powerful magnetic field of the scanner. At this stage, a second radiofrequency electromagnetic field is turned on causing the protons to absorb some of its energy. Afterwards, this radiofrequency electromagnetic field is turned off. During this time, the protons release previously absorbed energy at a radiofrequency, which can be detected by the scanner. The position of protons in the body can be determined by applying additional magnetic fields during the scan, which allows an image of the body to be built up. Moreover, the CMRI test represents the visuals of heart's structure including muscle, valves and chambers. Additionally, it determines how well blood flows through the heart and major vessels. Figure 1.13 depicts a CMRI recorded under the rest and stress condition to determine the perfusion.

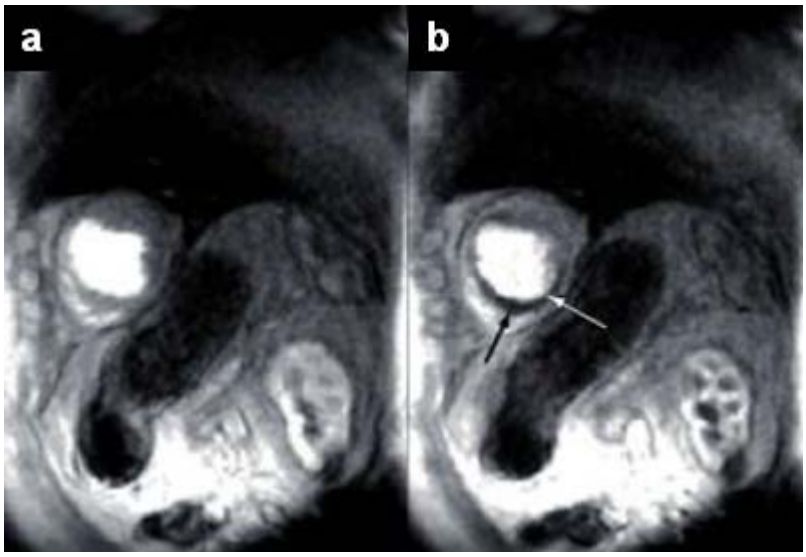

Figure 1.13: Cardiac MRI. (a) recorded under rest, (b) recorded under stress (arrow head pointing to sub endo-cardial perfusion defect.) [11].

MSCT

Traditional X-ray gets internal image of a section of the body only from one angle. The MSCT provides multiple X-ray images of a body section from various angles. It gives high-resolution images of bones and soft tissues inside the body to help clinicians identify defects easily and accurately. MSCT captures series of cross sectional images of the body, which are put together to form complete three-dimensional picture. Cardiac MSCT, could produce images of the beating heart, and visualize calcium and internal blockages in CAs. Moreover, the advent of the technically improved 16-row MSCT scanner, with higher spatial and temporal resolution, has permitted more reliable detection of coronary plaques and significant obstructive coronary lesions [14]. Figure 1.14 depicts the visual illustration of occlusion and RV branch in the mid part of the RCA produced as the output of MSCT.

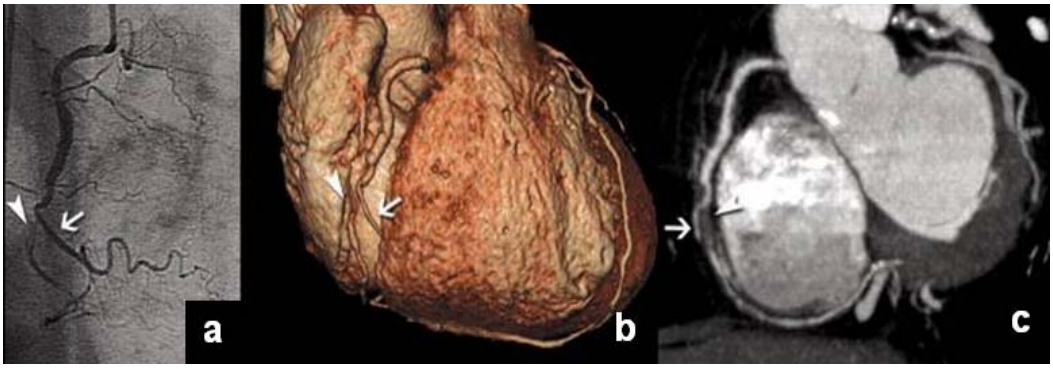

Figure 1.14: MSCT Imaging. (Arrow head points to an occlusion and arrow points to RV branch of the RCA.) (a) conventional angiography image; (b) corresponding volume rendered CT image; (c) CT of maximum intensity projection [14].

1.4.2 Invasive diagnostic methods

As mentioned at the beginning of this section, all these invasive diagnostic methods are catheter based imaging techniques with contrast agents or imaging substance carried to the desired location inside the vessel by a catheter [8]. This section briefly describes X-ray angiography, IVUS, OCT and FFR techniques, which are used as the invasive diagnostic methods in cardiac clinical procedures.

X-ray angiography

X-ray angiography or coronary angiography remains the main investigation for identifying CA narrowing related to CA disease and is a definitive, gold standard diagnostic procedure, which is a widely recommended as a preliminary diagnostic modality in cardiac clinical procedures [15]. It uses special dye (contrast agent) and X-rays to examine the CAs and provides the excellent two dimensional visualizations of the CA lumen. It is important to note that this research study is also based on the coronary angiography. Hence, this section discusses about the angiography procedure carried out in the cardiac catheterization lab (cath lab) and is also known as cardiac catheterization. The comprehensive discussion and analysis of this image modality is included in Chapter 2.

According to the cardiac catheterization procedure, the instruments for diagnosis and intervention of the CAs can be introduced through several access points in the human body such as radial artery, brachial artery or femoral artery. Out of them, the femoral artery is often favored for its size, ease of insertion, and least tortuous path to the heart. As the initial step, the shaved and sterilized lateral groin of the patient is anesthetized with local anesthesia. Then the Cardiologist locates the insertion position in the femoral artery and inserts the seldinger needle into the femoral artery at an angel between 35^0 and 45^0. As the next step, a guide wire is inserted through the seldinger needle in to the femoral artery. After the successful insertion of the guide wire the seldinger needle is removed and an arterial sheath with dilator is inserted over the guide wire. After that, the guide wire and dilator are removed from the arterial sheath. Now, the sheath is in place to receive a catheter. Thereafter, a soft flexible catheter is pushed and threaded up to the heart and this procedure is monitored using a continuous X-ray imaging device called a fluoroscope. At this point the tip of the catheter is positioned just inside the CA (ostium of the CA) to be imaged. In order to visualize the CA lumen, a special dye (contrast agent) is injected into the CA through the catheter. The dye allows the fluoroscope to take X-ray images called angiograms of the arteries' interior. Any blockages will be clearly identified by the arteries filled with the dye. Figure 1.15 depicts the visual illustrations of cardiac catheterization and a view of a coronary angiogram of CX artery.

During coronary angiography, full-motion X-ray images are viewed and recorded with the use of a video camera, as contrast agent is manually injected into the CA. In the majority of modern cardiac catheterization suites, the images are recorded digitally. Many labs also film a cine-angiographic 35 mm copy for review and archiving purposes. Various views or projections of the coronary angiograms are obtained by rotating the X-ray video camera around the patient and Chapter 2 broadly discusses about these angiogram views further.

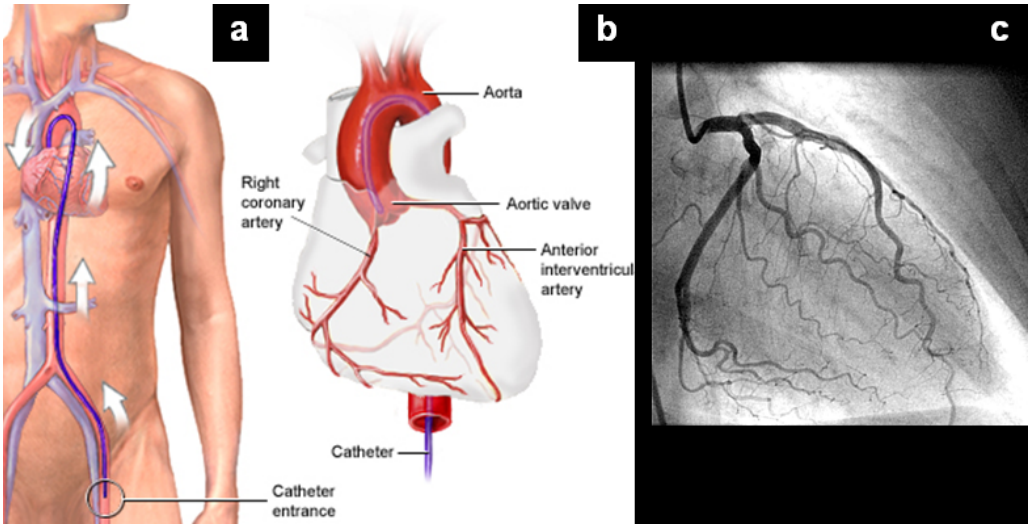

Figure 1.15: Angiogram procedure. (a) catheter placement; (b) placement of the tip of the catheter at the beginning of RCA; (c) coronary angiogram image [1].

IVUS

IVUS test generates images of inside the blood vessels and is based on sound signals. It uses a catheter with a tiny ultrasound wand to the top of it [16]. During the IVUS procedure, this ultrasound catheter is inserted into an artery in patients' groin area and moved up to the CA over the guide wire, so that it is placed distal to the lesion [17]. A computer measures the ultra sound waves reflect off blood vessels, and convert the ultra sound waves into images. Output provided by the IVUS can be used to analyze the CAs both qualitatively and qualitatively. Visualizing the inside of the normal CA, studying the morphology of atherosclerosis can be emphasized as major qualitative analysis based on IVUS. Further, measuring atheroma and vessel diameter are some of the instance for quantitative analysis that can be done using the IVUS. Moreover, IVUS can be used to determine changes in vascular dimensions during the development of atherosclerosis (arterial remodeling) [18]. Figure 1.16 represents visual illustration of IVUS based plaque characterization and arrows in the sub images represent plaque deposits in CA wall [17].

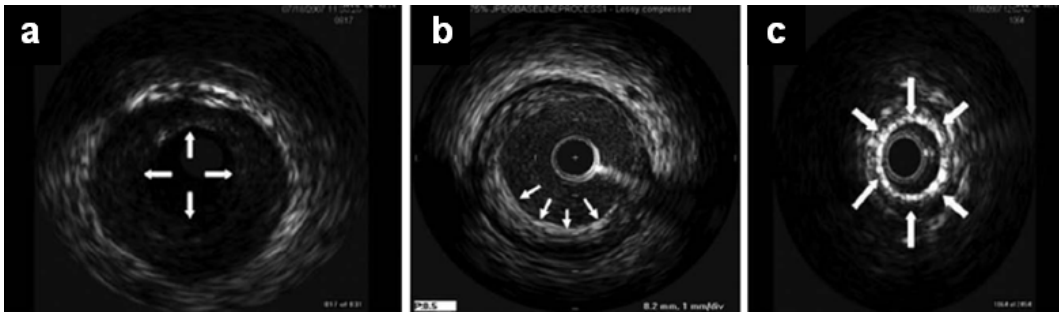

Figure 1.16: IVUS plaque characterization. (a) concentric soft plaque (white arrows); (b) fibrous plaque (white arrows); (c) fibro calcified plaque with a 360° arch of Calcium (White arrows) [17].

OCT

OCT is another medical image modality, which is used to get the internal images of the blood vessels. The image source of OCT is Near-Infrared (NIR) light. Compared to IVUS, OCT delivers high resolution internal images of the blood vessels. Similarly as in IVUS, a beam of NIR light is directed at the CA during the cardiac OCT procedure. Then some of the NIR light reflects from inside the artery tissue and some of it is scattered. This scattered NIR light causes an effect called "glare" and using OCT, the glare can be filtered out. The reflected NIR light that is not scattered can be detected and used to form the OCT image of the CA. OCT clearly visualizes the plaque inside an artery. Moreover, it assists to find out the extent of fat or clot in inside an artery. Not only that, but also OCT assists during the cardiac stenting procedure for taking precise measurements before and after placing stents in diseased arterial regions [19]. Figure 1.17 depicts two sub images of OCT of CA, which contained ruptured plaque with a thin fibrous cap at the site of an acute coronary syndrome culprit lesion [20]**.**

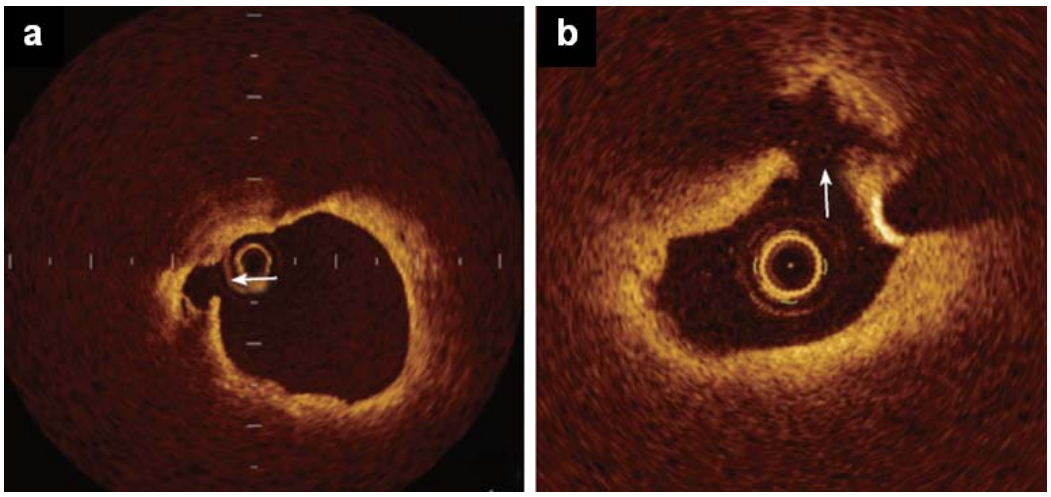

Figure 1.17: OCT imaging. (Arrows represent ruptured plaque with a thin fibrous cap at the site of an acute coronary syndrome culprit lesion.) [20].

FFR

FFR is a guide wire-based procedure that can accurately measure blood pressure and flow through a specific part of the CA. FFR measurement is defined as the ratio between the maximum achievable blood flow in a diseased CA and the theoretical maximum flow in a normal CA. Hence, the FFR value 1.0 is widely accepted as normal condition and the FFR value lower than 0.75-0.80 is generally considered to indication of myocardial ischeamia. In accordance with this measurement, it is clear that the FFR is a quantitative technique for evaluating the physiologic significance of a coronary stenosis and it can be measured during routine coronary angiography procedure. During the FFR test, the ratio between coronary pressure distal to a CA stenosis and aortic pressure under conditions of maximum myocardial hyperemia is calculated by using a specific pressure wire. This ratio represents the potential decrease in coronary flow distal to the coronary stenosis [21][22]. Figure 1.18 depicts the two FFR cases extracted from [23] for further clarification. Two angiography detected stenosis areas are marked in the two sub images represent in Figure 1.18 (arrow) and respective FFR readings are also included in those images for comparing the severity of the stenosis. Moreover, Appendix A enlists the strength and limitations of the cardiac medical image modalities discussed in this section.

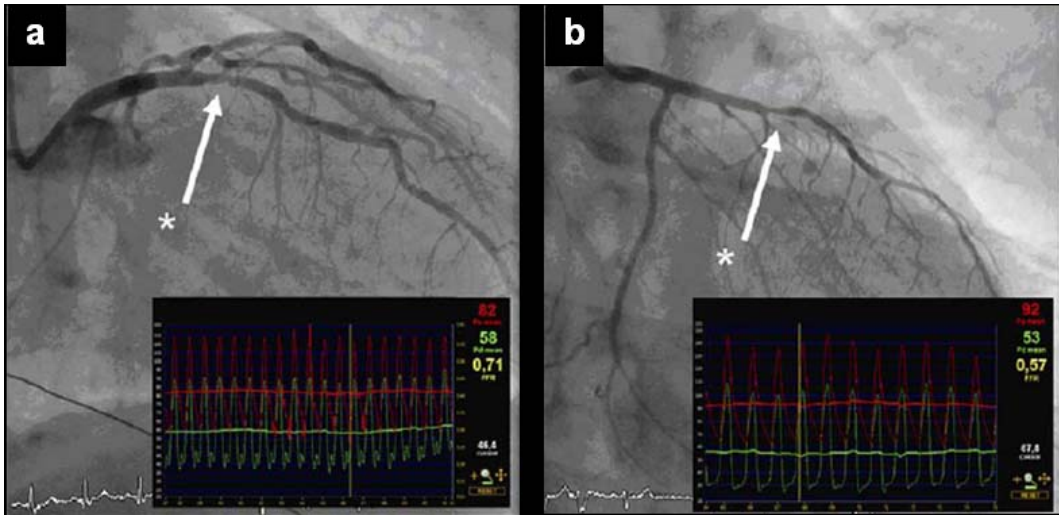

Figure 1.18: FFR results. (a) represents 0.71 FFR value for the marked stenosis area (arrow); (b) represents 0.57 FFR value for the marked stenosis area (arrow) [23].

1.5 Treatments for CA disease

Although CA disease cannot be cured, treatment can help manage the symptoms and reduce the risk of further problems. Hence, the objective of this section is to highlight the available treatment methods recommended by the Cardiologists for managing the CA disease. It is noted that the CA disease can be managed effectively with a combination of lifestyle changes, medicine and, in some cases, surgery. Nonetheless for most patients, treatment methods are recommended based on the diagnosis results provided by the cardiac image modalities mentioned in the section 1.4 above.

Positive lifestyle changes or CA disease preventing practices help patients to mitigate the risk of causing CA disease. The main objective of these practices is to reduce the risk of developing CA disease by maintaining the blood pressure and cholesterol levels are under control. Having a healthy balanced diet, being more physically active, keeping to a healthy weight according to the body mass index, giving up smoking and alcohol consumption, keeping diabetes level under control and taking any medication prescribed can be listed as the CA disease prevention practices.

CA disease can be controlled by medical management as well. Many different medicines are used to treat CA disease and the aim of these medicines is to either prevent narrowing of CA that reduce the risk of blood clot formation or widen the arteries. Antiplatelets, statins, beta-blockers, nitrates, ACE (Angiotensin-Converting Enzyme) inhibitors, angiotensin II receptor antagonists and Calcium channel blockers are the types of medicines prescribed for the CA disease.

If the blood vessels are narrowed as the result of a build-up of atheroma or if the symptoms cannot be controlled using medication, interventional procedures or surgery may be recommended by the Cardiologists. Coronary angioplasty and CA bypass graft are the main procedures used to treat blocked arteries.

A coronary angioplasty is invasive procedure used to widen blocked or narrowed CAs to improve blood flow to the heart muscle. It is also known as Percutaneous Coronary Intervention (PCI). Before the procedure is done; it is required to detect the location and extent of the blockages in CAs using a coronary angiogram. There are two types of coronary angioplasty procedures available namely; plain balloon angioplasty and angioplastry stenting. In balloon angioplasty, a small balloon-tipped catheter (balloon catheter) is guided to the site of blockage from the incision made in either groin or wrist, following the administration of local anesthesia. As depicted in Figure 1.19, once the catheter is correctly placed at the location of the blockage, the balloon is inflated to compress the plaque. As a result of that, the arterial lumen is widened and increases the blood flow within the treated CA. Subsequently, the balloon is deflated and removed along with the catheter.

The angioplasty stenting procedure is also similar to balloon angioplasty, but involves the use of small, expandable metallic scaffolding called “stent”, along with the balloon. Further, this stent is placed around the balloon in as a compressed form. As depicted in Figure 1.20, when the balloon is inflated, the stent expands and compresses the plaque. Finally, the balloon is deflated and removed, leaving the stent within the treated CA. Moreover, this stent acts as a support to keep the artery open.

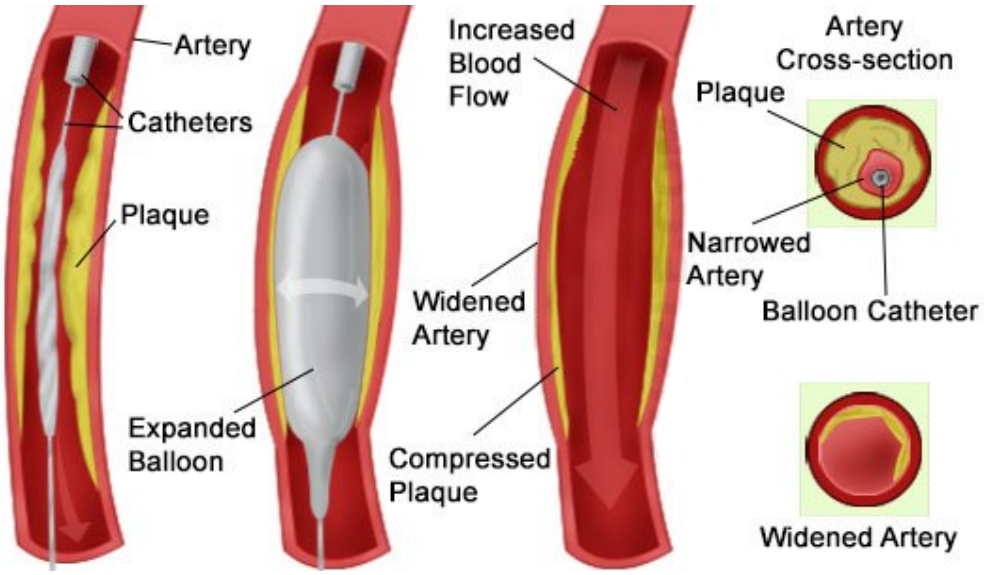

Figure 1.19: Steps of the balloon angioplasty [24].

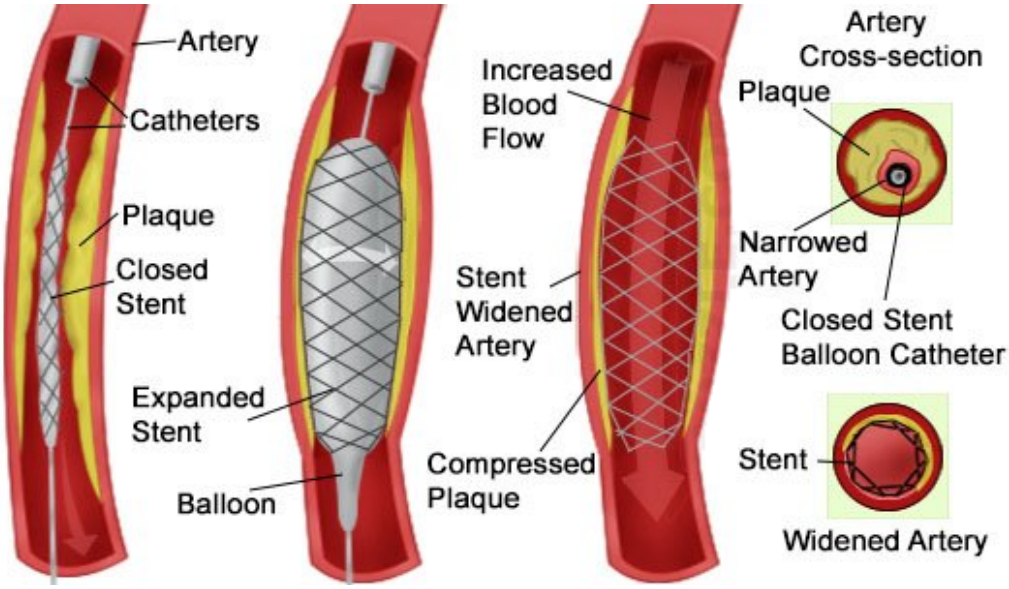

Figure 1.20: Steps of the stent angioplasty [24].

CA bypass grafting or bypass surgery is performed in patients whose arteries become narrowed or blocked completely. The Cardiologists recommend this surgery after analyzing the coronary angiogram of the patient. During the surgery, a blood vessel is inserted (grafted) between the aorta and a part of the CA beyond the narrowed or

blocked area. As a result of that, the blood bypasses the narrowed sections of CA and supplies the Oxygen and nutrients to the effected myocardium.

1.6 Problem in brief

According to the literature evidence and empirical studies, two main factors, which make negative consequences for angiography based stenosis assessment has been identified. Those are subjective stenosis assessment and visual degradations in angiograms. The results of the recent research study have been published that the subjective stenosis assessment leads to overestimations and underestimations of the detected stenosis [23][25]. Further, it is proven by Tonino in his latest investigation of finding the relationship between angiography and functional severity of coronary artery stenosis in the Fractional Flow Reserve Versus Angiography in Multivessel Evaluation (FAME) study [23]. Further, it is apparent that this subjective stenosis assessment effects to the patient's quality of life adversely.

Noise, poor opacification, non-uniform illumination, motion and superimposition of vessels with other organs like heart, ribs and spine are considered as the factors, which cause visual degradations in angiograms[25-29]. These factors create some disturbances in subjective diagnosis procedures. Moreover, recent research attempts have reported that these visual degradation factors cause some hindrances when formulating objective stenosis diagnosis approaches based on coronary angiography [25-29]. These negative consequences of angiogram image modality have been clearly elaborated in Chapter 2 and Chapter 3 with the literature evidences.

Even though angiography has limitations in quantitative assessment and effects of visual degradations, it is still the most common modality for clinicians to assess the severity of stenosis during PCI[26]. One of the main reasons for that is, it provides excellent visualizations of arterial lumen, which can be used for stenosis diagnosis and treatment planning. Moreover, it is a low cost invasive image modality compared to IVUS, FFR and OCT and the equipment is readily available in most hospitals, even in less-developed countries. In addition to that, all cardiologists are familiar with the equipment, and have experience in interpreting the resulting images.

Further, the angiography is a relatively short imaging procedure, which facilitates effective clinical planning [30].

1.7 Study aim and objectives

The above brief problem discussion, has revealed the necessity of formulating an automated mechanism for precisely diagnosing CA disease quantitatively by processing the coronary angiograms [31]. Therefore, the potential to improve the angiography for objectively assessing the severity of the detected stenosis in CAs has been recognized.

During the cardiac catheterization, CCAs are also produced under different views. A CCA consists of a sequence of frames that visualize the flooding of contrast agent within the CA vasculature. This feature has been identified as a good indicator to formalize a mechanism to reveal the functional significance of the vessels using the angiography image modality. As a functional feature, it has been considered to compute the flow velocity of vessels along the frame sequence of the CCA. However, from the literature, it has been revealed that very few research studies have been carried out in this area over the past decade. Hence, it has been decided to start this research study to improve the angiography medical image modality in order to detect and quantify the stenosis through CCA processing.

Therefore, the prime aim of this research study is to device a novel method to improve the CCAs for quantitative coronary analysis by using a computer vision technique.

The following study objectives have been derived in order to achieve the above aim;

- Enhancing the CCA for better visualization of the CA vasculature:

In this study objective, it is intended to reduce the observed and reported visual degradation factors such as non-uniform illumination, noise and global motion from the direct CCA to be processed. Uniformly illuminated, noise reduced and global motion stabilized framed of the processed CCA will be produced after implementation of this objective.

- Segmentation of the CA for extracting the luminal information:

Prior to formalizing a mechanism for quantitative coronary analysis, it is mandatory to isolate the main arterial region, which is also known as foreground from each individual frame of the CCA to be processed. This will be the main reason for proposing an accurate segmentation method in this research study. Segmented vessel's edge points and the medial axis points have been recognized as the important luminal information for this study.

- Developing an algorithm for detecting uniformly deposited atherosclerotic plaque within a predefined region of the CA captured from the CCAs:

In this study, in order to detect the uniformly deposited atherosclerotic plaque regions, a clinically important main CA region is isolated from the segmented CA tree visualized in each and every frame of the processed CCA. Moreover, this plaque located in the pre-defined segmented CA region can be detected by analyzing the rapid variations, which have occurred among the extracted luminal information. In order to achieve that, it is necessary to compute the diameter of the pre-defined segmented CA region by using possible algorithms. Hence, it is easy to locate the vessel diameter drops to determine the plaque regions.

- Visualizing the severity level of the detected plaque as a supportive tool for making treatment decisions:

The main target of this objective is to visualize the computed luminal information and vessel diameter along the selected vessel region depicted in the processed CCA. Moreover, it is intended to model a separate diameter distribution graph in the same view of the application to be developed as a supportive indicator for making diagnostic decisions.

1.8 Organization of the thesis

This thesis is organized into eight chapters to specify the significant aspects and outcomes of this research study. Some of the important aspects of coronary angiography for the CA disease diagnosis have been discussed in Chapter 2. The

hardware organization of the catheterization laboratory, fluoroscopy function, angiography views are broadly discussed in this chapter. Moreover, the stenosis grading methods and the problems of this image modality has been elaborated using literature evidence. Finally, the recent research attempts done for enhancement of angiograms, vessel segmentation and quantitative coronary analysis have been elaborated as the literature review.

Chapter 3 emphasizes the overall research design and the pre-processing work carried out for enhancing the visual quality of the direct CCAs. Hence, this chapter discusses the proposed methodology for frame enhancement followed by the analysis of negative artifacts, which degrade the visual quality of the CCAs.

It is indeed important to extract the CA tree from the CCA frame, which is being processed to objectively assess the severity of detected stenosis. Thus, the objective of Chapter 4 is to emphasize on a scientific approach to segment the CAs from the processed CCAs. .

Chapter 5 elaborates on the experimental approaches implemented for extracting the clinically important luminal information such as vessel boundary, skeleton and vessel diameter. Moreover, a novel vessel path tracking algorithm and diameter detection algorithms have been presented in this chapter.

Chapter 6 explains the validation methods and evaluation results of this research study. The critical discussion on the proposed method and the validation results are included in Chapter 7. Finally, the recommendations and future extensions of this study have been clearly elaborated in Chapter 8.

1.9 Summary

This chapter provides comprehensive overview of the medical background of the domain of this research study. Firstly, it covers the anatomy of human heart and the blood vessels to emphasize the organization of these organs. Moreover, this chapter provides the detailed information about the anatomy of the main CAs namely; LAD, CX and RCA because those are the main blood supply channels to the heart muscles. CA disease and its consequences are discussed as the third section of the chapter.

After that, various non-invasive and invasive CA disease diagnosis techniques are presented with visual illustrations. In addition to that, a brief introduction about the main treatment methods recommended for CA disease is also presented clearly. Research problems, suggestions for improving this image modality and research objectives have been mentioned subsequently. Finally, the organization of this thesis according to its chapter contents is introduced to easily navigate to the relevant information of this study.

CHAPTER 2
CORONARY ANGIOGRAPHY AS A DIAGNOSTIC MODALITY

Coronary angiography is a definitive, gold standard and low cost diagnostic procedure for determining the presence and severity of CA disease. The introduction to this image modality and the catheterization procedure was already discussed in section 1.4.2. Hence, the main focus of this chapter is to elaborate some of the significant aspects of coronary angiography for CA disease diagnosis. The first section of this chapter introduces about the hardware organization of the catheterization laboratory (cath lab), fluoroscopy function and the aspects of contrast agent used for the catheterization comprehensively. Typically, the coronary angiograms are taken in different views to emphasize the various CA segments in order to clearly detect the diseased areas. The next section of the chapter contains information about these angiographic views with sufficient visual illustrations to easily recognize them separately. The angiography based stenosis grading methods have been presented as the third section of this chapter. In the subsequent section, the problems of this image modality have been elaborated with the literature evidence. Finally, this chapter is concluded by mentioning the recent research attempts carried out to improve the angiography image modality under three different areas namely; the enhancement of angiograms, vessel segmentation and quantitative coronary analysis.

2.1 Principles and functions of catheterization hardware and equipment

The objective of this section is to elaborate how the cardiac catheterization hardware components function together to produce the CCA for medical diagnosis. Therefore, initially, some important facts about the catheterization laboratory setup, main hardware components and the installation of them have been emphasized. After that, the attention is given to discuss about the fluoroscopy imaging system, which is the X-ray image modality used in the cardiac cath labs to generate the CCAs. Finally, this section explains about the features of the contrast material used to opacify the vessel structures during the angiography procedure.

2.1.1 Catheterization laboratory and setup

The cath lab is setup with digital imaging equipment and computers for fluoroscopy and CCA, which is used for assessment of CA disease. Fluoroscopy is an imaging technique used to obtain real-time moving images of internal structures of the human body [32]. The fluoroscope is the device used to obtain such medical images. It shows a continuous X-ray image on a monitor, which is akin to an X-ray movie [33]. In cardiac catheterization, the fluoroscopy assists the doctor in guiding the catheter into a specific location in the heart. Moreover, it produces CCAs, which are the fluoroscopic motion-picture, recording of a blood vessel or of a portion of the cardiovascular system obtained after injecting a patient with a non-toxic radio opaque medium (contrast agent) [34]. The cine X-ray camera attached with the fluoroscope records these CCAs.

Cath lab is a combined system of several major parts. Figure 2.1 depicts a schematic of the typical cath lab equipment and important parts of it are numbered as follows;

1	C- arm	2	X-ray source tube
3	Detector	4	Catheterization table
5	X-ray generator	6	Monitors
7	Control handle	8	Pedals
9	Control room with diagnostic applications		

Following sections briefly explain about the major parts of the cath lab;

The c-arm is the largest part of the cath lab system. It is installed either as a floor-mounted or ceiling suspended arc and consists of the X-ray source tube and the detector (Figure 2.1 label 1). According to Figure 2.1, it is clear that the X-ray source tube (label 2) is placed at the bottom of the c-arm and detector (label 3) is placed on top of it. As shown in Figure 2.2, the patient is laid on the cardiac catheterization table by positioning the detector of the c-arm above the patients' chest and the X-ray source tube below the patients' table (Figure 2.1 label 2). Moreover, the c-arm could

be rotated to the left or the right of the patient. These are known as the Left Anterior Oblique (LAO) and RAO views respectively. In addition to that, the c-arm can be rotate towards (cranial) and away (caudal) from the patients head. All these movements are achieved with the help of a control handle (Figure 2.1 label 7) that is situated near the hand of the operator. In addition to the c-arm movements, controls are also available to raise and lower the patients' table, raise and lower the camera attached with the detector, change the magnification and to increase and decrease the size of the shutters.

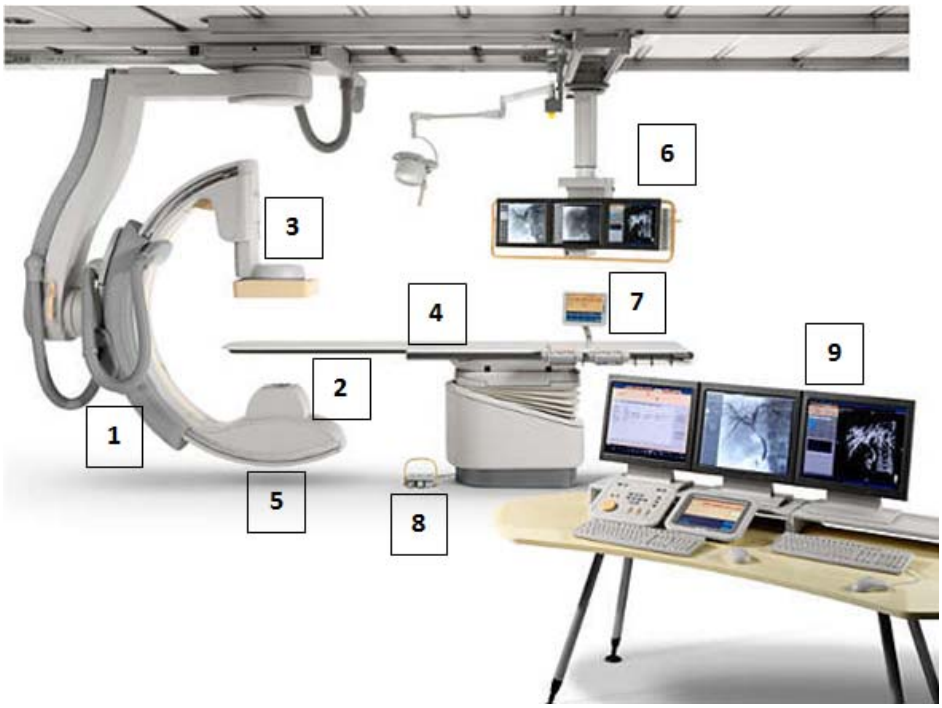

Figure 2.1: Parts of the cath lab [35].

The two pedals that activate fluoroscopy and cine filming lie on the floor, near the operator's feet and each mode is turned on by stepping on it (Figure 2.1 label 8). For example, the operator will first step on the fluoroscope pedal and confirm a position (during test injection of a small amount of contrast agent) and then switch over and press the cine pedal during the contrast agent injection.

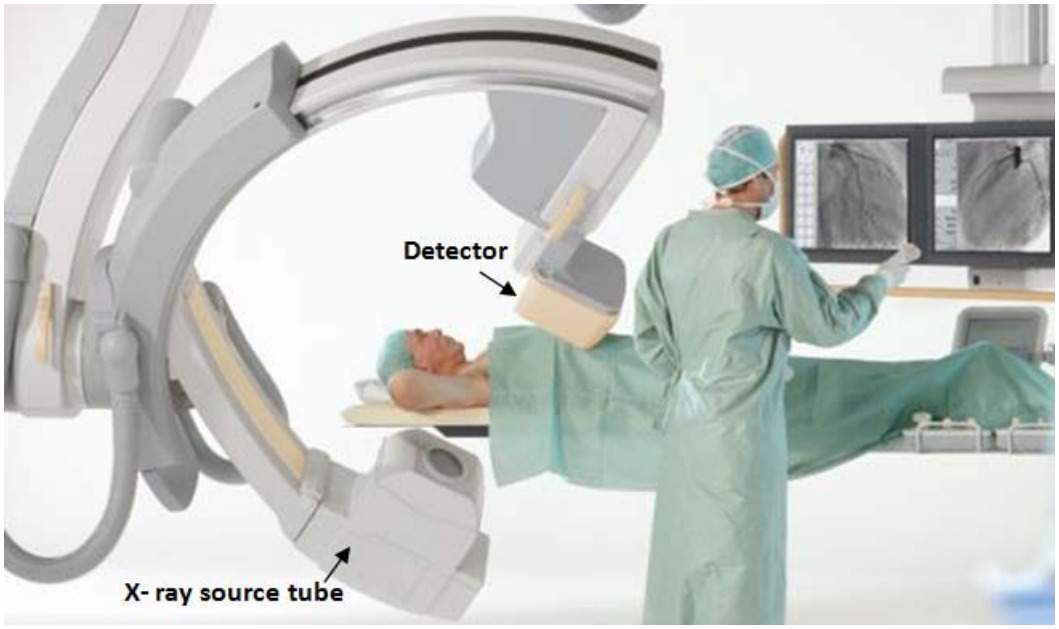

Figure 2.2: Patient placement between the c-arm [35].

The X-ray tube attached with the c-arm generates powerful X-ray pulses during the catheterization procedure. It should be a heavy-duty tube with high-heat capacity and improved heat dissipation. The X-ray generator, which is attached to the cath lab system energizes the X-ray tube by delivering the full current capacity of the X-ray tube in cine mode (Figure 2.1 label 5). The detector detects the X-rays, which pass through the patients' body in order to form the X-ray images. In older cath lab systems an X-ray image intensifier and a video camera are placed in the detector and in latest models a flat panel detector replaces the X-ray image intensifier.

The camera attached with the detector records the fluoroscopy images and those recorded images are visualized through the monitors, which are placed in the cath lab (Figure 2.1 label 6). A computer unit, which is installed with specialized digital image processing programs is located in the control room of the cath lab and is useful to diagnose and make decisions about the severity of the detected lesions (Figure 2.1 label 9).

As mentioned in this section, the CCAs are the fluoroscopic images that are used for making diagnostic decisions regarding the CA disease. Hence, it is important to

discuss about the fluoroscopy imaging system further, to identify its' X-ray image formation process and the next section of this chapter will elaborate it comprehensively.

2.1.2 Fluoroscopy imaging system

Fluoroscopy imaging system basically consists of the components that include an X-ray tube, spectral shaping filters, a field restriction device (collimator), an image receptor, an image processing computer and a display device. The schematic of a fluoroscopic system using an X-ray image intensifier and a video camera is depicted in Figure 2.3.

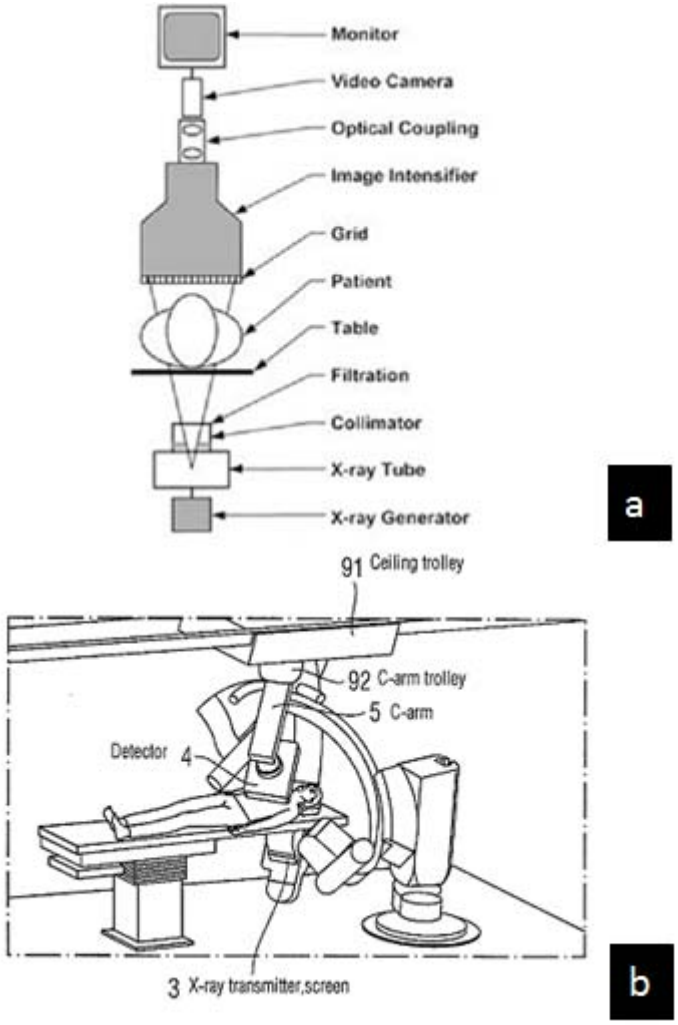

Figure 2.3: Schematic of a fluoroscopic system. (a) cross section; (b) 3-D view of angiography system [36].

The X-ray source tube of the fluoroscope consists of an X-ray generator, X-ray tube, collimator and filter. The high-voltage generator and X-ray tube are used in most fluoroscopy systems to generate X-ray pulses in order to record the anatomical structures of the human body. It is similar in design and construction to the X-ray tubes used in general radiographic applications. Fluoroscope used in angiographic systems produces clear images of moving vessels. In order to produce that, the fluoroscope needs short, powerful X-ray pulses and to achieve that it consists of a high-power X-ray generation system. Moreover, in cardiac studies, exposure time ranging from 1 to 10 milliseconds is required and the radiation output can be either continuous or pulsed [37]. Automatic exposure rate control maintains the radiation dose per frame at a predetermined level, adapting to the attenuation characteristics of the patient's anatomy and maintaining a consistent level of image quality throughput, which is required for the examination [37]. In order to limit the geometric extent of the X-ray field, either circular or rectangular shape collimator shutters are assembled in the X-ray tube. The shape of the collimation shutter depends on the shape of the image receptor of the fluoroscope. The beam hardening filters are placed in between the X-ray tube exit port and the collimator for filtration of the X-ray beam path, providing flexibility to manage the low dose and higher dose modes according to the conditions dictated during a fluoroscopic procedure. Further, it is important to note that the patients' table of the fluoroscope system does not absorb much radiation to avoid shadows, loss of signal and loss of contrast in the image.

The X-ray image intensifier or the image receptor of the fluoroscopy system is an electronic device that detects X-rays that passes through the patients' body to form X-ray images. It converts the detected X-ray beam intensity pattern into a visible image, which is suitable for capturing by a video camera and displaying on a video display monitor [32]. Further, it provides both real-time imaging capability, which allows patient positioning, catheter manipulation and recording of the angiographic injection. In order to achieve this, the X-ray image intensifier consists of four major components namely; an input phosphor layer, a photocathode, several electron optics and an output phosphor layer. Figure 2.4 depicts the comprehensive schematic of the

organization of these components in the X-ray image intensifier for further clarifications.

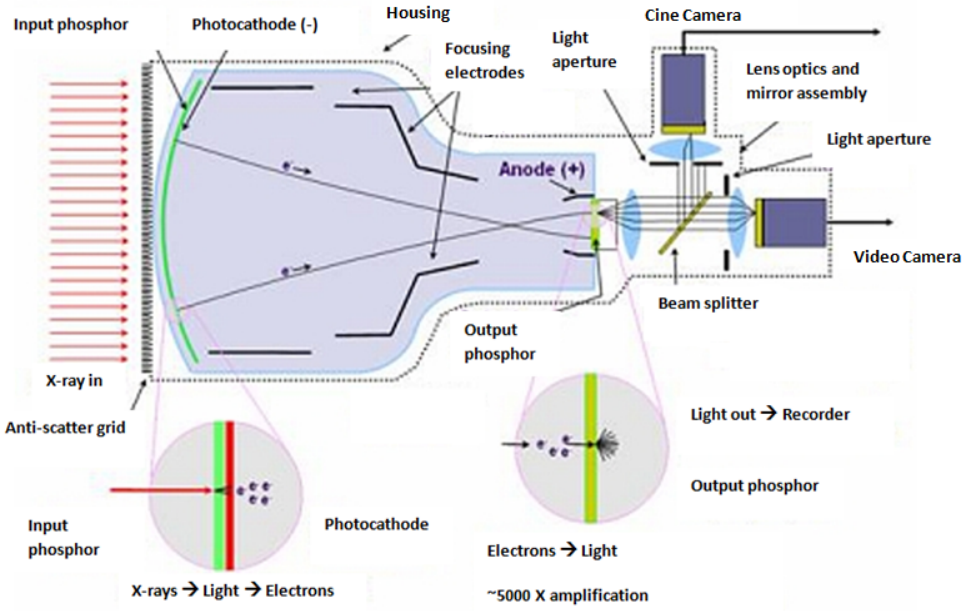

Figure 2.4: Components of an X-ray image intensifier [38].

The function of the X-ray image intensifier begins by converting the detected X-ray image into a visible light image. It is done by the input phosphor layer equipped with the X-ray image intensifier. As the next step, the photocathode which is placed in close proximity to the input phosphor layer releases electrons directly proportional to the amount of visible light from the input phosphor that is incident on its surface. These released electrons are steered, accelerated and multiplied in number by the electron optic components and finally contact the surface of the output phosphor layer in the X-ray image intensifier. The coated phosphor material in the output phosphor layer glows visibly when struck by high energy electrons and converts them into light. After that, a video camera, which is optically coupled to this phosphor screen observes the intensified image and forwards it to a computer for post-processing. Finally, these post-processed signals are rendered using the display devises to visualize the detected anatomical structures. The brightness of the images produced by the X-ray image intensifiers are achieved by increasing the electron

energy produced by the accelerating potential and decreasing the size of the image as it is transferred from the input to the output phosphor [32].

As shown in Figure 2.4, output phosphor layer of the X-ray image intensifier is coupled to a video camera. Further, a film camera is also assembled in angiography devises, which is used for the cardiac imaging to produce the CCAs. This film camera is a 35 mm motion picture camera and is optically attached to the image intensifier output phosphor (Figure 2.4). In order to record the fluoroscopic image with the video camera and film camera, the X-ray image intensifier should be able to divide the light coming from the output phosphor layer and direct it in two separate paths. This system of reflecting light in two directions is called beam splitting and it is done by a semi transparent mirror (beam splitter), which is placed between the image intensifier and the video camera tube. Ninety percent of the light is reflected to the film camera while the remaining light passes through the mirrors and is received by the video camera [39]. The video cameras used in X-ray image intensifier systems were originally analog devices borrowed from the broadcast television industry but later systems equipped with digital cameras based on charge-coupled device image sensors or complementary metal oxide semiconductor technology were used.

The modern angiographic suites are produced with the digital image processor unit, which is used for real time processing of the captured images by the video camera. Spatial filtering, temporal filtering, image-subtraction and integration algorithms are implemented with this image processor unit to post-process the images before rendering.

In modern fluoroscopy systems, the X-ray image intensifier and video camera components are replaced by a flat panel detector. The flat panel detector consists of an array of individual detector elements. These elements are square shape and 140–200 microns per side [36]. Further, those are fabricated using amorphous silicon thin-film technology onto glass substrates. A single detector may contain as many as 5 Million detector elements. However, these flat panel detectors are more beneficial than X-ray intensifier based detectors since it avoids the different types of imaging artifacts, which are associated with X-ray image intensifiers such as geometric “pin-

cushion" distortion, "S" distortion, veiling glare (glare extending from very bright areas) and vignetting (loss of brightness at periphery). Moreover, the dynamic range of the images produced by the flat panel detectors is wider than the X-ray image intensifier based detectors, therefore the quality of the images increases in the flat panel detectors.

2.1.3 Contrast material

During coronary angiography, the contrast material is needed to clearly visualize vessel structures because the radiographic contrast of blood is similar to the soft tissues. Contrast material consists of an iodine-containing compound, with maximum iodine concentrations of about 350 mg/cm^3 [32]. Contrast material is injected through a catheter ranging in diameter roughly from 1 to 3 mm and the radiographic images of the contrast-filled vessels are recorded using either film or video during the angiography procedure [32].

It is important to note that, these hardware devices are customized optimally during clinical procedures in order to obtain the better images for diagnosis. As a result of that, the CAs are recorded under different standard angiographic views for obtaining better visualizations of the different vascular sections to detect and assess the disease regions. The next section of this chapter will discuss about these standard angiography views and how these views used for the stenosis detection.

2.2 Angiography images

Multiple views from different angles of coronary angiograms need to be obtained in order to accurately diagnose CA disease. It is essential to ensure that all required CA segments are seen clearly in recorded angiograms without foreshortening or overlapping vessels [5]. In order to achieve that, there are standard angiography projection views available. This section will discuss about those standard angiography projection views used in interventional cardiology.

2.2.1 Angiography views

The c-arm is placed perpendicularly across the anterior posterior direction of the patient who is laid on the cardiac catheterization table and this positioning of the c-arm produces the default angiography view namely Anterior-Posterior (AP) view. However, in this default angiographic view, the spine sits in the middle of the CCA picture and the CAs lie directly in front of it. This will interfere with the visual quality of the CCA because the similarity in radiographic density between the spine and the contrast filled CAs interfere. Hence, multiple CCAs need to be recorded during the cardiac catheterization procedure under different standard angiography views. These angiography views are obtained by moving the c-arm in various angulations. Moreover, these angulations of each view are given by two major movements of the c-arm namely; rotation and skew. As described in section 2.1.1, the c-arm can be rotated towards the left and right directions of the patient and these views are known as the LAO and RAO views, respectively. The amount of angulation of the c-arm towards the patient's head or foot is known as cranial and caudal views, respectively. Cranial and caudal views are used to open overlapped coronary segments that are foreshortened or obscured in regular views [40]. Moreover, this nomenclature for radiographic projections is depicted in Figure 2.5 for further clarifications.

It is important to emphasize some visual indications in the angiogram images obtained under the prior mentioned angiography projections to recognize the exact view directly. Figure 2.6 highlights such visual indications for each angiography projection clearly. According to Figure 2.6 (a), in LAO view, the spine and catheter are placed on the right and left sides of the image respectively. Nonetheless in RAO and caudal angulations the catheter and spine are found on the left side of the image (Figure 2.6(b)). In AP and cranial projections, both the catheter and spine are located in the center of the image. Moreover, these projections visualize the shadow of diaphragm across the angiogram image as depicted in Figure 2.6(c).

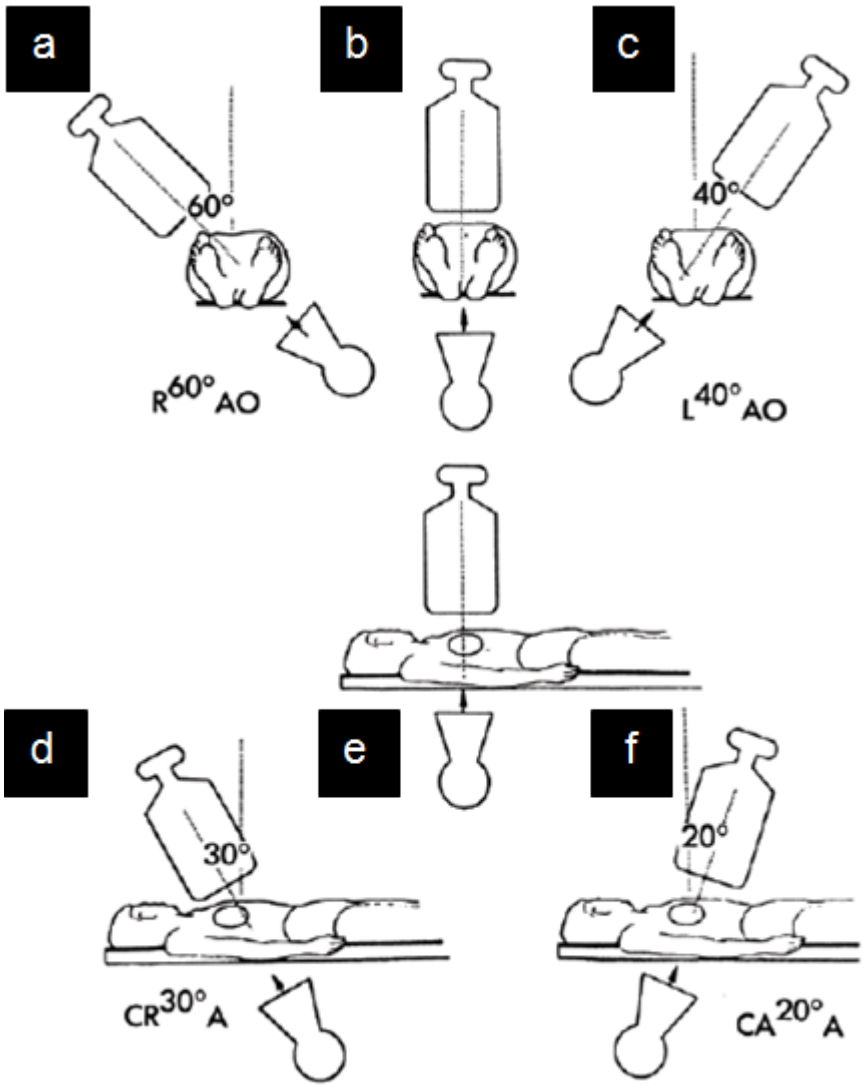

Figure 2.5: Nomenclature for angiography projections. (Arrow heads show the direction of the X-ray beam.) (a) RAO; (b) AP; (c) LAO; (d) cranial view; (e) AP viewed from patient's side; (f) caudal view [41].

These views highlight specific and distinct segments of the coronary anatomy and permit discrete visualization of underlying pathologic conditions. Understanding of the usefulness of various radiographic views (and nomenclature) is essential [40]. Following sections briefly discuss about the important aspects of each of the angiography views with visual illustrations.

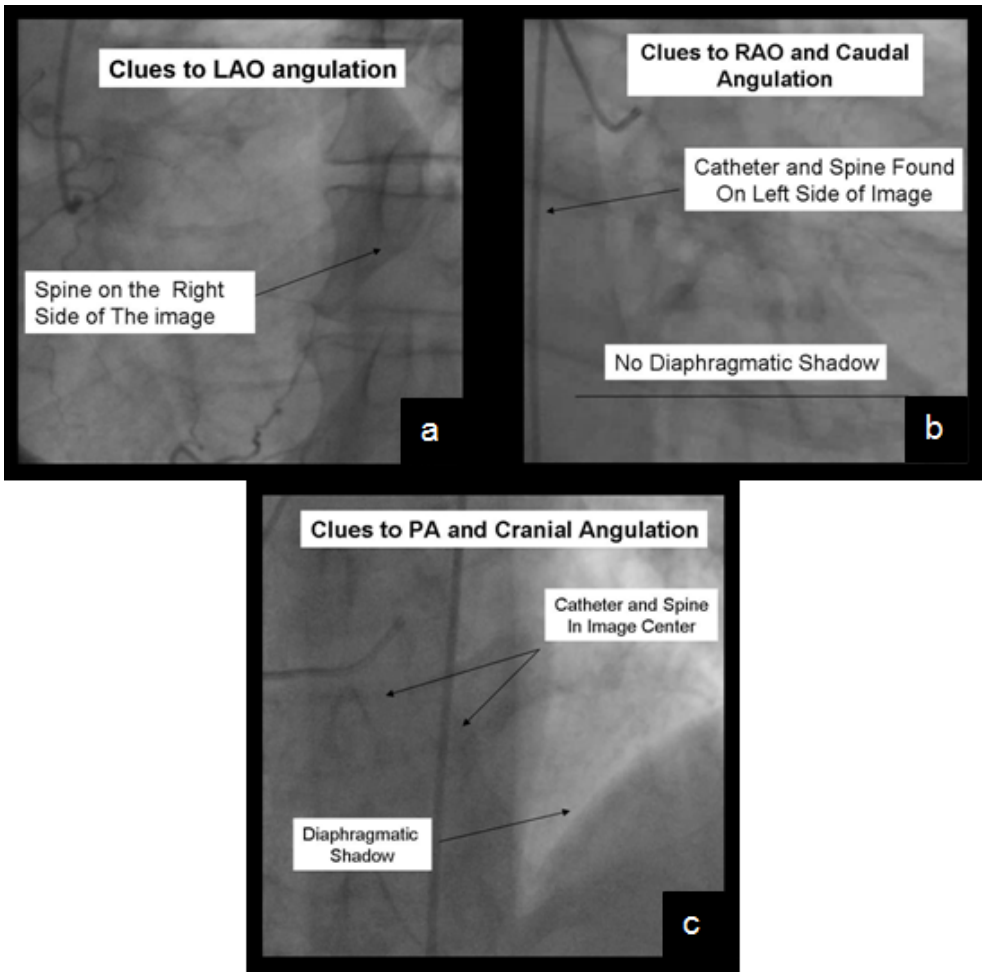

Figure 2.6: Clues to recognize the angiographic views. (a) LAO view; (b) RAO and caudal views; (c) AP and cranial views.

2.2.2 Views of LCA

During the cardiac catheterization procedure, the catheter is placed in the left CA orifice to obtain the CCAs of the LCA under the different angulations and c-arm movements. As a result of that, there are eight projections that have been identified as the standard views for LCA namely; LAO straight, RAO straight, AP caudal, LAO cranial, RAO cranial, LAO caudal (spider), RAO caudal and lateral. Following sections discuss about these projection views and vessel segments of LCA depicted in each view with visual illustrations.

LAO straight

The LAO straight view is obtained by rotating the c-arm from 40^0 to 60^0 angulations. In this view, the distal parts of the LCA are overlapped and the proximal parts of the vessels are foreshortening, particularly the CX[42]. However, steep angles of c-arm such as from 50 to 60 degrees may be good in studying the mid and distal parts of the LAD and the diagonal artery of the LCA. Figure 2.7 depicts the angiogram image, c-arm setup and LAD vasculature visualization under the LCA- LAO straight view for further clarification.

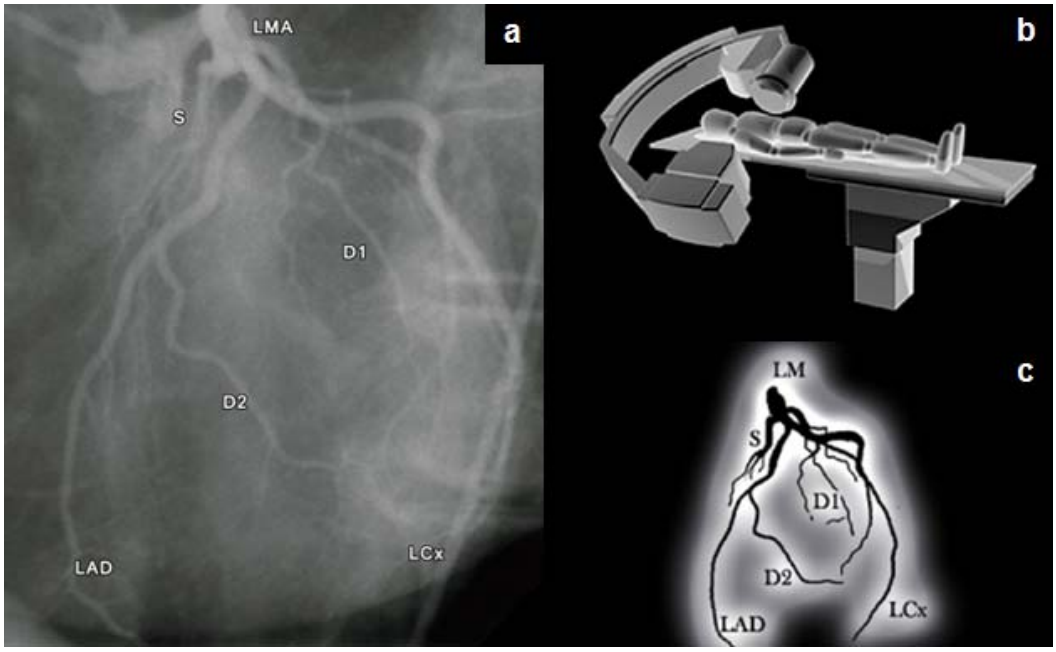

Figure 2.7: LCA - LAO straight view (60 degrees). (a) angiogram; (b) c-arm setup; (c) vasculature visualization.

RAO straight

The RAO straight view clearly visualizes the proximal portion of the LAD, which is the origin of the OMB of LCA and left postero-lateral branches of the CX. In this view, the LAD begins close to the spine and moves towards the left ventricular apex. Further, it visualizes one or more diagonals and several SP branches of LAD. In this view, the CX moves parallel to the spine. It provides the OMB and left postero-

lateral branches that come off at an angle and run roughly parallel to the LAD. The visual illustrations of LCA-RAO straight view are depicted in Figure 2.8.

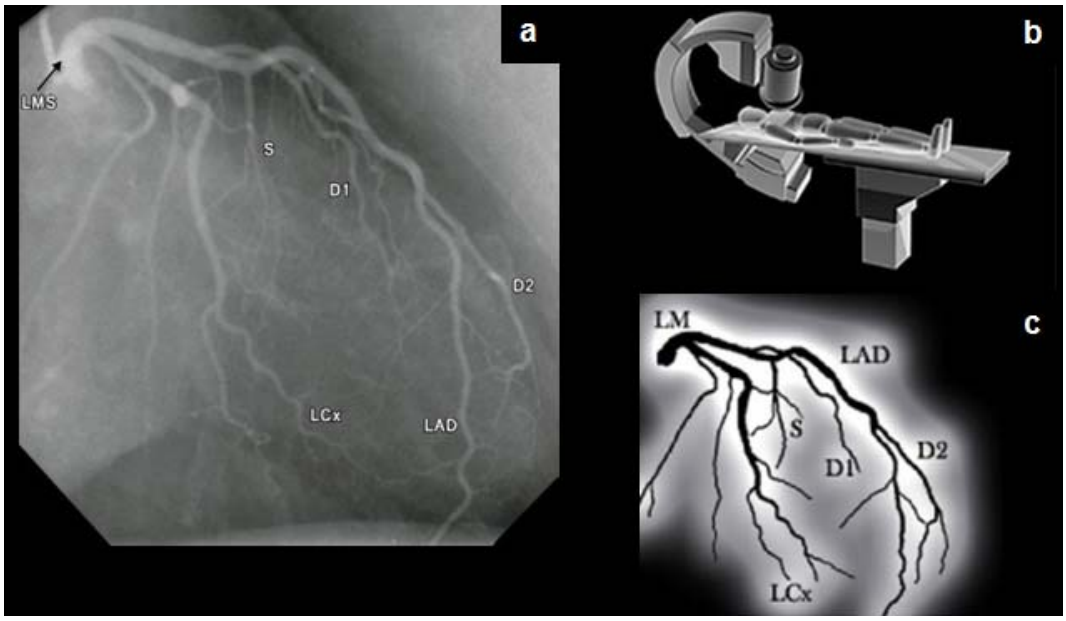

Figure 2.8: RAO straight view (30 degrees). (a) angiogram; (b) c-arm setup; (c) vasculature visualization.

AP caudal

This view is also known as shallow RAO view and displays the proximal segments of the Left Main Coronary Artery (LMCA) and CX. Figure 2.9 depicts the visual illustration of this view.

LAO cranial

The LAO cranial view visualizes the LMCA (slightly foreshortened), LAD, septal and diagonal branches of the LAD clearly. In this view, it is easy to detect and recognize the septal and diagonal branches easily because, these branch vessels are visualized in left and right side of the viewport respectively. Moreover, it visualizes the beginning of the LAD close to the spine and then moves away towards the left ventricular apex. Cranial angulation of the view tilts the LMCA down and permits to view the LAD-CX bifurcation. The CX in the RAO-cranial view moves away from

the LAD and runs towards the spine. It curves downwards and inferiorly runs roughly parallel to the LAD before branching off. In this projection, visual degradation of the angiogram is observed as a result of the Diaphragm. Nonetheless, by setting up the proper angulations, the density of the diaphragm can be moved down or out of the view. Figure 2.10 clearly visualizes the structural representations of the CAs under the LAO cranial view.

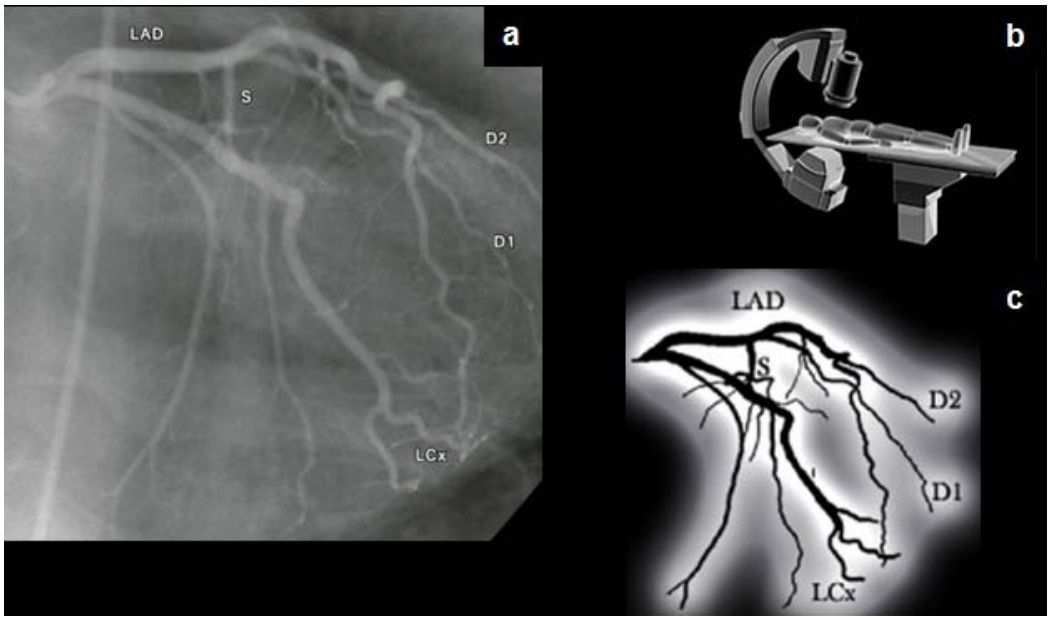

Figure 2.9: LCA – AP caudal view (30 degrees). (a) angiogram; (b) c-arm setup; (c) vasculature visualization.

LAO caudal (spider)

The LAO caudal view is also known as the "spider" view because it lays out the main branches of the LMCA in a divergent manner [40]. In this view, the LMCA and LAD are foreshortened but the ostium of the LCA and the LAD-CX bifurcation is clearly depicted. Moreover, the proximal and mid portions of the CX are clearly presented with the origins of OMBs. LAO caudal is a superior view for visualizing the origin of the ramus intermediate CA and the origin of OMBs. However the CCAs of this view suffer from poor image quality caused by overlapping of the diaphragm and

spine within the blood vessel viewing area [40]. Figure 2.11 illustrates this view for further clarifications.

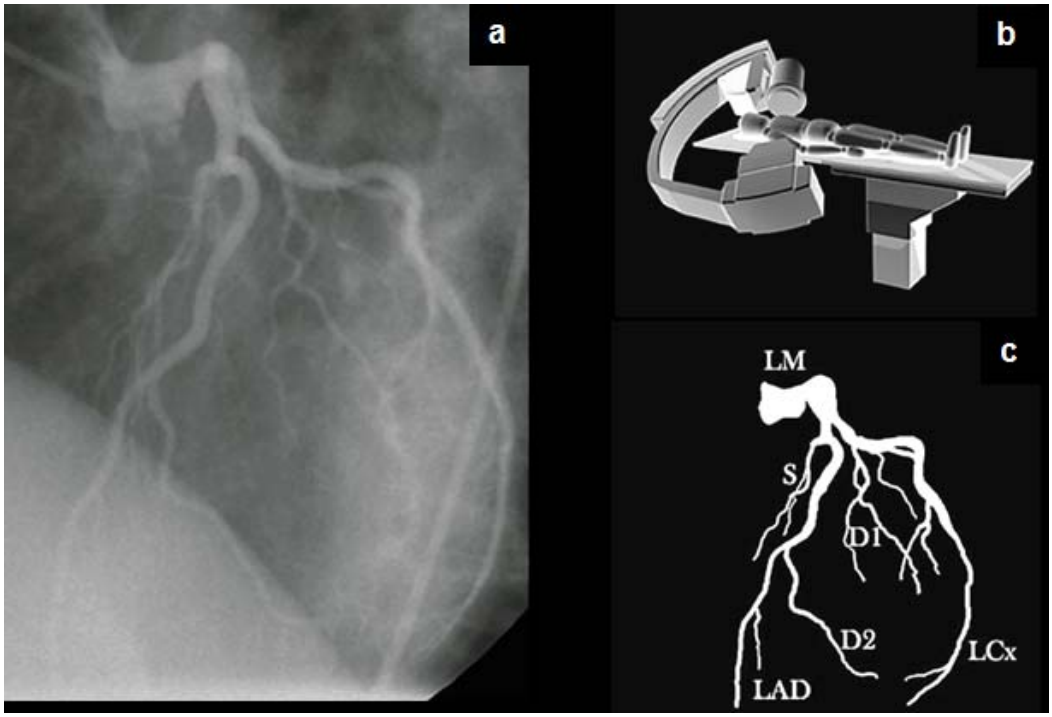

Figure 2.10: LCA – LAO (45 degrees) cranial (30 degrees) view. (a) angiogram; (b) c-arm setup; (c) vasculature visualization.

RAO cranial

The RAO cranial view is used to visualize the mid and distal sections of the LAD. The origins of the diagonal branches of the LAD and bifurcations in diagonal branches are clearly visualized in RAO cranial view. The proximal LAD and CX usually are overlapped. Not only that but also the marginal branches are also overlapped in this view. Apart from that, the CX artery is foreshortened, but posterior lateral branches are clearly visualized. The vessel representations in RAO cranial view is clearly depicted in Figure 2.12.

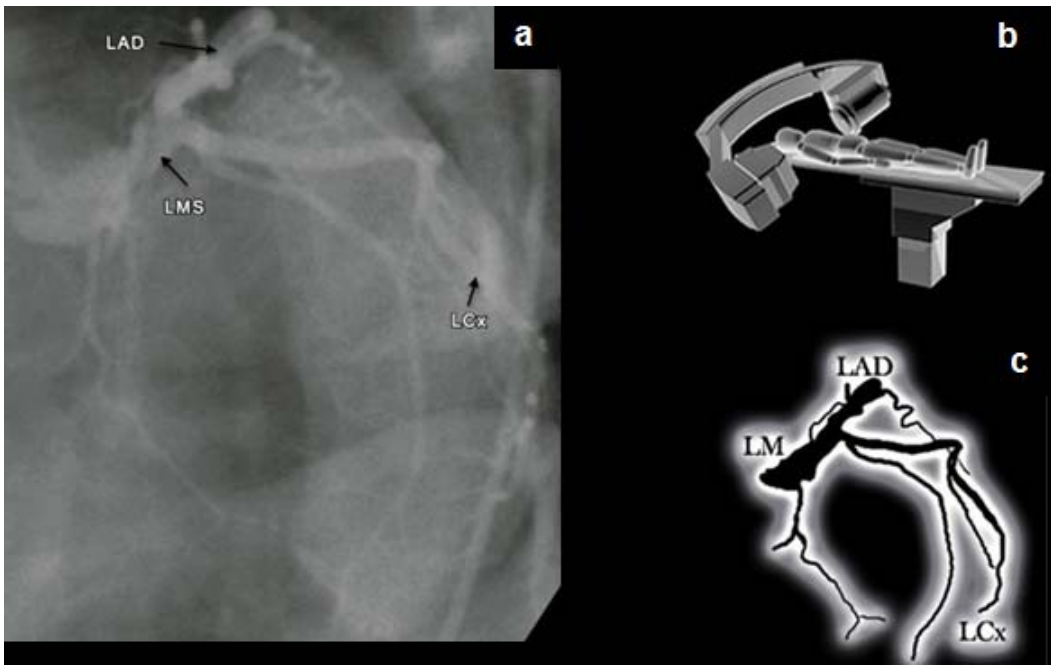

Figure 2.11: LCA – LAO (50 degrees) caudal (30 degrees) view. (a) angiogram; (b) c-arm setup; (c) vasculature visualization.

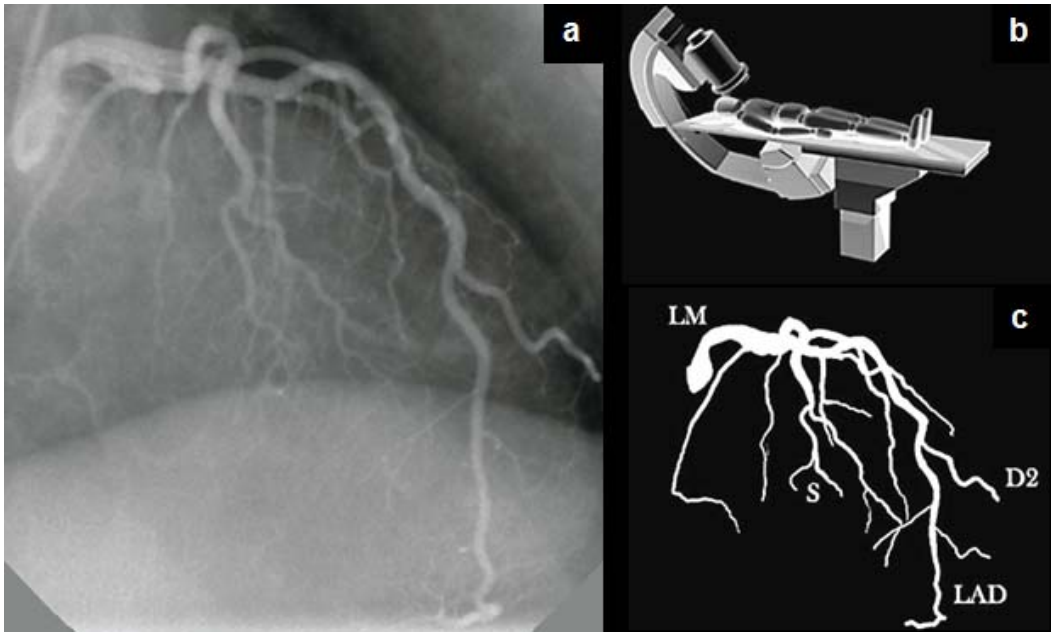

Figure 2.12: LCA – RAO (30 degrees) cranial (30 degrees) view. (a) angiogram; (b) c-arm setup; (c) vasculature visualization.

RAO caudal

The RAO caudal view is also considered as one of the best angiography views of LCA and depicts the LMCA bifurcation, proximal LAD, proximal to mid CX, origin and trunk of the OMB and the ramus intermediate branch. Figure 2.13 depicts the vessel structure visualizations and c-arm setup under this view. Moreover, this RAO cranial view is used as one of the best views to visualize the CX artery in clinical procedures. Nonetheless, The LAD beyond the proximal segment is obscured by overlapped diagonals in this view and is considered as a limitation of this view [40].

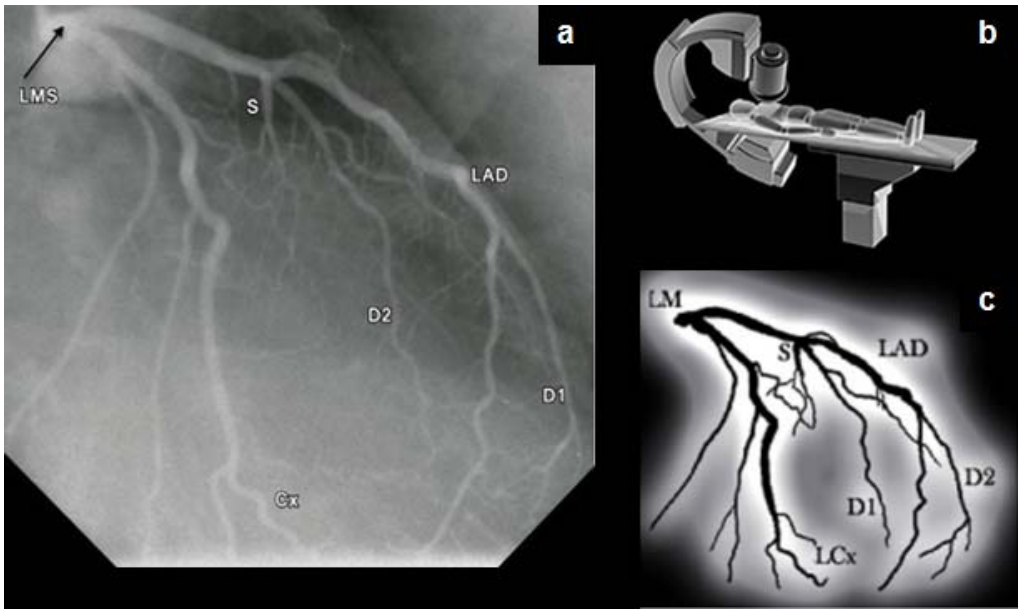

Figure 2.13: LCA – RAO (30 degrees) caudal (30 degrees) view. (a) angiogram; (b) c-arm setup; (c) vasculature visualization.

Lateral

A lateral view is obtained by rotating the c-arm by 90 degrees and placing it parallel with the floor (Figure 2.14(b)). This view provides the best visualizations of the mid and distal parts of the LAD. Further, in this view, the LAD and the CX arteries are well separated and the diagonals are overlapped. Figure 2.14 depicts the visuals of LCA taken under the lateral view.

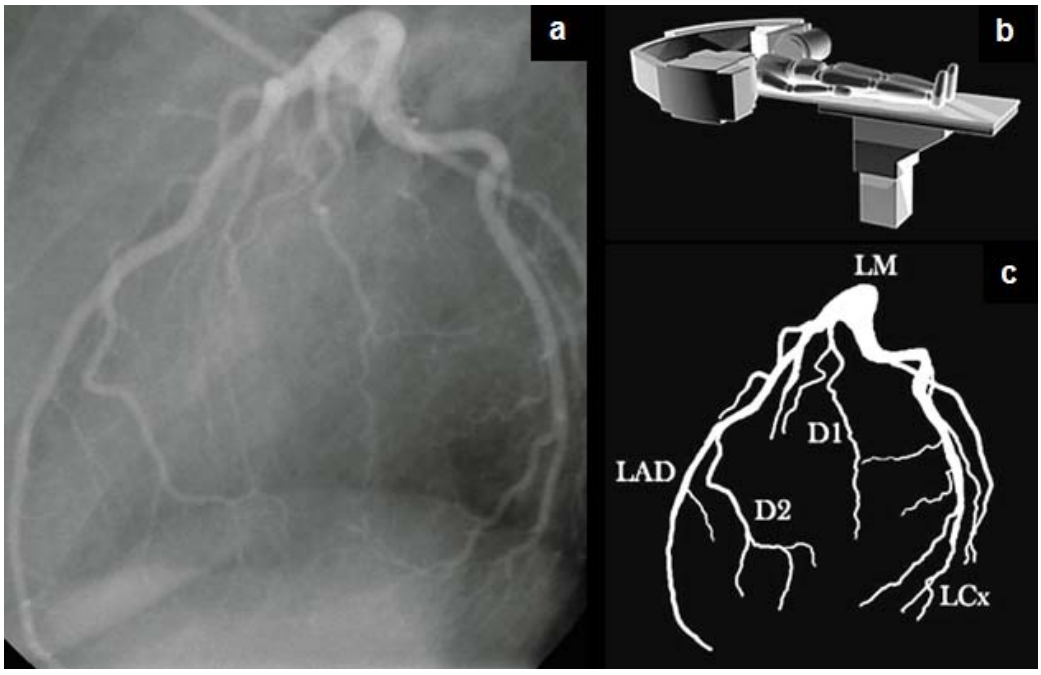

Figure 2.14: LCA – LAO lateral view. (a) angiogram; (b) c-arm setup; (c) vasculature visualization.

2.2.3 Views of RCA

During the cardiac catheterization procedure, the catheter is placed at the orifice of the RCA to obtain the CCAs of the RCA under different angulations and c-arm movements. As a result of that, there are six projections, which have been identified as the standard views for RCA namely; AP view, LAO straight, RAO straight, AP cranial, LAO cranial and lateral. Following sections discuss about these projection views and vessel segments of RCA depicted in each view with visual illustrations.

AP view

As mentioned in section 1.2.3, the RCA arises from the anterior position of the right coronary cusp and travels in the atrio-ventricular groove. In the AP view, the RCA begins close to the spine and runs roughly parallel to it. Moreover, the AMB, PDA and right ventricular branch of the RCA are clearly visualized in this AP view. Figure 2.15 illustrates the RCA representation for further clarification.

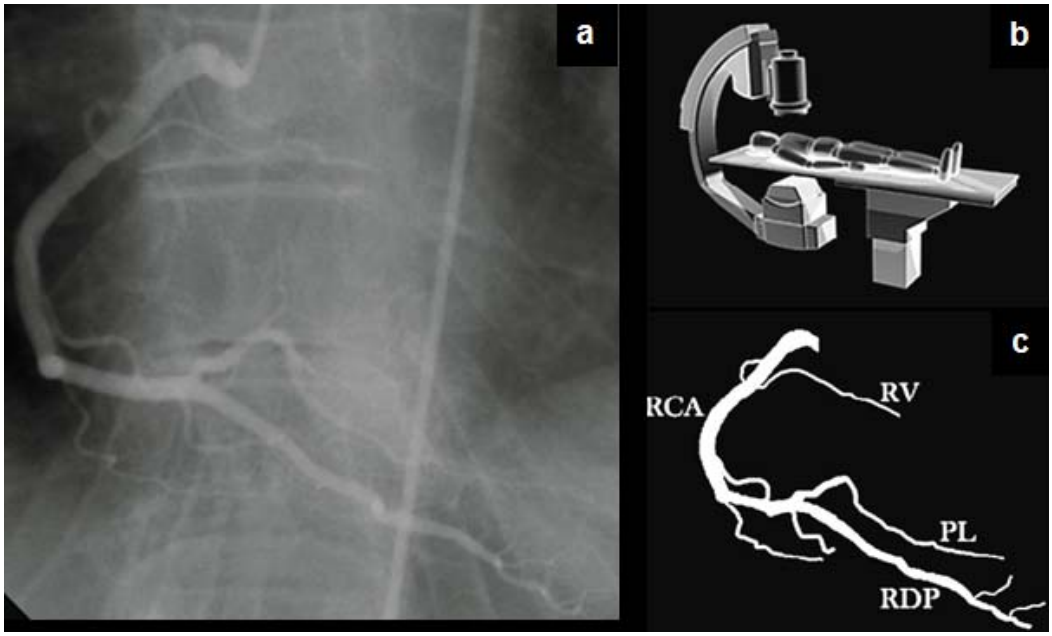

Figure 2.15: RCA – AP view. (a) angiogram; (b) c-arm setup; (c) vasculature visualization.

LAO straight

The LAO straight view is used to view the ostium and proximal portion of the RCA. As shown in Figure 2.16, the PDA and posterior lateral branches are foreshortened in this view and also the origins of those branches are obscured by overlapping.

RAO straight

In the straight RAO view, the RCA begins close to the spine and runs roughly parallel to it. The PDA and posterior lateral branches come off the RCA at nearly right angles. Hence, this view provides the excellent visualizations of the mid portions of the RCA, the origin of the AMB, the PDA and posterior lateral branches. Moreover, this view is also a superior view that demonstrates the SP branches. Figure 2.17 depicts the visual illustration of this view for further clarifications.

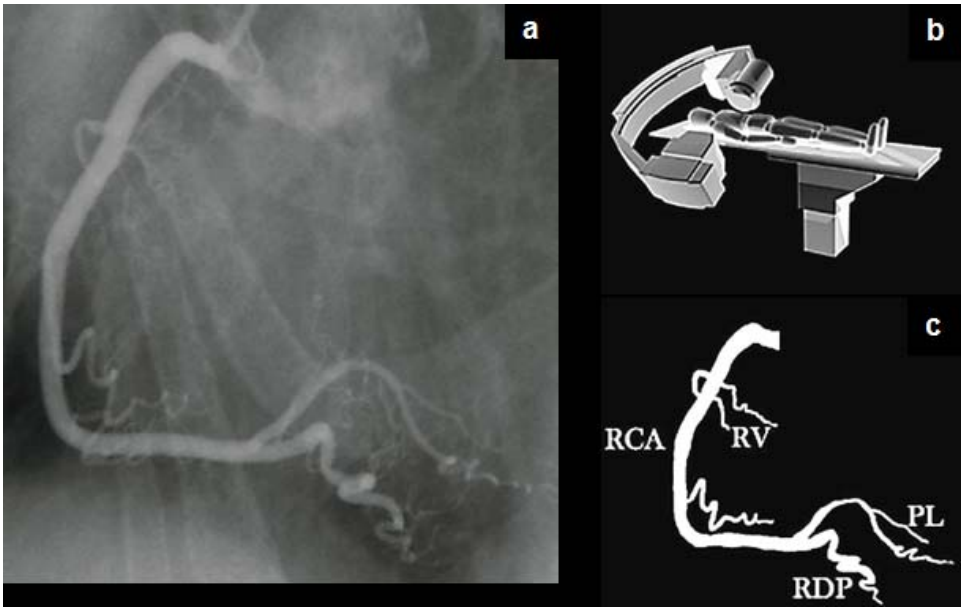

Figure 2.16: RCA – LAO straight view (45 degrees). (a) angiogram; (b) c-arm setup; (c) vasculature visualization.

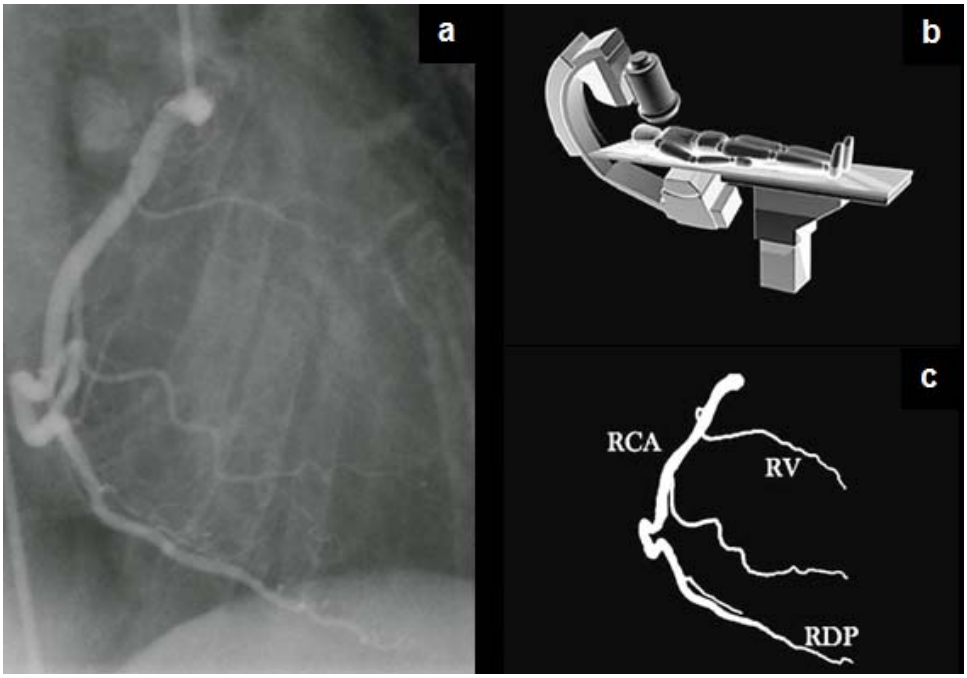

Figure 2.17: RCA – RAO straight view (30 degrees). (a) angiogram; (b) c-arm setup; (c) vasculature visualization.

AP cranial

The AP cranial view is the best view to visualize the origin of the RCA, the PDA and posterior lateral branches of a dominant RCA system. The mid segment of the RCA is foreshortened in this view and Figure 2.18 depicts the vessel structure representation obtained under this angiography view.

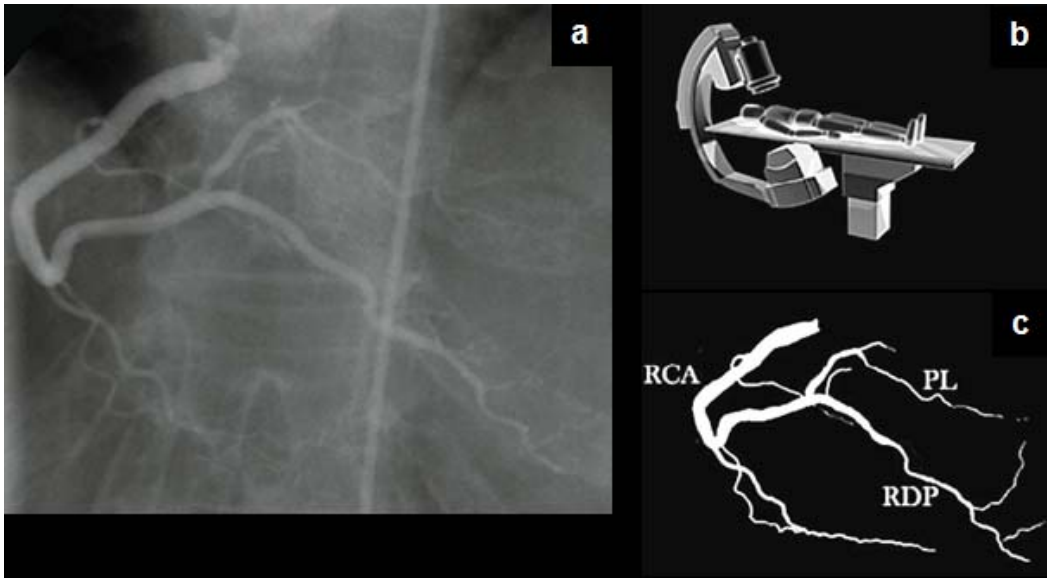

Figure 2.18: RCA – AP cranial view (30 degrees). (a) angiogram; (b) c-arm setup; (c) vasculature visualization.

LAO cranial

As depicted in Figure 2.19, the LAO cranial view visualizes the origin of the RCA, the entire length of the mid RCA, the PDA and PDA bifurcation. Normally, the PDA and posterior lateral branches are slightly foreshortened in this view. Having proper cranial angulations can tilt the PDA down to see the vessel contour and avoid foreshortening. Moreover, this view depends on deep inspiration to clear the diaphragm.

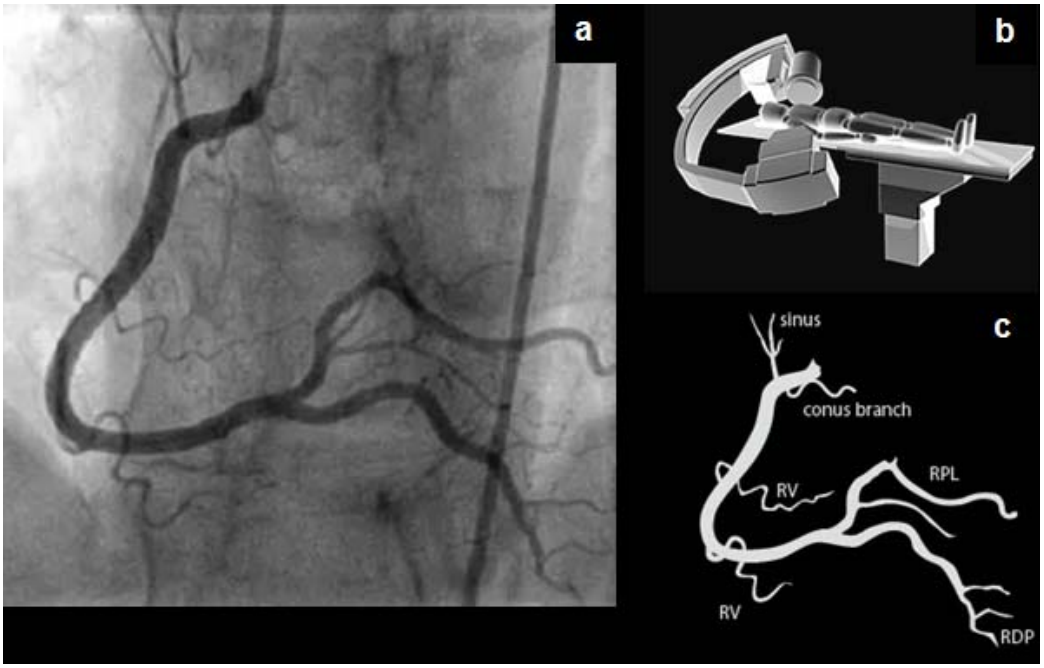

Figure 2.19: RCA – LAO (20 degrees) cranial (25 degrees) view. (a) angiogram; (b) c-arm setup; (c) vasculature visualization.

Lateral

The lateral view depicts the origin and mid segment of the RCA. The PDA and posterior lateral branches of the RCA are foreshortened in this view. The RCA representation obtained under this view is clearly depicted in Figure 2.20 for further visual analysis.

Table 2.1 summarizes the angiographic projections and the optimal visualization of the LCA and RCA [42]. According to the Table 2.1, it enlists the recommended standard angiographic projections for fourteen CA segments namely; Left main ostium, Left main bifurcation, LAD proximal, LAD mid, LAD distal, LAD diagonal, CX proximal, CX distal, OM bifurcation, RCA proximal, RCA mid, RCA distal, PDA and Posterior Left Ventricular (PLV).

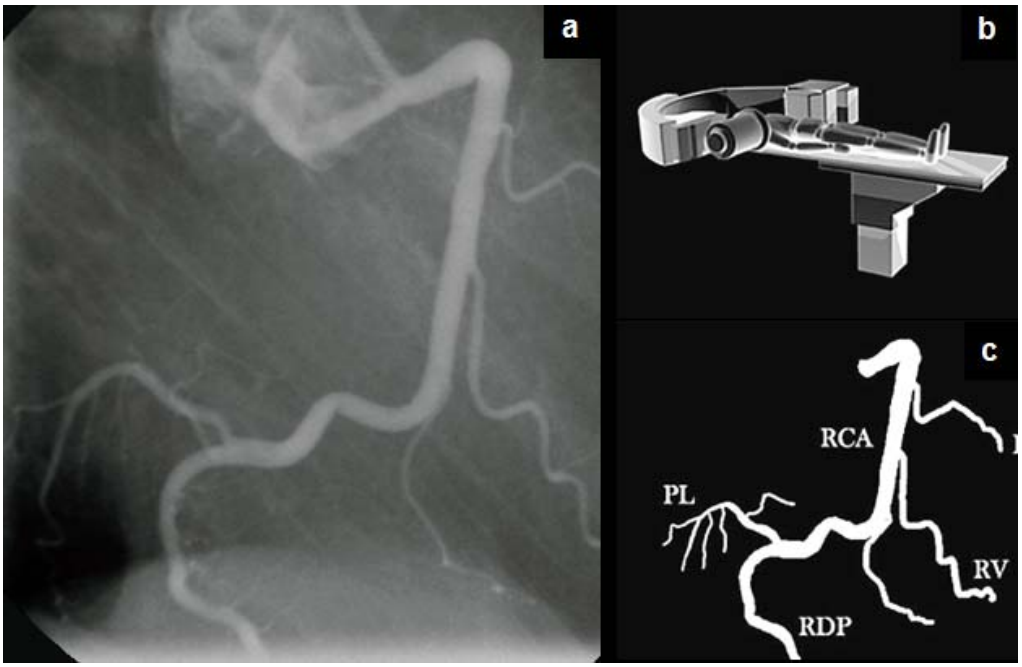

Figure 2.20: RCA – lateral view. (a) angiogram; (b) c-arm setup; (c) vasculature visualization.

During the cardiac catheterization procedure, a set of CCAs are recoded separately according to the aforementioned projection angles. These recoded CCAs are used for detecting and grading the stenosis in CAs. The next section of this chapter will explain angiography based stenosis grading method, which is used in cardiac clinical diagnosis process.

2.3 Assessment of coronary stenosis

The coronary stenosis or degree of lumen narrowing is measured as the estimated percentage lumen reduction of the most severely narrowed segment compared with the adjacent normal vessel segment, seen in the most apparent angiography projection[40]. As mentioned in section 1.3, coronary stenosis occurs due to eccentrically or concentrically deposited plaque regions. Figure 2.21 depicts these eccentric and concentric plaque deposits with the severity level of them (eccentric plaque presents 50% of severity and concentric plaque represents 90% of severity).

Table 2.1: Angiographic projections and optimal visualization [42].

CA Segment	LAO 40-50^0, caudal 25-40^0 (spider)	AP/RAO 5-15^0, caudal 30^0	RAO 30-45^0, caudal 30-40^0	AP/RAO 5-10^0, cranial 35-45^0	LAO 30-45^0, cranial 25-35^0	Lateral caudo-cranial 10-30^0	LAO 45-60^0	RAO 30-45^0
Left main ostium	++	+	+	+++	+++	-	-	-
Left main bifurcation	+++	+++	++	-	-	-	-	-
LAD proximal	++	++	+++	++	++	+	-	-
LAD mid	-	+	+	+++	++	++	-	-
LAD distal	+	+	+++	+	-	+++	-	++
LAD/ diagonal	++	+	-	++	+++	-	-	-
CX proximal	+	+++	+++	-	-	-	-	-
CX distal	+	+	++	+++	++	+	++	-
OM bifurcation	++	+++	++	-	-	-	+	-
RCA proximal	-	-	-	+	+++	-	++	-
RCA mid	-	-	-	-	+	+++	++	+++
RCA distal	-	-	-	+++	+++	-	++	-
PDA	-	-	-	+++	++	-	+	++
PLV	+	-	-	+++	++	+	+	-

View not recommended; + occasionally useful; ++ very useful; +++ ideal view.

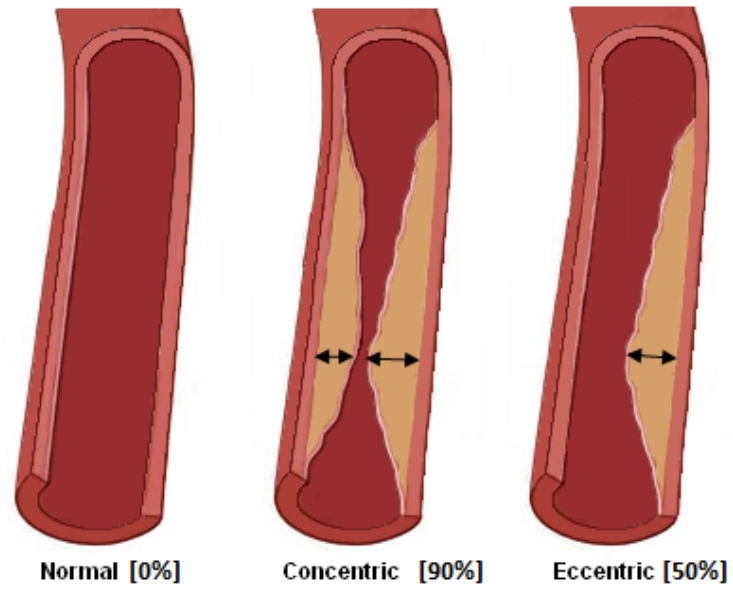

Figure 2.21: Different types of stenosis [43].

Since the coronary angiography provides excellent visualizations of CA vasculature, clinicians carefully observe the vasculature recorded in the angiograms to detect these plaque types. Presumably, the severity level of the detected stenosis is determined subjectively by analyzing these X-ray projections. Consequently, the percentage of detected stenosis severity is marked by giving an arbitrary value based on the clinicians' experience. Hence, these measurements consist of either overestimations or underestimations [25]. It has been reported that there can be a ±20% variation between the readings of two or more experienced cardiologists [40].

Hence, it is apparent that this subjective grading of severity of the detected stenosis is erroneous. As a solution for that, it is possible to have severity range criteria for grading the detected stenosis. Hence, four categories of lesion severity for grading the detected stenosis have been described as follows; 1 - minimal or mild CA disease, narrowing <50%, 2 - moderate, stenosis between 50% and 75%, 3- severe, stenosis between 75% and 95% and 4 - total occlusion [40]. This schema is simplistic but is subjective and may not be applicable when a vessel is diffusely diseased.

The American College of Cardiology and American Heart Association (ACC/AHA) lesion classification system was one of the first angiography scoring systems developed, comprising 11 angiographic variables with all lesions categorized into types A, B1, B2 and C [44]. The lesion categories described in this system are based on anticipated rates of success. Hence, it was expected that low-risk type A lesions would have a success rate of >85%, moderate-risk type B lesions were predicted to have a 60% to 85% success rate, and high-risk type C lesions had a <60% success rate. Moreover, the characteristics of each lesion class differed by degree of proximal tortuosity, angulation of the stenosis segment, the length of the lesion, and the presence of total occlusion, bifurcation lesions, thrombus or friable and vein graft lesions [45]. Table 2.2 enlists the characteristics considered according to this grading system [46].

Due to various reasons, angiography based stenosis grading consists of some obstructions. The next section will elaborate the revealed problems in angiography and its' assessments with the literature evidence.

Table 2.2: American College of Cardiology/American Heart Association Task Force (ACC/AHA) classification of the primary target stenosis[46].

Type A	Type B- I and B-II	Type C
Discrete (< 10 mm length)	Tubular (10–20 mm length)	Diffuse (>2 cm length)
Concentric	Eccentric	Diffuse
Readily accessible	Moderate tortuosity of proximal segment	Excessive tortuosity of proximal segment
Non-angulated segment, $<45^0$	Moderately angulated segment, $>45^0$, $<90^0$	Extremely angulated segments $>90^0$
Less than totally occlusive	Total occlusion < 3 months old	Total occlusion >3 months old
No major branch involvement	Bifurcation lesions	Inability to protect major side branches. Degenerated vein grafts with friable lesions
Smooth contour	Irregular contour	
Not ostial in location	Ostial in location	
Little or no calcification	Moderate to heavy calcification	
Absence of thrombus	Some thrombus present	

Note: B1 = 1 characteristic only; B2 = 2 or more characteristics

2.4 Problems in Coronary Angiography

This section will briefly review the problems of coronary angiography in detecting and assessing stenosis severity. According to the literature evidence and empirical studies, two main factors, which cause negative consequences for angiography based stenosis assessment have been identified namely; subjective stenosis assessment and visual degradations in angiograms. Following two sub sections discuss about the impact of these consequences comprehensively.

2.4.1 Subjective stenosis assessment

Angiogram based stenosis assessment is generally a subjective process and depends on the experience of the clinicians. Section 2.3 explained about the available subjective stenosis grading methods widely used in clinical diagnosis. These subjective assessments lead to overestimations or underestimations of the detected stenosis and are often inaccurate in predicting, which lesions cause ischeamia [23]

[25]. Moreover, in most catheterization procedures, lesions with a diameter stenosis of ≥ 50% on the angiogram are generally considered for revascularization and it is not the optimal decision for all clinical cases.

In recent past, Tonino et al. has conducted a research study to determine the relationship between angiographic stenosis severity and functional stenosis severity as measured by the FFR [23]. The results of study [23] have clearly revealed the negative impact of the angiography based subjective stenosis assessment. For study [23], 1329 lesions were selected from 509 patient cases. Initially, the operator categorized the lesions according to the visual angiographic stenosis severity into 50% - 70%, 71% - 90% and 91% - 99% diameter stenosis groups. Then the FFR was done for all subjects and if the FFR of a particular stenosis >80 was considered as functionally non-significant stenosis (no need to place a stent). Table 2.3 presents the results obtained from this research study and Figure 2.22 depicts the visual illustrations of the results of the same study for more clarifications.

FFR is a quantitative stenosis assessment method based on the functional significance of the CA stenosis (Section 1.4.2). Using the FFR for study [23], it has enabled to compare the significance of the angiography based subjective stenosis analysis results with the FFR based quantitatively assessed results. Hence, the most important finding in this study is that most of the stenosis declared as significant through angiography based subjective assessment are reported as functionally insignificant stenosis according to the FFR study. This factor is clearly indicated by the figures in Table 2.3. According to this Table 2.3, 670 lesions were reported as significant stenosis according to the angiography assessment under the 50%-70% category, but 402 cases out of those 670 were reported as functionally insignificant stenosis in FFR study. Moreover, 96 lesions were reported as significant stenosis according to the angiography assessment under the 91%-99% category, but only 7 cases out of those 96 were reported as functionally significant stenosis in FFR study and all other cases are functionally insignificant. This will emphasize in the visual proofs given in Figure 2.22 further.

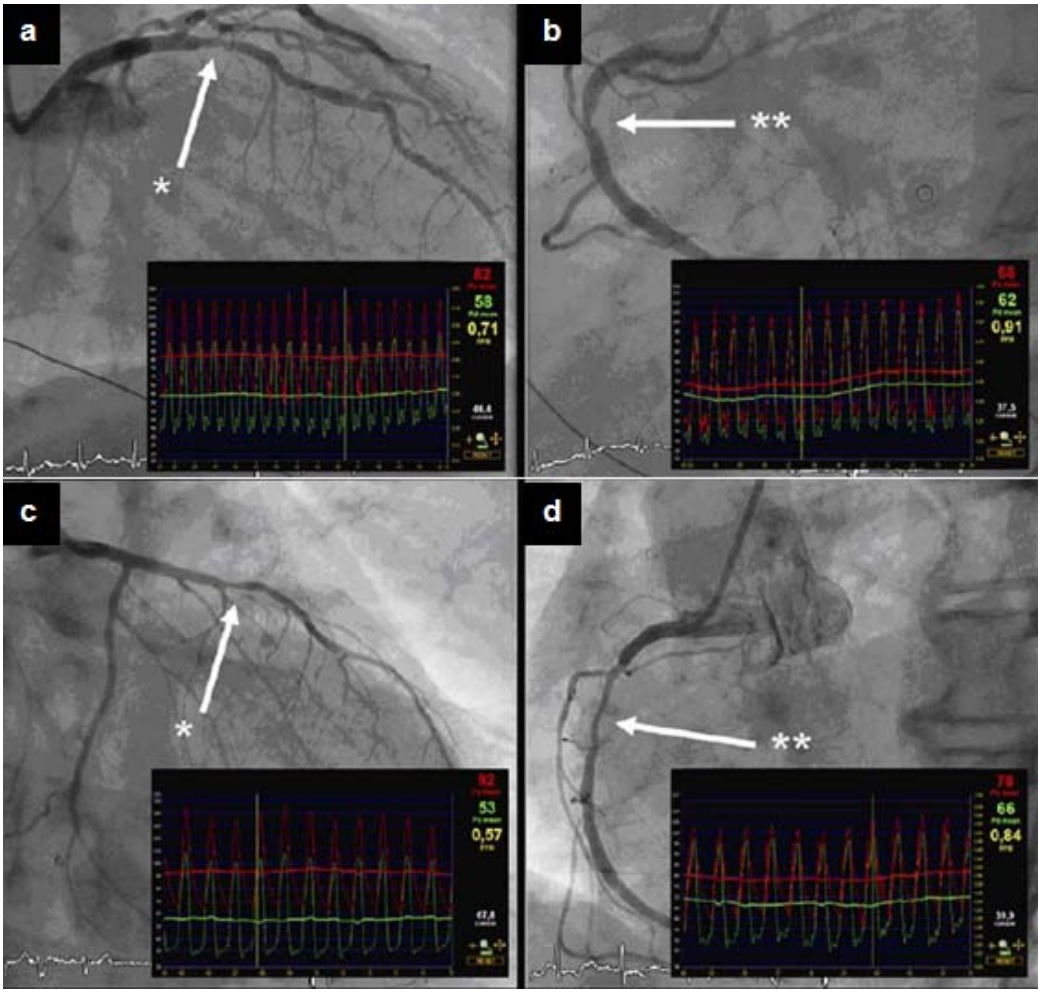

Figure 2.22: Mismatches between the visual assessment and function assessment of stenosis. (a) 50%-70% angiography category with 0.71 FFR; (b) 50%-70% angiography category with 0.91 FFR; (c) 71%-90% angiography category with 0.57 FFR; (d) 71%-90% angiography category with 0.84 FFR (arrow heads represent the stenosis location, * represents critical and ** represents non-critical lesions according to the FFR) [23].

Hence, it is clear that the subjective assessment of stenosis provides erroneous results in angiography. Not only that but also the visual degradation, which occurs in angiography also makes some negative impact of stenosis assessment and the next section will emphasize the consequences of these factors in detail.

Table 2.3: Results of the angiographic versus functional severity of CA stenosis obtained by Tonino et al [23].

		Angiogram Severity		
		50% to 70% Category *n*=670, 47%	**71% to 90% Category *n*=513, 39%**	**91% to 99% Category *n*=96, 15%**
FFR Severity	**FFR>0.80 Functionally non – significant stenosis**	402 cases, 65%	104 cases, 20%	7 cases, 4%
	FFR<=0.80 Functionally significant stenosis	218 cases, 35%	409 cases, 80%	189 cases, 96%

n = number of cases

2.4.2 Visual degradations in angiogram

Visual degradations in angiograms mainly occur due to the physical organization of the organs in the chest and the artifacts that occur during the angiogram procedure. Vessel overlap and superimposition of other tissues such as ribs, spine or cardiac chambers on CAs can be considered as degradation, which occurs due to the physical organization of the organs in the chest [26][40]. Vessel overlap makes obstructions in vessel delineation. Clear recognition of CA vasculature in angiography view is essential to segment the CAs and locate the stenosis area [25]. This process becomes tedious or even impossible when the blood vessels in the image are overlapped. Superimposition of ribs, spine or cardiac chambers on blood vessels also provides unclear visualizations of CAs in the angiogram image and causes obstructions to recognize the blood vessels clearly. Poor opacification, noise, non-uniform illumination and motion are considered as the negative impacts that occur during the angiogram procedure [25][27-29]. The impact of these factors will be discussed in detail in Chapter 3.

2.5 Research background of the study

Even though the coronary angiography consists of visual problems, global motion artifacts and subjective diagnosis, it is still the standard technique for guiding PCI in patients with CA disease [26]. Therefore, various research attempts have been done

in recent past to improve coronary angiography under the various areas such as the visual enhancement of the angiograms, segmentation of CA vasculature and quantitative coronary analysis. This section emphasizes some of the important background computer vision theories and recent research attempts carried out under aforementioned aspects.

2.5.1 Background studies for enhancement of angiography

The objective of this section is to emphasize the various research attempts made in recent past to find the solution for the identified coronary angiography problems. It has been reported that the literature on enhancing direct coronary angiography images for visualization purposes is very limited [47]. However, in this section, some of the research attempts conducted for enhancing the angiography based on techniques such as filtering, circular sampling, non-linear approach using stick, pseudo color processing, contrast stretching and wavelet based noise removal are presented.

It is apparent that various filtering techniques are being used for enhancing angiography images by reducing noise and non-uniform illumination. Angiogram enhancement technique mentioned in [48][49] is based on directional filter banks and those directional filters were implemented using high pass filters. The directional images obtained from the filter bank could be considered as the results obtained by the decomposition of the original image based on the gradient direction. Further, it has the capability to reducing the noise as an added advantage.

The circular sampling technique was implemented in the study published in [50] for removing noise and the non-vessel regions from the angiography images. It has been mentioned that the circular sampling samples a vessel structure around a sampling point by extending the sample circles spatially. The noisy segments are miss-segmented in this approach and those miss-segmented areas can be removed from the angiogram image in order to enhance it.

It is apparent that the noise associated with the images is also increased during the traditional enhancement techniques, which are based on unsharp masking. Tu and his

team have published a non-linear model for enhancing the angiography image details without having such negative effects and that suggested model was known as stick-guided lateral inhibition [47]. This proposed model simulates the enhancing mechanisms integrated in the eyes of human beings and of many animals and its' implementation is based on asymmetric sticks [51]. The sticks are a set of line segments passing through the current pixel and are able to approximate the edges in images without co-relating with noise patches. Therefore, sticks can smoothen out noise patches without damaging the real edges of the angiogram [52]. Results of this study have provided high observer agreement value for stick based method rather than unsharp mask based enhancement method.

Pseudo coloring of angiogram images can be used as an enhancement technique to improve its' visual quality. It is done by mapping each pixel value in a gray scale image in to a color according to a table or function [53]. Pseudo color processing could accentuate blood vessels in angiography images.

Research study conducted for extracting the CA tree in [26] has applied "temporal" wavelet transformation for noise removal and matched filters for blood vessel enhancement. In wavelet transformation, the input image is decomposed into sub regions by using low pass and high pass filters. Hence, the noise is automatically shifted into the specific decomposed images. This noise has been removed by thresholding the image.

Contrast Limited Adaptive Histogram Equalization (CLAHE) method has been applied in a recent research study for improving the contrast of the angiograms during its pre-processing phase [54][55]. In CLAHE, the histogram is cut at some threshold and then equalization is applied. It is an adaptive technique because an image is enhanced by applying CLAHE on small data regions called tiles rather than the entire image [56]. The resulting neighboring tiles are then combined back faultlessly using bilinear interpolation. The contrast in the homogeneous region can be limited so that noise amplification can be avoided [56].

Motion is another negative artifact in CCAs. Hence, motion stabilization becomes another pre-processing activity in CCA based processing. However, it has been

reported that the motion of anatomy is quiet complex and cannot be accurately corrected by estimating models with low degree of freedom such as rigid or affine transformation [29]. The literature survey of this study reveals that the feature descriptor based method, image registration and optical flow based methods are among the major techniques for motion stabilization in CCAs and provided acceptable results for determining the cardiac dynamics.

A Scale Invariant Feature Transform (SIFT) based motion estimation and video stabilization technique was described in a recent research study [57]. In this study, SIFT was used to obtain the key points between two consecutive frames. The shortest distance between SIFT feature in two consecutive frames were calculated during the SIFT feature matching step of this study to determine the Global Motion Vector (GMV).

An optical flow and elastic registration based technique has been published in [58] for analyzing the CA dynamics. In their method, the vessel skeletons are extracted from original images and the optical flow field along skeletons is estimated to determine the arterial dynamics. Consequently, the estimated arterial dynamics are transformed into autoregressive model and elastic registration between skeletons of the same vessel branch at two different time intervals to quantitatively determine the motion of CAs.

2.5.2 Background studies for vessel segmentation

Segmentation subdivides an image into its constituent regions or objects [59]. Accurate segmentation of CAs in angiograms is a challenging task. The major reasons for that are; poor signal to noise ratio due to poor X-ray penetration, overlapping vessels, superimposition of vessels with various anatomical structures such as ribs, spines or heart chambers, vessel foreshortening, noise because of uneven distribution of the contrast agent, environment noise influence of image processing and visual degradation that occurs due to the non-uniform illumination [25][26]. Various segmentation methods based on coronary angiography have been reported in recent past and the aim of this section is to highlight the significant features and methods of those studies under various categories. Segmentation

methods based on coronary angiography can be categorized under the criteria such as pattern recognition approaches, model based approaches, tracking based approaches and Artificial Intelligence based approaches [60]. Following sections will be elaborated on the research background of CA segmentation under aforementioned criteria.

Pattern recognition approaches

Pattern recognition techniques can automatically detect or classify the image object or features. For vessel extraction, it is concerned with the automatic detection of vessel structures [60]. Filter based approach, region growing approaches, skeleton based approaches, mathematical morphology schemes, matching filters method and multi scale based method can be considered as various approaches used for pattern recognition based segmentation [61].

Filter based approach:

Filters are widely used in image segmentation to remove noise and improve the digital image feature desired to be extracted [62]. In this approach, image is convolved with either a single or multiple filters to extract the object of interest. Designing different filters to detect the vessels with different orientation and size plays a significant role in extracting vessel contours [60]. It is important to highlight Frangi's vessel enhancement filter, which is widely accepted in vessel enhancement of medical images in recent past because of its ability to filter out the tubular structures from the image to be processed. The blood vessels can be considered as tubular structures and the application of Frangi's filter is crucial in blood vessel segmentation [63].

It is important to note that the proposed segmentation method, which has been implemented in this research study is also based on Frangi's vessel enhancement filter. Hence, it is significant indeed to elaborate the implementation steps of the Frangi's filter in this section. Frangi's filter is implemented based on the second order partial derivatives of the input image and it can be calculated by convolution input image with an appropriate kernel. It provides second order four directional

images based on the gradient variation along the horizontal, vertical and two diagonal directions of the input image. Later, a Hessian matrix is calculated using the second order derivative images obtained in the previous step. Two eigenvalues and four eigenvectors are produced for each pixel point of the input image as the result of the Hessian matrix calculation. Those resulting eigenvalues and eigenvectors are used to determine the vesselness of the processed image using the norm defined by Frangi et al. and it enlists in Table 2.4.

Table 2.4: Possible structure orientations in 2D images depending on the eigenvalues λ_1 and λ_2 of Hessian matrix [63].

λ_1	λ_2	**Orientation pattern**
N	N	Noisy, no predefined direction
L	H-	Tubular structure (bright)
L	H+	Tubular structure (dark)
H-	H-	Blob-like structure (bright)
H+	H+	Blob-like structure (dark).

H=high, L=low, N=noisy, usually small, +/- indicate the sign of the eigenvalue.

Various research attempts have been reported to segment the CAs based on Frangi's filter. Wang and his team have published a CA segmentation method based on Frangi's filter and region growing technique [64]. During the pre-processing, they have generated the second order directional derivative images through convolution of input angiogram image with the second order partial derivatives of the Gaussian filter of scale σ. Moreover, they have applied Frangi's filter under different scales of σ to select the optimum vessel enhancement result. Consequently, the region growing method was applied on the enhanced images to improve the spatial connectively of the detected blood vessels. Moreover, they have interactively selected multi seed points in vessel regions and allowed those points to grow within the region growing processes simultaneously. As a result of that, several dispersal regions were produced and the homogeneous regions were merged together through homogeneous test. The homogeneity test was established according to the analysis of image features by gray scale histogram and K-means clustering. Experimental results of this study have

elaborated its' capability for noise suppression and the extraction of small and distal vessels of CA vasculature.

A novel hybrid region growing method with a differential geometry vessel detector for the segmentation and identification of the cardiac coronary tree in angiograms was published by Lara et al [54][65]. In this study, they have applied CLAHE to the angiography images as the initial pre-processing method to enhance the contrast [66]. Consequently, Fangi's filter based vessel resemblance function was implemented to separate the vascular regions from the background. Pixels in those extracted vessel regions have been selected as the seed point for the automatic region growing method. However, the initial seed point is given interactively and circular filtering technique around the seed point was applied to determine the background pixels and the blood vessels. Finally contour detection was applied and the largest contour was extracted out as the CA vasculature. Moreover, this study has reported an accuracy of 87.58% for CA segmentation.

Two recent research studies done by Sasidharan and Shashank also used Frangi's filter based approaches to segment the CAs in their research studies [67][68]. In Sasidharans' approach CAs are segmented using three major phases namely; application of noise adaptive fuzzy switching median filter, application of Frangi's vessel detection and region growing. Noise adaptive fuzzy switching median filter was applied as a pre-processing technique to remove impulse noise and enhance the angiography image. Subsequently, the Frangi's filter was applied to detect the CAs. Moreover, they have used histogram based analysis to automatically detect the seed point for implementing the region growing phase. Additionally, this segmentation method was declared as a fully automatic segmentation approach and it was one of the significant features of this study. The segmentation method proposed by Shashank and team also used the Frangi's filter based approach to segment the blood vessels. Additionally, they have applied rotation invariant anisotropic diffusion filtering for further enhancing the results.

Region growing approaches:

Region growing segment the image by merging pixels to a region based on either value similarity or special similarity. O'Brien and Ezquerra automatically segment the CA vasculature based on a region growing approach [69]. In this study, region growing was performed to extract the initial approximation of the vessel structure. After that they have extracted the vessel skeleton and some remaining undetected vessel segments. Subsequently, the vessel regions and non-vessel regions were extracted from the angiography image.

Köse has proposed a fully automatic segmentation method by considering the spatial coherence of the angiogram images [50]. According to his publication, the proposed method can handle complex structures such as sharp curved, branched vessels, and vessels with varying length on a noisy and changing background. The method initially removes the background from the angiogram image by using an averaging technique that calculates the average intensity within the region of interests with a given dimension. Subsequently, a circular sampling technique is applied to determine the blood vessel regions. In this approach, the intersections between sampling circles and sampled blood vessel were determined to calculate the intersection distribution. The dominant intersections were checked to segment the vessel structure in the angiogram to be processed and segmented vessel regions were extracted out as the results. Finally, a circular filtering technique was applied to remove small noisy fragments from the resulting image.

Skeleton based approaches:

Skeleton based methods are used to extract the centerline of blood vessels. Moreover, these methods can be used to create the vessel tree by connecting these extracted vessel centerlines. Various methods can be used to extract the vessel centerline such as application of thresholding and then object connectivity, thresholding followed by thinning procedure and extraction based on graph description are some of the instances [60]. Research study of O'Brien and Ezquerra, which was discussed under the region growing segmentation can also be stated here as an instance for a skeleton based CA segmentation method [69].

Mathematical morphology schemes:

Mathematical morphology could be considered as a tool for extracting image components that are useful in the representation and description of region shape [70]. Sun et al. have been reported that the mathematical morphology is an ideal operator for vessel extraction because, it can use uniform operator to deal with different vessel structures such as branching and crossing [31]. Moreover, they have proposed a vessel segmentation method using combined morphological operations and watershed operation. In their study, they have used morphological top hat operation for enhancing the vessel tree in angiograms. Moreover, they have designed two filters namely fuzzy morphological open filter and fuzzy morphological duel opening filter to eliminate the noise in the enhanced images and to avoid widening the vessels due to the vessel-like noise remaining in the enhanced images respectively. Consequently, morphological watershed was applied to the resulting enhanced images to detect the vessel boundary.

Research study done by Eiho and Qian had used mathematical morphology to completely extract the CA vasculature from coronary angiography [71]. Initially they have enhanced the shape of the vessel by applying the top hat operation. Secondly, morphological erosion followed by half-thresholding operations were applied to remove the non-vessel areas from the enhanced angiogram image. As the next step, the whole vessel tree had been extracted based on the given seed point by considering intensity similarity of the neighboring pixels. Then the vessel skeleton has been obtained through the thinning operation followed by dilation operation. Finally, the watershed transformation operation has been applied to the binary image to extract the edges.

Matching filters method:

Matching filters approach is one of the pattern recognition techniques, which can be used for segmentation of vessel structures from angiography. In order to extract the object of interest, the image is convolved with multiple matched filters. Moreover, the match filters are usually followed with some other image processing operations like thresholding to get the final vessel contours [60]. CA segmentation method

suggested by Lin and Ching used match filter approach for their study published in [26] to extract the CA vasculature by processing CCAs. The proposed method consisted of two major stages namely signal based image segmentation and vessel feature extraction such as vessel diameter. As the initial step of segmentation stage, a temporal Fourier analysis was employed to eliminate the stationary background and slow moving objects in the CCA images. Subsequently, the 3D wavelet transformation was applied to reduce the noisy structures in the partially processed CCA images. Consequently, a set of matched filters was applied to enhance the CAs. The proposed matched filters were created based on two parameters namely; orientation and size. Hence, 72 filters of twelve orientations and six sizes have been applied. Finally, a clustering analysis, histogram technique, and size filtering were utilized to obtain a binary image that consists of the final segmented CA tree.

Multi scale based method:

Multi scale segmentation approach can also be categorized under pattern matching approach and implemented by varying the image resolution. The main important aspect of this technique is increased processing speed. In multi scale segmentation, the strong structures can be segmented at the low resolution level and weak structures, such as branch vessels, can be segmented at higher resolution [60]. Lee et al. have suggested a method for quantitative coronary analysis by using a combination gradient segmentation (wavelet edge detection) and region segmentation [72]. In this study, the multi scale masks of wavelet transformation were generated and applied together with the angiogram images to generate the series of multi scale images with different gradient strength scales.

Model based approaches

In addition to the pattern recognition approaches, it is possible to use model based approaches for segmentation of blood vessels from angiography. Model based approaches apply explicit vessel models to extract the vasculature and some literature evidence has emphasized the application of parametric deformable models to segment the CA vasculature significantly. Moreover, these parametric deformable model techniques find object contours using parametric curves that deform under the

influence of internal and external forces. Active contour models or *snakes* are a special case of a more general technique of matching a deformable model by means of energy minimization [73] .

A recent research study emphasized the application of snake model to locate the vessel boundaries of coronary angiograms [74]. According to the research method described in [74], the investigators have introduced a certain mechanism to overcome two problems of snake model, which are lower capture range and non-availability of evolution stop mechanism through dynamic gradient flow and adaptive balloon force respectively.

Parametric model approaches define objects of interest parametrically. In tubular object segmentation applications, objects of interest are described either as a set of overlapping ellipsoids or a circular vessel model. Moreover, in parametric model approaches, the parameters of the model used are estimated from the image [60]. Zou et al. have proposed a parametric model based consecutive scan line tracking method for extracting CA vasculature from digital subtraction angiograms [75]. Consecutive scan line profiles were fitted by a parametric model based on local intensity information of the angiogram image to be processed. As a result of this scan line fitting to local intensity profile of the image, the vessel center point can be detected along the scan line. Moreover, derivative of the center point provides the tracking direction for continuing the vessel tracking. An adaptive tracking strategy was applied with appropriate termination criteria to track each vessel segment. When tracking stops, to prevent premature termination and to detect bifurcations, a "Look Ahead Detection" scheme was used to search for possible continuation points of the same vessel segment or those of its bifurcated segments. The proposed algorithm can automatically extract almost complete CA vasculature from digital subtracted angiography images.

Tracking based approaches

Tracking based approaches apply local operators on a focus known to be a vessel and track it. Vessel tracking approaches apply local operators starting from an initial point, detecting vessel centerline or boundaries by analyzing the pixels orthogonal to

the tracking direction [60]. Van der Zwet, Pinto, Serruys and Reiber have invented a tracking based method to find the path lines of the CAs in coronary angiograms [76]. According to their investigation, the path lines are detected using two algorithms namely tracking algorithm and box algorithm. Tracking algorithm was used to find all curves in the angiogram image, which were candidates for being a path line. Box algorithm was used to provide the seed points that may possibly belong to the path line, which was being searched.

Moreover, Shoujun et al. has proposed a fully automatic tracking based method that can adapt to varying vessel curvatures and diameters resulting from arterial stenoses or aneurysms [77]. The proposed vessel segmentation method has been implemented based on probabilistic vessel tracking and fuzzy structure pattern inferring. Multi scale Gabor filtering and Hessian matrix analysis were used during the pre-processing phase of this study to enhance and extract vessel features from the original angiographic image, leading to a vessel feature map as well as a vessel direction map. In tracking, vessel feature map was analyzed automatically for detection a seed point. After that, two operators namely; probabilistic tracking operator and a vessel structure pattern detector worked together based on the detected seed point to extract vessel segments or branches one at a time. A multi feature based fuzzy inferring function, which is implemented based on vessel structure pattern detector has been implemented in this study to gather the local structure pattern. The identified structure pattern, such as crossing or bifurcation, was used to control the tracking process, for example, to keep tracking the current segment or start tracking a new one, depending on the detected pattern.

Artificial Intelligence based approaches

Artificial Intelligence based segmentation methods utilize knowledge to guide the segmentation process to extract the vessel structures [60]. Image acquisition technique or general blood vessel model can be used as prior knowledge to guide the Artificial Intelligence based segmentation process. Artificial Intelligence based segmentation method possesses high level of accuracy but the computational complexity is much larger than the other segmentation methods.

Stansfield has proposed a rule-based expert system for automatic segmentation of CAs from digital subtracted angiograms [78]. Her proposed system consists of three processing stages namely pre-processing stage and the two stages embodied in the expert system itself. During the pre-processing stage, both an edge and a region analysis are performed separately and later those two representations were combined. Subsequently, the region segmentation was performed by analyzing the detected edges. Later on, the detected regions were divided into "strips" based on their shape and those were placed along with the edge segments created by the edge analysis. At the end of pre-processing, the resulting image served as input to the expert system. The main function of the expert system was to isolate the CAs in the segmented image, while eliminating remaining noise structures from the partially processed angiography images. Moreover, this expert system was rule based and consisted of three components namely; database or short term memory, a knowledge base or long term memory and a rule interpreter, which controls the problem solving process. The expert system itself is separated into two independent stages namely the low level stage and the high level stage. In the low level stage of expert system, a domain independent knowledge of image segmentation, grouping, and geometric relations was applied to the segmented image created by the pre-processing stage. In this stage, the rules are applied to join line segments, to merge regions and to establish such relations as adjacent and parallel. It provided the refined segmentation and a set of relations between the objects in the segmented image as the results. In the high-level stage, it has applied a domain dependent knowledge of cardiac anatomy and physiology to interpret this segmented image. Moreover, in this stage, it can recognize blood vessels and noise separately. Subsequently, a final segmented image is created containing only detected blood vessels in high-level stage of the Stansfield's rule-based expert system.

2.5.3 Background studies for quantitative coronary analysis

Angiography based quantitative coronary analysis is done to obtain parameters that quantify the coronary artery lumen to determine the severity of the coronary stenosis [79]. It is done based on better contrast coronary angiograms. Moreover, the approaches suggested for vessel skeleton extraction and vessel path tracking are

widespread in research studies carried out in the recent past. Hence, the objective of this section is to elaborate some of the important research attempts made for quantitative coronary analysis to distinguish the rationale of objective assessment of stenosis.

Zou et.al have proposed a model based consecutive scan line tracking method for extracting CA vessel networks [75]. In their proposed method, the consecutive scan line profiles are fitted by a parametric imaging model to estimate local vessel center point, radius, edge locations and direction. Moreover, an adaptive tracking strategy has been proposed with possible termination criteria to track each vessel segment. Possible continuation points of the same vessel segment or those of its bifurcated segments are searched by using a specific look-ahead detection scheme, which is implemented in this study. This is useful for preventing premature termination of tracking and detection of bifurcations. Moreover, the initial seed point and tracking direction is set interactively for this proposed tracking method and it extracts the majority of the vascular network from the angiography image as the results.

Lin and Ching have proposed a gradient vector flow based feature extraction method for the segmented CA vasculature in [26]. In their study, the CA segmentation results are depicted in a binary image and it is used for determining the medial axis of the CAs. The vectors in the gradient vector flow field are created from the segmentation image to obtain the medial axis of the vessel. Hence, it provides a polygonal path with two end points on the medial axis of a vessel and it is denoted as the initial snake model. Moreover, the vector flow pushes the polygonal path towards the center of the vessel and provides the medial axis of the vessel when the snake converges to it at minimum cost. The edges of the vessels are obtained by applying canny edge detection and vessel diameter is calculated by modeling two perpendicular lines to left and right side boundaries from the medial axis [80].

Canny edge detection is also used in the research study, which is discussed in this thesis, for extraction of the vessel boundaries. Therefore, it is worth to state the main implementation steps of Canny edge detection algorithm as stated in [80]. Accordingly, this algorithm extracts the edges of the objects through five main steps

namely; smoothing, finding gradients, non-maximum suppression, double thresholding and edge tracking by hysteresis. Figure 2.23 depicts the visual illustrations of these implementation steps clearly. In order to noise being mistaken as edges, smoothing is applied as the initial step of this edge detection algorithm to reduce the noise (Figure 2.23 (b)). Generally, the edges are placed where the gradients of the image has large gradient magnitudes. Hence, it calculates the gradient magnitude of the image by using sobel filter as the second step (Figure 2.23 (c)). Moreover, the gradient orientation is also calculated to determine the edge direction. The objective of the non-muximum suppression is to transform the blurred edges detected in the previous step to sharp edges. In order to achieve that, it will preserve all local maxima by deleting everything else in the gradient image (Figure 2.23 (d)). Consequently, double thresholding is applied to the non-maximum suppression result to determine the potential edges. Within the double thresholding, edge pixels stronger than the high threshold are marked as strong edges, edge pixels weaker than the low threshold are deemphasized and edge pixels between the two thresholds are marked as weak edges (Figure 2.23 (e)). Finally, within the edge tracking by hysteresis operation, all edges that are not connected to the strong edges are deemphasized further and strong edges are preserved to generate the final results (Figure 2.23 (f) and (g)).

Hernandez-Vela and his team have published a CA segmentation and centerline extraction method in [81]. The proposed method is implemented based on graph-cuts theory. Moreover, this graph-cuts theory has been applied in this study to model vessel structures to obtain a globally optimal segmentation of the CA tree in angiography images and to achieve accurate detection of both the centerline and the vessel borders. At this juncture, they have combined the computed features like vesselness (the local vessel appearance), geodesic paths (the local connectivity to other vessel regions), and a new multi scale edge map (a new multiscale version of the adaptive canny detector) based on the angiography image to be processed in order to customize the graph-cuts approach for segmentation of tubular structures. The segmented binary image is used to determine the vessel centerlines. Within the procedure, the distance map of the binary segmentation image is computed.

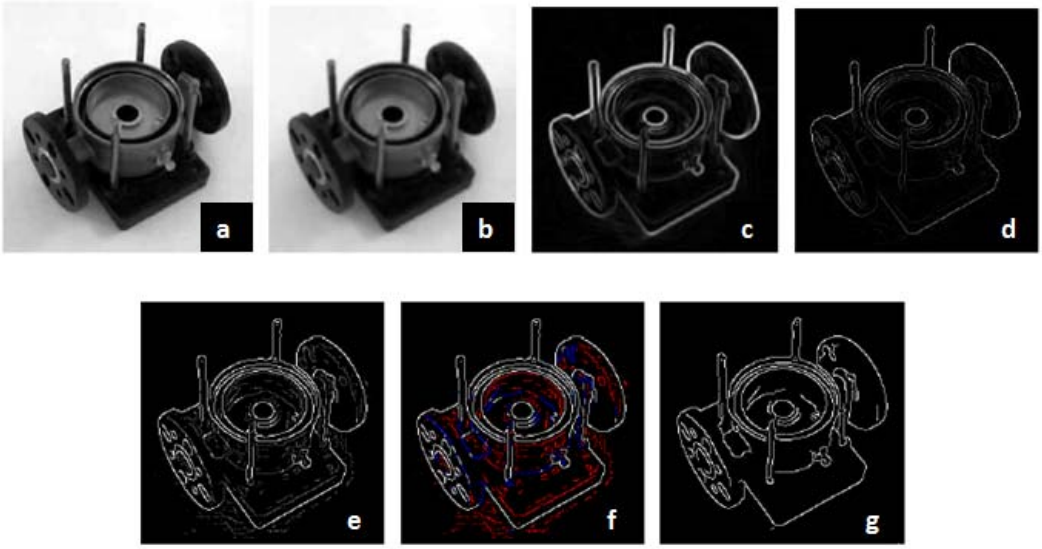

Figure 2.23: Steps of canny edge detection. (a) original image; (b) smoothed image; (c) gradient magnitude; (d) edges after non-maximum suppression; (e) double thresholding; (f) edge tracking by hysteresis; (g) detected edges.

Consequently, non-maxima suppression is applied to find local maxima and a classic ridge transversal method is applied to connect the local maxima. The ridge transversal stops when it finds another centerline or it exits the segmented area.

A novel method has been proposed for structural matching of CA junctions recorded in CCA by Yumei in [82]. This method is basically used to track the correspondence of vessel branches among the consecutive CCA frames. Multi scale Hessian matrix based approach has been used for vessel enhancement and segmentation. Segmented vessel tree is saved as a binary image and it is used for extraction of blood vessel junctions and tracking the extracted junctions. Prior to extracting the vessel junctions, vessel skeleton is obtained by applying morphology-based image thinning technique. Subsequently, the vessel junctions are extracted by traversing the blood vessel skeleton and a graph of junctions is obtained as the results. Additionally, significant features of the vessel junctions such as its position, the intensity of its neighbors, its branch angles and branch widths have been computed. Finally, junction tracking is performed between two consecutive frames in the CCA to find

the correspondence between the branches represented in the computed graphs among two consecutive frames of the CCA to be processed. It is done by computing the difference of the two identical junctions' descriptors computed for two consecutive CCA frames.

The research study mentioned in this thesis is used Zhang and Suen's fast parallel thinning algorithm to obtain the skeleton of the blood vessels [83]. It is proven that this thinning algorithm can efficiently generate single pixel width skeletons of different shapes of objects efficiently. Moreover, the algorithm removes all the contour points of the image except those points that belong to the skeleton. The algorithm repeatedly executes certain operations and within iteration, the algorithm has further divided into two sub iterations to preserve the connectivity among the skeleton pixels. Moreover, Figure 2.24 depicts the visual illustrations of these sub iterations and the original Zhang and Suen's fast parallel thinning algorithm has been published [83]. Accordingly, the first sub iteration removes only the south-east boundary points and the north-west corner points, which do not belong to the skeleton (Figure 2.24 (a)). Just as, within the second sub iteration, it removes only the north-east boundary points and the south-east corner points, which do not belong to a skeleton (Figure 2.24 (b)).

Another CA tree extraction method has been published by Haris et al. and they have introduced circular sampling based vessel path tracking method in their study [84][85]. Moreover, the approximate centerline and borders of the coronary arterial tree are extracted through a recursive artery tracking method, which is implemented based on circular template analysis for the local artery border detection. In the latter stage of the proposed method, accurate skeleton and borders of each artery segment of the arterial tree are computed based on the morphological tools of homotopy modification and watershed transform. The structural descriptions of the CA tree (skeleton and borders) along with accurate information for the CA dimensions have been produced as the output of this research study.

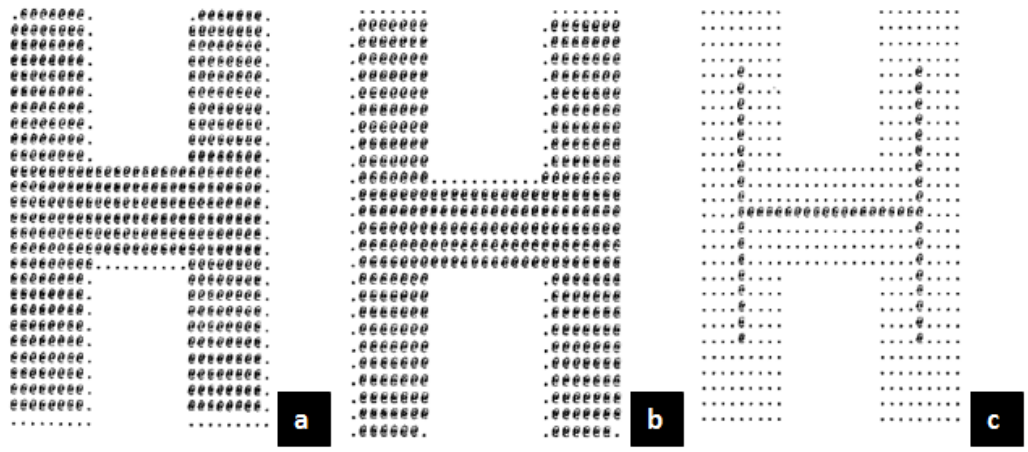

Figure 2.24: Zhang and Suen's thinning algorithm steps. (a) results of first sub iteration; (b) results of second sub iteration; (c) generated skeleton ('@' indicates the image pixels, '.' Indicates removed pixels.).

Adaptive tracking algorithm has been proposed by Sun to automatically identify the vessel contours in coronary angiograms [86]. Proposed tracking algorithm starts with the given seed point and exploit the spatial continuity of the vessel's centerline, orientation, diameter, and density. Moreover, the algorithm consists of an extrapolation-update process, which is guided by a matched filter. Furthermore, this proposed tracking method has been tested using synthetic images, digital subtraction angiograms, and CCAs to verify its' robustness and efficiency.

A new deformable spline based method for determining vessel boundaries, and enhancing their centerline features has been published by Klein et al [87]. In this proposed method, vessels are represented by B-spline snakes, and are optimized on filter outputs with dynamic programming. Moreover, vessel centerlines were defined mathematically as a line drawn between two edges such that, at any point along its length, its perpendiculars intersect the edges at equal distances from itself. The diameter stenosis is determined from a computed vessel centerline. In order to achieve that, the first point of the centerline is given initially. Consequently, vessel centerline is tracked iteratively to compute the diameter of the vessel. In order to do that, a T-shaped structure is used and it is positioned on the given center point as its'

long arms perpendicular to a short stem. Subsequently, the "T" is rotated and an orientation in which the two resulting distances along the arms to the edges are equal is sought. The intersection of the stem and arms of the "T" then becomes the next point on the centerline. This process is repeated until the end of the marked centerline of the vessel.

Moreover, Shoujun et al. has proposed a fully automatic tracking based method that can adapt to varying vessel curvatures and diameters resulting from arterial stenosis or aneurysms [77]. A probabilistic vessel tracking and fuzzy structure pattern inferring technique have been implemented in this study for vessel segmentation.

2.6 Summary

This chapter has emphasized on how angiography is used for CA disease diagnosis and its' strength and weaknesses. Initially, the setup of cath lab and the function of the fluoroscope used for imaging were discussed. Then the angiographic views were clearly elaborated with visual illustrations. How the views are used for grading the stenosis had been discussed in the next section of the chapter. After that, the proven limitations in angiography in subjective stenosis assessment have been mentioned with evidence. The background studies carried out with respect to this image modality has been elaborated as the last section of this chapter. .

CHAPTER 3
FRAME ENHANCEMENT AND ALIGNMENT

The process of generating CCAs and its visual representations have been discussed comprehensively in Chapter 02. Even though these CCA frames are produced directly by the fluoroscope, past researches and empirical results have shown that those produced CCA frames are degraded by various types of artifacts. Moreover, those negative artifacts result in severe obstructions for segmentation the vessel structures and quantitative analysis of stenosis. Hence, it is worth analyzing those artifacts and to implement an effective process to enhance the CCA frames to obtain the optimal quality required for the subsequent processing.

Initially, the chapter emphasizes the complete design of the proposed quantitative coronary analysis method of this research study for improving the CCA for objective diagnosis. Later, the chapter is focused to discuss about the first phase of this proposed method, which is known as pre-processing. Within this section, it elaborates the effect of already recognized negative visual artifacts in CCAs with visual illustrations. Finally, the main implantation stages of the proposed pre-processing phase such as frame enhancement, frame alignment and mask creation will be detailed comprehensively.

3.1 Overview of the proposed method

In order to achieve the study objectives stated in section 1.7, a novel method has been proposed as depicted in the flow chart of Figure 3.1. According to the flowchart, the direct CCA is input to this proposed method. An individual frame extracted from this input CCA is processed at a time by passing it through the four main processing phases namely; pre-processing, segmentation, vessel tracking and calculation. Although this is an iterative process, the same processing phases will be implemented on each and every frame of the input CCA continuously. Within iteration, it logs the diameter of the selected vessel segment and length of the vessel skeleton with respect to the current frame to be processed. These log data can be

used to generate visualizations of the vessel diameter to determine the suspected regions.

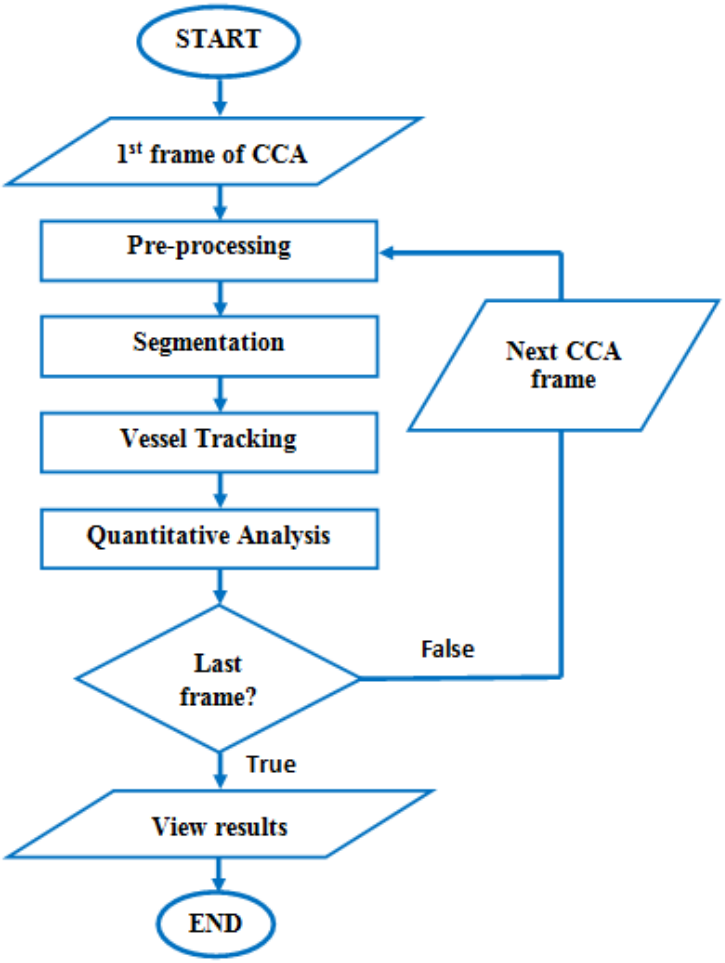

Figure 3.1: Flow chart of the proposed method.

The objective of the pre-processing phase is to enhance the visual quality of the CAs shown in the CCA frame to be processed. It is achieved by reducing the recognized visual degradation artifacts from the CCA frame such as noise, non-uniform illumination and global motion. Moreover, in this phase, some image processing techniques have been applied to emphasize the blood vessels by reducing the background details shown in the frame. This enhanced frame is input to the subsequent segmentation phase to extract the main CA depending on the angiography view. Subsequently, this segmented frame is input to the vessel tracking

phase to track the vessel skeleton starting from the catheter engaged point visualized in the frame to be processed.

The vessel diameter and length of vessel skeleton calculations are done in the last implementation phase of this proposed method, which is known as quantitative analysis. Meantime the calculated vessel diameter and length of vessel skeleton are logged for both result analysis and detection of stenosis regions in the processed main CA segment. This chapter broadly discusses about the implementation steps of the pre-processing phase and the remaining implementation phases of this proposed method will be elaborated comprehensively in the following chapters.

Ethics Review Committee of the Faculty of Medicine, University of Colombo has granted the ethical clearance to extract the CCAs, which are required for validating the results of this proposed method. Hence, the direct CCAs recorded under the three standard angiography views were selected for data validation namely; LAO Cranial in RCA catheterization and AP Caudal and AP Cranial views in LCA catheterization. The main reason for selecting the aforementioned angiogram views for creating the dataset is that those views provide excellent visualizations for the main CAs namely RCA, CX and LAD respectively.

3.2 Visual degradations in CCA frame

It is necessary to obtain clear X-ray images for CCAs because, spatial indistinctness of CCA frames cause incorrect assessments in subsequent quantitative approaches followed in this study. The quality of angiographic X-ray images is determined in terms of contrast and spatial resolution. Moreover, it has been reported that these angiographic quality factors depend on the following effects: geometric distortions, the resolution of the detector, scatter and veiling glare, non-uniform opacification, noise and motion [30]. Fluoroscope with a flat panel detector has some inbuilt mechanics to evade the geometric distortions, scatter and veiling glare from the angiography images. However, non-uniform illumination, noise and motion are still present in the angiography images and cause some visual degradation in recorded angiography images. Following sections will emphasize the characteristics and consequences of those artifacts for the CCAs in detail.

3.2.1 Non-uniform illumination and poor opacification

Non-uniform illumination in CCAs degrades the visual quality of the angiography and formulates some incorrect vessel segments in computer based vessel recognition or segmentation procedures. This phenomenon visualizes an individual vessel breaking into several segments. Moreover, it makes some hindrances to clearly recognize which branch segment belongs to which CA in the frame to be processed. Hence, it makes some difficulties to automatically segment the CAs accurately [25]. Figure 3.2 (a) depicts this artifact for further clarifications. In this figure, the affected area is circled and within that area, it is hard to identify which vessel branch belongs to which CA apparently.

It is reported that the poor contrast opacification of the vessel may lead to a false impression of an angiographically significant lesion or lucency, which could be considered a clot [40]. Further, inadequate mixing of contrast material and blood could be seen as a luminal irregularity. It occurs when there is a strong presence of blood and contrast agents in the vessels, the thick vessels have more contrast to noise ratios than the small narrow ones [25]. Figure 3.2 (b) clearly depicts this artifact. Contrast of the vessel depicted in the circular area is extremely poor when compared to the main blood vessel. In order to overcome this issue, a bolus injection of contrast material must be delivered continuously until the adequate opacification level is reached and the angiogram could be interpreted correctly. Moreover, it is possible to enhance the delivery of contrast material by using a larger catheter or a power injector. Even though the injection of contrast agent is controlled mechanically still there is a possibility of getting low contrast angiography images. Hence, it is necessary to find a method to overcome this problem automatically.

As shown in Figure 3.2 (c), the occurrence of indistinguishable white or gray color patches on vessel regions is also problematic in automatic processing of CCAs [27]. As shown in Figure 3.2 (c), this haziness occurs when the X-ray beams are positioned perpendicularly to the plaque deposit during the image acquisition. Apart from that, the inconsistent delivery of contrast agent also causes the same visual degradation. The affected areas are visualized as white or gray color patches, making

it hard to distinguish the availability of stenosis in the vessel and to measure the degree of that stenosis. Further, this effect reduces the spatial coherence of the vessel structures and provides number of incorrectly segmented disconnected vessel segments as a result of such segmentation. Therefore, it causes obstructions in quantitative assessment of lumen diameter of the vessels.

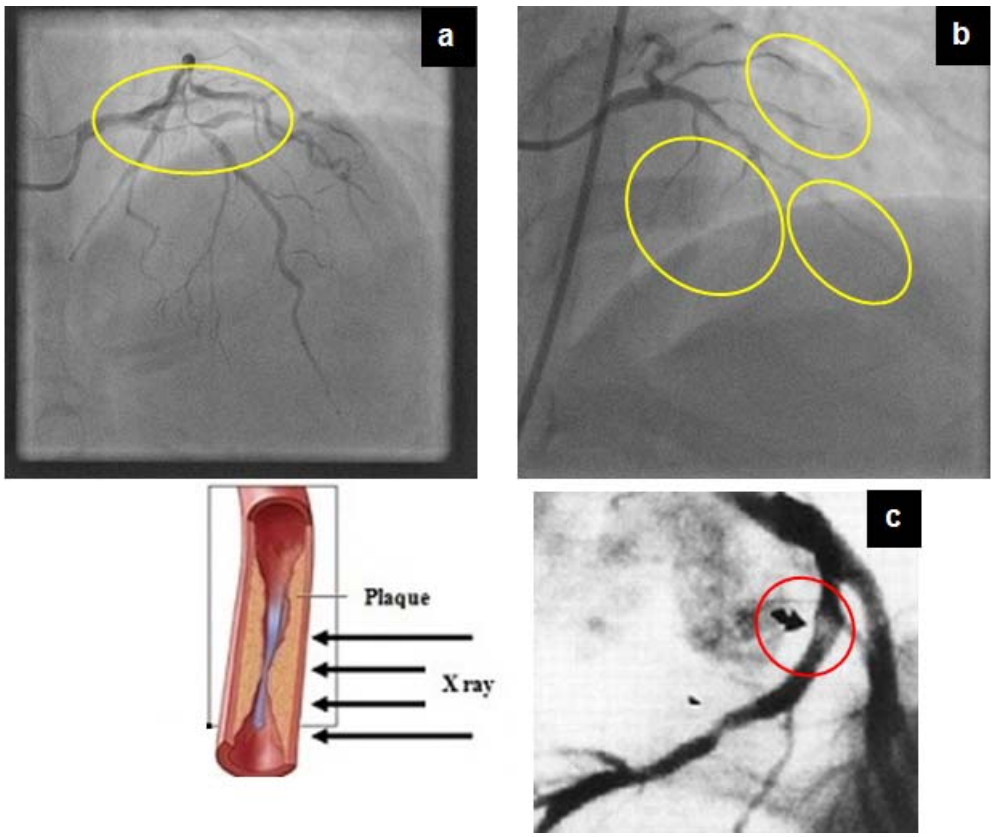

Figure 3.2: Effect of non-uniform illumination and poor opacification of angiogram. (a) non- uniform illumination; (b) poor contrast; (c) haziness.

3.2.2 Noise

CCA frames reduce the ability to identify the defects in some blood vessels due to the low contrast embedded by the noise. Accordingly, the effective approaches to remove noise become mandatory. Angiograms are characterized by noise, which is caused by two main sources; quantum noise and electrical noise [30] [47]. Quantum noise occurs due to the random distribution of X-ray photons on the image area

during the image formation in fluoroscope. During the image formation, part of an X-ray beam forms the exposure to one small area within a receptor of the fluoroscope. Due to this random exposure of X-ray photons, at some points, there might be clusters of several photons and, also, there exists some areas where only a few photons are collected. This uneven distribution of photons shows up in the image as quantum noise [88]. Figure 3.3 clearly depicts this effect by using two angiogram images. Figure 3.3 (a) shows an image, which is captured under low radiation dose where as Figure 3.3 (b) shows the same vessel structures, which were captured under high radiation dose. It determines that the image captured under low radiation dose suffers from quantum noise and has low contrast to characterize the blood vessels precisely compared to the high radiation dose image. In addition to the quantum noise, the electrical system adds Gaussian noise and impulse noise to the CCAs [30][57][68].

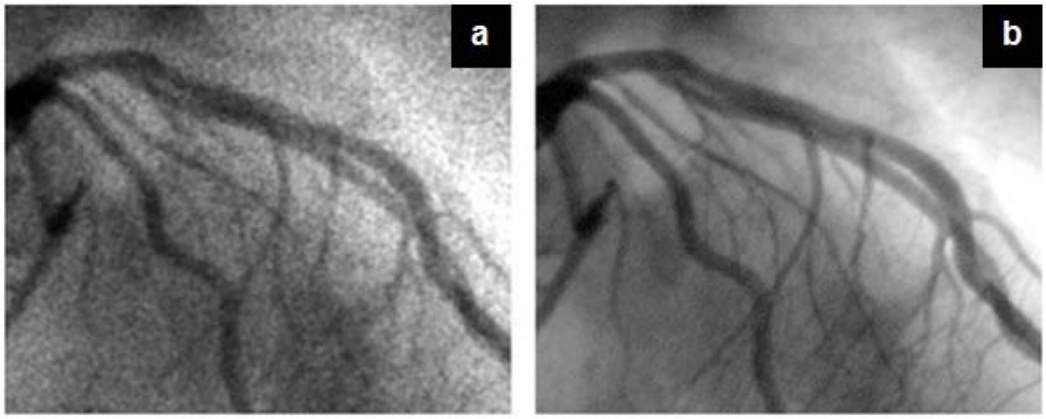

Figure 3.3: Effect of radiation dose for angiography. (a) low radiation does image; (b) high radiation dose image.

3.2.3 Motion

Unlike renal or cerebral angiograms, CCAs are recorded with motion, which is another factor that affects the quality of the CCAs. Mainly, there are three types of motions in CCAs namely global, radial and the local motions. Global and radial motions occur due to the systolic and diastolic movements of the heart [89]. Global

motion produces rapid displacements of vessel structures from its' initial recorded point, and radial motion makes tiny movements in distal parts of the main CAs. Local motion occurs due to the flow of the contrast agent within the CAs, and it is the important motion category used to determine the functional significance of arterial flow [90]. CAs are adhering to the epicardium of the heart and follow dynamic performances of the related myocardium during heart beat. Hence cardiac motion can be directly determined by arterial motion as depicted in Figure 3.4 [58]. The figure consists of non-uniformly illuminated four consecutive frames of a CCA and the catheter engaged area shown in each frame is marked using a white square for better visualization of the artifact. The placement of this marked region is displaced in the four consecutive frames of Figure 3.4 as a result of global motion. Not only that, but also the distribution of contrast agent gradually increases in all the four frames as a result of the local motion.

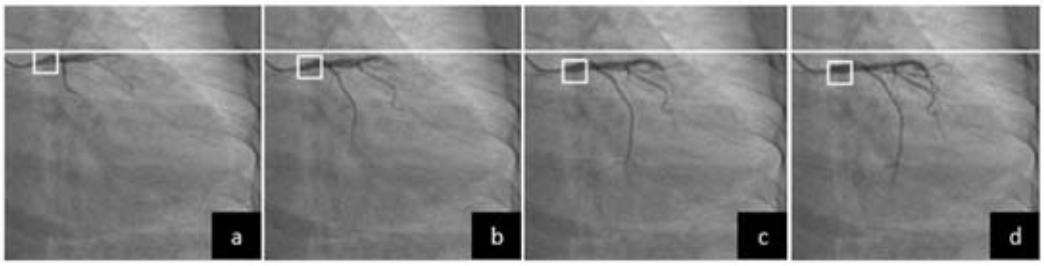

Figure 3.4: Motion artifacts in CCAs. (White square indicates the catheter-engaged region.)

As visualized in Figure 3.4, the CAs are displaced from its initial position due to global motion. Hence, it is clear that the blood vessel structures are not aligned among the consecutive CCA frames due to this global motion. It causes some obstructions in automatic vessel tracking using CCAs because it is required to segment and track the CAs within the whole frame sequence. This can be simplified if the vessel structures are positioned in a stable place in each frame of the CCA to be processed. Moreover, this global motion can generate some frames in a CCA, which represents superimposition of CAs with background tissues like spine and

diaphragm. This may cause some problems to characterize the CAs from the background structures in some processing phases.

It is apparent that the requirement of finding a solution to evade the aforementioned visual problems from the CCA frames is crucial. Hence, it is mandatory to empirically find a methodology to obtain uniformly illuminated, noise reduced visually aligned frames as a prior step of this proposed study. The pre-processing phase of this study has addressed these issues empirically and the following sections of the chapter discuss the steps of pre-processing phase comprehensively.

3.3 Proposed method for pre-processing phase

It has already been mentioned that the frames extracted from direct CCA are used in this research study to process and quantitatively analyze the severity of stenosis. Generally, the direct CCAs consist of a frame sequence, which visualizes different scenes such as the catheter engagement, filling of contrast agent within the CAs and representing filled vessel structures. Figure 3.5 depicts a frame sequence of a sample CCA, which can be used to clearly identify those visual scenes separately. According to Figure 3.5, frames, which are labeled from 1 to 7, 8 to 14 and 15 to 20 represent catheter engagement, filling of contrast agent within the CAs and filled vessel structures respectively. Out of those scenes, the frames visualizing the filling of contrast agent within the vessel structure and frame prior to start visualizing the first drop of contrast agent flooding are important to determine the functional features of CAs because, it is required to have a frame sequence that depicts the flooding of contrast agent within the arteries to determine the functional significance of CAs. Hence, those frames are selected from input CCAs for processing. This factor can be further clarified using Figure 3.5. In this figure, those frames labeled from 7 to 14 are marked as selected frames because those frames are responsible to visualize the required scenes. The frame recorded prior to start visualizing the first drop of contrast agent clearly visualizes the successful catheter engagement with the selected CA. Moreover, this frame clearly represents the background of the frame and initial placement of the catheter clearly. This feature is important to frame alignment and vessel path tracking, which will be discussed in future sections in this thesis. Once

the frame selection has been completed a direct CCA can be denoted as a sequence of frames as shown in equation (3.1).

$$f_0^s(x,y) = [f_0^1(x,y), f_0^2(x,y), f_0^3(x,y) \dots \dots \dots f_0^n(x,y)] \quad (3.1)$$

Where $f_0(x,y)$ represents the direct CCA frame with (x,y) spatial coordinates and the superscript s of each frame $f_0(x,y)$ indicates the frame sequence number starting from *1* to n. It can be used to directly identify any frame of CCA to be processed. Moreover, the subscript of f indicates a certain operational step of the proposed method and initially it is assigned *0* to mark the non-processed direct CCA frames.

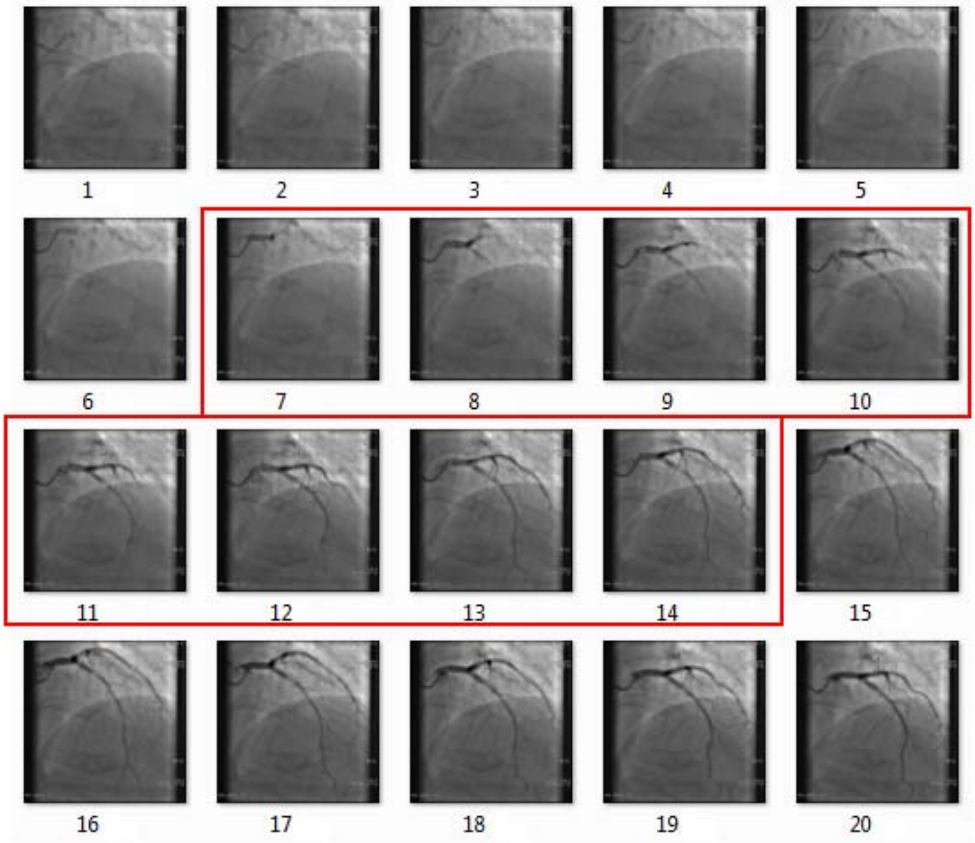

Figure 3.5: Visuals of selected frames of a CCA for processing. (Frames from 7 to 14 have been selected in this CCA for processing.)

As mentioned in section 3.1 above, the input CCA frames are processed repeatedly and the flowchart depicted in Figure 3.1 clearly represents the processing phases of the proposed method. The main focus of this chapter is to elaborate the pre-processing phase of the study and Figure 3.6 depicts the implementation stages of that proposed pre-processing phase. According to Figure 3.6, the input direct CCA frame ($f_0(x,y)$) is processed under three processing stages namely frame enhancement, frame alignment and mask creation. As a result of that, the pre-processing phase produces visually aligned enhanced frames and mask image as the output. The next sections of this chapter will elaborate the implementation stages of the proposed pre-processing phase of this study in detail.

3.4 Frame enhancement

The objective of frame enhancement is to convert direct CCA frames into noise free uniformly illuminated frames. There are some reported factors in the area of angiographic image enhancement, which have been widely accepted by cardiologists [47]. Those are:

- The image enhancement is used for visualization purposes only, and not for quantitative analysis.
- Detailed image structures should not be lost during the enhancing procedure.
- The original dimensions of vascular structures should be preserved in the enhanced image.

Moreover, those factors are also persevered in this frame enhancement stage.

As mentioned in section 3.2, it has been revealed that the direct CCA frames suffer from quantum noise and impulse noise. The CCAs used to test in this study have been produced by the fluoroscope with flat panel detectors and those machines have some inbuilt mechanisms to reduce the effect of quantum noise such as binning.

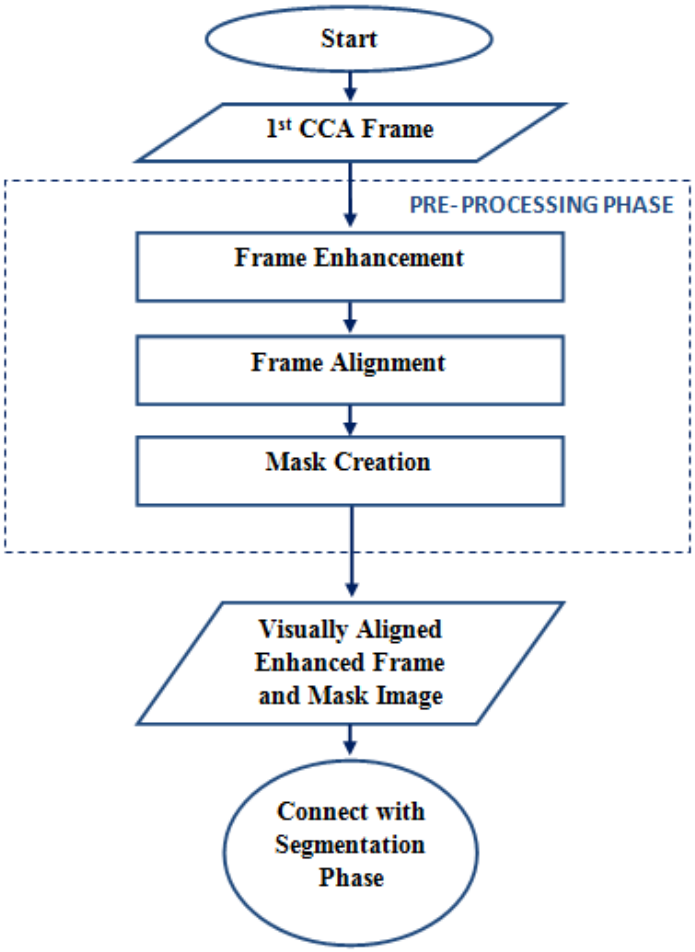

Figure 3.6: Implementation stages of pre-processing phase.

Further, it has been reported that this quantum noise can be minimized through the spatial filtering techniques [91]. Some spatial filtering methods have been implemented during the segmentation phase of this study. Hence, it will be minimize the remaining quantum noise in the CCA frames to be processed. In order to eliminate the impulse noise, a median filter with kernel size 3×3 was applied to the input direct CCA frame to be processed [57]. The frame obtained after the noise reduction is denoted as $f_1(x,y)$ and it can be characterized by two components namely illumination (i) and reflectance (r) as shown in equation (3.2);

$$f_1(x,y) = i(x,y) \times r(x,y) \tag{3.2}$$

Where; $0 < i(x,y) < \infty$, $0 < r(x,y) < 1$ (*0 – total absorption, 1 – total reflectance*) and x,y represent the spatial coordinates of the image function $f_I(x,y)$.

Subsequently, this noise-reduced frame was further processed to remove the effect of non-uniform illumination. In order to achieve that, homomorphic butterworth high pass filter was applied to attenuate the illumination component (i) from the CCA frame [92]. Conventionally, the illumination (i) and reflectance (r) components of an image are not separable. Homomorphic filtering is a method in which the illumination and reflectance components can be filtered individually [93]. Due to that, homomorphic filter was selected to obtain the expected uniform illumination of the CCA frames to be processed. It consists of several steps and those steps have been elaborated subsequently.

As the initial step, the CCA frame $f_I(x,y)$ is mapped into the natural logarithm domain. As a result of that, the frame is transformed to the sum of its illumination and reflectance components as shown in equation (3.3).

$$p(x,y) = ln\{i(x,y)\} + ln\{r(x,y)\} \tag{3.3}$$

Where, $p(x,y)$ denotes the resulting frame obtained after applying natural logarithmic on $f_I(x,y)$;

After that, the Discrete Fourier Transform (DFT) is applied to partially processed frame to transform it into the frequency domain. Equation (3.4) represents the transformation of $p(x,y)$ in to DFT;

$$F\{p(x,y)\} = F[ln\{i(x,y)\}] + F[ln\{r(x,y)\}] \tag{3.4}$$

Becomes

$$p(u,v) = i(u,v) + r(u,v)$$

Where, F denotes the application of DFT, $i(u,v)$ and $r(u,v)$ are the Fourier transforms of $ln\{i(x,y)\}$ and $ln\{r(x,y)\}$. (u,v) represents coordinates of the frequency spectrum obtained by the DFT.

It has been reported that the illumination components of the CCA frame can be easily identified through the low frequency content in the frequency domain because the illumination is considered as a slowly varying pattern in a particular image [48]. Hence, the butterworth high pass filter was applied to emphasize the high frequency components of the frame to be processed. These high frequency components are responsible in saving the ridge structures in the frame and for attenuating the low frequency bands, which are responsible for illumination. In order to filter out the high frequency bands, convolution was done between the DFT frame ($p(u,v)$) and the butterworth high pass filter ($b(u,v)$). Equation (3.5) represents this operation and $h(u,v)$ denotes the resulting filtered frame obtained finally.

$$h(u,v) = p(u,v) * b(u,v) \tag{3.5}$$

$b(u,v)$ is obtained convoluting the $p(x,y)$ by the butterworth high pass filter function (*hpf*) given in equation (3.6);

$$hpf = \frac{1}{1 + \{D_0/D(u,v)\}^{2n}} \tag{3.6}$$

Where, D_0 is the distance from origin to cutoff frequency in the DFT frequency spectrum, $D(u,v)$ is the radial distance from the origin and n is the order. According to the study mentioned in [48], values of both D_0 and n have been set as 10 and 2 respectively. As a result of filtering, high frequency components relevant to the image reflectance are emphasized and low frequency components relevant to the illumination are deemphasized. After the filtering, inverse DFT has been applied to transform the image into natural logarithm domain as shown in equation (3.7);

$$l(x,y) = F^{-1}\{h(u,v)\} = F^{-1}\{b(u,v).i(u,v)\} + F^{-1}\{b(u,v).r(u,v)\} \tag{3.7}$$

Where F^{-1} denotes the inverse DFT operation and $l(x,y)$ is the resulting image

$$i' = F^{-1}\{b(u,v).i(u,v)\}$$

$$r' = F^{-1}\{b(u,v).r(u,v)\}$$

Hence;

$$l(x,y) = i' + r'$$

Then, to get back the homomorphic filtered CCA frame to the spatial domain, the transformation of natural logarithm has been inversed, which is exponential. Equation (3.8) represents this operation.

$$f_2(x,y) = exp[l(x,y)] = exp[(i'(x,y)] \times exp[(r'(x,y)] \tag{3.8}$$

Hence;

$$f_2(x,y) = i_0(x,y) \times r_0(x,y)$$

Where, $f_2(x,y)$ denotes the homomorphic filtered image. $i_0(x,y)$ and $r_0(x,y)$ are the illumination and reflectance components of the homomorphic filtered image, which satisfy the following conditions $i_0(x,y) \neq i(x,y)$ and $r_0(x,y) \neq r(x,y)$.

As a result of aforementioned implementation steps, the processed CCA frame has been converted in to a uniformly illuminated frame. Moreover, this uniformly illuminated frame has been normalized by using equation (3.9) to obtain the better contrast among the vessel structures [48].

$$f_3(x,y) = \begin{cases} M_d + \sqrt{\dfrac{V_d(f_2(x,y) - M)^2}{V}} & if\ f_2(x,y) > M \\ M_d - \sqrt{\dfrac{V_d(f_2(x,y) - M)^2}{V}} & if\ f_2(x,y) \leq M \end{cases} \tag{3.9}$$

Where M and V denote the estimated mean and variance of input frame ($f_2(x,y)$) and M_d and V_d are desired mean and variance values respectively. $f_3(x,y)$ is the output frame. As mentioned in [48], M_d was set as $M/2$ and V_d was set as ($V \times 4$) to obtain better results. It is important to note that the radial distance and order parameters of butterworth high pass filter and M_d, V_d parameters of normalization are adjustable according to CCA obtained under different machines.

Figure 3.7 depicts visual illustrations of the frame enhancement stage. It contains three direct CCA frames ($f_1(x,y)$), which visualizes the LAD, CX and RCA arteries and enhanced versions of those frames ($f_3(x,y)$) respectively. Hence, it is apparent

that this frame enhancement stage of pre-processing phase provides noise reduced uniformly illuminated better contrast CCA frames as the output. These enhanced frames ($f_3(x,y)$) are then input to the next stage of the pre-processing phase, which will be discussed in the next section.

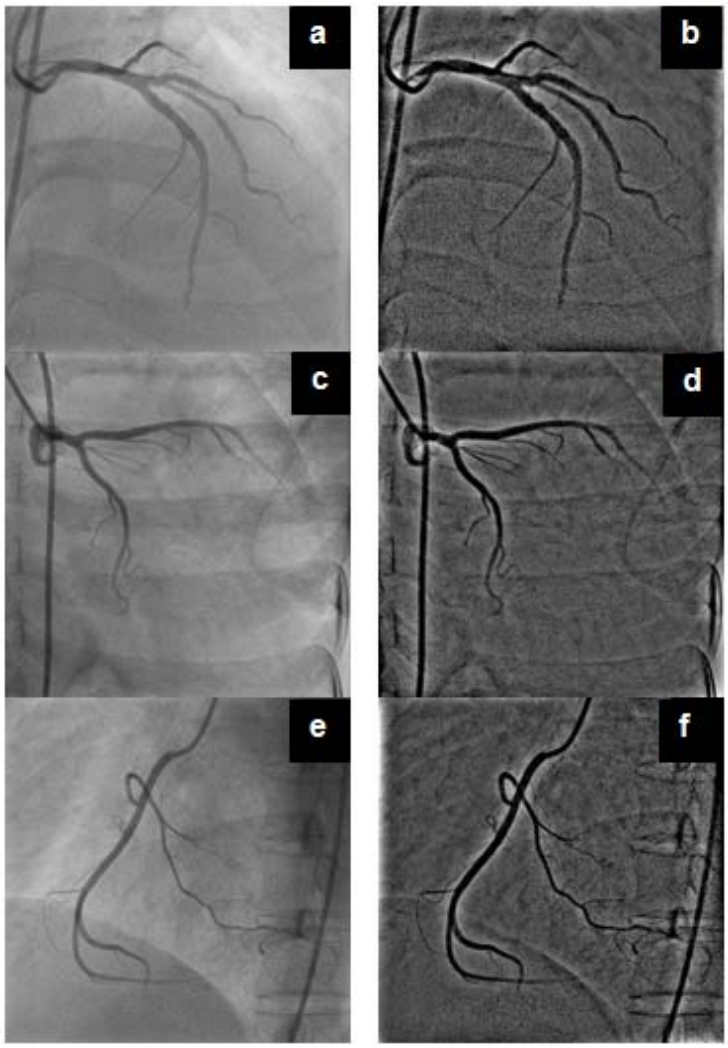

Figure 3.7: Frame enhancement. (a) LAD; (c) CX; (e) RCA; (b) enhanced LAD; (d) enhanced CX; (f) enhanced RCA.

3.5 Frame alignment

As mentioned in section 3.2.3, the CCAs are implicitly recorded with global motion thus it changes the placements of vessel structure from one frame to another. Due to

this, it is difficult to obtain visual correlation of the vessel structure across the CCA frames sequence (Figure 3.4) [57] [94]. Nonetheless, the visual correlation of the marked or dyed arteries across the frames is crucial prior to determining the functional significance of the CAs because it causes some obstructions in automatic vessel tracking. Further, it requires additional computation steps to determine the placement of vessel's starting point (catheter engaged point) in each frame due to the non-existence of visual correlation. Therefore, it is significant indeed to suggest a method to stabilize global motion artifact in the CCA frames using the enhanced frames produced in the previous step of the pre-processing stage. Hence, in this study, a frame alignment stage has been implemented for determining the global motion among the consecutive CCA frames and reconstructing those frames to achieve the desired vessel alignment.

In order to determine the global motion, it is required to calculate the GMV among the consecutive CCA frames and is calculated based on the template matching Image Processing technique. Further, this calculated GMV presents the displacement of the blood vessels (frame content) among the two consecutive frames as depicted in Figure 3.4. Subsequently, the frame reconstruction step will be performed to adjust the frame contents according to the calculated GMV. As a result of that, visual alignment among frame content can be achieved and it visualizes the spreading of contrast agent within the vessel structure starting from one fixed point.

In conventional template matching, the given template is matched with the reference image to find the region of interest based on the spatial contents coherence [95]. However, when considering about angiogram images the conventional template matching will fail in some situations because, the arteries recorded in angiogram frames are different from frame to frame due to vessel structure deformation due to motion artifact and non-uniform distribution of contrast agent within the CAs. This issue has been successfully addressed by the proposed frame alignment stage. The next sections of this chapter elaborate the implementation steps of this frame alignment stage based on its' five implementation steps namely; (i) template selection, (ii) template matching, (iii) false matching correction, (iv) calculating the GMV and (v) frame reconstruction.

3.5.1 Template selection

The proposed content alignment begins with the template selection step. In this step, the initial template is selected interactively from the first frame of the input pre-processed CCA. As shown in Figure 3.8(a), this selected template is located at $F_{x,y}$ point of the initial frame and it has w width and h height. The values of w and h depend on pixel width and height of the arbitrarily selected template. In addition to the template selection, it is necessary to select another region around the selected template as the search window in order to set the boundary for the subsequent template matching step. Figure 3.8(b) depicts the template search window located at $G_{x,y}$ point of the initial frame. It has m width and n height where $m>w$ and $n>h$. The matching will provide elegant results if the selected template consists of a clear object within it. Therefore, selecting a template around the catheter engaged area visualized in the first frame of the CCA provides successful results during the template matching steps because the catheter engaged area is clearly visualized in all recorded frames of most CCA cases. Hence, it is recommended to select the initial template from such an area in the first frame of the CCA to be processed.

3.5.2 Template matching

Template matching step begins after the template selection step and repeats until the last frame of the CCA is processed. Within this step, the template selected from the initial frame (location: $F_{x,y}$ and dimensions: $w \times h$) is matched with the next frame using the search window of size m width and n height as shown below;

Iteration	Previous frame	Current frame	Remarks
1		f_3^1	Template selection
2	f_3^1	f_3^2	Match frame *1* with frame *2*
3	f_3^2	f_3^3	Match frame *2* with frame *3*
	..	..	
n-1	f_3^{n-2}	f_3^{n-1}	Match frame *n-2* with frame *n-1*
n	f_3^{n-1}	f_3^n	Match frame *n-1* with frame *n*

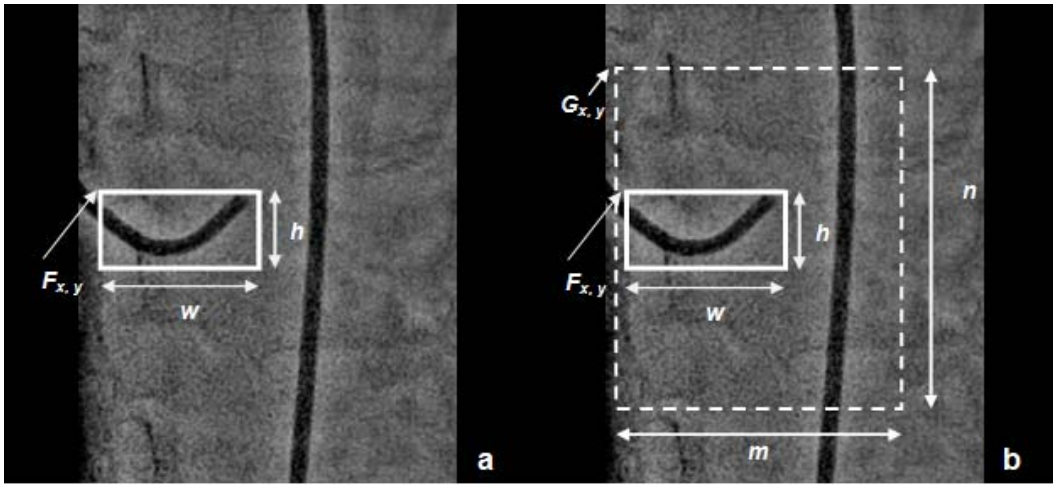

Figure 3.8: Template selection. (a) selected initial template; (b) selected template matching window.

The Correlation Coefficient (CC) is selected as the similarity measure for the template matching step because it produces the lowest false matching occurrences in the preliminary experiment [95]. Equation (3.10) denotes the CC method applied in the template matching step;

$$CC = \sum_{x',y'} [T'(x',y').I'(x+x',y+y')]^2 \tag{3.10}$$

Where;

$$T'(x',y') = T(x',y') - T_{mean}$$

$$I'(x+x',y+y') = I(x+x',y+y') - I_{mean}$$

T and *I* denote the template and the search window of the current frame in the CCA respectively. (*x, y*) denotes the coordinates of the search window and (*x', y'*) denotes the coordinates of the template starting from top left corner of it. T_{mean} gives the mean intensity of the template and I_{mean} gives the mean intensity of the search window, which is computed based on the region under the template.

In order to keep the computational output of the CC method, floating point matrix of size (*m–w+1*) width and (*n–h+1*) height are created intermediary in each iteration and is denoted as template matching result matrix *R*. The coordinate point, which

contains the maximum value in R is selected as the best match point and is denoted as R_{max}. Subsequently, this template matched point (R_{max}) is marked in the current frame and is denoted as $C_{x,y}$ where $C_{x,y} \neq F_{x,y}$. Inequality between $C_{x,y}$ point and $F_{x,y}$ point is caused by global motion, which occur due to the heart beat. A visual illustration of the template matching step is depicted in Figure 3.9. Sub image (a) and (b) in Figure 3.9 depict the reference (template at $F_{x,y}$ point) and matched templates (template at $C_{x,y}$ point) in two consecutive frames of a particular CCA. Moreover, Figure 3.9(c) depicts the template matching result matrix (R) created based on the search window in Figure 3.9 (d). The point, which has the maximum value for CC is marked in that image as R_{max}. Additionally, the coordinates with respect to R_{max} is marked in the search window depicted in Figure 3.9(d) as $C_{x,y}$ to represent the template matched region.

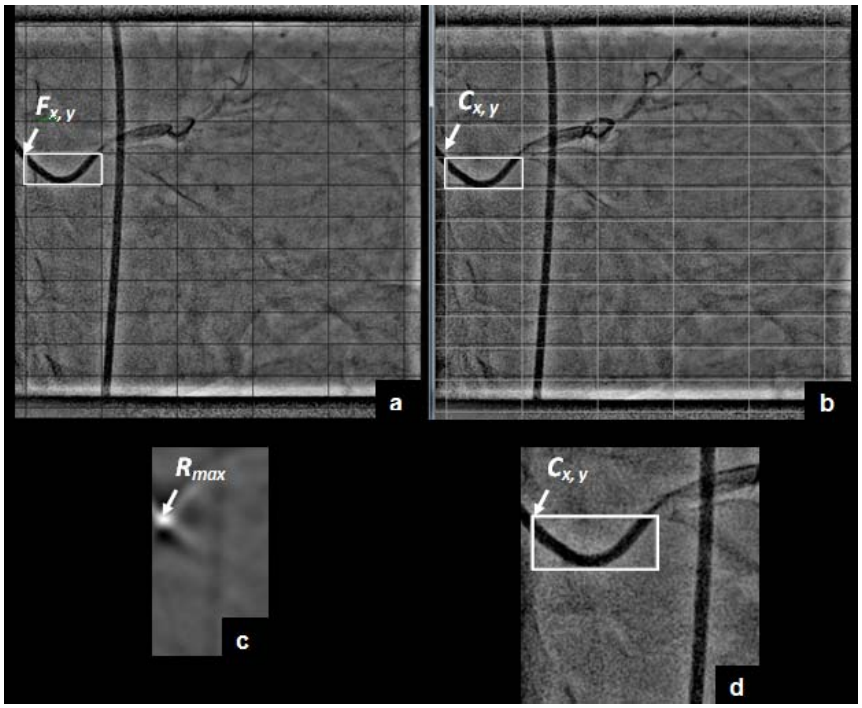

Figure 3.9: Template matching step between two consecutive frames. (a) marked template $F_{x,y}$ point in previous frame; (b) matched template at $C_{x,y}$ point in current frame; (c) template matching result matrix R; (d) matched template at $C_{x,y}$ point in the search window extracted from the current frame.

Figure 3.10 clearly illustrates the global motion captured through template matching. Due to that, the templates are displaced between the two consecutive frames and as a result of that, the vessel structures are not visually aligned. Hence, it is clear that the application of template matching is ensured to determine the GMV of the CCA to be processed.

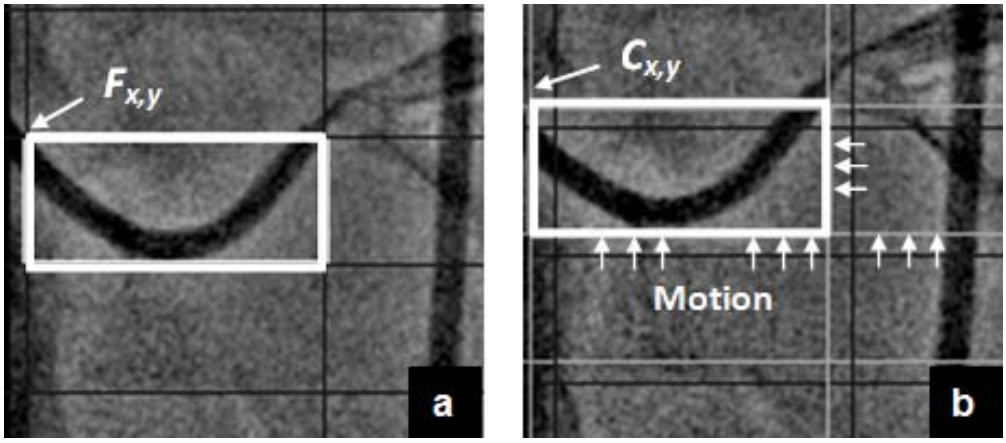

Figure 3.10: Template matching step between two consecutive frames. (a) selected template at $F_{x,y}$ point; (b) matched template at $C_{x,y}$ point.

3.5.3 False matching correction

Conventionally, template matching always provides spatially and visually correct matches. However, the empirical results of this study have revealed that, the template matching provides spatially correct but visually incorrect matches rarely in certain matching occurrences of some CCAs. This type of matching is considered as a false matching in frame alignment. The reasons for attaining false matching are the deformations in vessel structures due to the motion artifacts and non-uniform distribution of the contrast agent. However, these reasons technically matter template matching and lead to occur incorrect matching results in rare occasions. The template matching executes the results based on a similarity measure and finds the matching region from the current frame only by considering the spatial coherence of both reference and matched templates. Hence, it does not perform the execution by considering the similarity of visual features in the reference template. Due to motion artifacts and non-uniform distribution of the contrast agent, the intensity distribution

of the current frame can changed and it leads to this false matches. Figure 3.11 depicts this exception clearly. According to this figure, label *x* of image (a) depicts marked template and both labels *y* and *z* in image (b) denotes the false and expected correct matching templates respectively. Hence, it is apparent that this exception leads to the defective frame alignment. Therefore, a mechanism required to formalize matching the visual contents of the template in addition to matching the spatial coherence. This was the objective of this false matching correction step. Next, the technique, which is used to detect and correct the false matches in template matching has been elaborated in detail.

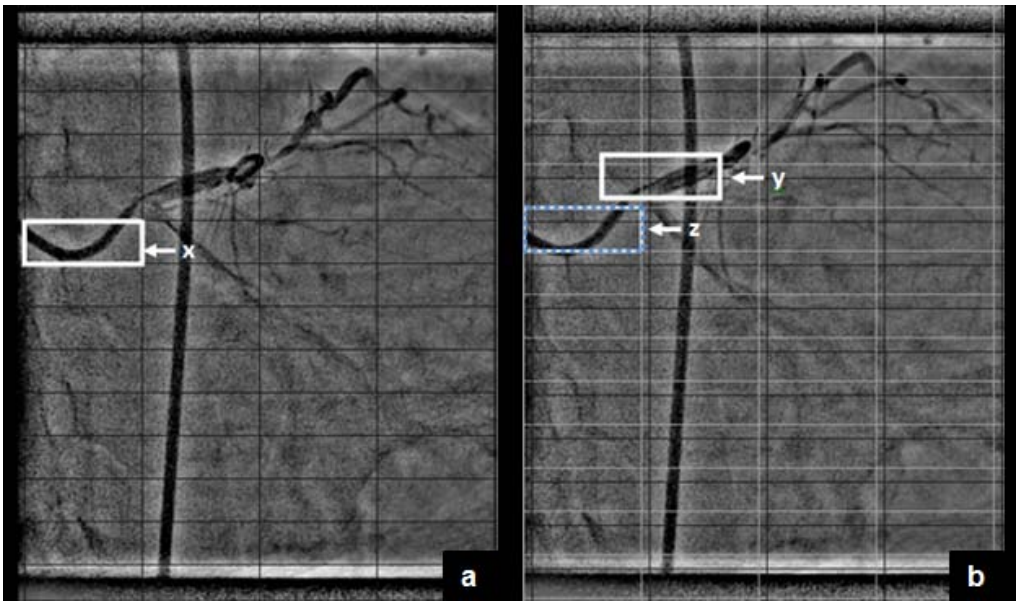

Figure 3.11: False template matching occurrence. (a) initial frame; *x* denotes the selected template; (b) Matching frame; *y* denotes the false template and *z* denotes the expected correct template.

False matching detection is done by comparing the shape similarity of the vessel structures existing in the reference and matched templates. In order to achieve that, the reference and matched templates obtained from the previous and current frames are extracted in to two separate images and a sequence of operations is implemented to isolate the vessel structures. Figure 3.12 depicts the application of different operations for the template images in (a) and (b), which are extracted from previous

and current frames. As the initial operation, the edge based segmentation was applied to both template images to mark the different visual segments in those images [78]. It is illustrated in Figure 3.12 (c) and (d). According to these visual illustrations, it is clear that all the segmented edges do not correspond to the blood vessel structures. In order to emphasize the blood vessel structures from the template images, image thresholding operation is applied (threshold is set empirically as 50). Due to thresholding, the blood vessel structures and some of the background structures have been extracted as the foreground objects. Figure 3.12 (e) and (f) depict the effect of image thresholding for the template images for further clarifications. Nonetheless, it has been experimentally observed that the largest objects emphasized in the thresholded template images were the vessel structures. Therefore, contour detection was applied for both thresholded template images separately and largest detected contour was extracted as the vessel structures in each template images as shown in Figure 3.12 (g) and (h). Those processed template images are now suitable for determining the shape similarity.

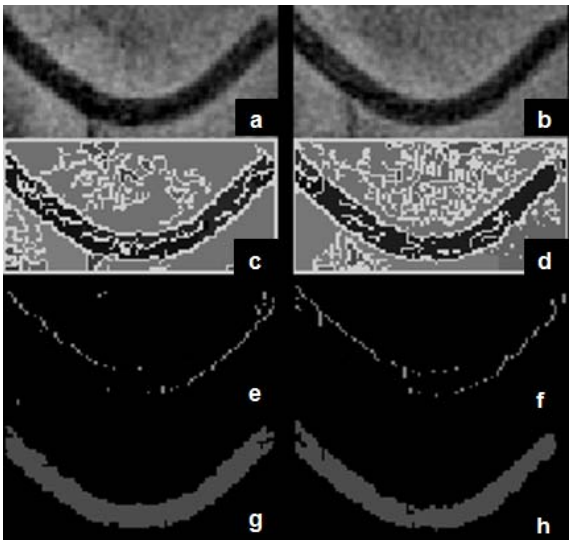

Figure 3.12: Steps of shape matching of template images. (a) and (b) reference and matched template images; (c) and (d) edge segmented images of template images in (a) and (b); (e) and (f) threshold results of edge segmented images in (c) and (d); (g) and (h) vessel segment isolated images of the threshold result images in (e) and (f).

The shape similarity between the blood vessel structures in the template images are determined based on the Histogram based Oriented Gradient (HOG) descriptor [96]. The HOG descriptor is a feature descriptor used for object detection in computer vision. It counts the occurrences of gradient orientation in localized portions of an image to generate the HOG descriptor ID. Moreover, the local object appearance and shape within an image can be described by the distribution of intensity gradients or edge directions. The HOG descriptor is also implemented based on the gradient orientation. Hence, the HOG descriptor has been selected as the ideal technique for determining the shape similarity of the vessels in template images.

The implementation of HOG descriptor can be achieved by dividing template image into small regions, called cells, and for each cell compiling a histogram of edge orientations for the pixels within the cell. Hence, in this study, it has been selected 4×4 cells and 8×8 blocks to calculate the histograms of gradient orientation and there are four cells in one block. Figure 3.13 depicts a sample implemented HOG descriptor for a scaled template image (64×8 size). It consists of 16 ×2 total blocks. Further, it represents the computed histogram of gradient orientation in each block. Moreover, each of these histograms has 9 bins to represent orientation of voted pixels from 0^0- 180^0. The length of the bin in each histogram indicates the dominant direction of gradient magnitude. Eventually, the combination of these histograms forms the ID for the HOG descriptor.

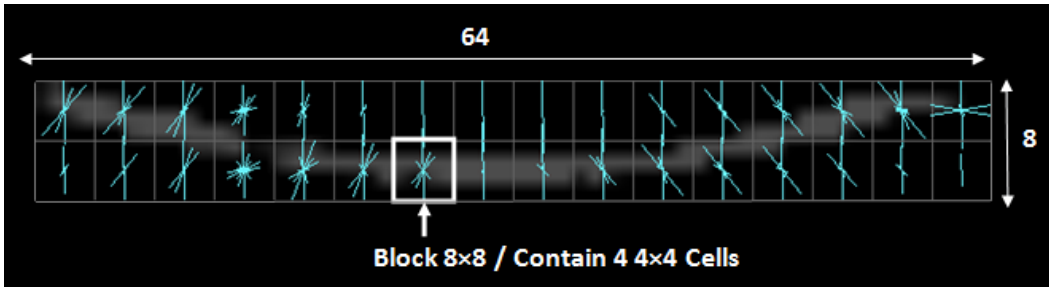

Figure 3.13: Implementation of HOG descriptor.

After calculating the HOG descriptor for both template images, the Euclidean distance between those HOG descriptors (HOG distance – DHOG) has been calculated to formalize a mechanism to determine whether the current template match is false match or not. Therefore, following algorithm was implemented to detect the false matching occurrences.

```
False Matching Detection (d_mean, d_std, d_temp )
begin
     if (d_temp == 0) ||
          [((d_mean- d_std ) <=d_temp) && (d_temp <= (d_mean+ d_std ))] then
         Correct match
     else
         if d_temp > (d_mean + d_std) then
             if  (d_temp / (d_mean + d_std)) > distanceFactor then
                 Detect as FP matching
                 Apply correction process
             else
                compute D_HOG
                if (D_HOG >= D_HOGThreshold) then
                      Detect as FP match
                     Apply correction process
                else
                      Correct match
                end if
             end if
         else
             if ((d_mean - d_std)/ d_temp) > distanceFactor  then
                 Detect as FP matching
                 Apply correction process
             else
                Compute D_HOG
                if (D_HOG >= D_HOGThreshold) then
                      Detect as FP match
                     Apply correction process
                else
                      Correct match
                end if
             end if
         end if
    end if
end
```

NOTE: FP stands for False Matching

d_{temp} is the displacement between the templates and d_{mean} and d_{std} are mean template displacement and standard deviation of template displacement of the CCA being processed. Distance factor (*distanceFactor*) is a constant and it has been emphirically

set as 2 for this study. It means, if any template distance (d_{temp}) greater than 2 times upper distance boundary ($d_{mean} + d_{std}$) or if any template distance (d_{temp}) less than 2 times lower distance boundary ($d_{mean} - d_{std}$) is considered as false match. Apart from that, the computed HOG distance value is compared with a threshold HOG distance value ($D_{HOGThreshold}$), which is 45 and it is determined during one of the preliminary experiments of this study. Figure 3.14 depicts the detected true (image (a) and (b)) and false (image (e) and (f)) template matching occurrences of a CCA with their respective HOG descriptor visualizations to further clarify the technique.

A template re-correction method is also implemented to re-correct any false matching occurrences. It is done using the matched point obtained in the previous template matching iteration. e.g. If the false matching detection occurs in n^{th} iteration of the content alignment, it will use the matched coordinates obtained in the $(n\text{-}1)^{th}$ iteration to re-correct it. In this re-correction method, re-corrected template matching point is marked explicitly from $P_{x,y}$ position in the current frame where $P_{x,y}$ equals to the $C_{x,y}$ point of previous iterations' template matching step.

It was revealed that this re-correction method provides a near equal matched area for the reference template. The reason for that is, deformations occur among the vessel structures due to the radial motion among the arteries. Therefore, it is necessary to smoothen the re-corrected point to find the best match point. Euclidean distance between the reference template and the matched template region in the current frame is taken as the metric to find the best matched point.

In order to smoothen the re-corrected point, the Euclidean distance is calculated between the template at $F_{x,y}$ point of the previous frame and the re-corrected template marked in $P_{x,y}$ point in current frame, and the result is denoted as ED_i. Subsequently, a block matching is applied within a K region around $P_{x,y}$ point in the current frame to detect a more closer matching region to the reference template at $F_{x,y}$. Moreover, K is set as (*template width* /*4*) because it is obvious that the re-corrected best match point should be placed proximal to the $P_{x,y}$. Euclidean distance values are calculated separately between the template at $F_{x,y}$ point and re-positioned template within the selected region K around $P_{x,y}$. At the end of this block matching, the point, which has

the minimum Euclidean distance is selected and is denoted as ED_m. Finally, the coordinate point, which provides ED_i is selected as re-corrected best matched location if $ED_i \leq ED_m$. Otherwise ED_m is selected as the re-corrected best matched point during this false matching correction step.

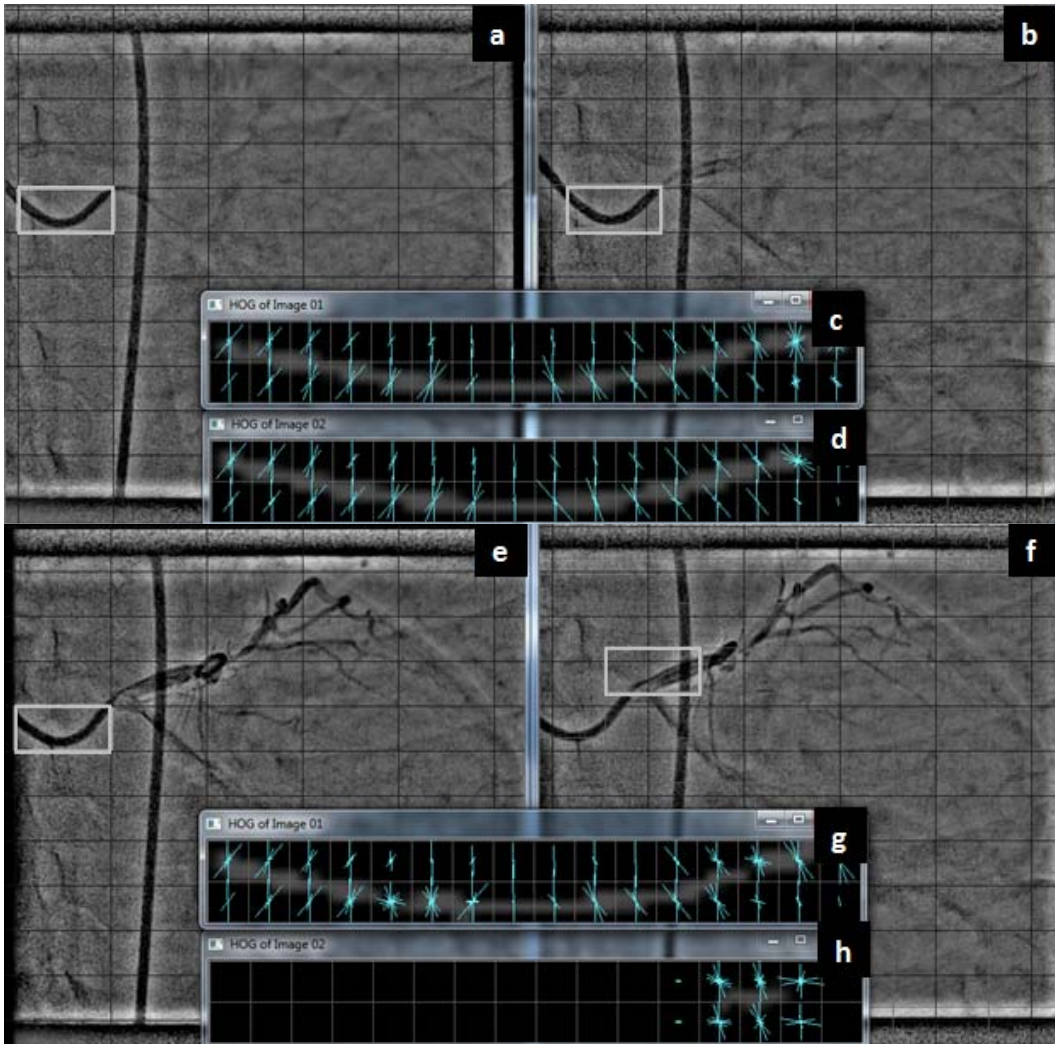

Figure 3.14: Detection of true and false matching occurrence based on HOG descriptor. (a) and (b) two consecutive frames with true matched templates; (e) and (f) two consecutive frames with false matched templates; (c) and (d) HOG descriptors of true match (DHOG =17.6416); (g) and (h) HOG descriptor of false templates (DHOG =49.4431).

3.5.4 Calculating the GMV

In order to construct the global motion stabilized frames, it is required to compute the motion vector $M_{x,y}$ of two consecutive frames using the equation (3.11);

$$M_{x,y} = \left(C_x - F_x, C_y - F_y\right) \tag{3.11}$$

Where C_x and C_y denote the *x, y* coordinates of the matched point obtained from $C_{x,y}$ point in the current frame, and F_x and F_y denote the *x, y* coordinates of the selected template point at $F_{x,y}$ point in the previous frame.

3.5.5 Frame re-construction.

In order to construct a motion stabilized frame, the current frame is translated to a calculated distance towards the direction determined by the motion vector. If (C_x–F_x) is negative, the current frame must be shifted to the right direction by M_x, distance; else it is shifted to -M_x distance left. Similarly, if (C_y–F_y) is negative, the current frame must be shifted downwards M_y distance; else it is shifted upwards –M_y distance. As a result of this translation, a global motion stabilized frame is constructed from the enhanced frame $f_3(x,y)$ and this resulting frame denoted as $f_4(x,y)$.

This global motion stabilized frame is used as the input for the template matching step of the next iteration of the proposed method for selecting the template from $F_{x,y}$ point with dimensions of ($w \times h$). After the first iteration, the aforementioned template selection step is done automatically using the newly constructed frame $f_4^s(x,y)$ where $s = 1,2,3,\ldots..,n$. This procedure is repeated until the last frame of the input CCA and a set of global motion eliminated angiogram images are produced as the output.

Figure 3.15 provides summarized views of pre-processing phase to clearly recognize its effect to the CCAs. The top row of Figure 3.15 depicts non-uniformly illuminated four consecutive frames ($f_0(x,y)$) of a CCA. Catheter engaged area shown in each frame is marked using a white square for better visualization of the motion artifact.

As mentioned in section 3.2.3, the cardiac motion (global motion) can be directly determine by arterial motion.

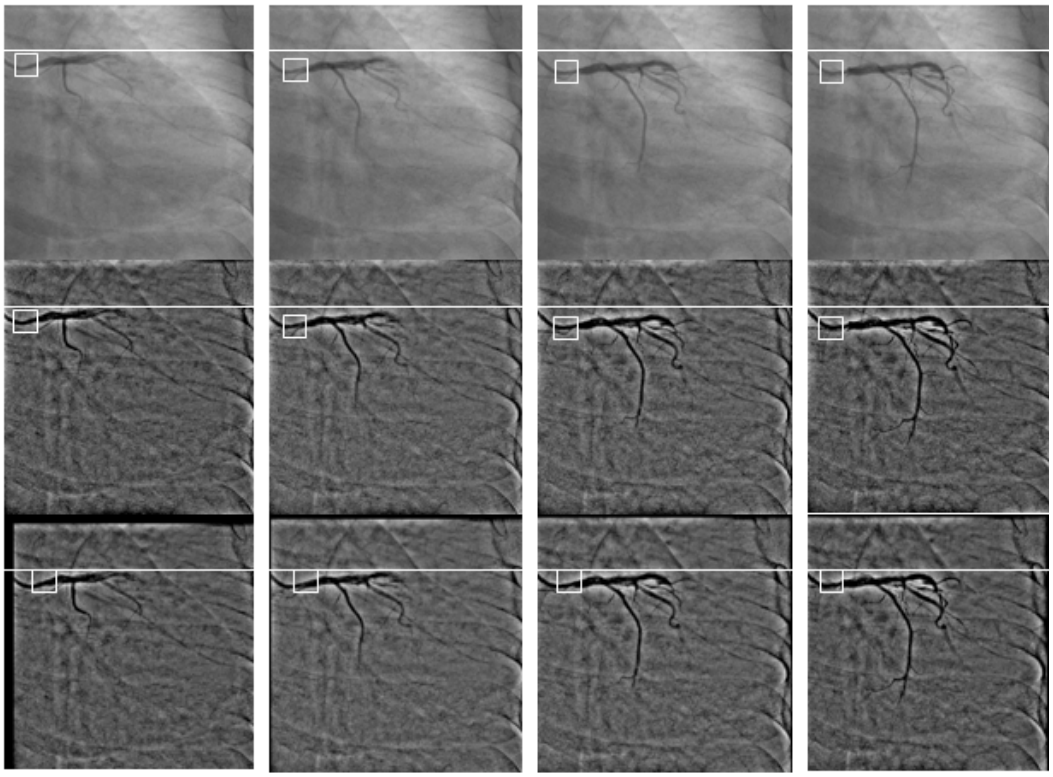

Figure 3.15: Summary view of pre-processing phase. (Top row represents four consecutive frames of direct CCA (f_1^s). Middle row represents enhanced frames (f_3^s) and bottom row represents content aligned framesf_4^s.)

It is revealed in the CCA views shown in Figure 3.15 clearly because the placement of this marked region is displaced in the four consecutive frames of the figure due to this global motion. The middle row represents the uniformly illuminated corresponding four frames ($f_3(x,y)$) obtained after the frame enhancement. Moreover, the frame contents in these frames are still not aligned with each other due to global motion. The frames depicted in the bottom row represent the corresponding contented aligned frames ($f_4(x,y)$) of the enhanced frames. Moreover, it is visualized that the placement of the marked region is positioned in the same location of the four consecutive frames due to global motion stabilization. These uniformly illuminated

content aligned frames are one of the outputs of this pre-processing phase. Consequently, these frames are input to the next phase of the proposed method, which is known as segmentation for further processing.

3.6 Mask Creation

It is apparent to extract the catheter region and the CA tree visualized in each CCA frame as the foreground during the segmentation phase. In order to achieve that, a mask image has been created to represent the accumulated foreground area of the CCA to be processed and it was the objective of this stage [97]. Mask image is the other output generated by pre-processing phase of this study and consists of two major steps namely; creating the accumulated foreground image and enhancement.

Initial step of mask creation is done after the frame reconstruction step of content alignment. Though the content alignment is an iterative procedure, the accumulated foreground image created by mask creation is also performed iteratively. The accumulated foreground image creation was done by executing three operations to the copies of two consecutive frames, which are processed within each repetitive step of the content alignment. As the first operation, the frame difference between the copies of two consecutive frames of the CCA to be processed is computed. This frame difference depicts the intersection area where the foreground objects (catheter and CA tree) are moving within the CCA frame. Figure 3.16 (c) depicts the frame difference image of the two consecutive frames visualized in (a) and (b) for further clarifications of the aforementioned operation. This frame difference operation generates some noise blobs in addition to the foreground intersection area. Those noise blobs highlighted by Figure 3.16 (c) should be minimized significantly to obtain the best mask image. As the second operation, thresholding is applied to the frame difference image to obtain clearly separated background and foreground regions of the frame difference image as depicted in Figure 3.16(d). Setting the threshold is done manually and it depends on the visual contents represented in the CCAs. The amount of noise blobs in the frame difference image is reduced mostly due to the application of thresholding operation.

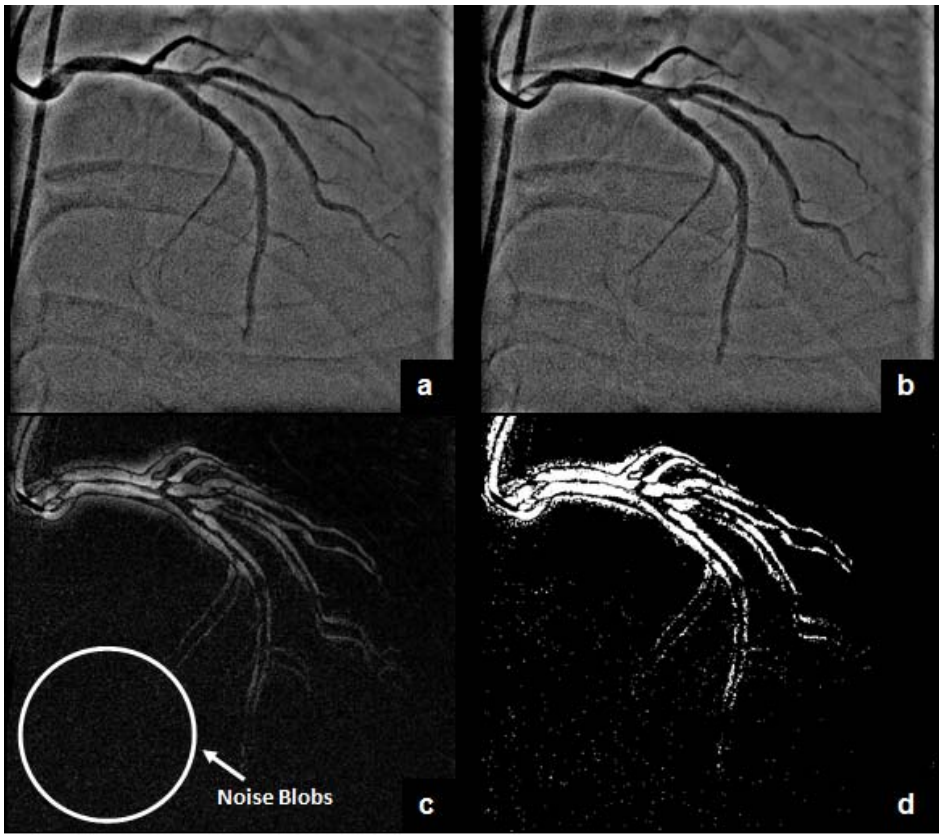

Figure 3.16: Frame difference in accumulated foreground image creation. (a) and (b) two consecutive CCA frames; (c) frame difference image; (d) thresholding result.

Afterwards, the contents of this threshold frame difference image are copied to another matrix to form the initial mask image. The content of this initial mask image is accumulated repeatedly with the content of thresholded frame difference image generated within the content alignment iterations of the proposed pre-processing phase. Figure 3.17 depicts the initial mask image of a sample CCA. According to that, white region represents the accumulated foreground displacement area and black region represents the background area of the CCA.

Enhancement step begins after creating the initial mask image. This will be performed after the content alignment (Figure 3.6). The objective of this enhancement step is to further improve the initial mask image by reducing noise blobs further and merge the concave areas within the foreground region. Therefore,

the tiny white blobs in binary mask image (area < 10) are eliminated through contour detection and removal. Consequently, the morphological dilation operation is applied to expand and merge the concave areas within the foreground region of the mask image. This created mask image is denoted as $f_m(x,y)$ and will be used in segmentation phase to extract the foreground of the frame through background subtraction.

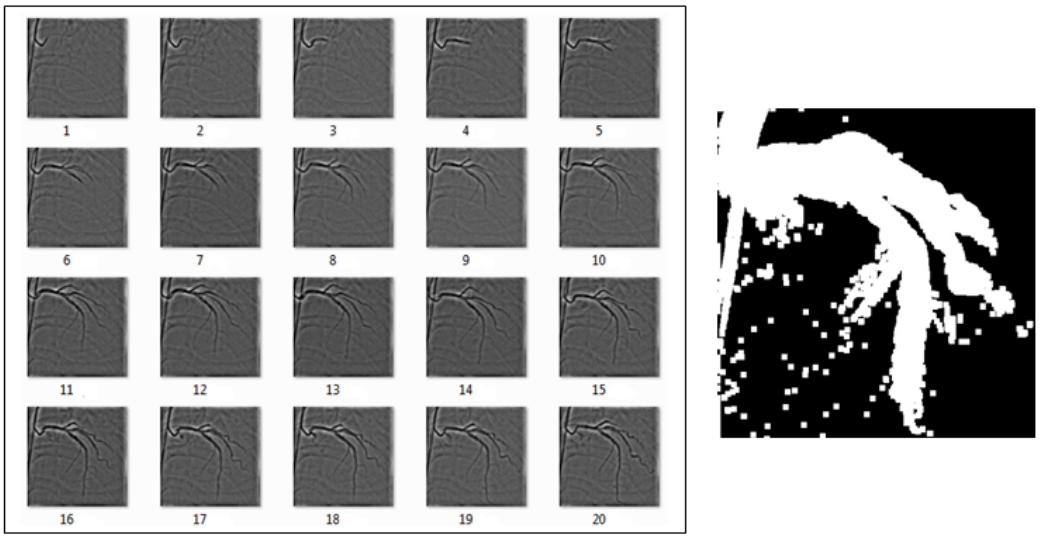

Figure 3.17: Mask image of a sample CCA. (left – CCA frames, right – mask image.)

3.7 Summary

This chapter presented the design and implementation steps of proposed quantitative coronary analysis method of this research study and elaborated the pre-processing phase comprehensively. Noise, non-uniform illumination and global motion are reported as the main factors, which degrade the visual quality of the CCAs and major consequences for making some obstructions in processing of CCAs. This study introduces a mechanism to remove non-uniform illumination through homomorphic filtering. Moreover, it introduces a novel approach to obtain visual alignment of the arterial flow visualized in the CCA frames by removing the global motion artifact. The proposed method was implemented based on an improved template matching

technique that can be adapted to match the deformed vessel structures in CCAs. Further, the steps of creating mask image, which is required for foreground extraction in segmentation phase has been explained. The uniformly illuminated content aligned CCAs produced from this phase can input to consequent vessel segmentation phase.

CHAPTER 4
SEGMENTATION

For quantitative coronary analysis, it is significant indeed to extract the CA tree from the CCA frame, which is being processed. This phase of study is known as segmentation and a scientific approach has been suggested to extract the CA vasculature from the CCA frames. Uniformly illuminated content aligned CCA frames ($f_4(x,y)$) and mask image with respect to the CCA to be processed ($f_m(x,y)$) are inputs to the proposed segmentation method of this study to extract the CA tree. The proposed method for vessel segmentation has been discussed comprehensively in the initial section of this chapter. Thereafter, the implementation steps of the proposed segmentation phase have been elaborated in detail within the next three sections namely; foreground enhancement, structure filling and foreground extraction.

4.1 Proposed method for vessel segmentation

The proposed vessel segmentation method is mainly based on a spatial filtering and region growing approach. It follows Frangi's filter for vessel enhancement, which was widely accepted for vessel enhancement in recent past research studies [63][98]. The main objective of this phase is to extract the foreground area from the CCA frames. As mentioned in section 3.6, CAs and parts of the catheter recorded in each frame of CCA are considered as foreground objects. Moreover, this segmentation method does not depend on any kind of prior knowledge about vessel regions of CCAs.

Uniformly illuminated content aligned CCA frames ($f_4(x,y)$) and mask image of the CCA to be processed ($f_m(x,y)$) are input to the segmentation phase and the output frames almost clearly extract the complete vascular tree in the CCA frame to be processed. The main implementation stages of the proposed segmentation phase are depicted in Figure 4.1 and already published in [98]. According to the figure, it mainly consists of three main implementation stages namely; foreground enhancement, structure filling and foreground extraction. Following sections elaborate the steps of the implementation stages of the segmentation phase in detail.

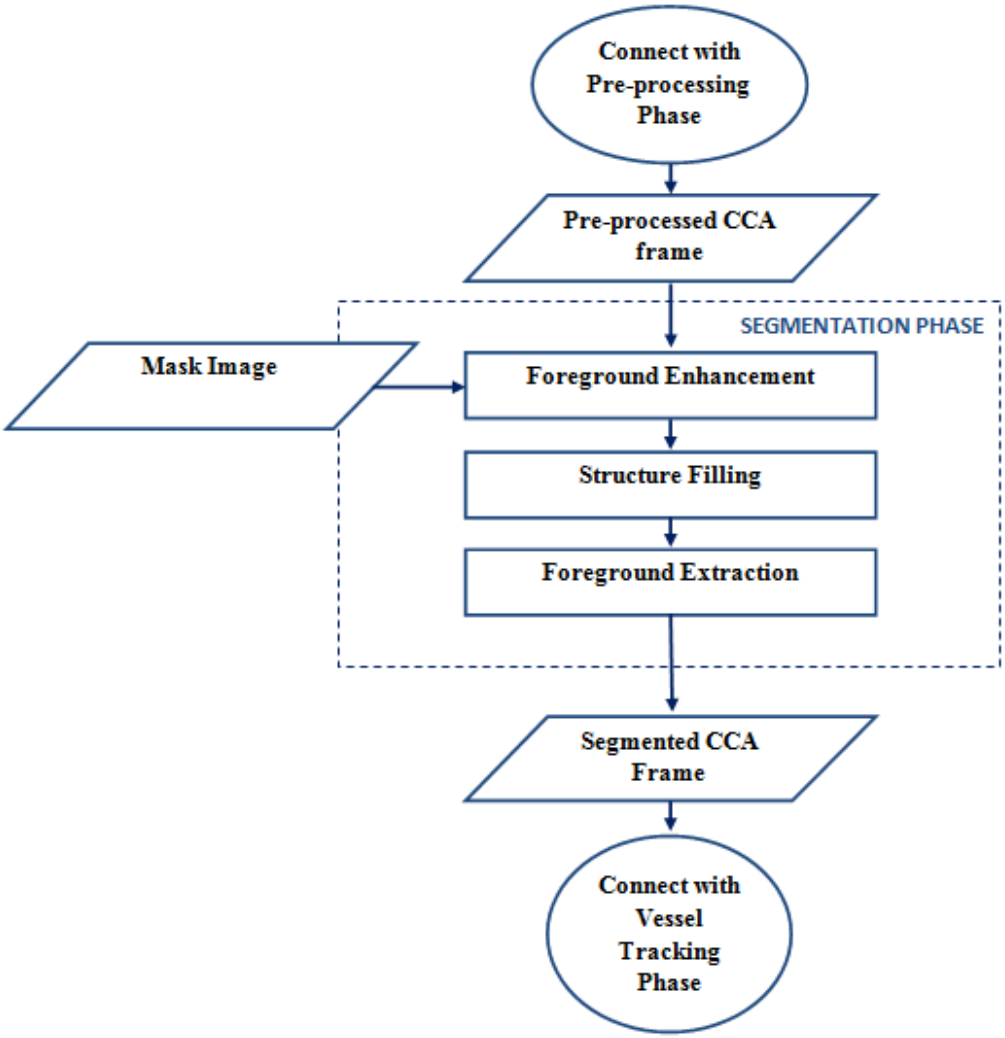

Figure 4.1: Implementation stages of segmentation phase.

4.2 Foreground enhancement

The main objective of the foreground enhancement is to further emphasize the vessel structures by smoothening the CCA frame to be processed. It consists of three implementation steps namely; background subtraction, obtaining the directional second order partial derivative images and application of Frangi's filter. Following sections explains those implementation steps in detail.

4.2.1 Background subtraction

The objective of background subtraction is to reduce the effect of superimposition of vessels with other anatomical structures like ribs, spine or heart chambers. In order to achieve this, mask ($f_m(x,y)$) created in pre-processing phase is subtracted from the current CCA frame ($f_4(x,y)$) to be processed. The resulting image obtained from background subtraction is denoted as $f_5(x,y)$. It preserves only the accumulated foreground area in each CCA frame where the vessel can be displaced throughout the frame sequence of the CCA to be processed and remove the background structures visualized in the CCA frames considerably. Further, this background subtraction step reduces the quantum noise distributed in the background regions of the frame greatly. Figure 4.2 depicts the visual illustrations of background subtraction. Figure 4.2 (a), (d), (g) represents three pre-processed frames ($f_4(x,y)$) of LAD, CX and RCA CAs and (b), (e), (h) images represents the respective mask images ($f_m(x,y)$). Moreover, Figure 4.2 (c), (f), (i) images represents the extracted foreground ($f_5(x,y)$) of respective frames in (a), (d) and (g) images.

4.2.2 Obtaining the directional second order partial derivative images

It is mandatory to obtain the directional second order partial derivative images of CCA frame ($f_5(x,y)$) to apply the Frangi's filter. These derivative images can be calculated by applying convolution of a second order partial derivatives of a Gaussian filter $G(u,v)$ at a scale σ. Equations (4.1), (4.2), (4.3) and (4.4) elaborate the formation of these derivative images denoted as $I_{u,u}$, $I_{u,v}$, $I_{v,u}$ and $I_{v,v}$.

$$I_{u,u} = f_4(x,y) * F1 \tag{4.1}$$

$$I_{u,v} = f_4(x,y) * F2 \tag{4.2}$$

$$I_{v,u} = f_4(x,y) * F2 \tag{4.3}$$

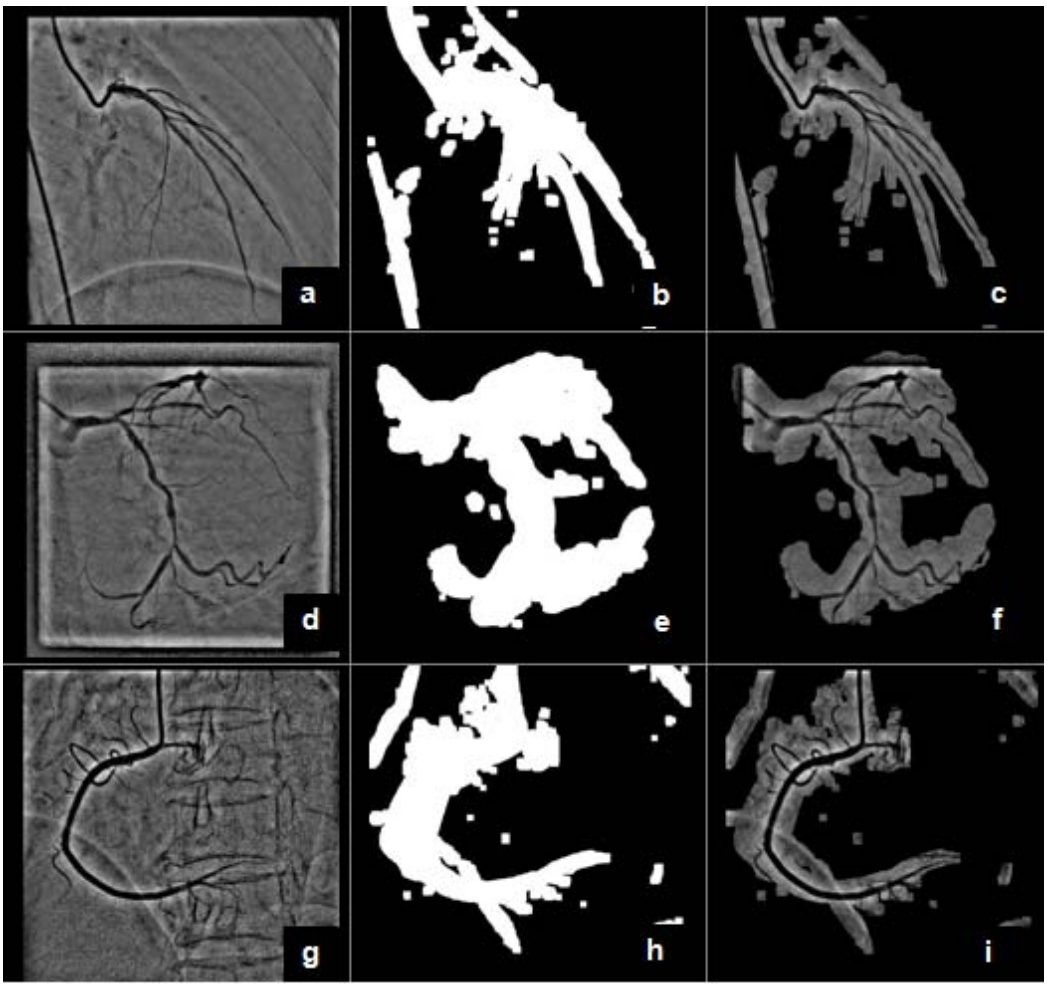

Figure 4.2: Background subtraction. (a), (d), (g) pre-processed frames ($f_4(x,y)$) of LAD, CX and RCA; (b), (e), (h) respective mask images ($f_m(x,y)$); (c), (f), (i) extracted foreground ($f_5(x,y)$).

$$I_{v,v} = f_4(x, y) * F3 \tag{4.4}$$

Where *F1*, *F2* and *F3* are the second order partial derivative of Gaussian filter obtained through (4.5), (4.6) and (4.7) respectively;

$$F1 = \frac{\partial^2 G}{\partial u \partial u} \tag{4.5}$$

$$F2 = \frac{\partial^2 G}{\partial u \partial v} \tag{4.6}$$

$$F3 = \frac{\partial^2 G}{\partial v \partial v} \tag{4.7}$$

Where *G* denotes the Gaussian function of scalar σ as shown in the equation (4.8);

$$G(u, v) = \frac{1}{\sqrt{2\pi\sigma^2}} e^{\frac{-u^2+v^2}{2\sigma^2}} \tag{4.8}$$

The empirical studies revealed that it provides best gradient approximations of the CCA frame when σ is set as 1.25. Figure 4.3 depicts the second order derivatives of a Gaussian kernel at scale 5, which generates for (4.5), (4.6) and (4.7). According to the figure, it conceives the second derivative of a Gaussian kernel as probe kernel that measures the contrast between the regions inside and outside the range (-5, 5) in the direction of the derivative [63]. Moreover, the implementation of the Gaussian convolution further smoothens the foreground area of the CCA frame.

4.2.3 Application of Frangi's filter.

Frangi's filter was applied in foreground enhancement stage because it has proven capability to extract the tubular structures recorded in angiograms [54] [64] [67] [68]. Blood vessels visualized in angiograms can be considered as tubular structures. Thus, the Frangi's filter is the ideal filter to emphasize the vessel regions in CCA frames.

Frangi's method describes three-dimensional curved surface as two dimensional coordinates of pixels and their corresponding gray-values. Hence, the two-dimensional coordinates of pixels in image can be denoted as (*x, y*) and *I* denoted the corresponding gray-value in (*x, y*) coordinates of the image [64]. Moreover, the curvature of the curved surface in the CCA frame can be defined with Hessian matrix (*H*) as shown in the equation (4.9);

$$H = \begin{bmatrix} I_{uu}(x, y) & I_{uv}(x, y) \\ I_{vu}(x, y) & I_{vv}(x, y) \end{bmatrix} \tag{4.9}$$

Where, $I_{uu}(x,y)$, $I_{uv}(x,y) = I_{vu}(x,y)$ and $I_{vv}(x,y)$ are the directional second order partial derivatives of CCA frame $f_5(x,y)$ produced in equations (4.1), (4.2), (4.3) and (4.4).

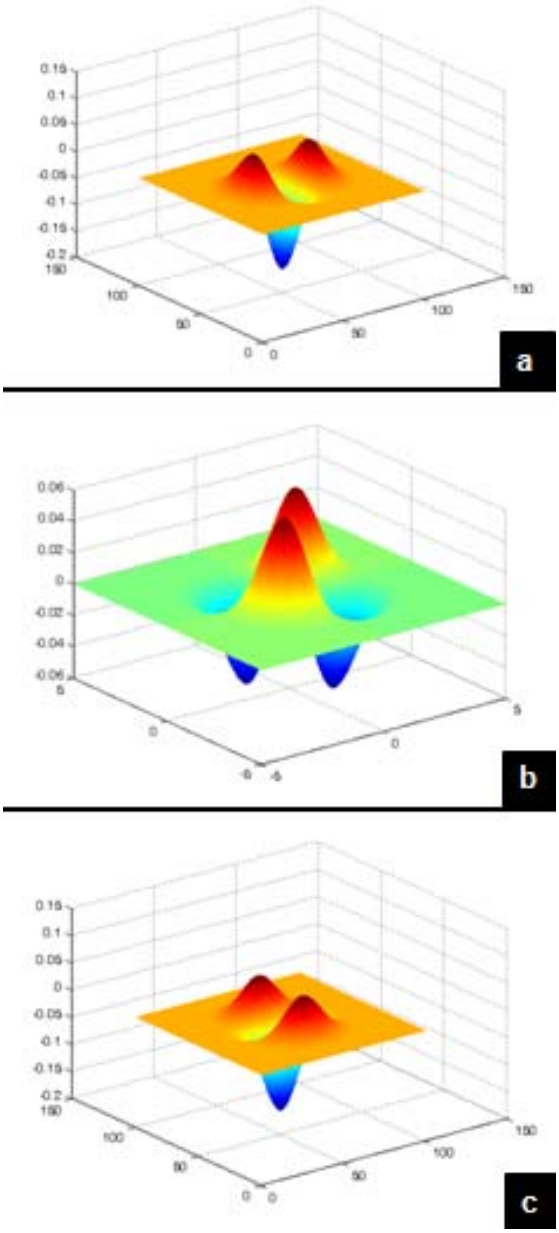

Figure 4.3: Second order derivatives of a Gaussian kernel. (a) F1; (b) F2; (c) F3.

Two eigenvalues denoted as λ_1 and λ_2 and corresponding eigenvectors produced by the simplification of Hessian matrix given in equation (4.9) can be used to define the vesselness feature of the CCA frames. Moreover, this vesselness feature will be

determined based on the norm proposed by Frangi et al. which is based on the eigenvector of Hessian matrix. The proposed norm is emphasized in Table 2.4 for further clarifications [63]. Hence, to make the final conclusion regarding the vesselness feature of the processed CCA frame, it is mandatory to obtain the eigenvalues for each point in 2D CCA frame to be processed by computing the corresponding Hessian matrix. From an analysis of the eigenvalues and eigenvectors of the Hessian matrix, it is noticeable that the strongest eigenvalue of the Hessian matrix and its corresponding eigenvector in a point (x,y) gives the strongest curvature of 2D-surface and its direction. In this situation the computed eigenvalues are ordered as $|\lambda_1| \geq |\lambda_2|$. The eigenvector corresponding to the weaker eigenvalue represents the surface direction perpendicular to the strongest curvature and the computed eigenvalues satisfy the condition $\lambda_1 > 0$ *and* $\lambda_2 \approx 0$ [54]. Based on all aforementioned facts in this section the vessel resemblance function is stated as shown in equation (4.10) to enhance the foreground of the CCA frame to be processed;

$$f_6(x,y) = \begin{cases} 255 & if(\lambda_1 > 1) \\ 0 & otherwise \end{cases} \tag{21}$$

Where $f_6(x,y)$ is the foreground enhanced image provided as the result of this step.

Figure 4.4 depicts the visual illustrations of the results obtained after application of Frangi's filter. Brighter regions in that figure emphasize the enhanced foreground of LAD, CX and RCA CAs respectively.

4.3 Structure filling

The resulting frames obtained after the foreground enhancement step consist of some discontinuities of vasculature. Images in Figure 4.5(a), 4.6(a) and 4.7(a) depict this issue clearly. These images conceive the enhanced foreground of LAD, CX and RCA CAs respectively and disconnected regions in those CAs are circled to clearly recognize the problem. The reason for this is the uneven distribution of contrast agent in angiography. As a result of that, in most angiogram cases, the CAs are not visualized by uniform intensity. Therefore, the brighter regions in detected blood vessels are deemphasized and darker regions are preserves by providing results with

disconnections in the detected vessel tree. This causes under segmentation during the foreground extraction step and it is a great obstruction that needs to be surmounted prior to the foreground extraction. Therefore, the main objective of this structure filling step is to improve the spatial coherence of foreground by achieving the connectivity between the disconnected blood vessel areas in foreground enhanced frames denoted as $f_6(x,y)$.

Figure 4.4: Results of Frangi filter. (a) LAD; (b) CX; (c) RCA CAs.

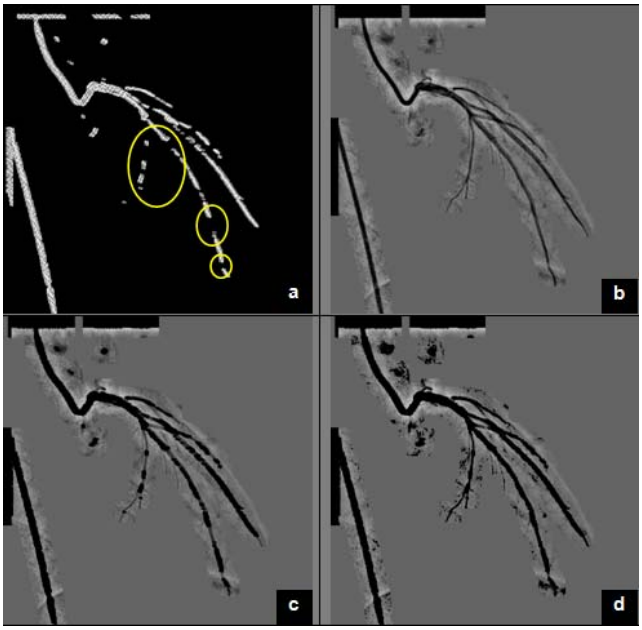

Figure 4.5: Structure filling of LAD. (a) disconnected regions in $f_6(x,y)$; (b) foreground mask denoted as $f_7(x,y)$; (c) overlapping $f_6(x,y)$ on $f_7(x,y)$; (d) structured filled image.

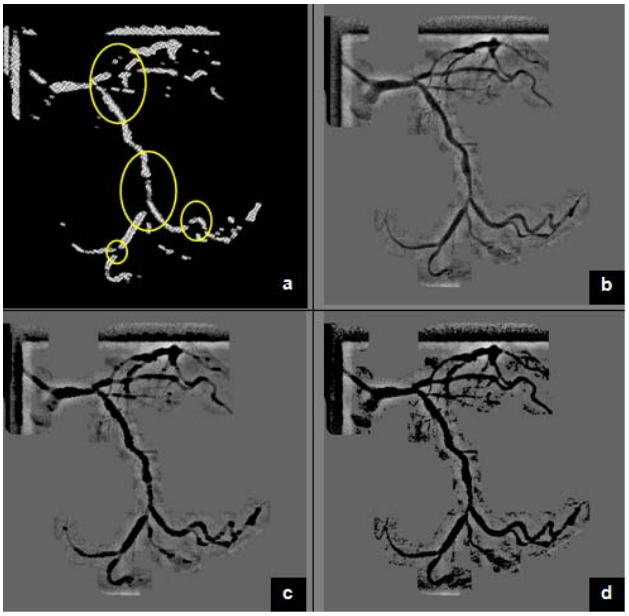

Figure 4.6: Structure filling of CX. (a) disconnected regions in $f_6(x,y)$; (b) foreground mask denoted as $f_7(x,y)$; (c) overlapping $f_6(x,y)$ on $f_7(x,y)$; (d) structured filled image.

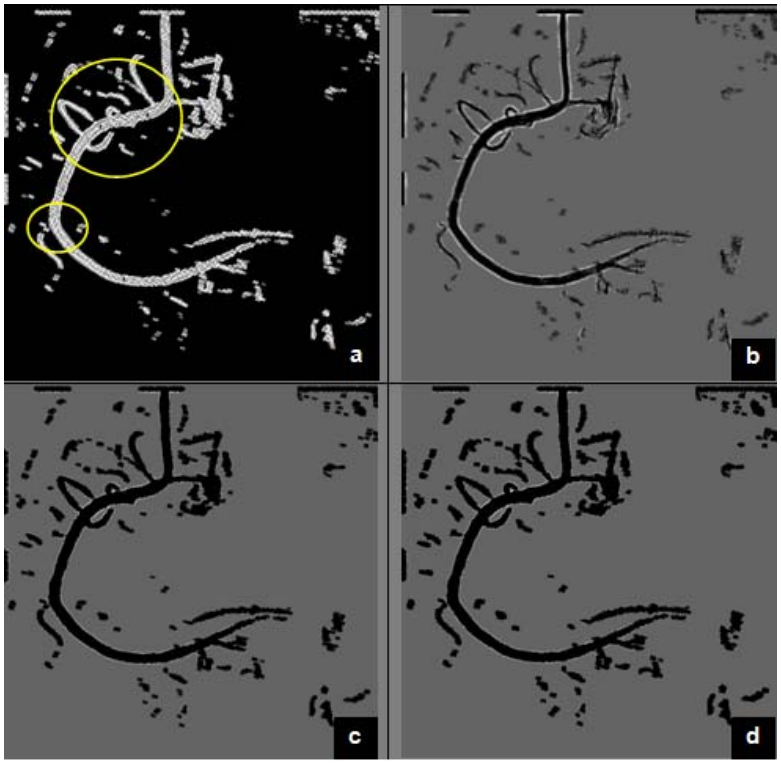

Figure 4.7: Structure filling of RCA. (a) disconnected regions in $f_6(x,y)$; (b) foreground mask denoted as $f_7(x,y)$; (c) overlapping $f_6(x,y)$ on $f_7(x,y)$; (d) structured filled image.

A sequence of operations have been employed to obtain the spatial coherence of the detected foreground depicted in $f_6(x,y)$. As the initial step, a foreground mask image denoted as $f_7(x,y)$ has been created using the foreground enhanced frame ($f_6(x,y)$). In order to achieve that, a copy of foreground enhanced frame ($f_6(x,y)$) is dilated manually by repeating the dilation over and over again until all the disconnected blobs are connected and it is denoted as $f_d(x,y)$. After that, a foreground mask image ($f_7(x,y)$) has been created by using the dilated foreground enhanced frame ($f_d(x,y)$) and the corresponding pre-processed frame denoted as $f_4(x,y)$ using the matching function shown in equation (4.11).

$$f_7(x,y) = \begin{cases} T_{f_4(x,y)} & if\,(T_{f_d(x,y)} = 255) \\ 100 & otherwise \end{cases} \tag{4.11}$$

Where, T denotes the intensity of the coordinates in x, y of the respective image.

Images in Figure 4.5(b), 4.6(b) and 4.7(b) depict the three foreground mask images created for LAD, CX and RCA CAs respectively. Foreground enhanced frame ($f_6(x,y)$) is then overlapped onto the foreground mask ($f_7(x,y)$) using the equation (4.12) to recognize the branches, which need to be connected.

$$f_7(x,y) = \begin{cases} 0 & if(T_{f_6(x,y)} = 255) \\ f_7(x,y) & otherwise \end{cases} \tag{4.12}$$

Where, T denotes the intensity of the coordinates in x, y of the respective image.

Images in Figure 4.5(c), 4.6(c) and 4.7(c) depict the three overlapped images created for LAD, CX and RCA CAs respectively. Moreover, in these overlapped images, the disconnected regions visualized in the foreground enhanced frame ($f_6(x,y)$) are now linked with the intensities of the $f_4(x,y)$ frame.

Finally, to achieve the desired connectivity over the entire foreground and represent it in a uniform manner, all the coordinates in the overlapped frame ($f_7(x,y)$) is updated using the equation (4.13).

$$f_7(x,y) = \begin{cases} 0 & if(0 \leq T_{f_7(x,y)} \leq 90) \\ 100 & otherwise \end{cases} \tag{4.13}$$

Where, T denotes the intensity of the coordinates in x, y of the respective image.

The intensity ranging from 0 to 90 is responsible for visualizing the full CA vasculature extracted to the foreground mask image and is determined based on the dynamic range of the intensity histograms of foreground mask images created in this stage. This structure filled frame denoted as $f_7(x,y)$ is returned as the output of this stage and the images in Figure 4.5(d), 4.6(d) and 4.7(d) depict the three visual illustrations created for LAD, CX and RCA CAs respectively. Finally, it is possible to achieve the connectivity and desired uniform intensity over the whole CA vasculature depicted in the CCA frame to be processed. These resulting frames are used for subsequent foreground extraction, which will be discussed in the next section.

4.4 Foreground extraction

The objective of foreground extraction is to specifically mark the CA vasculature with catheter engagement region as desired foreground and extract them as the segmentation results. A structure filled image ($f_7(x,y)$) produced in the previous stage is used as the input to mark the aforementioned foreground region. In order to achieve that, a region growing technique known as "flood fill" is used. The seed point for the flood fill operation is selected interactively from the catheter engaged point of the structure filled image ($f_7(x,y)$). Finally, it is mandatory to extract the flood filled foreground region as the result of the segmentation phase. The result frame is denoted as $f_8(x,y)$ and is generated using the equation (4.14).

$$f_8(x,y) = \begin{cases} 0 & if\,(T_{f_7(x,y)} = 50) \\ 255 & otherwise \end{cases} \tag{4.14}$$

Where, T denotes the intensity of the coordinates in x, y of the respective image and 50 is taken as the filled intensity used in the flood fill operation because it does not make any interference with both foreground and background pixels in image $f_7(x,y)$ because this input image ($f_7(x,y)$) is a binary image. As a result of the flood fill operation, $f_8(x,y)$ image has formed and the foreground region of this result image has intensity 50 and background region has intensity 255. Figure 4.8 (b), (d) and (f) depict the segmentation results of LAD, CX and RCA CAs with respect to the direct CCA frames depicted in (a), (c) and (e) in the same figure.

4.5 Summary

This chapter has elaborated the proposed method for segmentation of the CCAs to be processed. The catheter engaged point and the complete CA vasculature depicted in each CCA are extracted into a separate image as a result of this proposed method. Initially the chapter discussed about the proposed segmentation method for foreground extraction followed in this study. It consists of three main implementation stages namely foreground enhancement, structure filling and foreground extraction. Latter sections of the chapter have discussed these implementation stages comprehensively with visual illustrations for further clarifications. The results provided in this segmentation phase are directly applied for

the next phase of the study, which is known as vessel tracking and luminal information extraction and it will be discussed in the next chapter.

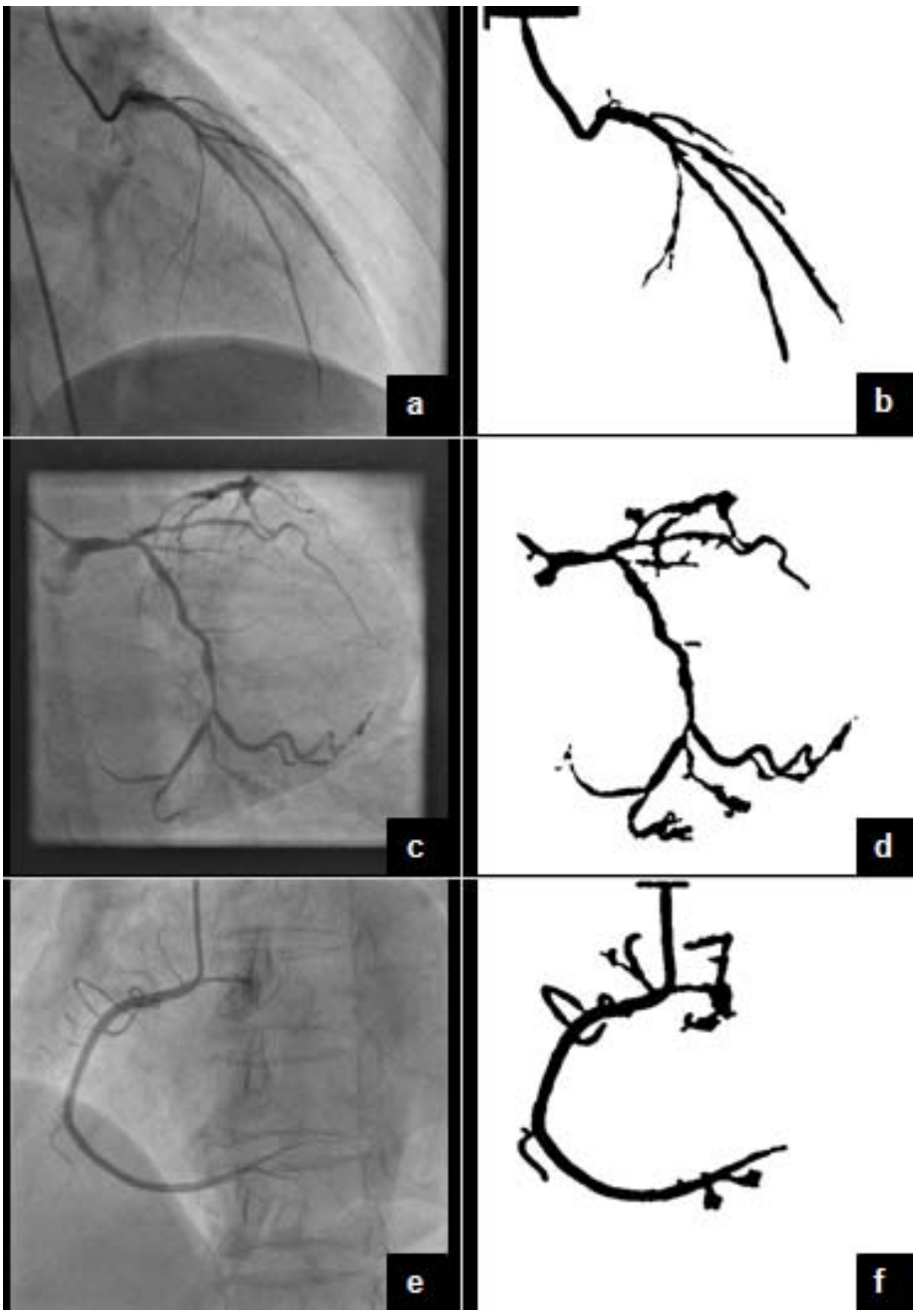

Figure 4.8: Foreground extraction. (a), (c), (e) direct CCA frames of LAD, CX and RCA; (b), (d), (f) respective segmentation results.

CHAPTER 5
VESSEL TRACKING AND FEATURE EXTRACTION

Subjective stenosis analysis and lack of quantification methods for determining the severity of stenosis are considered as major drawbacks in angiography image modality. Thus, it is crucial to suggest an accurate quantification method to improve this medical image modality for objective clinical assessments. Therefore, the main aim of this chapter is to elaborate the design and implementation stages of the proposed vessel tracking and quantitative analysis phases of this research study. In here, the segmentation image denoted as $f_8(x,y)$ is further processed to obtain the CA luminal information such as blood vessel boundary, skeleton and diameter along the vessel skeleton. The proposed vessel path tracking method has been explained clearly in the first section of this chapter. Consequently, the methods proposed for quantitative analysis and representation of the results have been elaborated with visual illustrations.

5.1 Vessel path tracking

The objective of vessel path tracking phase is to store the consecutive pixel points of the skeleton of a pre defined CA segment in to a specific data structure. These stored pixel points will be utilized in subsequent quantitative analysis phase. Segmented frames ($f_8(x,y)$) produced in the segmentation phase are input to the vessel path tracking phase and it consists of two main implementation stages namely; vessel isolation and skeleton path tracking. Selecting a vessel segment from the segmented vessel network and obtaining the skeleton and boundary of that extracted segment will be done in vessel isolation stage. Moreover, storing the consecutive pixel points of the skeleton of the isolated vessel segment in to a specific data structure will be done in skeleton path tracking stage.

Figure 5.1 depicts three CCA frames, which are used to provide visual illustrations of the various implementation steps discussed in this chapter. Hence, Figure 5.1 (a), (c) and (e) depict LAD, CX and RCA CAs extracted from three direct CCA cases respectively. Moreover, Figure 5.1 (b), (d) and (f) depict segmentation results of

those selected frames respectively. Three important parts visualized in CCA frames have been labeled in each image of Figure 5.1 and those are; catheter segment, catheter engagement point and vessel network. Identification of those parts in CCA frame is important to clearly understand the implementation steps described in this chapter. Following subsections elaborate the implementation steps of vessel isolation and skeleton path tracking stages in detail.

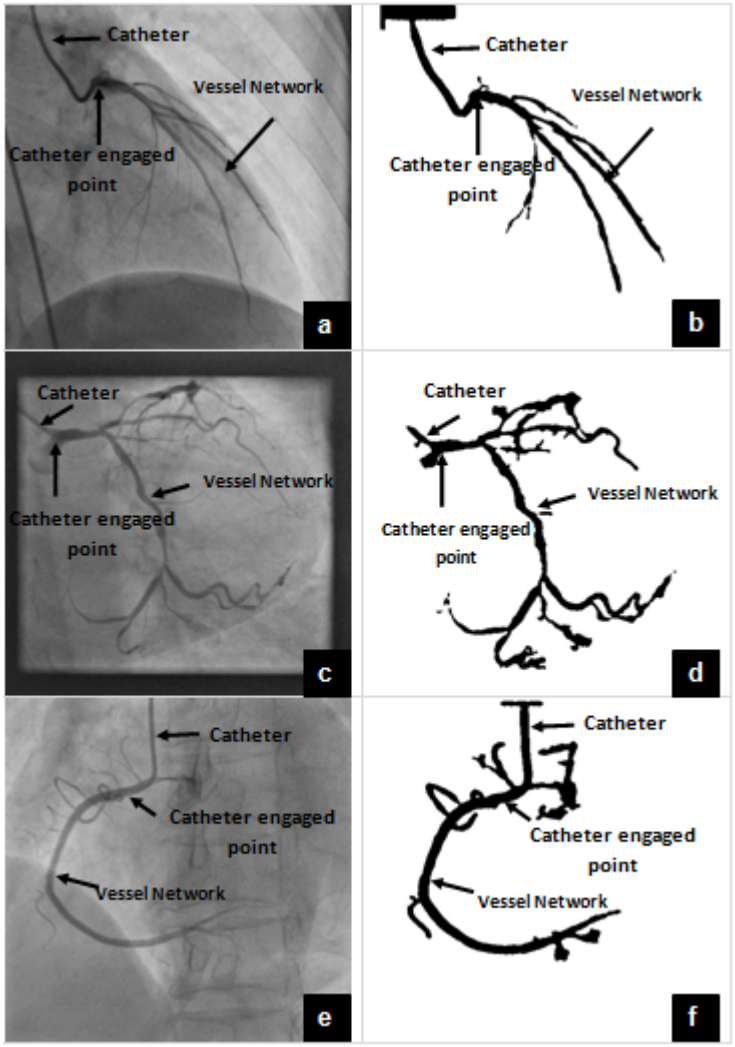

Figure 5.1: Selected frames. (a), (c), (e) direct CCA frames representing LAD, CX and RCA; (b), (d), (f) respective segmentation result ($f_8(x,y)$) of (a), (c) and (e) images.

5.1.1 Vessel isolation

The objective of vessel isolation is to separate a clinically important vessel segment from the segmented vasculature. In order to achieve that, it is required to select a clinically important vessel segment from the input CCA frame ($f_8(x,y)$). In this study, main arterial segments of LAD, CX and RCA are considered as the clinically import vessel segments.

The proposed vessel selection step has to be done as an interactive activity. Within this method, vessel cut lines are marked across the capillaries and unwanted branches to make them disconnected from the desired main artery. As a result of this vessel cut operation the whole vessel network is broken down into multiple blobs explicitly. Moreover, it has been experimentally observed that the main artery segment that remains in the frame is the largest segment out of all available blobs in the frame. Hence, contour detection is applied to the CCA frame and the largest detected contour is extracted to save it as a separate image. This resulting frame is denoted as $f_9(x,y)$ and it contains the isolated main vessel segment. Moreover, subsequent quantitative analysis will also be applied only for this isolated main vessel segment in $f_9(x,y)$ image.

Figure 5.2 depicts the visual illustrations of the vessel isolation stage. Images (a), (c) and (e) of Figure 5.2 represent the segmentation results of three selected CCA frames. The red color lines in these images indicate the interactively marked vessel cut lines. It has been clearly depicted that the branch vessels visualized in these CCA frames have been disconnected from the root artery segment due to the existence of vessel cut lines. As a consequence of that, the roots CAs in these three cases have been preserved successfully and those are depicted in Figure 5.2 (b), (d) and (f). Moreover, it is important to note that this isolated segment contains the three important parts mentioned in section 5.1 namely; the catheter segment, catheter engage point and isolated root CA segment.

Afterwards, image thinning and canny edge detection operations are applied separately to the $f_9(x,y)$ image to obtain the skeleton and boundary of the isolated segment respectively [80]. Zhang and Suen's fast parallel thinning algorithm has

been applied to obtain the skeleton because, it provides a connected skeleton with single pixel width [83]. Having a single pixel width skeleton is an important aspect for subsequent skeleton path tracking because it efficiently tracks the tiny skeleton rather than tracking a larger one. Selecting a canny edge detector for boundary detection is significant because it provides a low error rate in edge detection (high noise suppression), contains excellent edge localization and provides single detection response per edge [99].

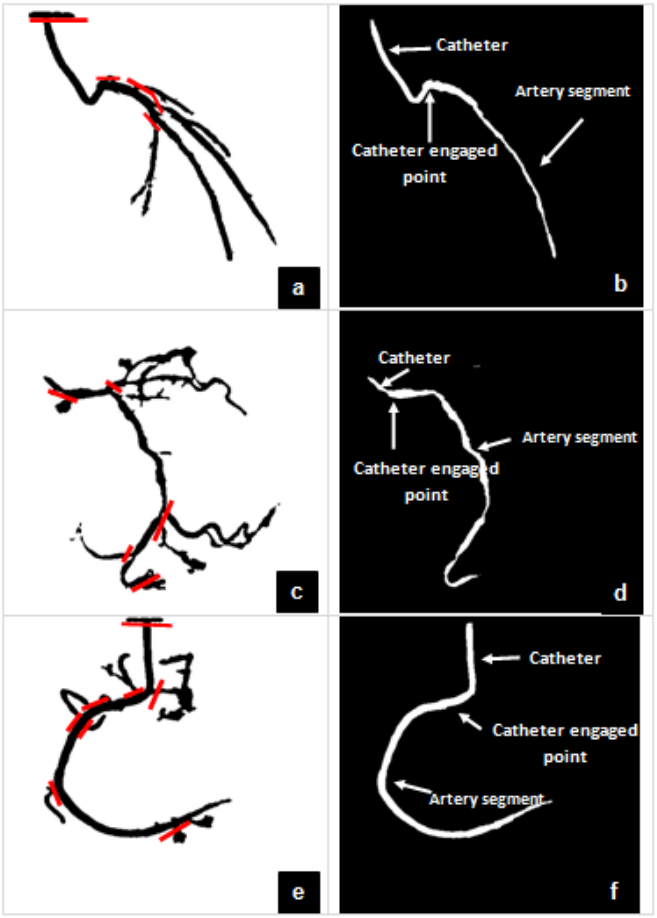

Figure 5.2: Vessel isolation. (a), (c), (e) vessel cut operation on LAD, CX and RCA (red color lines represents vessel cut lines); (b), (d), (f) isolated segments ($f_9(x,y)$) of respective (a), (c) and (e) images.

The skeleton image is denoted as $f_s(x,y)$ and boundary image is denoted as $f_b(x,y)$. Figure 5.3 depicts the visual illustrations of the thinning and boundary detection results of $f_9(x,y)$ images depicted in Figure 5.2. Images (a), (c) and (e) of Figure 5.3 represent the skeletons of $f_9(x,y)$ images in Figure 5.2 (b), (d) and (f) respectively. Additionally, images (b), (d) and (f) of Figure 5.3 represent the detected boundary (detected skeleton is also marked in each image) of Figure 5.2 (b), (d) and (f) respectively. Moreover, it is important to note that these skeleton images also contain the skeletons of three important parts mentioned in section 5.1 namely; the catheter segment, catheter engage point and isolated root CA segment. This resulting skeleton image ($f_s(x,y)$) is used for subsequent skeleton path tracking and boundary image ($f_b(x,y)$) is used for quantitative coronary analysis. The next section will elaborate the skeleton path tracking stage of vessel path tracking phase.

5.1.2 Skeleton path tracking

Skeleton path tracking is the second implementation stage performed after the vessel isolation stage. The skeleton path tracking stage is implemented to store the consecutive pixel points of the skeleton visualized in skeleton image $f_s(x,y)$ in to a specific data structure. In order to achieve that, a committed algorithm has been proposed and it is named as Skeleton Path Tracker (SPT) algorithm. It will perform tacking based on a given seed point and marked tracking direction. In this section, initially the proposed SPT algorithm will be discussed and the application of this algorithm for processing the CCA will be discussed subsequently.

SPT algorithm

The proposed SPT algorithm is a simple line-tracking algorithm, which is based on the pixel connectivity. Skeleton image ($f_s(x,y)$) obtained in the vessel isolation stage is input to this algorithm and it is apparent that this skeleton image ($f_s(x,y)$) is a binary image. Hence, all the on pixels (*intensity value = 255*) in this image represent the skeleton and off pixels (*intensity value = 0*) represent the background. Within the tracking algorithm, two arrays are maintained to keep the pixel points of the skeleton. These arrays are named as skeleton point array and tagged point array. Skeleton point array contains the tracked pixel points along the vessel skeleton and tagged

point array contains the pixels, which are tagged during the tracking process. Moreover, maintaining a tagged point array is crucial in this tracking algorithm because it is used to avoid reversing the tracking and precede the tracking process to the end of the skeleton. Completed skeleton point array with tracked pixel points along the vessel skeleton will be the expected output of this proposed algorithm.

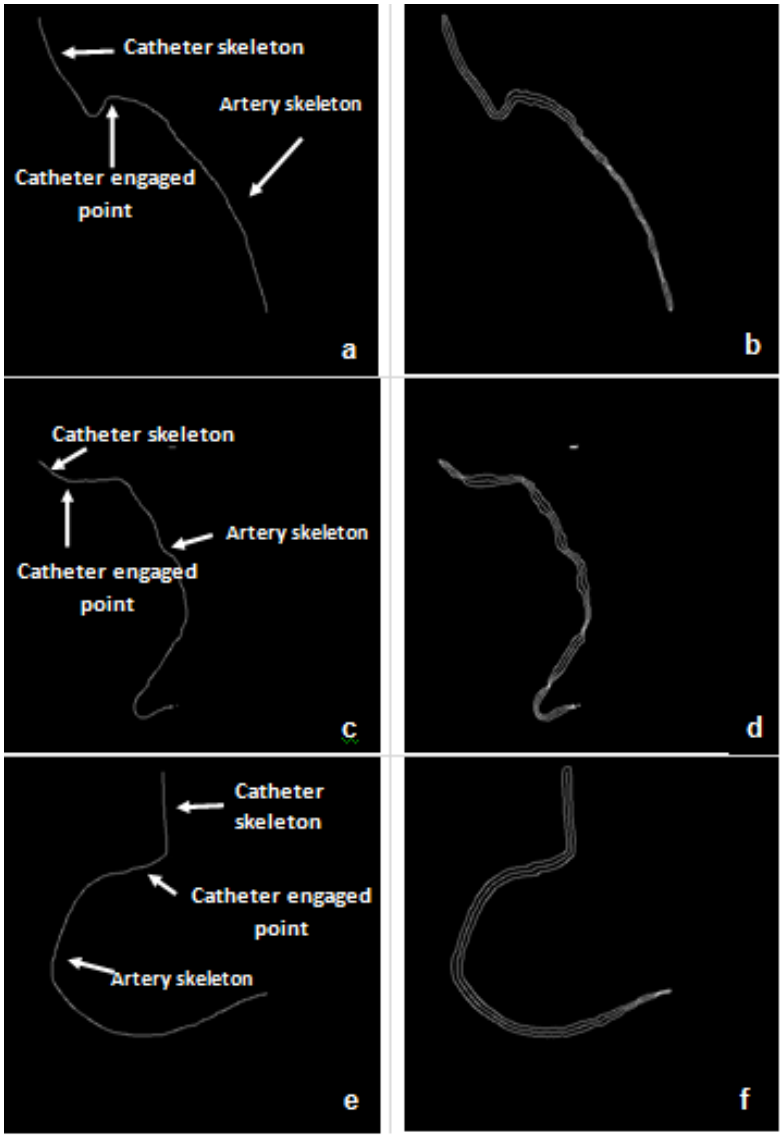

Figure 5.3: Vessel skeleton and boundary extraction. (a), (c), (e) vessel skeleton of selected LAD, CX and RCA segments; (b), (d), (f) detected boundary of selected LAD, CX and RCA segments.

Setting seed point and tracking direction:

In order to start the execution of SPT algorithm, it is necessary to set a seed point and mark the tracking direction. Seed point is a pixel point, which is on the detected skeleton of the input image $f_s(x,y)$ and is marked interactively. According to the Figure 5.3 (a), (c) and (e), it is apparent that this detected skeleton consists of a catheter portion skeleton and a vessel portion skeleton. Hence, two possible tracking directions occur starting from the seed point namely forward and reverse direction. Moreover, forward direction means tracking towards the vessel skeleton portion starting from the seed point and reverse direction means tracking towards the catheter portion starting from the seed point. Even though there are two tracking directions available, forward tracking will be the desired approach in this study. Hence, it is required to always mark forward direction as the tracking direction and essential to deny reverse tracking.

Figure 5.4 emphasizes important steps of marking the tracking directions. Figure 5.4 (a) depicts a sample skeleton image ($f_s(x,y)$) and assume that it is required to track this skeleton starting from the given seed point. A 10×10 pixel region around the seed point is marked in the same image and image (b) of Figure 5.4 expands this marked region for better visualizing the pixel positions. On pixels in Figure 5.4 (b) represent the skeleton pixels and off pixels represent the background. Moreover, the given seed point is colored in gray, in the same image to clearly identify its position.

Forward tracking direction is marked interactively based on the seed point position. Figure 5.4 (c) emphasizes the eight neighboring pixels of the seed point. Moreover, the on pixels in this Figure 5.4 (c) denote the pixels on the skeleton. The skeleton's forward and reverse direction can be visually determined by analyzing the placement of the on pixels in this eight neighboring window. According to that, the reverse tracking will occur if the SPT algorithm starts to track the upper on pixel from the seed point and forward tracking will occur if the SPT algorithm starts to track the lower on pixel from the seed point. Hence, to avoid reverse tracking, it is mandatory to interactively select the reverse direction on pixel and update it as off pixel (*intensity value = 0*). This operation is clearly depicted in Figure 5.4 (d). As a

consequence of this operation the skeleton is broken down into two parts and SPT algorithm start to track the on pixels in the forward direction stating from the seed point. Figure 5.4 (e) denotes the forward tracking and skeleton representation at the end of marking the tracking direction.

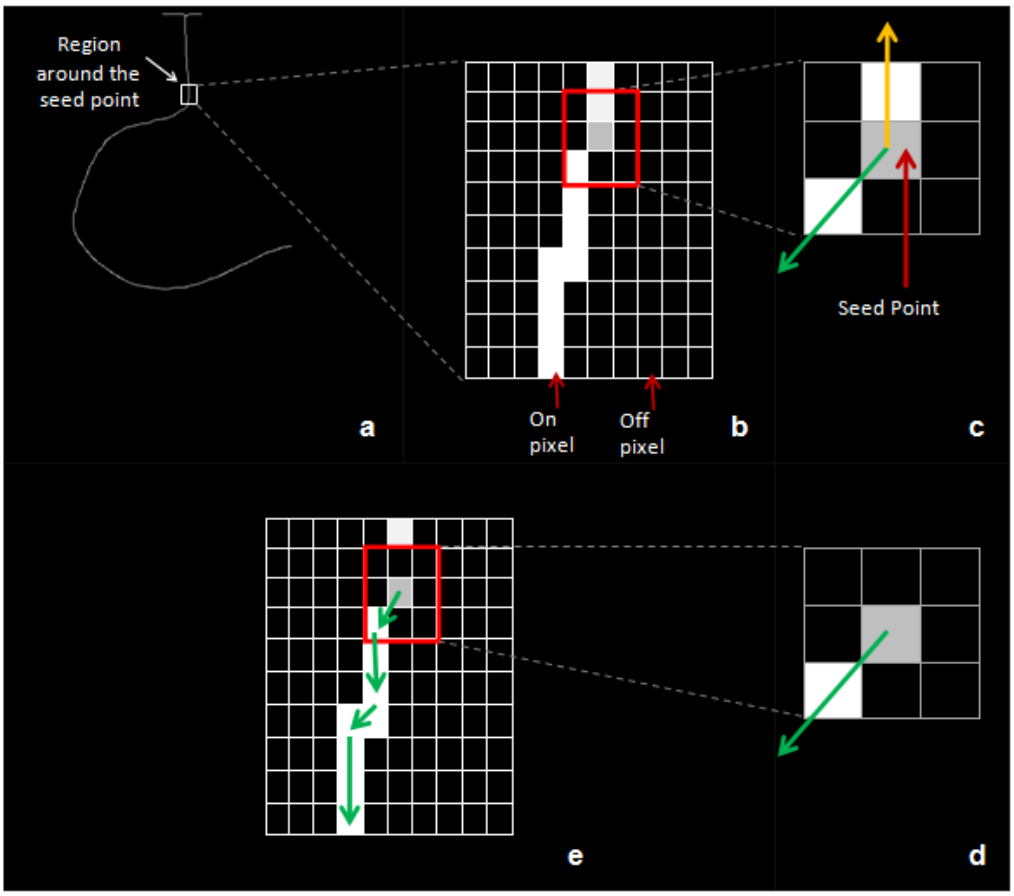

Figure 5.4: Setting tracking direction. (a) skeleton image ($f_s(x,y)$);(b) expanded area of skeleton image in (a); (c) eight neighbors of the seed point; (d) eight neighbors of the seed point after setting the tracking direction; (e) expanded area of skeleton image in (a) after setting the tracking direction. (Yellow arrow – reverse tracking direction, green arrow – forward tracking direction.).

SPT Algorithm steps:

The proposed SPT algorithm is initiated to track the skeleton path after setting a seed point and tracking direction, and is given below;

Skeleton Path Tracker (marked seed point)

BEGIN

1. Set marked seed point as the current seed point.
2. Add current seed point into skeleton point array.
3. Find candidate pixels from eight neighbors of current seed point.
4. Add possible candidate pixels to skeleton point array and candidate point array.
5. If there is no candidate pixel, end up the tracking.
6. If there exist one candidate pixel set it as next seed point and continue with step 9.
7. If there exist more than one candidate pixel in candidate point array, compute the candidate density value for each candidate pixel.
8. Find the candidate pixel with highest candidate density value and set it as the next seed point.
9. Add current seed point in to the tagged point array.
10. Add candidate pixels in to tagged point array except candidate pixel with highest candidate density value and reset candidate key point array unless candidate point array is empty.
11. Continue with step 3.

END

SPT algorithm repeatedly tracks the skeleton path starting from the given seed point until it finds a seed point with zero candidate pixel. Here the candidate pixel means the pixels in eight neighbors of current seed point that can be selected as the next seed point to proceed with the next iteration. Any on pixel in the eight neighbors of current seed point, which is not previously selected as a seed point and not marked as a tagged pixel can be a candidate pixel. One seed point can have zero or more

candidate pixels. If there exist more candidate pixels for a seed point, one out of those available candidate pixels can become the next seed point otherwise it will end the tracking process. Hence, a temporary array is maintained to keep the candidate pixels in iterations and it is denoted as candidate point array. According to these factors it is apparent that this proposed SPT algorithm tracks one pixel per iteration.

The initial step of the proposed SPT algorithm is setting the current seed point. User interactively marked seed point is passed to this algorithm and it is set as the current seed point. After that, this initial current seed point is added into the skeleton point array. Then, the iterative process begins and the steps of the iterative process executed until it finds a seed point with zero candidate pixels. The first step within the iteration is finding candidate pixels of the current seed point. As stated earlier in this section, any on pixel in the eight neighbors of current seed point, which was not previously selected as a seed point and not marked as a tagged pixel is detected and add to both skeleton point array and candidate point array. At this juncture, it can produce one of the three possible values for the candidate pixel count and these values are 0, 1 and >1. Depending on this candidate pixel count there are three possible cases that could arise. These three cases are listed below;

- **Case 1: Current seed point has no candidate pixels:** It means that there are no more on pixels in the skeleton image to be tracked and terminates the tracking process.

- **Case 2: Current seed point has 1 candidate pixel:** In this situation the detected candidate pixel is implicitly set as the next seed point to proceed with the next iteration. Moreover, current seed point is added into the tagged point array and the candidate point array is reset for the next iteration.

- **Case 3: Current seed point has more than 1 candidate pixel:** In this case the candidate density value is calculated for each and every detected candidate pixel. After that, the candidate pixel with highest candidate density value will be selected as the next seed point. Moreover, current seed point and each candidate pixel, except the candidate pixel with highest candidate

density value are added in to the tagged point array consecutively. Finally the candidate point array is reset for the next iteration.

It has introduced a new term called "candidate density value" in above Case 3. Simply, it means the white pixel count around the eight neighboring candidate pixels, which should be previously untagged and not equal to the current seed point. Moreover, Table 5.1 elaborates the behavior of the three cases of proposed SPT algorithm. In Table 5.1, arrow heads indicate tracking direction, Yellow cells indicate tracked pixels and White cells indicate skeleton pixels. Finally, the skeleton point array with tracked skeleton pixels is returned as the output and it will be used in the next phase of the proposed method to determine the vessel diameter. The complete pseudo code of the SPT algorithm and its execution has been included in to Appendix B for further clarifications. Next section will elaborate the application of this proposed SPT algorithm for processing CCA used in this study.

Application of SPT algorithm for processing CCA:

Segmented frames ($f_8(x,y)$ produced in the segmentation phase is input to the vessel path tracking phase. Like in other implementation phases, one CCA frame is processed at a time. Hence the clinically important main vessel segment is extracted from the segmented frame during the vessel isolation stage and it is denoted as $f_9(x,y)$ image. Additionally, both the skeleton image ($f_s(x,y)$) and boundary image ($f_b(x,y)$) of $f_9(x,y)$ is also produced and the proposed SPT algorithm is executed on this skeleton image ($f_s(x,y)$) to track the skeleton.

As mentioned in section 3.3, the first frame of a CCA used to process in this study visualizes the successful catheter engagement and the rest of the frames visualize filling of contrast agent within the CA vasculature. Therefore, it has to track the skeleton of the catheter when this SPT algorithm is applied to the first frame of the CCA to be processed.

Table 5.1: Three cases of SPT algorithm.

Sample Skeleton Image	8 neighbors of current seed point	Remarks
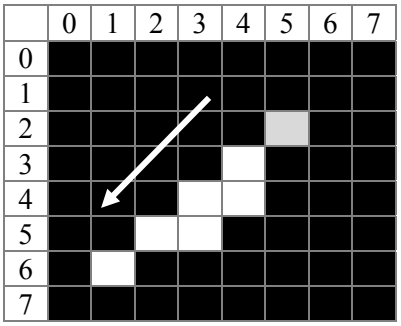	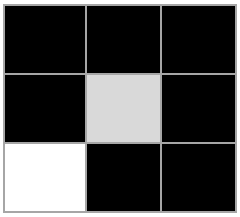 [5,2] point is selected as the seed point and it has a single candidate pixel, which is [4,3] point.	This is an instance for condition 2 of SPT algorithm. Hence it selects [4, 3] point as next seed point.
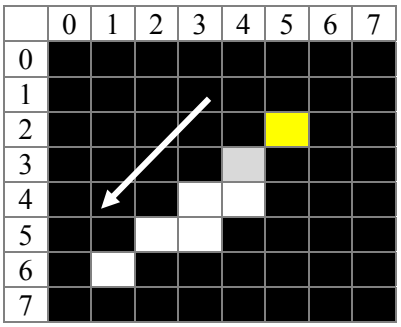	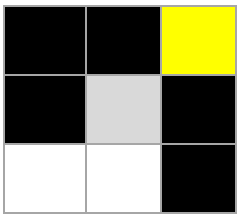 [4,3] point is selected as the seed point and it has two candidate pixels, which are [3,4] and [4,4] points.	This is an instance for condition 3 of SPT algorithm. Hence it is necessary to compute the candidate density of two candidate pixels. Candidate density of [3,4] is 3 and [4,4] is 2. Hence [3,4] point is selected as next seed point.
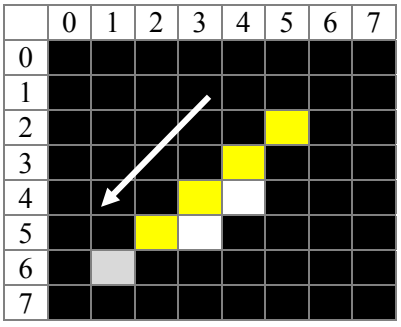	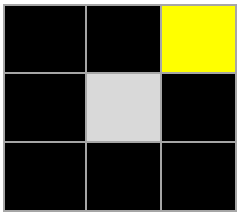 [1,6] point is selected as the seed point and it has 0 candidate pixels.	This is an instance for condition 1 of SPT algorithm. The skeleton path tracking ends up at this point.

This is an important aspect of this study because the last skeleton point of the catheter skeleton signifies the catheter engagement point of the blood vessel. Hence, this pixel point can be used to automatically set the initial seed point for tracking the vessel skeleton of the subsequent skeleton image of the CCA to be processed. Further, the position of the catheter engagement point has been fixed during the frame alignment stage of the pre-processing phase. As a consequence of that, the variation of the placement of catheter engaged point throughout the frame sequence has become lower. Figure 5.5 has provided visual illustrations of the execution of proposed SPT algorithm on four consecutive skeleton images of a certain CCA. Image (a) of Figure 5.5 depicts the first frame of the selected CCA and it visualizes the skeleton of the catheter. Seed point is marked on this catheter skeleton and last track point of the catheter skeleton is also highlighted in the same image. Moreover, this last track point is automatically set as the initial seed point of the subsequent skeleton images and it is emphasized in images (b), (c) and (d) of Figure 5.5. Furthermore, the SPT algorithm executes automatically based on this initially set seed point and perform tracking continuously until it satisfies the case 1.

The skeleton point array produced in this vessel path tracking phase is input to the subsequent quantitative analysis phase with the relevant boundary image, which is denoted as $f_b(x,y)$ to extract the clinically important luminal information. The implementation steps of this quantitative analysis phase will be elaborated in the next section of this chapter.

5.2 Quantitative analysis

Quantitative analysis is the last implementation phase of the proposed methodology and its objective is to formalize an acceptable standard for assessment of CA dimensions using a quantitative approach. The skeleton point array and boundary image ($f_b(x,y)$) produced in previous vessel path tracking phase is input to this quantitative analysis phase and it calculates the vessel diameter along the vessel skeleton as the output. The proposed algorithm for calculating vessel diameter is based on the geometry of vessel boundary and skeleton. Following section elaborates the steps of this proposed Vessel Diameter Calculation (VDC) algorithm.

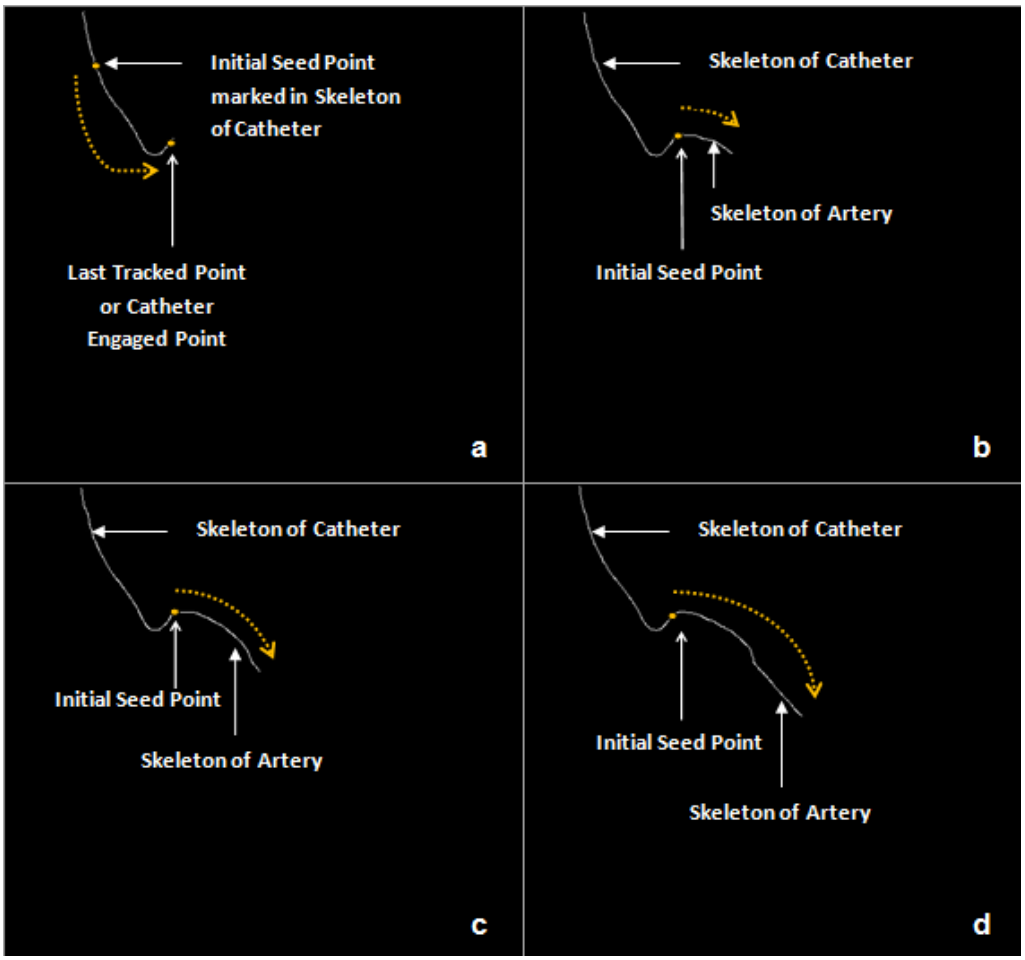

Figure 5.5: Skeleton path tracking in CCA. (a) skeleton image of the first frame visualizes catheter engagement with artery; (b),(c) and (d) three consecutive frames of the same CCA (Yellow colored arrow indicates tracking direction).

5.2.1 Vessel Diameter Calculation (VDC) algorithm

In this algorithm, the vessel diameter is calculated simply based on the vessel skeleton. Moreover, within VDC algorithm, it tracks two perpendicular lines, which are drawn from each and every skeleton point to left and right boundary points of the vessel. A sample model depicted in Figure 5.6 is used to elaborate the steps of the VDC algorithm. In this model, green lines represent the vessel boundary and green dash line represents the vessel skeleton. *P1* is the first skeleton point and *P2* is another skeleton point, which locates *g* gap away from the *P1* point. The angle

between *P1-P2* line with horizontal axis is denoted as a^0. *P2-P3* and *P2-P4* are two perpendicular lines for *P2* point of length *g*.

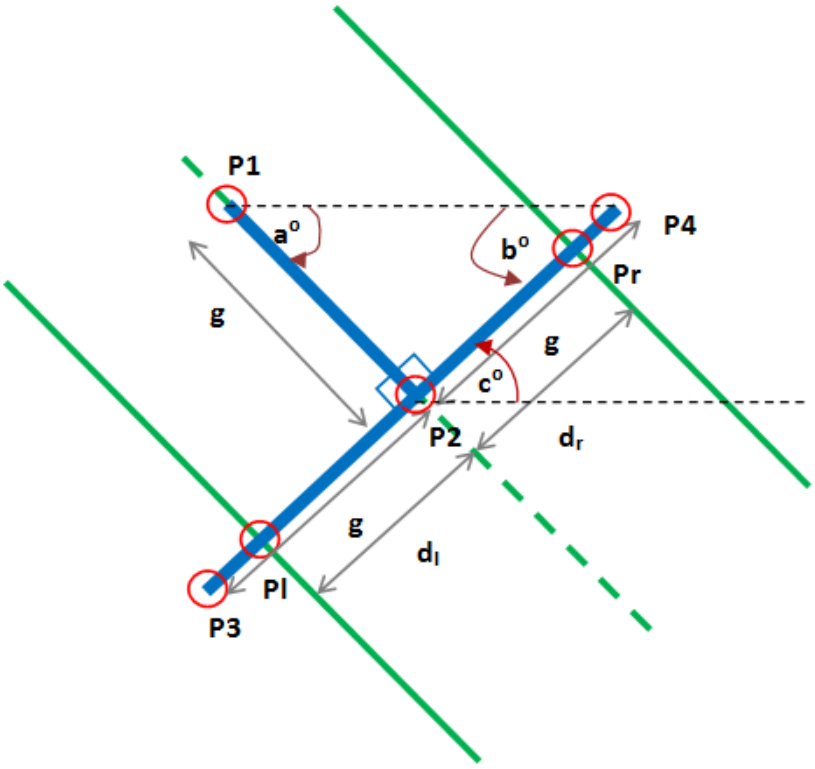

Figure 5.6: Vessel diameter calculation model.

Diameter calculation algorithm starts from the skeleton point, which belongs to the vessel segment denoted as *P2*. The gap *g* between *P1-P2* points has been set as 15 pixels because it should be greater than the maximum radius of typical CA [100]. The main steps of proposed VDC algorithm are stated below;

Step 1: Find the angle between *P1- P2* line with horizontal axis in degrees as mentioned in the equation (5.1);

$$a = tan^{-}\left(\left|\frac{P2_y - P1_y}{P2_x - P2_x} \times \frac{180}{\pi}\right|\right) \tag{5.1}$$

Step 2: Find *P3* point using the equation (5.2). Note that this *P3* point is perpendicular to the *P1-P2* line that intersects left side boundary of the vessel where *P2-P3* line exists;

$$P3 = \left(-V_y, V_x\right) \tag{5.2}$$

Where $V_x = (P1_x - P2_x)$ and $V_y = (P1_y - P2_y)$

Step 3: Find *P4* point using the equations (5.3) and (5.4). Note that this *P4* point is perpendicular to *P1-P2* line that intersects right side boundary of the vessel where *P2- P4* line exists;

$$P4_x = \left\lfloor P2_x + g\ cos\left(c \times \frac{\pi}{180}\right)\right\rfloor \tag{5.3}$$

$$P4_y = \left\lfloor P2_y + g\ sin\left(c \times \frac{\pi}{180}\right)\right\rfloor \tag{5.4}$$

Step 4: Tracks the *P2- P3* line from *P3* point until the boundary intersection *Pl* is met and calculates the distance between *P2* to *Pl* as the radius *dl* from *P2* point to left side vessel boundary.

Step 5: Tracks the *P2- P4* line from *P4* point until the boundary intersection *Pr* is met and calculates the distance between *P2* to *Pr* as the radius *dr* from *P2* point to right side vessel boundary.

Step 6: Diameter of the vessel segment with respect to the *P2* point is given by *dl*+*dr*.

Step 7: Store calculated radius and diameter values

Step 8: Shift *P1* point to the next vessel skeleton point if exists and repeat the above steps 1 to 7.

Step 4 and 5 of VDC algorithm consists of line tracking from point *P3* to *P2* and *P4* to *P2* respectively. SPT algorithm implemented for vessel path tracking phase is re-used in VDC algorithm appropriately. The two perpendicular lines of point P2 denoted as *P2-P3* and *P2- P4* are modeled in a mask image, which has the same size as that of the boundary image ($f_b(x,y)$). Then SPT algorithm is executed to track these two lines one after the other. While tracking, it checks the intensity from the boundary image ($f_b(x,y)$) with respect to the calculated next seed point. If the intensity of the boundary image ($f_b(x,y)$) with respect to the next seed point equals to 255, it means the specific line intersects one of the boundaries of the artery. These intersection points are denoted as *Pl* and *Pr* depending on the line tracking direction. *Pl* is the intersection point when tracking is from point *P3* to *P2* and *Pr* is the intersection point when tracking is from point *P4* to *P2*.

This VDC algorithm is applied from second frame to last frame of the CCA to be processed because the development of vessel skeleton will be recorded from the second frame onwards. The first frame only represents the catheter engagement and it is used only for determining the catheter engagement point. Figure 5.7, 5.8 and 5.9 depict the visual illustration of implementation of the VDC algorithm of selected LAD, CX and RCA CAs for further clarifications. Image (a) of Figure 5.7, 5.8 and 5.9 depict the marked boundary and skeleton of the selected artery segment and image (b) of Figure 5.7, 5.8 and 5.9 depict the visual illustration of execution of the VDC algorithm.

5.2.2 Processing other CCA frames

At this juncture, it has been comprehensively elaborated all four major implementation phases of the proposed method as mentioned in section 3.1. According to the flow chart depicted in Figure 3.1, it will check whether it has more frames to process. If the CCA currently being processed has more frames, the next frame is extracted and input to the pre-processing phase to proceed with the next iteration. At the end of each iteration step except the first, the computed information such as radius to the left side boundary, radius to the right side boundary and vessel diameter are recorded in a log according to the skeleton point. The count of skeleton

points in each frame indicates the length of the skeleton. Moreover, these log records are organized according to the CCA frame number being processed. Finally, this proposed method returns the log file with aforementioned luminal information as the output. Additionally, the information stored in the log file of a certain CCA case can be further utilized to visualize a respective CCA frame as a supportive tool in making clinical decisions.

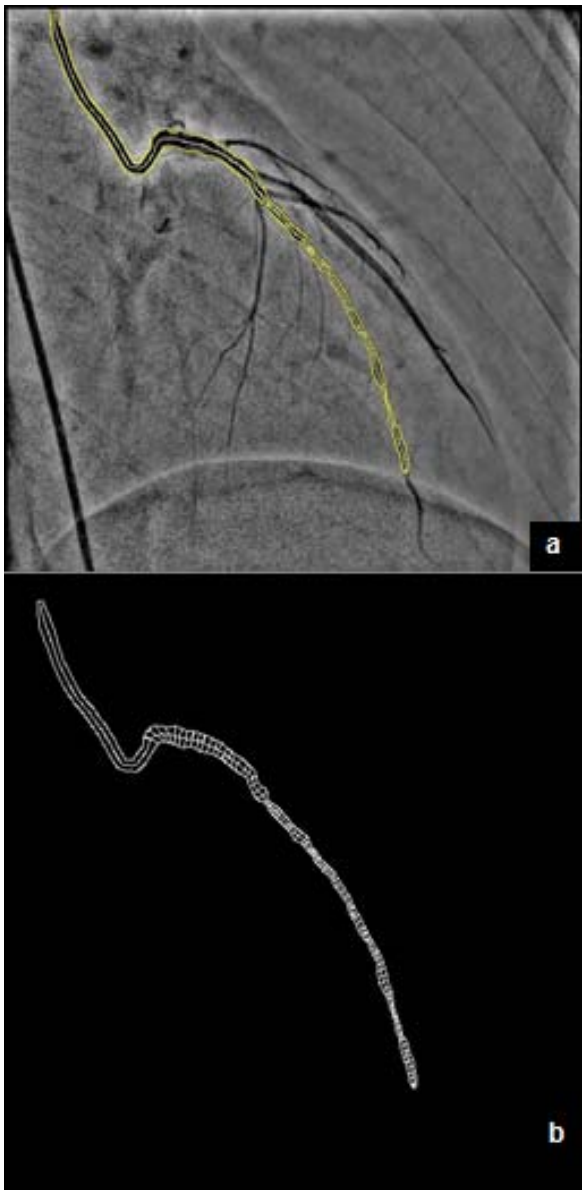

Figure 5.7: Vessel diameter calculation of LAD. (a) enhanced frame with marked LAD segment; (b) execution of VDC algorithm.

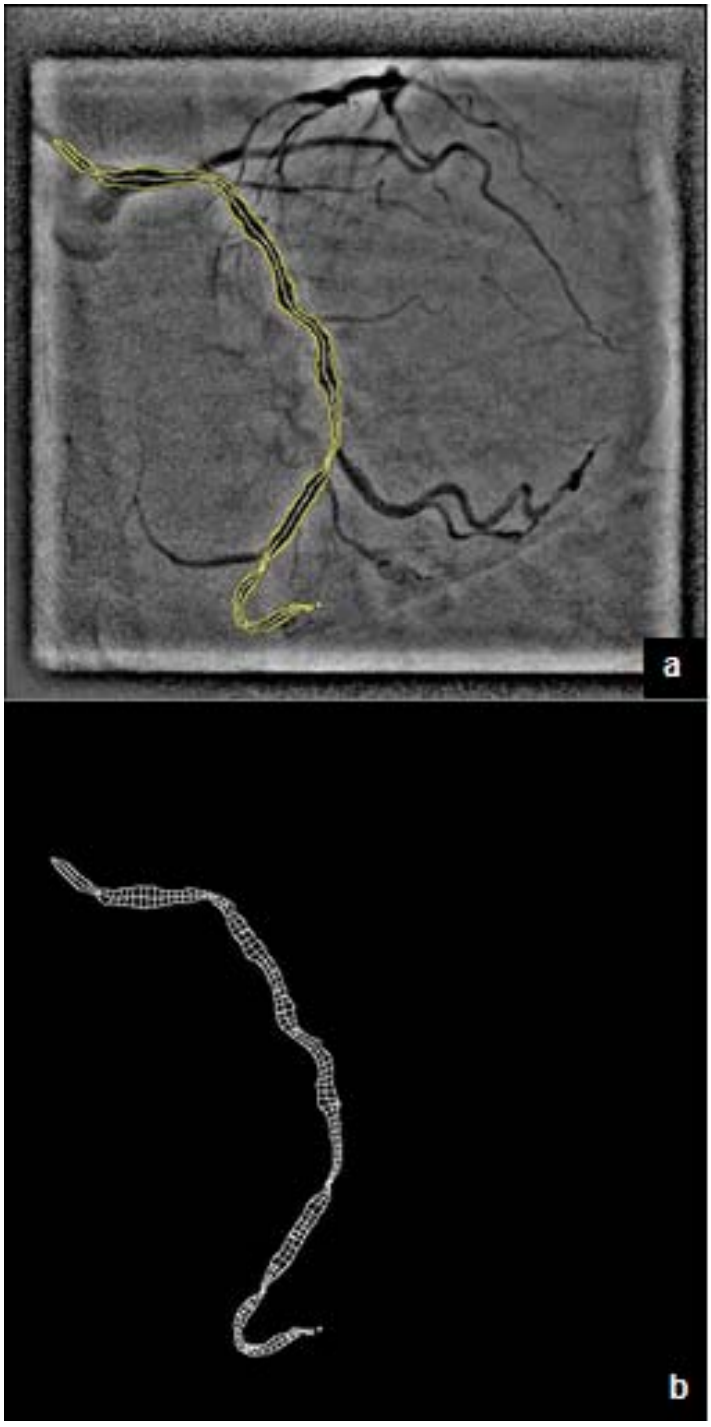

Figure 5.8: Vessel diameter calculation of CX. (a) enhanced frame with marked CX; (b) execution of VDC algorithm.

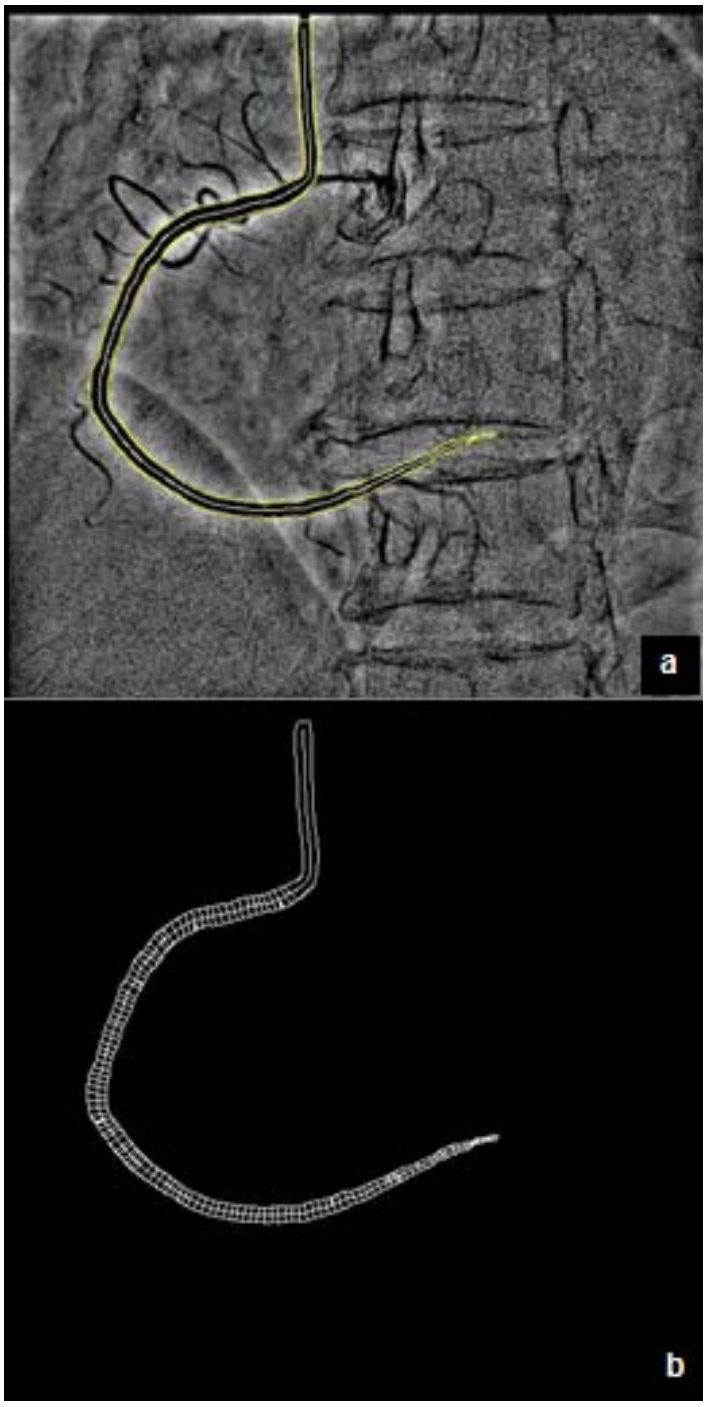

Figure 5.9: Vessel diameter calculation of RCA. (a) enhanced frame with marked RCA segment; (b) execution of VDC algorithm.

Figure 5.10 depicts a sample CCA frame with calculated diameter values along the skeleton of the selected CA segment. These diameter results can be used to determine the CA obstructions and it will be discussed in the next chapter. Moreover, Appendix C emphasizes the main processing steps of this proposed quantitative coronary analysis method with series of visual illustrations for further clarifications.

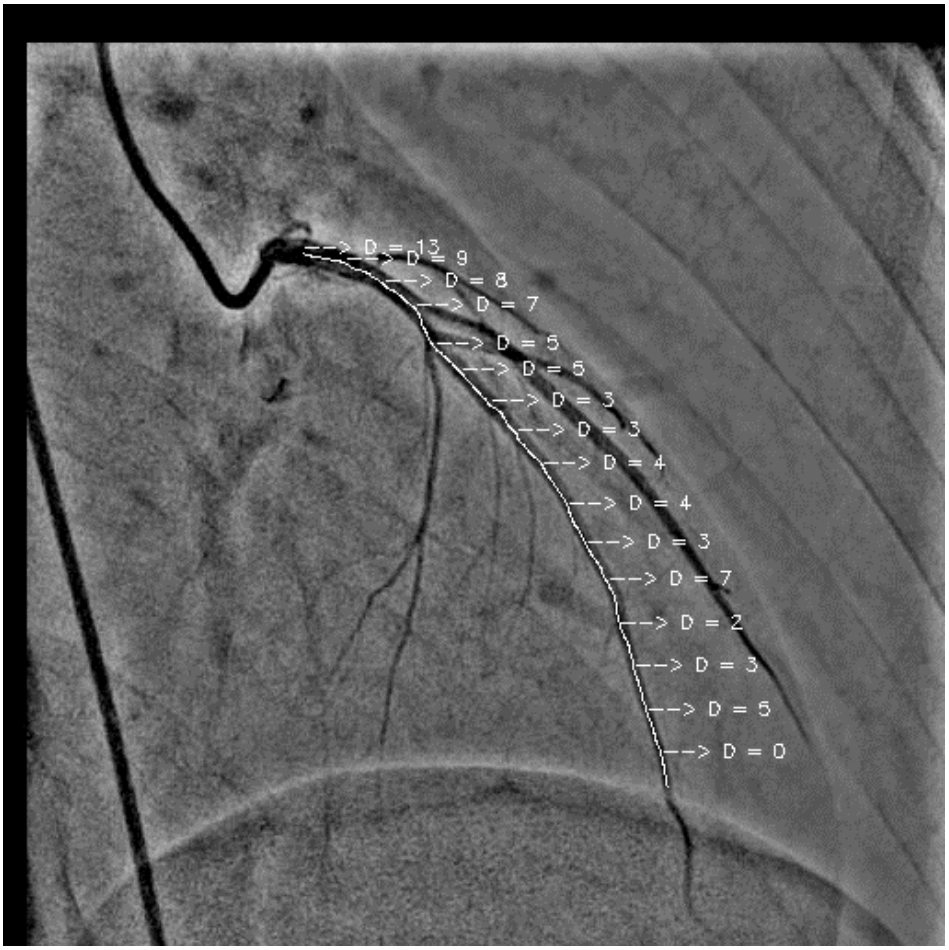

Figure 5.10: Display diameter results.

5.3 Summary

This chapter mainly elaborated the experimental approaches executed to implement the vessel path tracking and quantitative analysis phases of the proposed method of this research study. The clinically important vessel segment is extracted from the input segmented frame ($f_8(x,y)$) and the skeleton ($f_s(x,y)$) and boundary ($f_b(x,y)$) of

that selected arterial segment is extracted separately. Consequently, vessel skeleton path is tracked using the proposed SPT algorithm and pixels' coordinates on the skeleton path are stored in a specific array. Subsequently, the boundary image and stored skeleton points are used to determine the vessel diameter through VDC algorithm. Computed luminal information is recorded in a log file and those stored records have been used to provide the visualizations to make the objective assessment of the CA disease. Experimental setups and results of this research study are organized in the next chapter.

CHAPTER 6
VALIDATION METHODS AND RESULTS

The objective of this chapter is to experimentally validate the various aspects of the implementation phases of the proposed quantitative coronary analysis method mentioned in Chapters 3, 4 and 5. In particular, the robustness of the frame alignment, accuracy of the segmentation algorithm and the technical feasibility of VDC algorithm have been evaluated using a randomly selected clinical data set.

6.1 Data extraction

The direct CCAs produced by Philips Medical System were used for the experiments and those were recorded at a frame rate of 15fps with 512×512 resolution. The selected CCAs for creating the dataset were recorded under the three standard angiography views namely LAO cranial, AP caudal and AP cranial views. The main reason for selecting the aforementioned angiogram views for creating the dataset is that those views provide excellent visualizations for the main CAs namely RCA, CX and LAD respectively.

6.2 Validation in pre-processing phase

Algorithms developed for frame alignment is validated in this set-up. In order to achieve this, fifty direct CCA cases, which have been recorded under the three angiography views mentioned in section 6.1 were selected randomly to create a data set. Hence, 24 CCA cases were selected under LAO Cranial view, 13 CCA cases were selected under the AP Caudal view and 13 cases were selected under the AP Cranial view.

Moreover, the proposed validation method consists of three main steps namely; finding the best similarity measure for template matching, finding the value for $D_{HOGThreshold}$ and assessing the robustness of the proposed frame alignment algorithm. Following sub sections have broadly emphasized the implemented procedures and obtained results for each of those validation steps.

6.2.1 Finding the best similarity measure for Template Matching

In order to find the best similarity measure for the template matching, the proposed frame alignment algorithm was executed separately on the created dataset under the six different similarity measures defined in open source computer vision and machine learning software library called OpenCV. Hence, a total of 1372 × 6 template matching steps were presented in the executed dataset under each similarity measure. Further, the visually observed template matching judgment, calculated HOG distance (D_{HOG}) and the Euclidean distance between matched templates for each matching step were recorded.

Each matching instance is determined as either as successful match or mismatch based on the visually observed template matching judgment made by experts and is used as the ground truth for the validation process. Moreover, these successful template matching instances are denoted as positive matches and unsuccessful matches are indicated as negative matches. Subsequently, the positive matching percentage for each CCA under the six similarity measures was computed separately to determine the best similarity measure and the results are enlisted in Table 6.1. Based on the results presented in Table 6.1, CC was selected as the best similarity measure for the frame alignment algorithm because it possesses the highest positive matching percentage.

Table 6.1: Positive matching percentage under various similarity measures.

Similarity Measure	True Positive Matching %
Square Difference	83.61
Normalized Square Difference	87.66
Correlation	90.31
Correlation Normalized	86.19
Correlation Coefficient (CC)	91.76
Normalize Correlation Coefficient	91.72

Further, Table 6.2 summarizes the positive matching results obtained under the CC similarity measure for each test case according to the selected angiography view. Moreover, the analysis results have shown the positive matching percentages under

the selected views as follows; LAO cranial view of RCA: 91.68%; AP caudal view of LCA: 92.47%; AP cranial view of LCA: 91.11%. Average positive matching percentage was reported as 91.76%.

Table 6.2: Positive matching percentage under CC similarity measures.

Test Case	RCA		LCA			
	LAO_CRANIAL		AP_CAUDAL		AP_CRANIAL	
	Total Matches	Positive Matches	Total Matches	Positive Matches	Total Matches	Positive Matches
1	19	19	13	13	23	23
2	23	23	21	6	44	44
3	20	20	26	26	12	12
4	19	19	16	16	19	19
5	15	15	22	22	18	18
6	17	17	23	23	18	18
7	30	30	36	36	36	36
8	33	33	36	36	30	30
9	29	29	34	34	30	30
10	28	28	36	36	20	20
11	21	21	24	8	18	18
12	40	26	32	32	24	24
13	30	30	23	23	18	2
14	24	24	23	23	24	18
15	12	12	24	24	24	11
16	22	22	23	23	23	18
17	21	7	13	13	21	21
18	19	9	20	20	21	21
19	19	19	8	8	15	15
20	16	16	12	8	12	12
Total	457	419	465	430	450	410
True positive %		91.68		92.47		91.11

6.2.2 Finding a value for $D_{HOGThreshold}$

In order to find the threshold value for $D_{HOGThreshold}$, F1 score was calculated for the possible threshold values ranging from 1 to 100 separately, according to the three selected angiography views. It has been calculated by using the visually observed template matching judgment and the recorded D_{HOG} values for each matching instance of the selected CCAs. True positive, false positive and false negative

matches needed for determining the F1 score and those were calculated using the equations (6.1), (6.2), and (6.3) respectively;

$$TP_{matches} = \|\{D_{HOG}\} < T\| \cap \|\{D_{HOG}\} == M\| \tag{6.1}$$

$$FP_{matches} = \|\{D_{HOG}\} < T\| \cap \|\{D_{HOG}\} == N\| \tag{6.2}$$

$$FN_{matches} = \|\{D_{HOG}\} \geq T\| \cap \|\{D_{HOG}\} == M\| \tag{6.3}$$

Where, $\{D_{HOG}\}$ indicates the set of HOG distance values obtained for each template matching instance according to the selected angiography view and T indicates the threshold values ranging from 1 to 100. Moreover, M and N denote the visually observed template matching judgment where M indicates the positive matching instance and N indicates negative matching instance respectively. Graphs depicted in Figure 6.1, 6.2 and 6.3 represent the F1 score variation against the threshold values ranging from 1 to 100 for three selected angiography views.

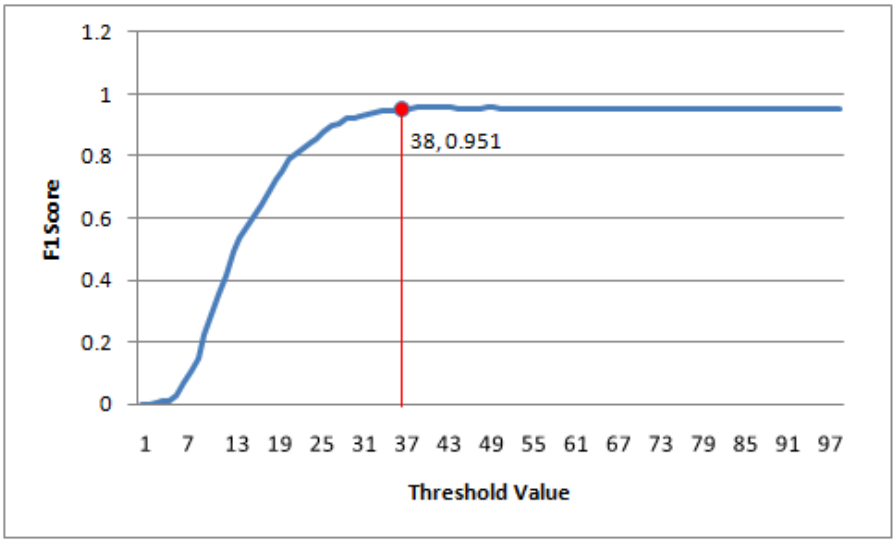

Figure 6.1: Distribution of F1 score against the possible threshold value range for RCA LAO cranial view (Maximum F1 score = 0.951 for threshold value 38).

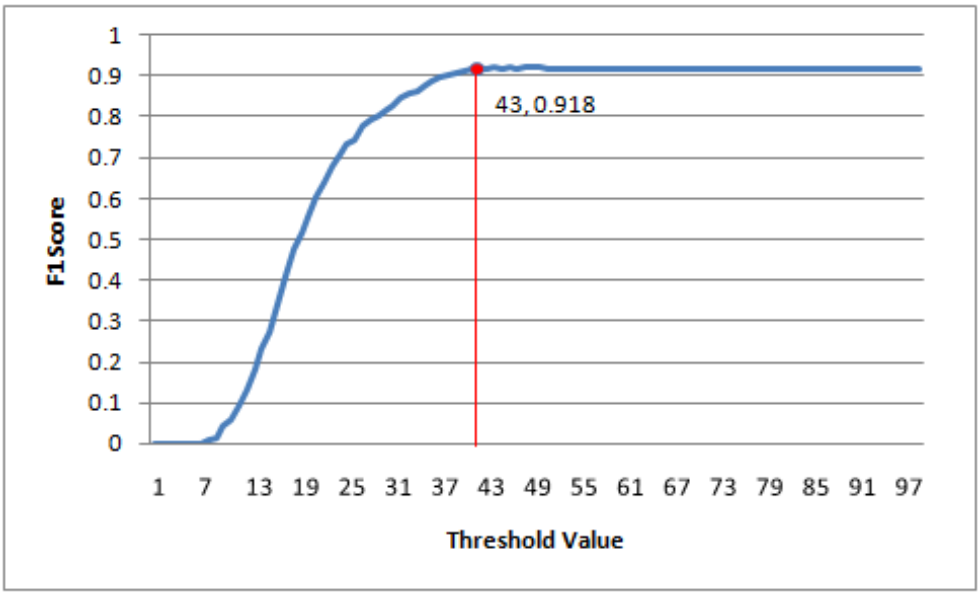

Figure 6.2: Distribution of F1 score against the possible threshold value range for LCA AP caudal view (Maximum F1 score = 0.918 for threshold value 43).

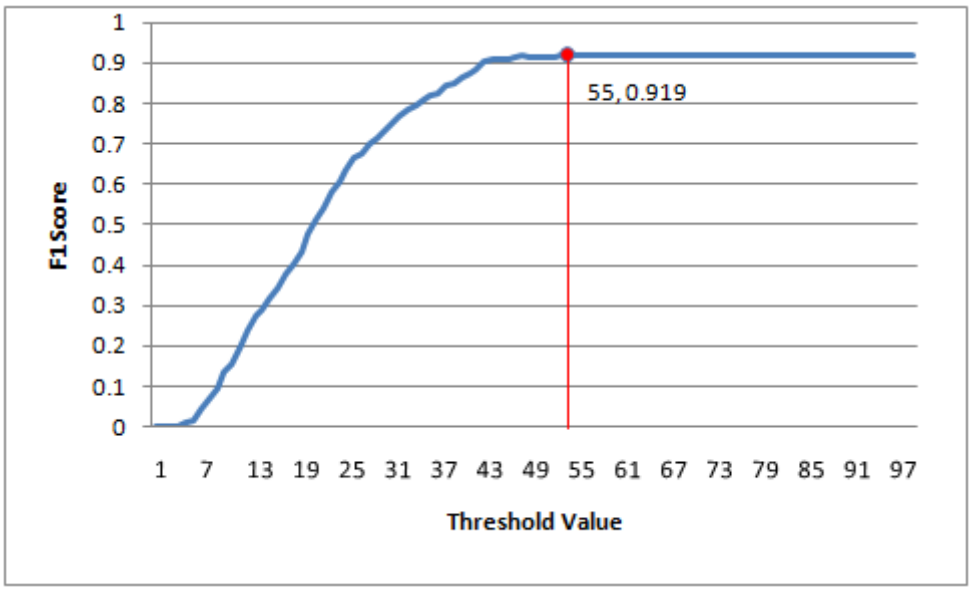

Figure 6.3: Distribution of F1 score against the possible threshold value range for LCA AP cranial view (Maximum F1 score = 0.919 for threshold value 55).

According to the results, it could be observed that those threshold values determined as 38, 43 and 55 have provided the maximum F1 score for RCA LAO cranial, LCA AP caudal and LCA AP cranial views respectively. Hence, the mean value of the obtained threshold values is selected as the $D_{HOGThreshold}$, which is 45.

6.2.3 Assessing the robustness of the proposed method

The proposed method was executed for the second time using the same data set and same template parameters used in the first test. During this execution the proposed false matching correction algorithm was enabled to detect and correct false matches. During this execution CC was set as the similarity measure for template matching operation and the $D_{HOGThreshold}$ was set as 45. Table 6.3 enlists the positive matches obtained as the results of this execution. Analysis of the results of this execution have revealed the following positive matching percentages under the selected views as follows; LAO cranial view of RCA: 97.82%; AP caudal view of LCA: 99.12%; AP cranial view of LCA: 95.33%. Average positive matching percentage was reported as 97.45%. Figure 6.4 graphically represents the effect of false matching detection algorithm for improving the robustness of the frame alignment stage.

6.3 Validation in segmentation phase

Accurate segmentation is one of the mandatory requirements of this research study because it directly affects the accuracy of subsequent quantitative analysis phase in this study. The proposed segmentation phase has been elaborated comprehensively in Chapter 4 and the objective of this section is to emphasize the validation methods and the results, which have been used to determine the segmentation accuracy.

A dataset of 39 CCA cases has been created to validate the proposed segmentation method. The selected CCAs were recorded under the three standard angiography views mentioned in section 6.1. Hence, 15 CCA cases recorded under the LAO Cranial (for RCA) view, 13 CCA cases recorded under the AP Caudal (for CX) view and 11 cases recorded under the AP Cranial (for LAD) view were selected to create the test data set.

Table 6.3: Positive matching results of CCAs under the CC similarity measure and DHOGThreshold = 45.

Test Case	RCA		LCA			
	LAO_CRANIAL		AP_CAUDAL		AP_CRANIAL	
	Total Matches	Positive Matches	Total Matches	Positive Matches	Total Matches	Positive Matches
1	19	19	13	13	23	20
2	23	23	21	21	44	44
3	20	20	26	26	12	12
4	19	19	16	16	19	19
5	15	15	22	22	18	18
6	17	17	23	23	18	18
7	30	30	36	36	36	23
8	33	33	36	36	30	30
9	29	29	34	34	30	30
10	28	28	36	36	20	20
11	21	21	24	24	18	18
12	40	40	32	32	24	24
13	30	30	23	23	18	18
14	24	24	23	23	24	24
15	12	12	24	24	24	24
16	22	22	23	23	23	18
17	21	21	13	13	21	21
18	19	9	20	20	21	21
19	19	19	8	8	15	15
20	16	16	12	8	12	12
Total	457	447	465	461	450	429
True positive %		97.82		99.12		95.33

6.3.1 Evaluation method

In order to validate the proposed segmentation method, the proposed segmentation algorithm was tested separately using the CCAs of the created data set. According to the pixels classification in the segmentation result, the segmentation accuracy (SegAcc) was calculated for each frame of the CCA being processed, using the equation (6.4);

$$segAcc(F) = \frac{\|seg(F) \cap GT(F)\|}{\|GT(F)\|} \tag{6.4}$$

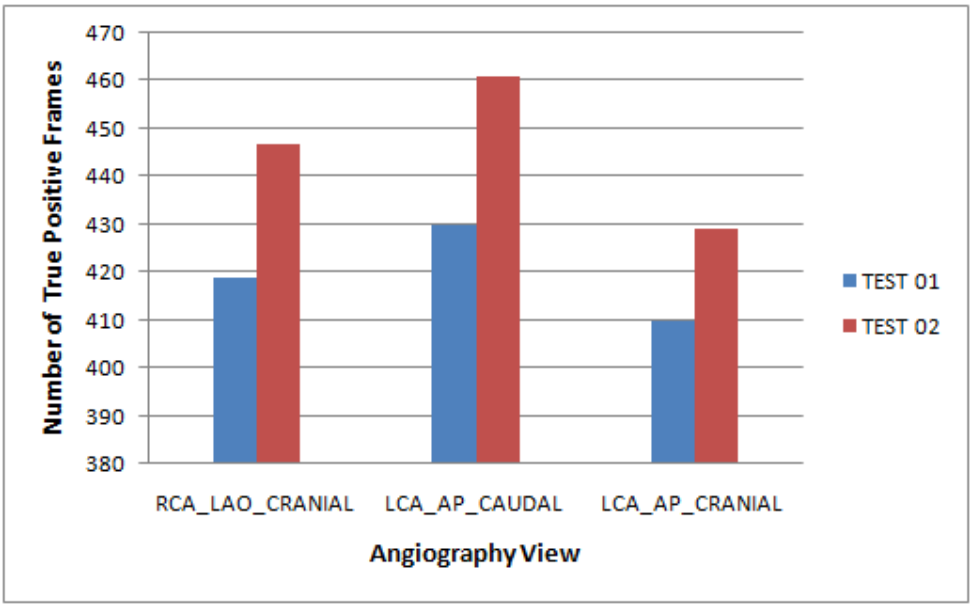

Figure 6.4: Positive matching percentage (False matching detection is disabled in TEST 01 and enabled in TEST 02).

Where, $||x||$ stands for the cardinality of x and x indicates the pixel count of the foreground. F is the input CCA frame and $Seg(F)$ is the segmented frame obtained from the proposed segmentation method. $GT(F)$ is the ground truth image of frame F. Ground truth images are created manually and those images are specific to the frame to be processed. Moreover, those ground truth images represent marked pixels, which belong to the main arterial region, which is emphasized according to the recorded angiogram view. All ground truth images were certified by a professional Radiographer in order to ensure the accuracy of them. Figure 6.5 visually illustrates three sample ground truth images of LAD, CX and RCA with the respective enhanced CCA frames for further clarifications.

Even though this metric determine the segmentation accuracy with respect to a specific CCA frame F, it is important to define the segmentation accuracy in relation to the entire angiography. Hence, the mean segmentation accuracy was determined for each CCA by analyzing the $segAcc(F)$ values computed for each and every frame of the processed CCA cases in the dataset.

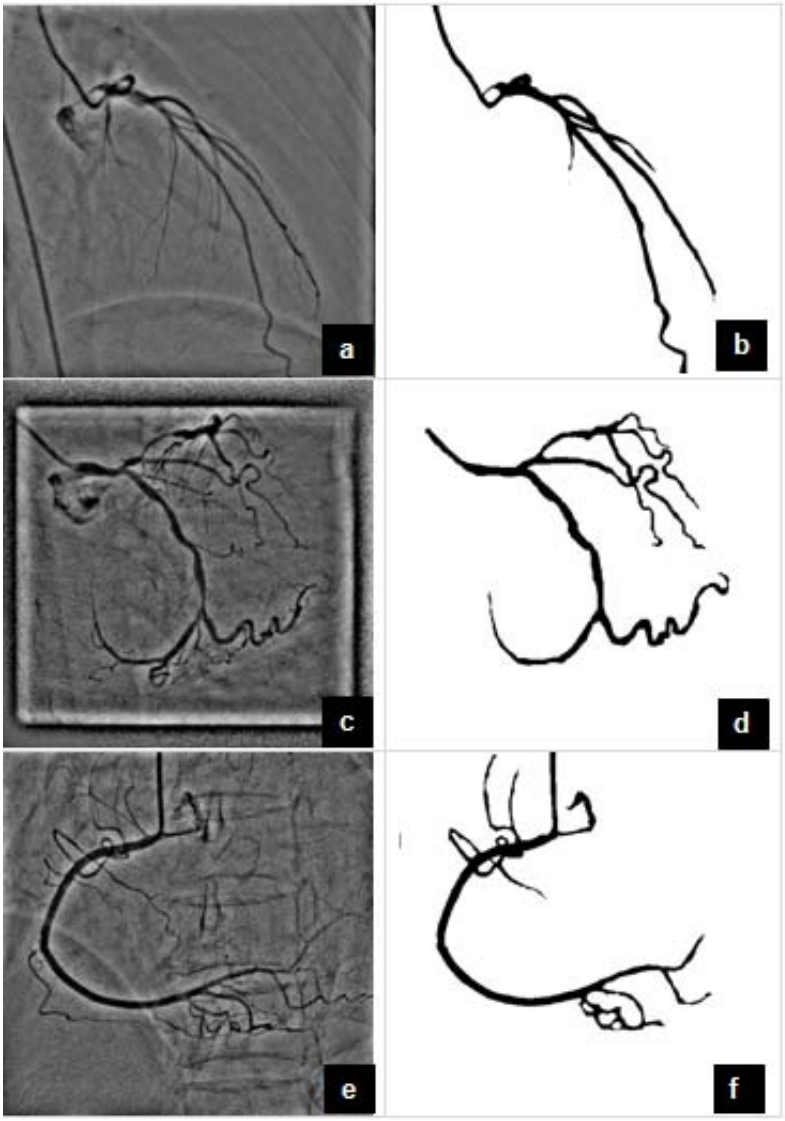

Figure 6.5: Example for ground truth frames. (a), (c), (e) enhanced CCA frame visualizing LAD, CX and RCA CAs respectively; (b), (d), (f) created ground truth images of LAD, CX and RCA segments of (a), (c) and (e) respectively.

It is also significant indeed to measure how the segmentation is wrong. It can be determined by computing both false positive and false negative pixels in the segmented frames. False positive consists of those pixels belong to the background, but are classified as foreground, and false negative consists of those pixels belong to the foreground, but are classified as background. Moreover, the equations (6.5) and

(6.6) can be used to compute the false positive error (fallout rate) and false negative error (miss rate) measurements of a given frame *F* respectively.

$$Error_{FP} = \frac{\left\| seg(F) \cap \overline{GT(F)} \right\|}{\left\| \overline{GT(F)} \right\|} \tag{6.5}$$

$$Error_{FN} = \frac{\left\| GT(F) \cap \overline{seg(F)} \right\|}{GT(F)} \tag{6.6}$$

Similarly in computing the segmentation accuracy, it is important to define the false positive and false negative assessments in relation to the entire angiography. Hence, the mean false positive and mean false negative measurements were determined for each CCA by analyzing both $Error_{FP}$ *and* $Error_{FN}$ values for each and every frame of the processed CCA cases in the dataset. Figure 6.6, 6.7 and 6.8 visually illustrate the assessment of segmentation accuracy, false positive and false negative of the extracted foreground of the three frames depicted in Figure 6.5 (a), (c) and (e) respectively. Figure 6.5 (b), (d) and (f) images were used as the ground truth images for these assessments. Image (a) of Figure 6.6, 6.7 and 6.8 depict the segmentation results obtained for processed frames in Figure 6.5 (a), (c) and (e) respectively. Image (b) of Figure 6.6, 6.7 and 6.8 depict the visual illustrations of assessment of segmentation accuracy. Purple colored regions in those images represent the intersected foreground region of both segmented frame and the ground truth image. Moreover, green colored regions represent non-intersected segmented foreground regions. Image (c) of Figure 6.6, 6.7 and 6.8 depict the visual illustrations of false negative assessment, which means assessing those pixels belonging to foreground but are classified as background pixels. Red colored regions in those images represent the false negative regions and green colored region represents accurate foreground pixels. Similarly, image (d) of Figure 6.6, 6.7 and 6.8 depict the visual illustrations for false positive assessment, which means assessing those pixels belonging to background, but are classified as foreground pixels. Red colored regions in those images represent the false positive regions and green colored region represents accurate foreground pixels.

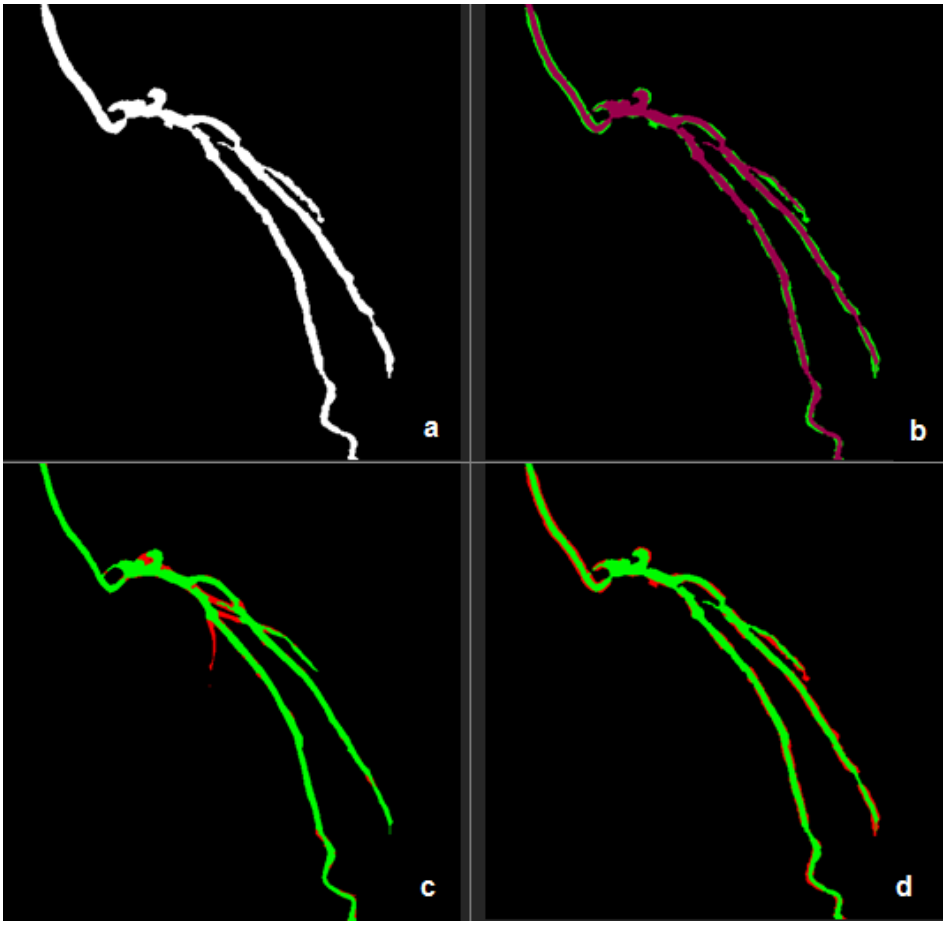

Figure 6.6: Validating LAD. (a) segmented LAD; (b) segmentation accuracy result (88.43%); (c) false negative result; (d) false positive result (Sensitivity: 0.884, miss rate: 0.116 and fall out rate: 0.012).

Further, the sensitivity (true positive rate) and fallout rates (false positive rate) were also calculated for each frame of the CCA being processed. Finally mean sensitivity and mean fallout rates were also computed by analyzing the calculated sensitivity and fallout rates for each and every frame of the individual CCAs of the selected dataset.

6.3.2 Results of segmentation phase

According to the measurements defined in section 6.3.1, Table 6.4 and 6.5 list the evaluation results obtained for LAD artery, Table 6.6 and 6.7 list the evaluation

results obtained for CX artery and Table 6.8 and 6.9 list the evaluation results obtained for the RCA artery.

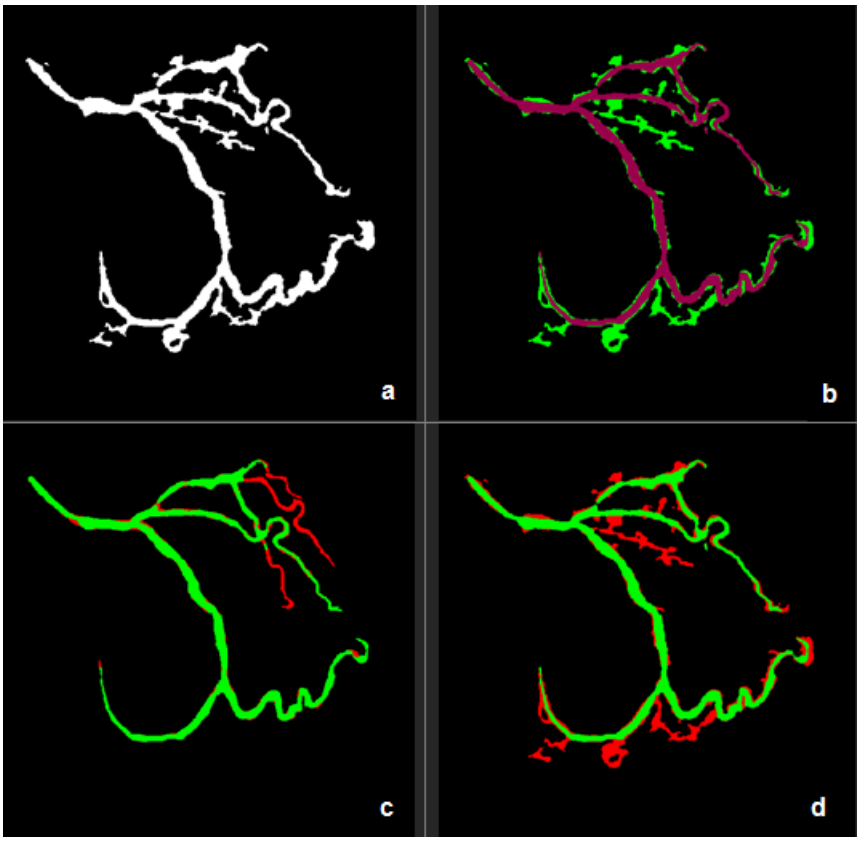

Figure 6.7: Validating CX. (a) segmented CX; (b) segmentation accuracy result (82.79%); (c) false negative result; (d) false positive result (Sensitivity: 0.828, miss rate: 0.171 and fall out rate: 0.029).

These tables mention the average validation results of true positive, true negative, false positive and false negative pixels' assessment according to the selected CCA case. Moreover, the computed mean segmentation accuracy, mean sensitivity and mean fallout rate were also presented according to the three main CAs. Further, the Table 6.10 summarizes the average segmentation accuracy, average sensitivity and average fallout rate obtained for the proposed segmentation method.

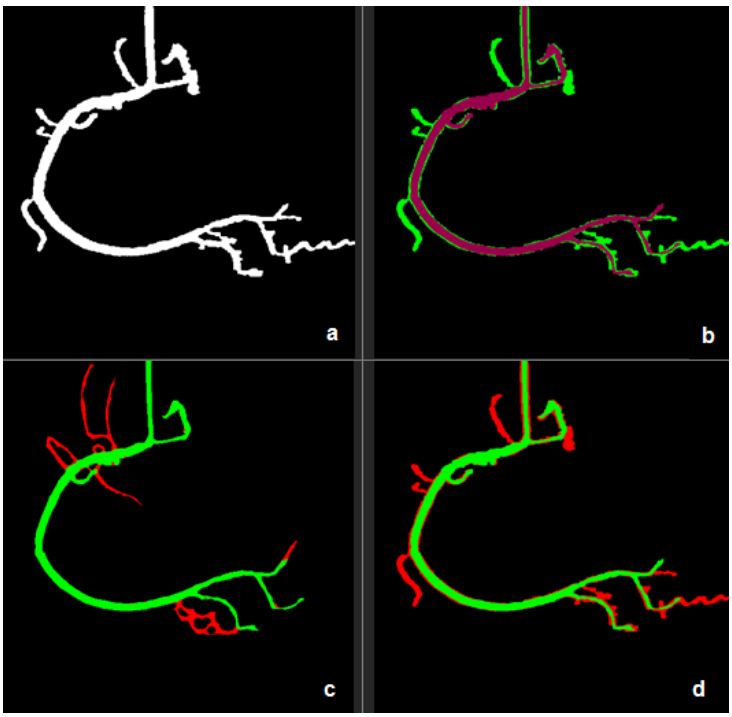

Figure 6.8: Validating RCA. (a) segmented RCA; (b) segmentation accuracy result (73.64%); (c) false negative result; (d) false positive result (Sensitivity: 0.736, miss rate: 0.263 and fall out rate: 0.028.

Table 6.4: Validation results of LAD artery.

File	Mean Segmentation Accuracy	Mean Miss Rate ($Error_{FN}$)	Mean Fallout ($Error_{FP}$)
C0418_12	93.37	0.31	0.052
C0605_09	94.15	0.12	0.054
C0641_14	98.42	0.12	0.012
C0643_10	97.04	0.17	0.023
C0660_11	96.00	0.50	0.008
C0661_12	94.00	0.08	0.060
C0664_07	94.53	0.49	0.020
C0864_10	85.57	0.30	0.130
C0867_10	90.90	0.19	0.081
C0870_08	95.51	0.04	0.046
C0899_07	95.91	0.13	0.038

Table 6.5: Validation results of CX artery.

File	Mean Segmentation Accuracy	Mean Miss Rate ($Error_{FN}$)	Mean Fallout ($Error_{FP}$)
C0413_12	97.25	0.27	0.016
C0418_08	90.14	0.12	0.097
C0522_14	92.73	0.04	0.076
C0605_08	96.30	0.17	0.029
C0641_09	97.19	0.08	0.026
C0643_09	95.98	0.03	0.041
C0660_09	77.91	0.09	0.235
C0664_05	96.00	0.27	0.024
C0666_08	82.56	0.18	0.174
C0864_08	91.33	0.28	0.073
C0870_07	94.04	0.36	0.037
C0897_06	97.38	0.13	0.020
C0899_08	93.98	0.47	0.037

Table 6.6: Validation results of RCA artery.

File	Mean Segmentation Accuracy	Mean Miss Rate ($Error_{FN}$)	Mean Fallout ($Error_{FP}$)
C0413_10	80.86	0.02	0.200
C0418_14	94.55	0.38	0.025
C0522_13	97.21	0.02	0.028
C0605_12	95.97	0.21	0.035
C0641_16	94.82	0.44	0.030
C0643_06	96.91	0.27	0.017
C0660_16	96.18	0.64	0.006
C0661_09	95.68	0.24	0.030
C0664_08	96.91	0.05	0.030
C0666_13	92.32	0.49	0.043
C0864_14	95.90	0.36	0.024
C0867_13	94.28	0.07	0.056
C0870_12	96.29	0.10	0.033
C0897_10	92.40	0.07	0.076
C0899_12	97.92	0.27	0.013

Table 6.7: Validation results summary of segmentation phase.

Artery	Average Segmentation Accuracy	Average Miss Rate ($Error_{FN}$)	Average Fallout ($Error_{FP}$)
CX	0.9252	0.19	0.068
LAD	0.9413	0.22	0.048
RCA	0.9455	0.24	0.043
Average Results	0.9373	0.22	0.053

In order to visually compare the results, a set of visual frames of a sample CCA is depicted in Figure 6.9 and the respective segmentation results obtained for the same CCA is depicted in Figure 6.10.

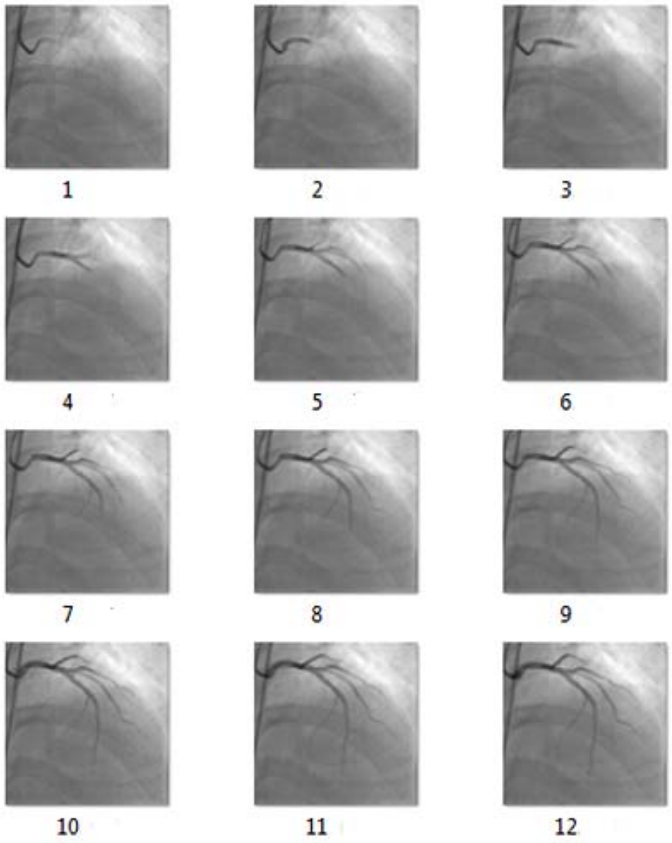

Figure 6.9: Selected visual frames of a sample CCA (LAD).

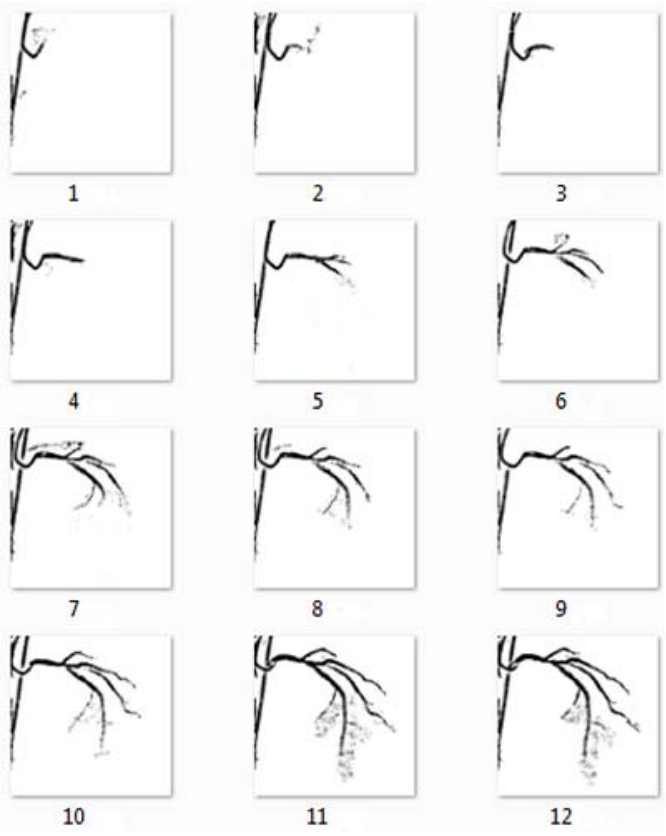

Figure 6.10: Segmentation frames of selected CCA.

6.4 Validation of vessel tracking and quantitative analysis phases

Blood vessel diameter analysis and obstruction analysis are considered as major aspects in quantitative coronary analysis. This section elaborates the validation methods followed to test the vessel path tracking (SPT algorithm) and quantitative analysis (VDC algorithm) algorithms. Moreover, the validation results have been presented to discuss about the technical supportability of the proposed quantitative coronary analysis method. Initially the proposed method has been validated to assess its technical supportability for quantitative coronary analysis and thereafter it is compared with a subjectively assessed clinical data set for evaluating its clinical feasibility. Flowing sections elaborates these validation methods in detail.

6.4.1 Assessment of technical supportability

Technical supportability is defined as the ability to extract the blood vessel features for quantitative coronary analysis. Vessel boundary, vessel skeleton and diameter along the vessel skeleton are considered as important features for determining the quantitative coronary analysis. The ability to extract the aforementioned features of the SPT algorithm and VDC algorithm using a data set of 50 CCAs had been experimentally analyzed. Hence, 24 CCA cases recorded under the LAO Cranial (for RCA) view, 13 CCA cases recorded under the AP Caudal (for CX) view and 13 cases recorded under the AP Cranial (for LAD) view were selected to create the test data set of 50 total CCA cases. The proposed two algorithms were executed for each and every frame in the selected data set separately and the computed values for desired features were logged separately. Calculated diameter distribution along the vessel skeleton was modeled automatically for each frame to determine the abnormalities within the lumen. A visual illustration of it is depicted in Figure 6.11 for clarification.

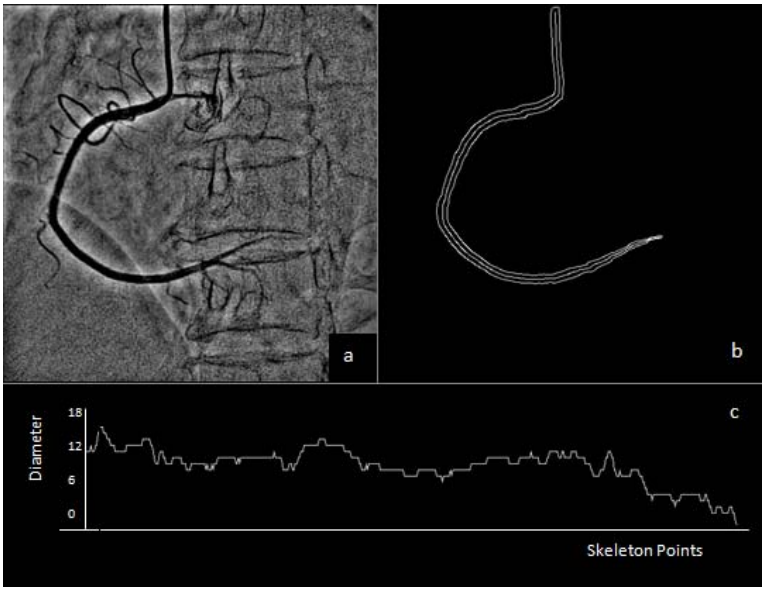

Figure 6.11: Visualizing the lumen features. (a) enhanced CCA frame of RCA; (b) skeleton and boundary detection of the selected vessel segment; (c) diameter distribution along the skeleton.

Percentage of stenosis determination is another demanding aspect in quantitative coronary analysis and this proposed method has addressed this issue successfully. Percentage of stenosis can be computed along the vessel skeleton based on the marked points. It is assumed that cross sections of the lumen of the vessel vary linearly. According to that assumption, the percentage of stenosis has to be determined relative to the line modeled between two end points of the marked stenosis region. Figure 6.12, 6.13 and 6.14 visually illustrate the results of the proposed quantitative analysis phase to determine the technical supportability. Image (a) of Figure 6.12, 6.13 and 6.14 depict three frames of the three selected test cases, which represent LAD, CX and RCA CAs respectively. Moreover, the clinically approved stenosis region is marked in each frame to determine the severity level. Image (b) of Figure 6.12, 6.13 and 6.14 represent the selected, tracked segmented vessel of the respective initial frame. Graph shown in (c) and (d) images of Figure 6.12, 6.13 and 6.14 clearly visualize the diameter variation and stenosis percentage variation along the marked region in selected frames respectively. According to the computed diameter percentage values, RCA stenosis marked in Figure 6.12 reports a maximum stenosis level 56.42%, CX artery stenosis marked in Figure 6.13 reports a maximum stenosis level 59.3% and LAD artery stenosis marked in Figure 6.14 reports a maximum stenosis level 81.11%.

6.4.2 Assessment of clinical feasibility

It is important to determine the clinical feasibility of this proposed quantitative coronary analysis method prior to utilizing it in the clinical procedures for detection and quantifying the stenosis. In order to achieve that goal, the proposed quantitative coronary analysis method was validated using a CCA dataset of 33 patient cases with respective medical diagnosis reports. The data set was created randomly and all the medical judgments recorded in the medical reports have been specified subjectively by the medical experts. Moreover, the subjectively assessed percentage of luminal obstruction and the placement of the stenosis were clearly marked in those selected reports.

During the validation process, the relevant CCA files in the patient cases of the data set are extracted and processed using the proposed method. Subsequently, the percentage stenosis has been determined with respect to the lesions marked in the respective medical report. Finally the computed stenosis severity is ranked according to the criteria mentioned in [40]. According to that, four categories of lesion severity for grading the detected stenosis have been described as follows;

- Stenosis <50% - minimal or mild CA disease
- Stenosis between 50% and 75% - moderate CA disease
- Stenosis between 75% and 95% - severe CA disease
- Stenosis > 95% - total occlusion

The results obtained in this validation process are enlisted in Appendix D. In addition to that, Figure 6.15 presents the summary of stenosis analysis results according to the aforementioned criteria under the subjective analysis method and the objective analysis method, which is proposed in this research study.

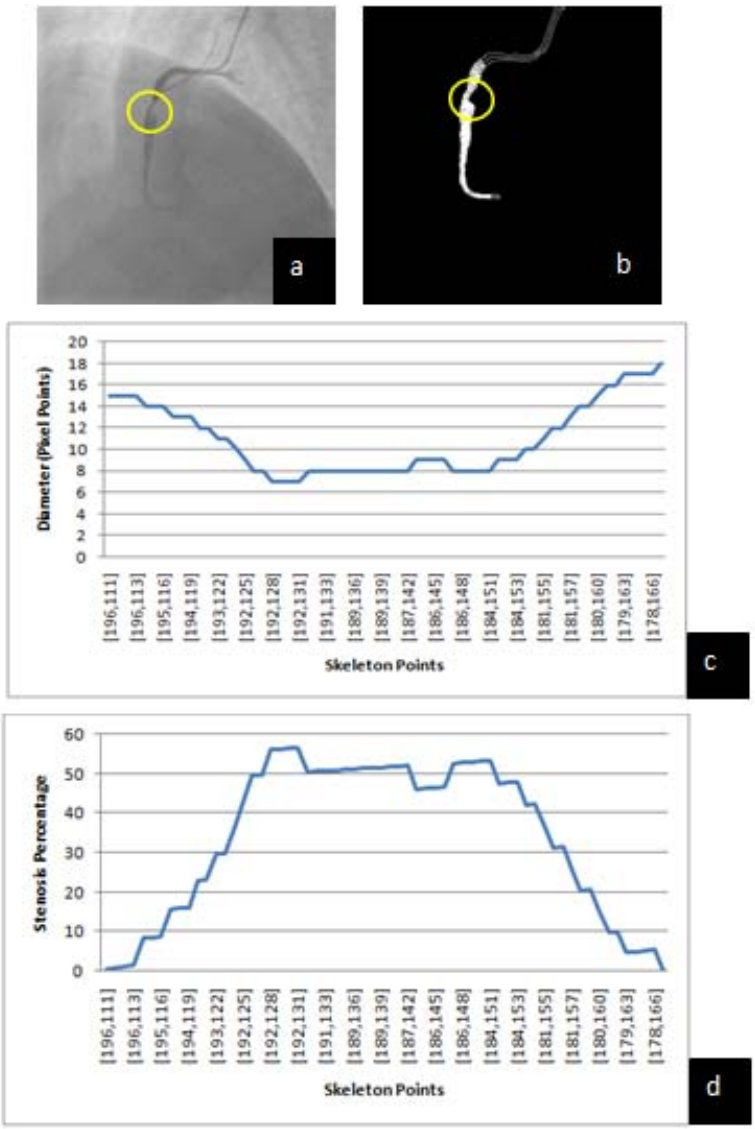

Figure 6.12: Quantitative analysis of RCA. (a) selected direct CCA frame with a stenosis region (stenosis region is circled); (b) selecting a vessel segment and tracking it for feature extraction; (c) vessel diameter variation along the stenosis region; (d) stenosis percentage variation along the stenosis region (Maximum stenosis severity level is 56.42%).

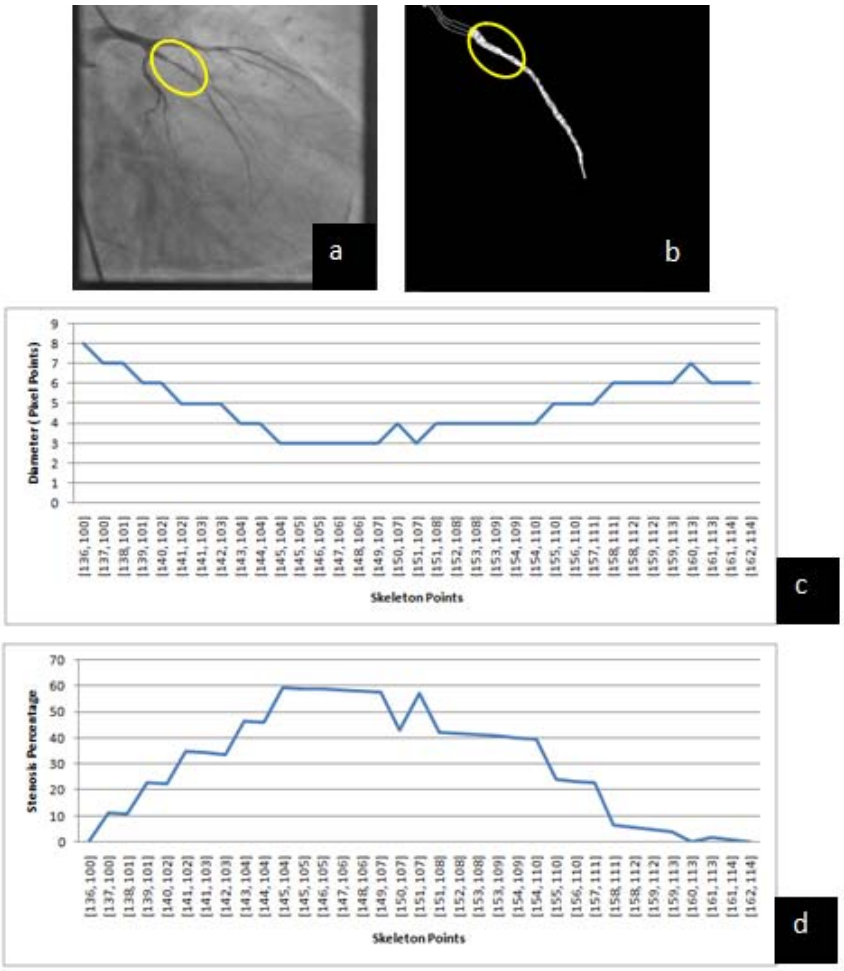

Figure 6.13: Quantitative analysis of CX. (a) selected direct CCA frame with a stenosis region (stenosis region is circled); (b) selecting a vessel segment and tracking it for feature extraction; (c) vessel diameter variation along the stenosis region; (d) stenosis percentage variation along the stenosis region (Maximum stenosis severity level is 59.3%).

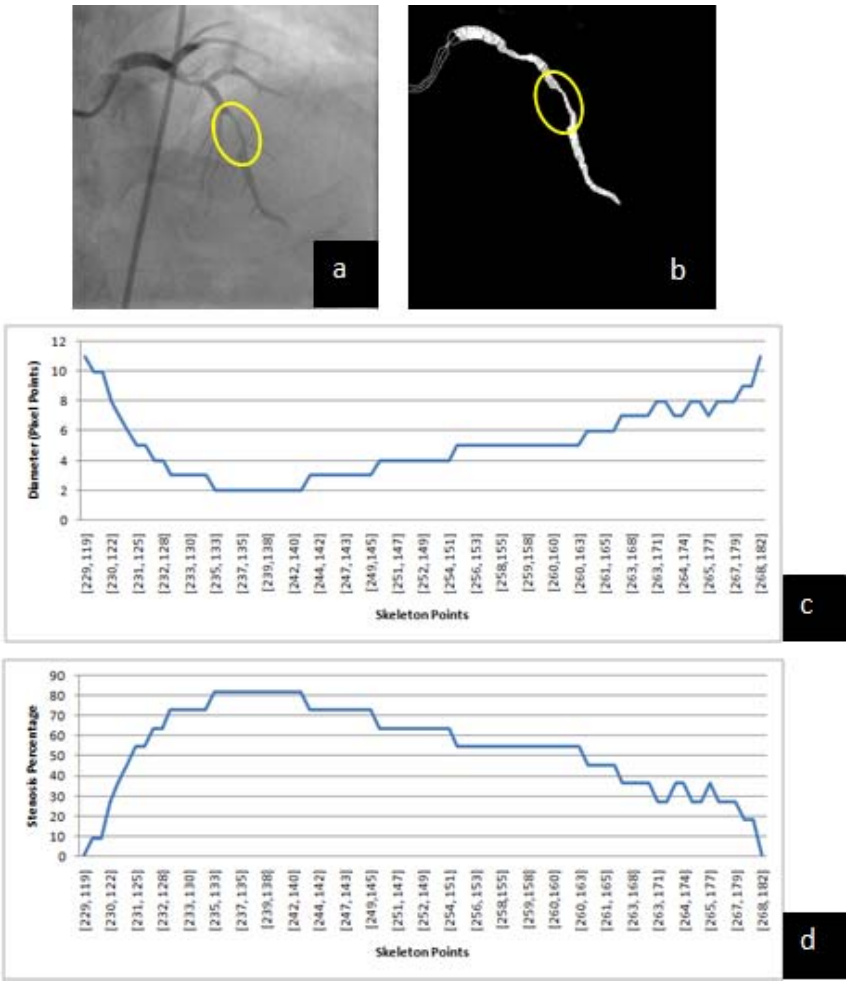

Figure 6.14: Quantitative analysis of LAD. (a) selected direct CCA frame with a stenosis region (stenosis region is circled); (b) selecting a vessel segment and tracking it for feature extraction; (c) vessel diameter variation along the stenosis region; (d) stenosis percentage variation along the stenosis region (Maximum stenosis severity level is 81.11%.).

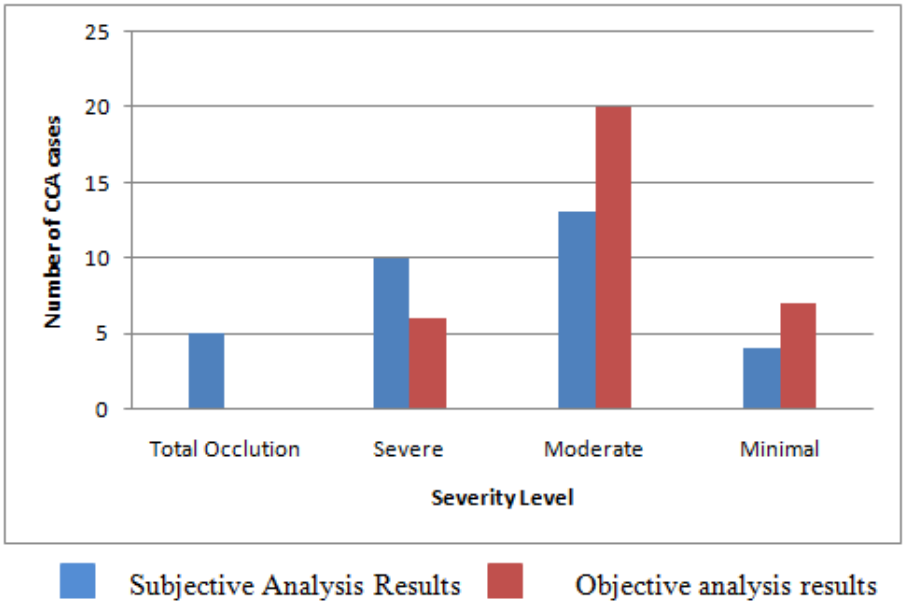

Figure 6.15: Summary of stenosis analysis results.

6.5 Summary

This chapter elaborated the validation methods and results of this study. Main implementation phases of the proposed quantitative coronary analysis method have been tested by using appropriate clinical data sets. Initially, a validation method was proposed for assessing the robustness of the frame alignment algorithm of the pre-processing phase. Subsequently, the accuracy of the proposed segmentation method was evaluated. Validation method proposed for assessing the technical supportability of the SPT algorithm and VDC algorithm is proposed in the latter section of the chapter. Finally, the clinical feasibility of the proposed method has been evaluated by using a subjectively assessed clinical data set. The next chapter critically reviews the results of this proposed quantitative coronary analysis method.

CHAPTER 7
DISCUSSION

The objective of this chapter is to critically discuss about the methodology and results of this research study. The chapter is divided into three sections based on the major implementation phases of the proposed method. Initially, the significant research aspects in the pre-processing phase are discussed. Secondly, the results of the segmentation phase are critically analyzed. Finally, the chapter converses about the results of both SPT and VDC algorithms and the clinical importance of the proposed quantitative coronary analysis method.

7.1 Discussion on the results of pre-processing phase

The proposed pre-processing phase contains two implementation stages namely; frame enhancement and frame alignment, which are directly applied for improving the visual quality of the CCA frames. This section reviews the experimental approaches of frame enhancement and the significant research improvements in the frame alignment stage.

7.1.1 Frame enhancement

In frame enhancement stage, techniques were proposed for reduction of noise and obtaining the uniform illumination in the CCA frames. Section 3.2.2 clearly elaborated that quantum noise and different kinds of electrical noise such as Gaussian and impulse noise as the types of noises that affect the CCAs. Thus, to reduce Gaussian and impulse noise most of the studies done in recent past have recommended to apply the Gaussian smoothing and median filtering operations respectively [54][57][64][65][68][69]. Hence, those reported smoothing techniques have been directly used even in this study to obtain the required enhancement of the CCA frames. Moreover, median filtering has been applied during the frame enhancement stage and Gaussian smoothing has been applied during the creation of directional second order partial derivative images in the segmentation phase.

The contrast of the CCA frames has been obtained by eliminating the unnecessary illumination frequencies and applying the normalization function mentioned in (1.9). The resulting enhanced frames are clearly depicted in Figure 3.7. Lara and team have used CLAHE method as the contrast enhancement technique in their proposed angiography segmentation study [54]. Even though CLAHE stretches the contrast of the image to obtain the visual quality, it cannot remove illumination frequencies recorded in the angiogram images, which cause the degradation of visual quality in the CCA frames. Moreover, it amplifies the noise signals in the CCA frames [101].

Figure 7.1 visually illustrates the consequences of various image enhancement methods after applying them for a direct CCA frame. Figure 7.1(b) depicts the adaptive thresholding result of direct CCA frame shown in image (a). It is difficult to determine the uniform threshold values for implementing the adaptive thresholding in order to eliminate non-uniform illumination recorded in CCA frames. Non-uniform threshold values causes failures or loss of spatial connectivity of the vessel structures and it leads to incorrect segmentation. Figure 7.1 (c) depicts the results obtained after applying the CLAHE technique to the direct CCA frame in image (a). This image clearly shows that the application of CLAHE does not only enhance the desired foreground region, additionally it has enhanced the non-uniformly illuminated background as well. Figure 7.1 (d) depicts the enhancement results provided by the proposed system. This image has deemphasized the illumination in the original image and preserved the whole vessel structure as it can be visualized in a clear manner.

Non-uniform illumination is a definite visual degradation effect recorded in the CCA frames and in this proposed enhancement method, the homomorphic filter has been applied to cut off the frequencies, which are responsible for the illumination. As a result of that, it would be possible to save the frequencies, which are reflected from the desired objects significantly. Hence, the pre-processing phase of this proposed method provided excellent results than using only CLAHE method. Additionally, this homomorphic filter based enhancement does not amplify the noise components in the frames to be processed because it performs the frame enhancement by subtracting unnecessary frequency bands from the original frame. Figure 3.7 depicts

the sample frame enhancement results for visually analyzing the results. By analyzing those given frames, it can be concluded that this proposed frame enhancement method provides better visualization of the CA vasculature without any loss to the quality of the image. Further, the original dimensions of the vascular structures are also being preserved within this enhancement technique and it is a mandatory requirement for subsequent quantitative coronary analysis.

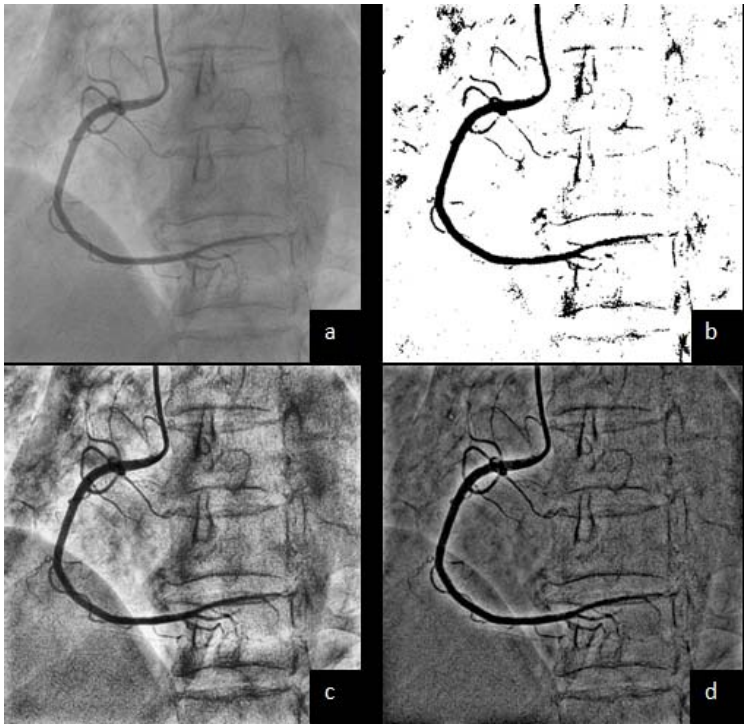

Figure 7.1: Effect of enhancement methods. (a) direct CCA frame; (b) application of adaptive thresholding method; (c) application of CLAHE method; (d) application of the proposed method.

7.1.2 Frame alignment

The proposed frame alignment stage has been implemented using an image registration technique called template matching [95]. The conventional template matching matches the given template with the reference image by checking the spatial resemblance of intensities and the matching features must not be isotropic and scale invariant. Therefore, in conventional template matching the visual contents in

the matched templates are also similar apart from the spatial intensity similarity of those matched regions. However, this fact fails in some template matching instances of this study. This failure was clearly emphasized in the empirical results given in Table 6.2. This Table 6.2 enlisted the number of correct (positive) template matching instances obtained for the selected data set according to the conventional template matching approach. Moreover, it has been reported that 1259 steps out of 1372 total template matching steps have been reported as positive matches and as a percentage, it is denoted at 91.76%. Even though this conventional template matching provides the highest positive matching rate, empirical results have shown that it possesses 8.24% chance of having false matching instances. However, it is important to note that all of these matching instances are almost correct according to the conventional template matching measurements because it is based only on the spatial resemblance of intensities but some of these matching instances are unacceptable according to this study because, those matching instances do not have the visual content resemblance among the matched templates. Figure 3.11 clearly emphasized this problem. The main reasons for obtaining these false matches are the occurrence of radial motion artifacts in vessels and contrast agent concentration variation among the frames. Therefore, it leads to rapid spatial differences between the template and the match region in the reference frame as shown in Figure 3.11. Moreover, these false matches incorrectly stabilize CCAs and create some impediments in obtaining the desired visual co-relation.

In order to overcome the aforementioned false matches problem, an algorithm has been implemented to detect and correct the false matches in template matching and this is a major improvement suggested to advance the results provided by the conventional template matching technique. According to this proposed algorithm, false matches are detected based on the displacement of the matched templates and HOG descriptor because, it has been experimentally observed that some false matches contain rapid distance displacements and some false matches contain shape dissimilarities between the matched templates. As depicted in Figure 3.14, HOG descriptor was used to determine the shape dissimilarities and was computed based on the segmented vessel regions depicted in the matched templates.

This improvement is clearly emphasized by the results shown in Table 6.3. According to the results, 1337 steps out of 1372 total template-matching steps were reported as positive matches and as a percentage, it is denoted as 97.45%. Hence, it improves the conventional template matching accuracy by 5.69% so that it can be adapted for matching the deformed structures represented in CCAs. The analysis results depicted in Figure 6.4 have further revealed this improvement of obtaining the positive template matching occurrences according to the selected angiography views. Hence, it can be concluded that the percentage improvement of obtaining positive template matching instances according to the selected angiography views is as follows; LAO cranial view of RCA: 6.14%; AP caudal view of LCA: 6.65%; AP cranial view of LCA: 4.22%. According to the experimental results, it has been revealed that the proposed adaptive template matching approach provides the matching results by considering both spatial intensity and feature resemblance among the reference and matched templates. Therefore, unlike the conventional template matching, this novel adaptive template matching method can tolerate the structural deformations in matching image significantly and provide visually acceptable matching results. This is the major improvement that has been suggested for the conventional template matching as a result of this research study, so that the templates from the angiograms can be adaptively matched with deformed vessel structures.

The global motion stabilization phase of the proposed method can provide the expected content alignment of the vessel structure (foreground) among the frames. This can be visually judged by looking at the catheter engaged area of both original and stabilized frame sequences shown in Figure 3.15. The catheter engaged area is marked as a white square and according to the results, motion stabilized frames depict catheter engaged area in a fixed location. This happens as a result of reconstructing the frame by eliminating global motion. This frame reconstruction is done based on the calculated motion vector. Hence, it is possible to detect the larger motion gaps and eliminate them significantly. As a result of that, continuous and smooth contrast agent flow within the vessel structure is visualized starting from the catheter engaged point. Obtaining this visual correlation among the CCA frames can

be used for segmentation of blood vessels among the CCA frame sequence starting from a fixed seed point. Hence, the visual co-relation among the CCA frame sequence obtained as a result of this study can be considered as an improvement suggested for the coronary angiography image modality.

Similar research work has been reported in a recent study and it has described global motion stabilization of CCAs using SIFT feature descriptor [57]. According to their study, the GMV has been determined based on SIFT feature matching between the two consecutive frames. It has been empirically observed that SIFT provides many miss-corresponding key point pairs in angiography as depicted in Figure 7.2. This illustration clearly emphasizes that most of the detected feature points are located in the background and that the detected feature points in vessel structures have not perform correct feature matching with the corresponding frame for all detected feature points. As a result of that, it provides erroneous GMVs for motion compensation.

Figure 7.2: SIFT feature matching.

Literature has expressed the application of optical flow based approaches for motion stabilization in angiograms [58]. Optical flow based approaches can change the geometric representation of the structure of the CA tree during the transformations applied for motion compensation. This artifact is clearly depicted in Figure 7.3.

Green lines in image (a) of Figure 7.3 represent the motion vectors calculated between the current frame and the previous frame and image (b) of the same image represents the motion stabilized frame. Comparing with the input frame this resulting frame emphasized the deformation in the viewport due to the transformation applied in motion compensation. As a result of that, the geometric representation of the vessel structure is changed and causes some obstructions in vessel segmentation phase.

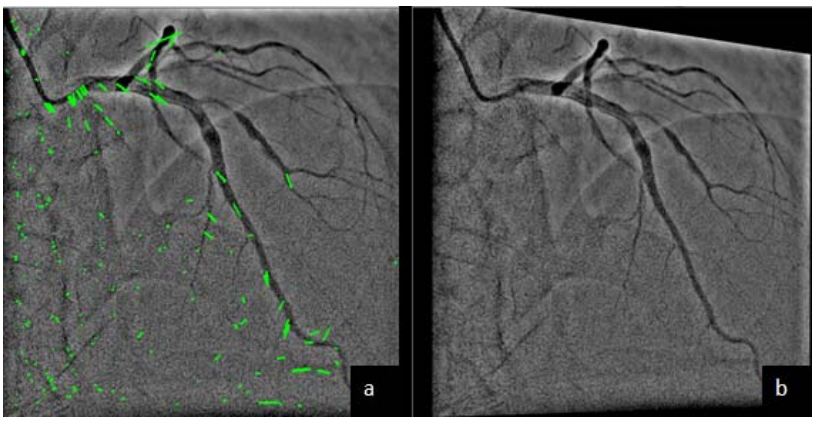

Figure 7.3: Effect of optical flow.

This proposed method works successfully with the camera motion free CCAs. Due to the camera motion, the template area can be shifted out from the view port in some matching instances and reconstruction of global motion reduction frame becomes highly difficult in such situations. Hence, it is necessary to input camera motion free CCA to this algorithm to obtain successful results.

7.2 Discussion on segmentation results

The vessel segmentation method that proposed in this study is mainly based on the spatial filtering and region growing approach. In order to perform the spatial filtering, Frangi's vessel enhancement filter was used and image morphological operations were used with the region growing. This section will critically discuss about the significance of applying Frangi's filter for the proposed segmentation method and the validation results of it.

7.2.1 Application of Fangi's filter

Frangi's filter will remove noise in digital images and improve the tubular structures in the digital image. Hence, it becomes the most important technique for determining the vesselness feature of the digital processing of angiograms. The theoretical foundation of the Frangi's filter has been mentioned in section 2.5.2.

Frangi's filter is implemented based on the second order partial derivatives of the input image and it can be calculated by convoluting the input image with a Gaussian kernel. It produces the second order four directional images based on the gradient variation along the horizontal, vertical and two diagonal directions of the input image and section 4.2.2 has clearly mentioned about the implementation steps of it. It is important to note that the image noise will be eliminated significantly during this calculation because of Gaussian smoothing.

Moreover, these resulting second order derivative images are used to determine the vesselness feature based on the Frangi's filter and it is done by using the Eigen values obtained by calculating the Hessian matrix. Section 4.2.3 clearly mentioned about the implementation steps of the Frangi's filter. Moreover, this filter removes the background anatomical structures such as ribs, diaphragm, spine and heart chambers recorded in the CCA frame to be processed. Hence, it will reduce the obstructions, which occur during the foreground extraction of the segmentation phase. This improvement is clearly depicted in Figure 7.4. Image (a) of Figure 7.4 depicts a direct CCA frame and it depicts the diaphragm and spine as the background structures. Figure 7.4 (b) depicts the pre-processed CCA frame and it visualizes the enhanced background anatomical structures clearly. Figure 7.4(c) depicts the second order derivative image (Gaussian smoothen image) of the same CCA frame depicted in image (a) and it highlights the vessel structures and the edges of the background anatomical structures only. Finally, Figure 7.4(d) depicts the Frangi'filtered results. Moreover, it has enhanced the tubular structures, which belong to the vessel network and the background structures have been greatly deemphasized in Figure 7.4 (d).

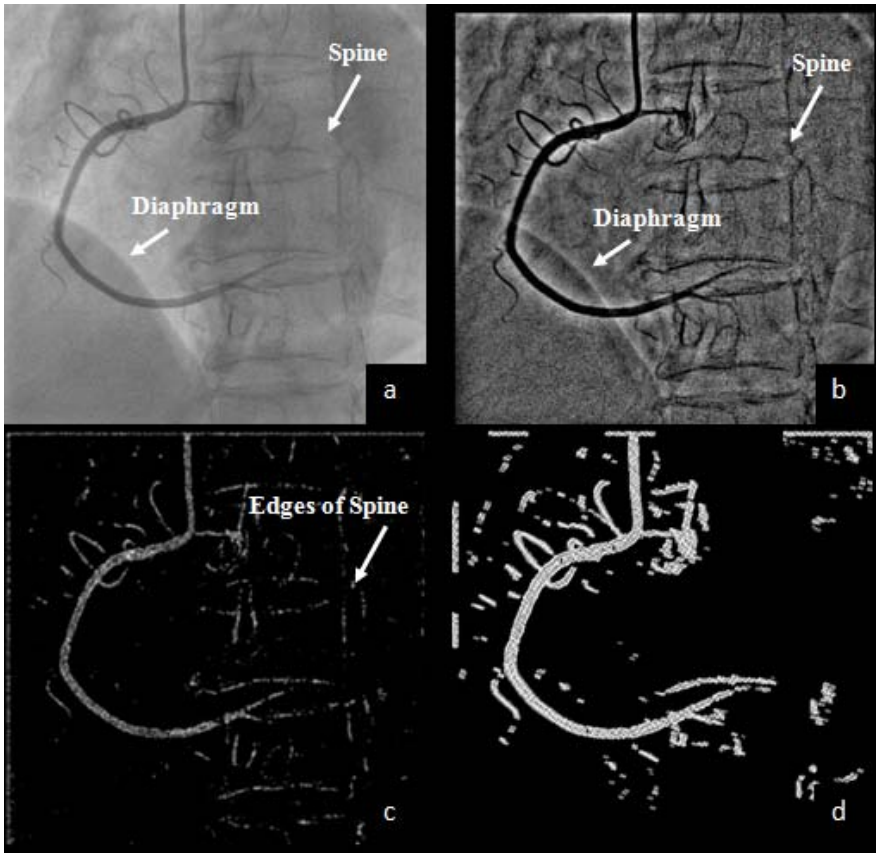

Figure 7.4: Effect of Frangi's filter. (a) direct CCA frame; (b) enhanced CCA frame; (c) Gaussian convolution result; (d) Frangi filtered image.

7.2.2 Discussion on segmentation results

The statistical evaluation method of the proposed segmentation method is given in section 6.3. Additionally, Table 6.4, 6.5 and 6.6 enlist the statistical evaluation results of the proposed segmentation method in accordance with the selected angiography views. According to those results CX, LAD and RCA arteries are successfully segmented and consist of 92.25%, 94.13% and 94.55% segmentation accuracy respectively. Moreover, in relation to Table 6.7, this proposed segmentation method possesses 93.73% average segmentation accuracy for extracting the needed vessel regions. Furthermore, an average miss rate ($Error_{FN}$) of 0.22 is reported with an extremely low fallout rate ($Error_{FP}$) of 0.05%. Hence, it can be concluded that this proposed segmentation method completely extracts almost complete CAs vasculature

containing the input CCA frame. This factor is further proven by the visual results depicted in Figure 6.10, which are generated using the complete CCA case depicted in Figure 6.9.

The result of the proposed segmentation method has been compared with the recent research study done by Lara et al [54]. They have proposed a semi automatic region growing segmentation method for extracting the angiography vessel structures and evaluation results of that study have proven that it has 87.58% of accuracy. However, the proposed segmentation method of this study possesses an accuracy level of 93.73% and emphasizes the segmentation strength beyond the existing recent direct coronary angiography segmentation methods.

Further, the empirical results have revealed that this proposed segmentation method failed to extract major vessels under the poor intensity conditions. Following requirements have been identified that cause some obstructions to obtain the successful segmentation results: (1) visualizing contrast agent flow within a lower intensity depth of input CCA, (2) projecting overlapped vessels to minimize the ambiguities of the structure, and (3) recording angiograms with noisy background during the angiography procedure; e.g. tolerance of quantum noise. Figure 7.5 (a) depicts a sample CCA frame, which contains a disconnected vessel tree from the catheter and Figure 7.5(b) depicts a CCA frame, which represents overlapped vessel tree. Having disconnected vessels in CCA frames does not segment the whole vessel tree beyond the disconnected point and overlapped vessels cause some ambiguities in recognizing the arterial branches separately.

7.3 Discussion on results of vessel tracking and quantitative analysis

Identification of vessel boundary, skeleton and the diameter are considered as the major factors for quantitative coronary analysis. Further, this information can be used to compute the anatomical variations of the selected vessel structure. The proposed vessel skeleton tracking algorithm (SPT algorithm) can track the marked vessels' skeleton starting from the catheter engaged point to the end of the skeleton and the pixel tracking gap is equal to the single pixel width. Hence, it can track all pixel points along the vessel skeleton.

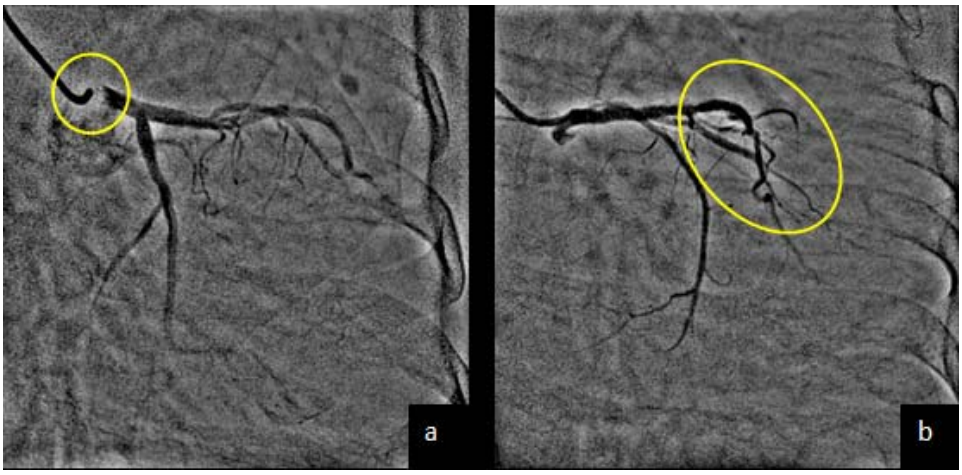

Figure 7.5: Constraints affected for segmentation phase. (a) vessel disconnections; (b) vessel overlapping.

Further, these tracked points are used to calculate the vessel diameter and it is based on segmented vessel geometry. As a result of that, it can calculate the vessel diameter based on each and every pixel points according to the tracked vessel skeleton. Three visual illustrations depicted in Figure 5.7, 5.8 and 5.9 visualize the aforementioned facts clearly. Those figures have clearly depicted the detected vessel structural features such as boundary and skeleton and the diameter calculation through the tracked vessel skeleton of LAD, CX and RCA arteries consecutively. In addition to that, Figure 5.10 has labeled the computed vessel diameter along the vessel skeleton to prove the clinical supportability of this proposed quantitative coronary analysis method. The complete vessel diameter variation along the vessel skeleton is also depicted in Figure 6.11 (c) and the analysis of valleys in this diameter distribution signals the suspected areas within the processed arterial segment.

Determining the percentage of stenosis diameter is another key assessment in quantitative coronary analysis and is addressed in this research study. Figure 6.12, 6.13 and 6.14 have emphasized this aspect clearly. Clinically approved stenosis areas detected in RCA, CX and LAD arteries are highlighted in image (a) of Figure 6.12, 6.13 and 6.14. Graphs depicted in image (c) of Figure 6.12, 6.13 and 6.14 represent

the variation of vessel diameter along the marked diseased region. According to the results, average diameter at the stenosis starting point ($Avg(D)$) and the minimum diameter ($Min(D)$) of these illustrated CAs are as follows; RCA: $Avg(D)$ = 15 pixel points , $Min(D)$ = 7 pixel points; CX: $Avg(D)$ = 8 pixel points , $Min(D)$ = 3 pixel points; LAD: $Avg(D)$ = 11 pixel points , $Min(D)$ = 2 pixel points. Apart from that, graphs shown in image (d) of Figure 6.12, 6.13 and 6.14 indicate the percentage of stenosis diameter variation along the marked diseased region. According to the results, the maximum percentage stenosis diameter at the minimum diameter point ($Min(D)$) of these illustrated CAs are as follows; RCA = 56.42%, CX = 59.3% and LAD = 81.11%. According to these results, RCA and CX arteries have moderate severe stenosis and LAD artery has severe stenosis.

The clinical supportability of the image processing system implemented in the existing commercial angiography machine has been analyzed and the image processing system used by the Philips Medical Systems has been used for this study. Similar to the method proposed in this study, those commercial systems have been implemented with semi-automatic segmentation and quantification method. However, some of the failures that occur in segmentation processes have been identified by it and those failures cause some obstructions in calculations. Figure 7.6 has illustrated two scenarios of observed failures that exist in the aforementioned image processing systems of the selected angiography machine.

Further, it is important to highlight that the objective analysis results of this proposed method totally depend on the segmentation accuracy because the SPT algorithm and VDC algorithm have been implemented upon the segmented vessels' structure and geometry. Though the proposed segmentation method provides high segmentation accuracy for segmentation of all three types of main CA, accuracy of the proposed quantitative analysis methods have been improved.

Affectivity between the subjective analysis and objective analysis of the detected stenosis can be clearly compared using the results enlists in Appendix D. It has emphasized the overestimations and underestimations occurred in subjective stenosis assessment compared to the objective assessment results. According to that, in the

selected dataset, there are 25 CCA cases, which have been reported as overestimations and 8 cases, which have been reported as underestimations compared to the objective assessment results. Additionally, there were 5 cases marked as total occluded stenosis in the subjective assessment and this severity level has been changed in objective analysis approach. 13 cases out of the data set have been categorized in to the same severity level during the objective assessment, which represents 39% of the selected patient cases. Summary of stenosis analysis results depicted in Figure 6.15 also emphasizes this matter further and according to the graph, a large number of CCA cases are ranked in the moderate severity level and the number of CCA cases, which are ranked under the total occlusion and sever categories is minimal. Hence, it emphasizes the importance of having an accurate objective stenosis assessment method in interventional cardiology, because most of the subjective assessment results are erroneous.

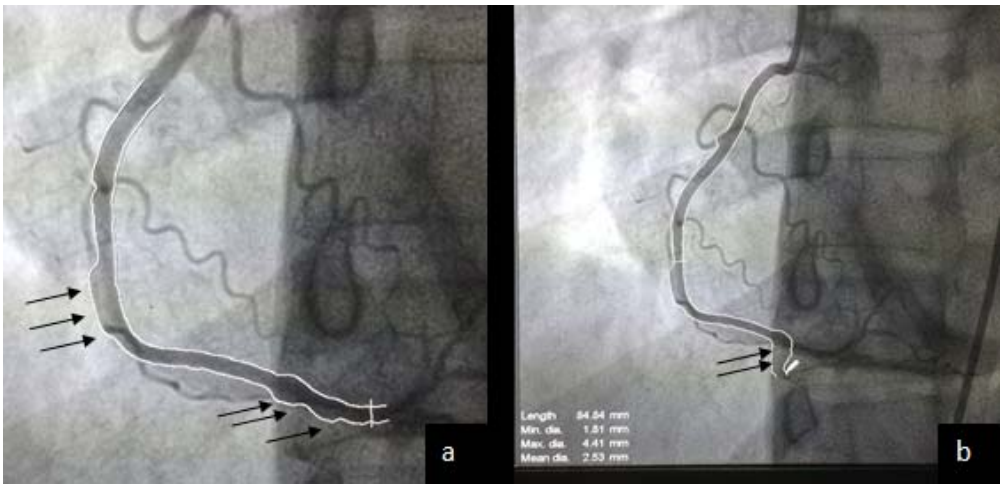

Figure 7.6: Drawbacks in image processing systems of commercial angiography machines. (a) incorrect boundary detection of vessels; (b) segmenting background structures as foreground (arrow heads indicate the problematic region, Manufacturer: Philips Medical Systems.).

Haris et al. mentioned the application of circular filtering for local search to track the CA vasculature in their research study [84]. Further, it has been declared that the vessel diameter can be extracted by calculating the greatest axis of the modeled

ellipse in circular filtering that better adjust with the pixels located at the vessel border. This approach is erroneous because the diameter line drawn based on opposite two vessel boundary intersection points are not perpendicular to the vessel centerline. Moreover, it is disparate from the proposed method of this study because it cannot produce diameter values for single pixel gaps along the vessel central line.

Active contour model based vessel segmentation method has been proposed by Lin and Ching [26]. In this study, they have used GVF to locate the medial axis of the vessel. It calculates the vessel diameter by modeling the perpendicular lines to opposite side boundaries after detecting medial axis of the vessel. However, some awkward results are produced when the snake model is used to obtain the correct medial axis of the vessel. Instead of snake model, image thinning has been used in this study for detection of the medial axis of the selected vessel segment. It provides accurate results for diameter calculation because the proposed segmentation method possesses high segmentation accuracy.

7.4 Way forward to determine the functional significance

Determining the stenosis severity based on the functional significance is another novel approach that can be considered based on the quantitative results obtained from this study. According to the vessel physiology, the amount of blood that flow through the blood vessel (also known as blood flow – q) depends on the pressure gradient (Δp) of the blood vessel and the resistance (R) as shown in the equation (7.1).

$$q = \frac{\Delta p}{R} \tag{7.1}$$

Where;

$$R = \frac{1}{r^4}$$

Where, r indicates the radius of the vessel. In accordance with equation (7.1) the blood flow increases when the resistance decreases and vice versa. Alternately, the resistance is increases when the radius decreases and vice versa. Hence, it can be stated that the blood flow resistance is low and therefore the blood flow is high before the stenosis area. Moreover, the blood flow resistance is high and blood flow is low within the stenosis area. Graph shown in Figure 7.7 clearly emphasizes this aspect. It has indicated the blood flow resistance variation along the skeleton points of the clinically approved stenosis region shown in Figure 6.14 (a). Here the calculated flow resistance is normalized within the range *0-100* to represent it with the distribution of stenosis diameter percentage. This graph clearly represents the increasing of flow resistance when the percentage of stenosis increases and decreasing of flow resistance when the percentage of stenosis decreases. Based on these results, it is possible to implicitly detect the co-relation between the blood flow variation within the arteries and diameter of the lumen.

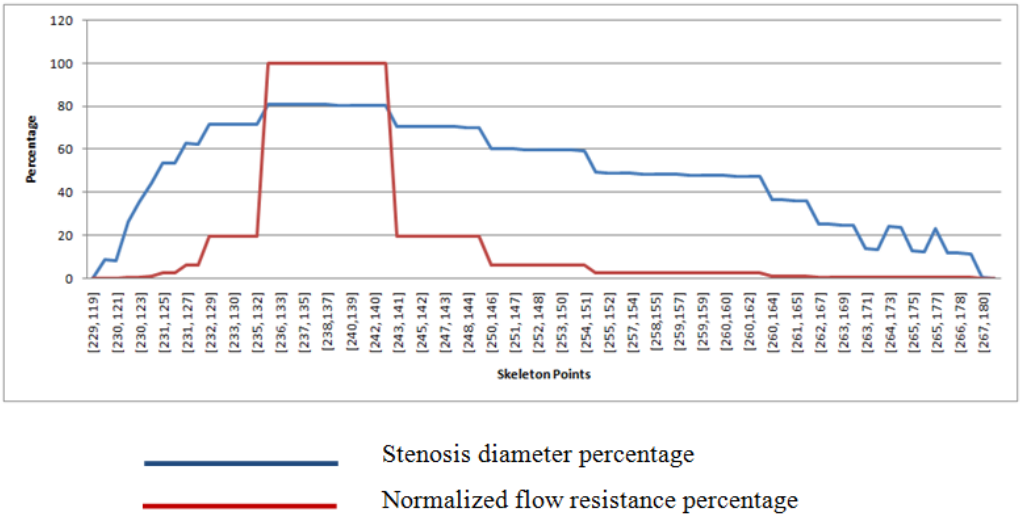

Figure 7.7: Flow resistance in stenosis region.

Flow velocity defines how fast blood is flowing within the arteries and it is the best measurement to determine the functional significance of the arteries. Moreover, the blood flow velocity (v) relates with the blood flow (q) and total cross sectional area (a) of the artery as shown in the equation (7.2);

$$v = \frac{q}{a} \tag{7.2}$$

The flow velocity can be defined as the distance that the contrast agent floods per unit time. The runtime of the angiogram is a known factor and the distance that the contrast agent floods can be determined as the length of the skeleton increased throughout the frame sequence. Based on this approach the flow velocity of the contrast agent flooding within the angiogram can be determined through an image processing approach. However, it has been realized that only 6- 15 frames are responsible in representing the contrast agent flooding within the complete CA vasculature. This will be insufficient to determine the flow velocity at each point along the skeleton of the CA being processed and it is not practical to increase the frame rate to obtain additional frames to approximate the flow velocity for each and every point of the vessel skeleton due to the patient being exposed for high radiation. However, it is apparent that there is great potential to apply the algorithms implemented in this study to determine the functional significance of the CAs by using the image modalities like biplane angiography. In biplane angiography, the traditional angiography procedure is used and additionally, it produces the images of the CAs in multiple angles. Using the images provided by all of those angles it is possible to construct the three dimensional representation of the CA network and more accurately determine the functional features using the three dimensional anatomical information. This scenario could be worked out in the future extensions of this current research study.

7.5 Summary

This chapter critically discussed about the significant aspects of the proposed method and the validation results of it. Initially the important aspects of frame enhancement and frame alignment stages of pre-processing phase were elaborated. The importance of implementing the segmentation method based on Frangi's filter and its evaluation results have been discussed subsequently in the chapter. Moreover, the chapter has emphasized the clinical supportability and usability of the proposed quantitative coronary analysis phase. Finally, the potential of using the obtained quantitative results for determining the functional features of the CAs had been mentioned.

CHAPTER 8
CONCLUSION AND RECOMMENDATIONS

This study introduces a quantitative coronary analysis method by using a computer vision technique to objectively assess CA disease. In order to achieve the research objectives the proposed method consists of four major implementation phases namely; pre-processing, segmentation, vessel tracking and quantitative analysis. All the stated research objectives have been successfully implemented and validated. Following sections elaborate the progress and completion of the research objectives and future research activities.

Enhancement of the CCA for better visualizing the CA vasculature:

Within the pre-processing phase, homomorphic filter based frame enhancement technique was presented and empirical results have proven that it provides better contrast to visualize the CA tree apart from some of the widely accepted conventional approaches like CLAHE and adaptive threshold. Moreover, the direct CCA frames were further improved to obtain the visual alignment of the arterial flow visualized in the CCA frames sequence by removing the global motion artifact. The proposed method was implemented based on improved template matching that can adapt to the vessel deformations. According to the results, a template matching accuracy of 97.45% is reported while conventional template matching has an accuracy of 91.76% in angiography domain.

Segmentation of the CA vasculature for extracting the luminal information:

The content aligned enhanced CCA frames produced within the pre-processing phase would extend the research further to obtain the co-related segmented CAs recorded in the CCAs. In order to achieve that, a novel vessel segmentation method has been proposed. It is based on Frangi's vessel enhancement filter and a region growing segmentation method known as flood fill. Frangi's filter is empirically proven and is a strongly recommended filter for vessel enhancement. The main vessel regions recorded in the CCA were completely segmented through this proposed method. Moreover, the experimental results have successfully proven that this proposed

segmentation method possess average segmentation accuracy of 93.73% and a lower fallout rate, which is 0.053.

Development of an algorithm for detecting uniformly deposited atherosclerotic plaque within a predefined region of the CA captured from the CCAs:

Two new algorithms have been implemented for vessel path tracking (SPT algorithm) and vessel diameter calculation (VDC algorithm) for detection of uniformly deposited atherosclerotic plaque within a predefined region of the CA. The proposed method is based on line-tracking and segmented vessel's geometry. It can compute the diameter of the selected vessel starting from the catheter engaged point and the stenosis diameter percentage. LAD, RCA and CX arteries recorded in the CCA were validated through this proposed method and experimental results have successfully proven its clinical supportability and usability.

Visualizing the severity level of the plaque detected as a supportive tool for making treatment decisions:

The quantitative analysis phase of the proposed method is the important component to achieve this study objective. The implemented coronary analysis algorithms can visualize the diameter variation along the processed vessel structure. Further, it visualizes the stenosis diameter percentage within the diseased vessel segments. Therefore, the algorithms developed in this research study can be used to compare the subjectively determined stenosis severity during the cardiac clinical procedures as a supportive tool.

Based on the results and discussion of this study, it can be concluded that this proposed methodology improves the angiography modality and permits to extract the quantitative details of the CA vasculature. Moreover, the proposed frame enhancement method could be able to eliminate the visual degradations recorded in the CCAs significantly and provides the visually enhanced, uniformly illuminated, better contrast images as the output. Adaptive template matching based motion stabilization method proposed in this study can reduce the global motion recoded in the CCA frames significantly and improve the visual alignment of the vessel

structures among the frame sequence of the CCA frames. This feature is greatly important to automatically determine the seed point for vessel skeleton tracking in the quantitative coronary analysis phase of the proposed method. Moreover, the proposed segmentation method can extract the complete vasculature depicted in the frame sequence of the CCA to be processed and the proposed quantitative analysis phase can calculate the vessel diameter along the mark vessel skeleton for a single pixel gap.

Future work

The quantitatively analyzed anatomical features such as vessel diameter, boundary and skeleton can be used for assessing the functional significance of the CAs. The potential of such an implementation has been clearly elaborated in section 7.4. However, it has been realized that the number of frames that can be extracted from the direct angiography for determining the functional significance is minimal. Moreover, it has been observed that there are only 6-15 frames, which are responsible for representing the contrast agent flooding within the complete CA vasculature in angiography, which is inadequate to determine the functional significance of CAs.

It is possible to extend this research towards a different angiography technique such as biplane angiography because it provides more views of CA vasculature under different angles. Hence, it has the potential to model the whole CA network in three-dimensional space and to determine the internal flow variation based on the concepts of computer vision, vessel physiology and fluid dynamics. Therefore, it can be concluded that the results provided by this study lay the foundation to implement a mechanism to determine the functional significance of the segmented vessel regions based on the flow velocity and it could be the next extension of this research.

REFERENCES

[1] W. Anne and G. Allison, *Ross and Wilson Anatomy and Physiology in Health and Illness*, 11th ed. Edinburgh; New York: Churchill Livingstone, 2010.

[2] A. Shaw, B. Smith, and D. C. Howlett, "Axial CTA of the heart," in *FRCR Part 1 Anatomy Mock Examinations*, Cambridge University Press, 2011, p. 61.

[3] W. F. Boron and E. L. Boulpaep, "The heart," in *Medical Physiology, 2e Updated Edition: with Sudent Consult Online Access*, Elsevier Health Sciences, 2012, p. 581.

[4] J. T. Dodge, B. G. Brown, E. L. Bolson, and H. T. Dodge, "Intrathoracic spatial location of specified coronary segments on the normal human heart. Applications in quantitative arteriography, assessment of regional risk and contraction, and anatomic display," *Circulation*, vol. 78, no. 5 Pt 1, pp. 1167–1180, Nov. 1988.

[5] D. S. Baim, *Grossman's Cardiac Catheterization, Angiography, and Intervention*. Lippincott Williams & Wilkins, 2006.

[6] R. J. Myerburg and M. J. Junttila, "Sudden cardiac death caused by coronary heart disease," *Circulation*, vol. 125, no. 8, pp. 1043–1052, Feb. 2012.

[7] W. H. Organization, "Causes of death," in *The Global Burden of Disease: 2004 Update*, World Health Organization, 2008, pp. 7–26.

[8] Y. Yang, "Image segmentation and shape analysis of blood vessels with applications to coronary atherosclerosis," Georgia Institute of Technology, Atlanta, Georgia, 2007.

[9] R. Blankstein, "Introduction to noninvasive cardiac imaging," *Circulation*, vol. 125, no. 3, pp. e267–e271, Jan. 2012.

[10] "Stress echocardiography: MedlinePlus Medical Encyclopedia." [Online]. Available: https://www.nlm.nih.gov/medlineplus/ency/article/007150.htm. [Accessed: 14-Feb-2016].

[11] R. Mastouri, S. G. Sawada, and J. Mahenthiran, “Current noninvasive imaging techniques for detection of coronary artery disease,” *Expert Rev. Cardiovasc. Ther.*, vol. 8, no. 1, pp. 77–91, 2010.

[12] R. Cardona and G. Gunabushanam, “Myocardial perfusion SPECT: background, indications, contraindications,” *MedScape*, Jul. 2014.

[13] “Single Photon Emission Computed Tomography (SPECT).” [Online]. Available: http://www.heart.org/HEARTORG/Conditions/HeartAttack/SymptomsDiagnosisofHeartAttack/Single-Photon-Emission-Computed-Tomography-SPECT_UCM_446358_Article.jsp#.Vr_-f7R951s. [Accessed: 14-Feb-2016].

[14] N. R. Mollet, F. Cademartiri, and P. J. de Feyter, “Non-invasive multislice CT coronary imaging,” *Heart*, vol. 91, no. 3, pp. 401–407, Mar. 2005.

[15] G. S. Wagner, O. Pahlm, and N. Kjell C., “Coronary angiography,” in *Multimodal Cardiovascular Imaging: Principles and Clinical Applications*, 1st ed., McGraw-Hill Medical, 2011, pp. 71–80.

[16] “Intravascular ultrasound : MedlinePlus Medical Encyclopedia.” [Online]. Available: https://www.nlm.nih.gov/medlineplus/ency/article/007266.htm. [Accessed: 17-Feb-2016].

[17] S. Bangalore and D. L. Bhatt, “Coronary intravascular ultrasound,” *Circulation*, vol. 127, no. 25, pp. e868–e874, Jun. 2013.

[18] S. E. Nissen and P. Yock, “Intravascular ultrasound novel pathophysiological insights and current clinical applications,” *Circulation*, vol. 103, no. 4, pp. 604–616, Jan. 2001.

[19] E. Grube, U. Gerckens, L. Buellesfeld, and P. J. Fitzgerald, “Intracoronary imaging with optical coherence tomography a new high-resolution technology providing striking visualization in the coronary artery,” *Circulation*, vol. 106, no. 18, pp. 2409–2410, Oct. 2002.

[20] M. Terashima, H. Kaneda, and T. Suzuki, “The role of optical coherence tomography in coronary intervention,” *Korean J. Intern. Med.*, vol. 27, no. 1, pp. 1–12, Mar. 2012.

[21] E. Jahangir and J. A. McPherson, “Fractional Flow Reserve Measurement: Background, Indications, Outcomes,” *Medscape*, Dec. 2015.

[22] P. Vranckx, D. E. Cutlip, E. P. McFadden, M. J. Kern, R. Mehran, and O. Muller, “Coronary pressure–derived fractional flow reserve measurements recommendations for standardization, recording, and reporting as a core laboratory technique. proposals for integration in clinical trials,” *Circ. Cardiovasc. Interv.*, vol. 5, no. 2, pp. 312–317, Apr. 2012.

[23] P. A. L. Tonino *et al.*, “Angiographic versus functional severity of coronary artery stenoses in the FAME study Fractional Flow Reserve Versus Angiography in multivessel evaluation,” *J. Am. Coll. Cardiol.*, vol. 55, no. 25, pp. 2816–2821, Jun. 2010.

[24] “Angioplasty and stent placement for the heart.” [Online]. Available: http://www.hopkinsmedicine.org/healthlibrary/test_procedures/cardiovascular/angioplasty_and_stent_placement_for_the_heart_92,p07981/. [Accessed: 02-Dec-2016].

[25] M. T. Dehkordi, S. Sadri, and A. Doosthoseini, “A review of coronary vessel segmentation algorithms,” *J. Med. Signals Sens.*, vol. 1, no. 1, pp. 49–54, 2011.

[26] C.-Y. Lin and Y.-T. Ching, “Extraction of Coronary Arterial Tree using cine X-ray angiograms,” *Biomed. Eng. Appl. Basis Commun.*, vol. 17, no. 03, pp. 111–120, Jun. 2005.

[27] A. Takagi, Y. Tsurumi, N. Magosaki, K. Suzuki, K. Nakamura, and H. Kasanuki, “Significance of angiographic haziness at the distal stent edge: analysis by intravascular ultrasound and quantitative coronary angiography,” *J. Cardiol.*, vol. 33, no. 6, pp. 307–316, Jun. 1999.

[28] M. Wang, C. Li, W. Cai, and X. Wu, "Coronary angiography image edge detection based on information measure," in *2010 WASE International Conference on Information Engineering (ICIE)*, 2010, vol. 1, pp. 141 –144.

[29] M. S. D. Kumar, D. Shen, L. Wei, R. Turlapthi, and J. S. Suri, "Motion correction strategies for interventional angiography images: a comparative approach," in *IEEE International Conference on Image Processing, 2007. ICIP 2007*, 2007, vol. 1, pp. I –497 –I –500.

[30] M. Schrijver, "Angiographic image analysis to assess the severity of coronary stenoses," info:eu-repo/semantics/doctoralThesis, Universiteit Twente, Enschede, 2002.

[31] K. Sun, S. Jiang, and Y. Wang, "Segmentation of coronary artery on angiogram by combined morphological operations and watershed," in *2nd International Conference on Biomedical Engineering and Informatics, 2009. BMEI '09*, 2009, pp. 1–4.

[32] K. Thayalan, "Fluoroscopy imaging," in *The Physics of Radiology and Imaging*, 1st ed., New Delhi, India ; Philadelphia: Jaypee Brothers Medical Pub, 2014, pp. 205–241.

[33] "Medical X-ray imaging - fluoroscopy." [Online]. Available: http://www.fda.gov/Radiation-EmittingProducts/RadiationEmittingProductsandProcedures/MedicalImaging/MedicalX-Rays/ucm115354.htm. [Accessed: 04-Mar-2016].

[34] Mosby, *Mosby's Pocket Dictionary of Medicine, Nursing & Health Professions*. Elsevier Health Sciences, 2009.

[35] "View details of Philips Allura Xper FD10." [Online]. Available: http://www.usa.philips.com/healthcare/product/HC722022CA/allura-xper-fd10-xray-system. [Accessed: 02-Dec-2016].

[36] E. L. Nickoloff, “AAPM/RSNA physics tutorial for residents: Physics of flat-panel fluoroscopy systems,” *RadioGraphics*, vol. 31, no. 2, pp. 591–602, Mar. 2011.

[37] M. S. V. Lysel, “X-Ray projection angiography,” in *The Biomedical Engineering Handbook 1*, 2nd ed., Springer Science & Business Media, 2000, pp. 61.8 – 61.18.

[38] “The image intensifier.” [Online]. Available: http://www.upstate.edu/radiology/education/rsna/fluoro/iisize.php. [Accessed: 02-Dec-2016].

[39] Q. B. Carroll, “Image intensification device,” in *Practical Radiographic Imaging*, 8th ed., Springfield, Ill: Charles C Thomas Pub Ltd, 2007, pp. 447–454.

[40] M. J. Kern, “Angiographic data,” in *Cardiac Catheterization Handbook: Expert Consult - Online and Print, 5e*, 5th ed., Philadelphia, PA: Mosby, 2011, pp. 145–218.

[41] M. J. Kern, *Cardiac Catheterization Handbook: Expert Consult - Online and Print, 5e*, 5th ed. Philadelphia, PA: Mosby, 2011.

[42] C. Di Mario and N. Sutaria, “Coronary angiography in the angioplasty era: projections with a meaning,” *Heart*, vol. 91, no. 7, pp. 968–976, Jul. 2005.

[43] “CardiacCathPro.com.” [Online]. Available: http://cardiaccathpro.com/CAD.html. [Accessed: 02-Dec-2016].

[44] S. C. Smith *et al.*, “ACC/AHA guidelines for percutaneous coronary intervention (Revision of the 1993 PTCA Guidelines)—executive summary A report of the american college of cardiology/american heart association task force on practice guidelines (Committee to revise the 1993 guidelines for percutaneous transluminal coronary angioplasty) Endorsed by the society for cardiac angiography and interventions,” *Circulation*, vol. 103, no. 24, pp. 3019–3041, Jun. 2001.

[45] L. W. Klein and R. J. Krone, “Cardiac interventions today - angiographic characterization of lesion morphology,” *Cardiac Interventions Today*, 2008.08-2008. [Online]. Available: http://citoday.com/2008/08/CIT0808_07.php/. [Accessed: 22-Mar-2016].

[46] O. Tayeh and F. Ettori, “Vascular access and angiographic lesion morphology in elective percutaneous coronary intervention,” *Egypt. Heart J.*, vol. 66, no. 1, pp. 27–33, Mar. 2014.

[47] S. Tu *et al.*, “Coronary angiography enhancement for visualization,” *Int. J. Cardiovasc. Imaging*, vol. 25, no. 7, pp. 657–667, Oct. 2009.

[48] M. A. U. Khan, M. K. Khan, and M. Aurangzeb Khan, “Coronary angiogram image enhancement using decimation-free directional filter banks,” in *IEEE International Conference on Acoustics, Speech, and Signal Processing, 2004. Proceedings. (ICASSP ’04)*, 2004, vol. 5, pp. V–441–4 vol.5.

[49] P. T. H. Truc, M. A. U. Khan, Y.-K. Lee, S. Lee, and T.-S. Kim, “Vessel enhancement filter using directional filter bank,” *Comput Vis Image Underst*, vol. 113, no. 1, pp. 101–112, Jan. 2009.

[50] C. Köse, “Fully automatic segmentation of coronary vessel structures in poor quality x-ray angiogram images,” in *Structural, Syntactic, and Statistical Pattern Recognition*, D.-Y. Yeung, J. T. Kwok, A. Fred, F. Roli, and D. de Ridder, Eds. Springer Berlin Heidelberg, 2006, pp. 74–82.

[51] S. Tu, Y. Wu, X. Lu, H. Huo, and T. Fang, “Stick-guided lateral inhibition for enhancement of low-contrast image,” 2007, vol. 6788, p. 67881W–67881W–8.

[52] C. Xiao, S. Zhang, S. Cheng, and Y. Chen, “A novel method for speckle reduction and edge enhancement in ultrasonic images,” 2005, vol. 5637, pp. 469–476.

[53] M. A. U. Khan, R. Bahadur Khan, S. Bilal, A. Jamil, and M. Ali Shah, “Enhancement of angiogram images using pseudo color processing,” *Inf. Technol. J.*, vol. 7, no. 1, pp. 210–214, Jan. 2008.

[54] D. S. D. Lara, A. W. C. Faria, A. de A. Araújo, and D. Menotti, “A novel hybrid method for the segmentation of the coronary artery tree in 2D angiograms,” *Int. J. Comput. Sci. Inf. Technol. IJCSIT*, vol. 5, no. 3, pp. 45–65, Jun. 2013.

[55] H. S. S. Ahmed and J. Nordin, “Improving diagnostic viewing of medical images using enhancement algorithms,” *J. Comput. Sci.*, vol. 7, no. 12, pp. 1831–1838.

[56] N. M. Sasi and V. K. Jayasree, “Contrast limited adaptive histogram equalization for qualitative enhancement of myocardial perfusion images.,” *Engineering*, vol. 5, pp. 326–331, 2013.

[57] A. Kusumawardhani, T. Mengko, I. Fahri, S. Soerianata, D. Firman, and H. Zakaria, “Coronary angiogram stabilization for QuBE values calculation using SIFT method,” in *2011 2nd International Conference on Instrumentation, Communications, Information Technology, and Biomedical Engineering (ICICI-BME)*, 2011, pp. 111–116.

[58] S. Zheng and D. Weirong, “Analysis of coronary arterial dynamics from x-ray angiographic sequences,” presented at the Second International Symposium on Computational Intelligence and Design, Changsha, 2009, vol. 1, pp. 201–204.

[59] R. C. Gonzalez and R. E. Woods, “Image segmentation,” in *Digital Image Processing*, 3rd ed., Addison-Wesley Pub (Sd), 1992, pp. 689–794.

[60] C. Kirbas and F. K. H. Quek, “Vessel extraction techniques and algorithms: a survey,” in *Third IEEE Symposium on Bioinformatics and Bioengineering, 2003. Proceedings*, 2003, pp. 238 – 245.

[61] R. M. Tayebi *et al.*, “Coronary artery segmentation in angiograms with pattern recognition techniques – a survey,” in *2013 International Conference on Advanced Computer Science Applications and Technologies (ACSAT)*, 2013, pp. 321–326.

[62] A. Dogra and P. Bhalla, “Image sharpening by gaussian and butterworth high pass filter,” *Biomed Pharmacol. J.*, vol. 7, no. 2, pp. 707–713, 2014.

[63] A. F. Frangi, W. J. Niessen, K. L. Vincken, and M. A. Viergever, “Multiscale vessel enhancement filtering,” in *Medical Image Computing and Computer-Assisted Interventation — MICCAI’98*, W. M. Wells, A. Colchester, and S. Delp, Eds. Springer Berlin Heidelberg, 1998, pp. 130–137.

[64] S. Wang, B. Li, and S. Zhou, “A segmentation method of coronary angiograms based on multi-scale filtering and region-growing,” in *2012 International Conference on Biomedical Engineering and Biotechnology (iCBEB)*, 2012, pp. 678–681.

[65] D. S. D. Lara, A. W. C. Faria, A. de A Araujo, and D. Menotti, “A semi-automatic method for segmentation of the coronary artery tree from angiography,” in *2009 XXII Brazilian Symposium on Computer Graphics and Image Processing (SIBGRAPI)*, 2009, pp. 194–201.

[66] K. Zuiderveld, *Graphics Gems IV*. San Diego, CA, USA: Academic Press Professional, Inc., 1994.

[67] Shashank, M. Bhattacharya, and G. K. Sharma, “Optimized coronary artery segmentation using frangi filter and anisotropic diffusion filtering,” in *2013 International Symposium on Computational and Business Intelligence (ISCBI)*, 2013, pp. 261–264.

[68] G. Sasidharan and A. George, “Frangi’s vessel detection approach for coronary angiogram segmentation,” *Int. J. Eng. Trends Technol.*, vol. 13, no. 5, pp. 213–217, Jul. 2014.

[69] J. F. O’Brien and N. F. Ezquerra, “Automated segmentation of coronary vessels in angiographic image sequences utilizing temporal, spatial, and structural constraints,” 1994, vol. 2359, pp. 25–37.

[70] R. C. Gonzalez and R. E. Woods, “Morphological image processing,” in *Digital Image Processing*, 3rd ed., Addison-Wesley Pub (Sd), 1992, pp. 627–687.

[71] S. Eiho and Y. Qian, “Detection of coronary artery tree using morphological operator,” in *Computers in Cardiology 1997*, 1997, pp. 525–528.

[72] T.-F. Lee, C.-Y. Lee, P.-J. Chao, C. Lee, C.-Y. Wang, and C.-H. Fang, “Quantitative coronary analysis medical image processing improved by combining wavelet edge detection and segmentation,” in *2009 Fourth International Conference on Innovative Computing, Information and Control (ICICIC)*, 2009, pp. 1196–1199.

[73] C. Kirbas and F. Quek, “A review of vessel extraction techniques and algorithms,” *ACM Comput Surv*, vol. 36, no. 2, pp. 81–121, Jun. 2004.

[74] S. Nirmala Devi and N. Kumaravel, “Comparison of active contour models for image segmentation in X-ray coronary angiogram images,” *J. Med. Eng. Technol.*, vol. 32, no. 5, pp. 408–418, Jan. 2008.

[75] P. Zou, P. Chan, and P. Rockett, “A model-based consecutive scanline tracking method for extracting vascular networks from 2-D digital subtraction angiograms,” *IEEE Trans. Med. Imaging*, vol. 28, no. 2, pp. 241–249, 2009.

[76] P. M. J. van der Zwet, I. M. F. Pinto, P. W. Serruys, and J. H. C. Reiber, “A new approach for the automated definition of path lines in digitized coronary angiograms,” *Int. J. Card. Imaging*, vol. 5, no. 2, pp. 75–83, 1990.

[77] Z. Shoujun, Y. Jian, W. Yongtian, and C. Wufan, “Automatic segmentation of coronary angiograms based on fuzzy inferring and probabilistic tracking,” *Biomed. Eng. OnLine*, vol. 9, no. 1, p. 40, Aug. 2010.

[78] S. A. Stansfield, “ANGY: A rule-based expert system for automatic segmentation of coronary vessels from digital subtracted angiograms,” *IEEE Trans. Pattern Anal. Mach. Intell.*, vol. PAMI-8, no. 2, pp. 188 –199, Mar. 1986.

[79] S. D. Tomasello and C. Luca, “Quantitative coronary angiography in the interventional cardiology,” in *Advances in the Diagnosis of Coronary Atherosclerosis*, InTech, 2011, pp. 255–270.

[80] J. Canny, “A computational approach to edge detection,” *IEEE Trans Pattern Anal Mach Intell*, vol. 8, no. 6, pp. 679–698, Jun. 1986.

[81] A. Hernandez-Vela *et al.*, “Accurate coronary centerline extraction, caliber estimation, and catheter detection in angiographies,” *IEEE Trans. Inf. Technol. Biomed.*, vol. 16, no. 6, pp. 1332–1340, Nov. 2012.

[82] W. Yumei, “Tracking of coronary arteries in angiogram sequence by structural matching of junctions,” Thesis, 2011.

[83] T. Y. Zhang and C. Y. Suen, “A fast parallel algorithm for thinning digital patterns,” *Commun ACM*, vol. 27, no. 3, pp. 236–239, Mar. 1984.

[84] K. Haris, S. N. Efstratiadis, N. Maglaveras, J. Gourassas, C. Pappas, and G. Louridas, “Coronary arterial tree extraction based on artery tracking and mathematical morphology,” in *Computers in Cardiology 1998*, 1998, pp. 769–772.

[85] K. Haris, S. N. Efstratiadis, N. Maglaveras, C. Pappas, J. Gourassas, and G. Louridas, “Model-based morphological segmentation and labeling of coronary angiograms,” *IEEE Trans. Med. Imaging*, vol. 18, no. 10, pp. 1003–1015, Oct. 1999.

[86] Y. Sun, “Automated identification of vessel contours in coronary arteriograms by an adaptive tracking algorithm,” *IEEE Trans. Med. Imaging*, vol. 8, no. 1, pp. 78–88, Mar. 1989.

[87] A. K. Klein, F. Lee, and A. A. Amini, “Quantitative coronary angiography with deformable spline models,” *IEEE Trans. Med. Imaging*, vol. 16, no. 5, pp. 468–482, Oct. 1997.

[88] P. Bifulco, M. Romano, M. Cesarelli, L. Iuppariello, and N. Pasquino, “Estimation of quantum noise in fluoroscopy by analyzing differences of static images,” presented at the 20th ImeKo TC-4 International Symposium, 2014, pp. 790–793.

[89] Z. Sun and Y. Zhou, “Assessing cardiac dynamics based on X-ray coronary angiograms,” *J. Multimed.*, vol. 8, pp. 48–55, Feb. 2013.

[90] F. Moscheni, F. Dufaux, and M. Kunt, “A new two-stage global/local motion estimation based on a background/foreground segmentation,” in *1995 International Conference on Acoustics, Speech, and Signal Processing, 1995. ICASSP-95*, 1995, vol. 4, pp. 2261–2264 vol.4.

[91] D. L. Bhatt, “Noise,” in *Cardiovascular Intervention: A Companion to Braunwald’s Heart Disease*, Elsevier Health Sciences, 2015, p. 99.

[92] P. Kalra and S. Peleg, “Fingerprint image enhancement,” in *Computer Vision, Graphics and Image Processing: 5th Indian Conference, ICVGIP 2006, Madurai, India, December 13-16, 2006, Proceedings*, Springer, 2007, pp. 951–961.

[93] R. C. Gonzalez, “Homomorphic filtering,” in *Digital Image Processing*, Pearson Education India, 2009, pp. 311–315.

[94] E. H. W. Meijering, K. J. Zuiderveld, and M. A. Viergever, “Image registration for digital subtraction angiography,” *Int. J. Comput. Vis.*, vol. 31, no. 2–3, pp. 227–246, Apr. 1999.

[95] G. Bradski and A. Kaehler, “Template matching,” in *Learning OpenCV: Computer Vision with the OpenCV Library*, 1st ed., O’Reilly Media, 2008, pp. 214–219.

[96] N. Dalal and B. Triggs, “Histograms of oriented gradients for human detection,” in *2005 IEEE Computer Society Conference on Computer Vision and Pattern Recognition (CVPR’05)*, 2005, vol. 1, pp. 886–893 vol. 1.

[97] K. A. S. H. Kulathilake, L. Ranathunga, G. R. Constantine, and N. A. Abdullah, “Region growing segmentation method for extracting vessel structures from coronary cine-angiograms,” in *Moratuwa Engineering Research Conference (MERCon), 2015*, 2015, pp. 142–147.

[98] K. A. S. H. Kulathilake, L. Ranathunga, G. R. Constantine, and N. A. Abdullah, “A segmentation method for extraction of main arteries from coronary cine-angiograms,” in *2015 Fifteenth International Conference on Advances in ICT for Emerging Regions (ICTer)*, 2015, pp. 9–15.

[99] A. C. Bovik, “Canny’s method,” in *Handbook of Image and Video Processing*, Academic Press, 2010, pp. 548–549.

[100] J. T. Dodge, B. G. Brown, E. L. Bolson, and H. T. Dodge, “Lumen diameter of normal human coronary arteries. Influence of age, sex, anatomic variation, and left ventricular hypertrophy or dilation.,” *Circulation*, vol. 86, no. 1, pp. 232–246, Jul. 1992.

[101] K. Kaur and N. Gupta, “Evaluating the performancne of DBLA Using CLAHE & dark channel prior,” *Int. J. Adv. Res. Comput. Sci. Softw. Eng.*, vol. 5, no. 5, pp. 960–969, May 2015.

APPENDIX A: STRENGTH AND LIMITATION ANALYSIS OF CARDIAC MEDICAL IMAGE MODALITIES

Image Modality	Strength	Limitations
Stress echo-cardiography	It is a low cost method. Global and regional left and right ventricular systolic function, valvular disease and hemodynamic can be assessed quickly and with reasonable accuracy.	A proportion of patients have inadequate or suboptimal images. The success of imaging varies from laboratory to laboratory and dependent on the sonographer expertise, physicians' proficiency and tolerance for technically difficult studies (e.g., obese patients). In approximately 10–20% of examinations, two or more of 16 (or 17) myocardial segments may not be well visualized.
SPECT	Provides physiological information through functional imaging. Can detect metabolic activity blood flow, intrinsic lesion localization	Gamma emissions harmful to the patients. Non-hybrid devices have poor spatial resolution. Tissue boundaries are ill-determined Longer scanning duration, exceeding 30-40 minutes
PET	It allows study of body functions and can help physicians detect alterations in biochemical processes that imply the possibility of diseases before changes in anatomy are detected using other imaging tests, such as CT or MRI. As the radioactivity is very short-lived, patients' exposure to radiation is low.	Time-consuming. The resolution of structures of the body with nuclear medicine may not be as clear as with other imaging techniques, such as CT or MRI.PET scanning can give false results if chemical balances within the body are not normal.A person who is very obese may not fit into the opening of a conventional PET/CT unit.

Image Modality	Strength	Limitations
Cardiac MRI	MRI does not have any ionizing radiation, thus permitting its use in children and pregnant women. It can produce high resolution and 3D images of the cardiac chambers and thoracic vessels. Unlike echocardiography, MRI can produce images of cardiovascular structures without interference from adjacent bone or air, which limits echocardiography. MRI is also less operator dependant than echocardiography.Velocity encoded techniques permit measurement of blood flow. MRI does not have the weakness of geometric assumptions (as do angiography and 2D echo-cardiography) in assessing ventricular volumes.	MRI requires more patient cooperation than other tests and claustrophobic patients may not be able to undergo the exam. The duration of examination is significantly longer compared with CT. Installation and operation of MRI equipment is costly. MRI has less spatial resolution than CT, which limits the evaluation of small structures such as the CAs.
MSCT	Small and rapidly moving anatomic structures could be visualized with good image quality. Coronary CT angiography investigation allows the accurate detection of CA stenosis. 3D imaging provides a real coronary mapping mode using 3D volume rendering.Cardiac CT has the potential to visualize earlier stages of coronary atherosclerosis.CT provides for accurate assessment of general cardiac morphology.	Compared to other diagnostic tests, CT scans deliver a relatively high dose of radiation to the patient. Allergic Reaction due to the contrast agents.

Image Modality	Strength	Limitations
X-ray angiography	Provide excellent visualizations of CA vasculature. Low cost.	It consists of some visual artifacts, which causes degradations such as; non-uniform illumination, noise. It provides only two dimensional images. Difficult to quantitatively analyze the CAs lumen. Subjective analysis leads to over estimations and under estimations of detected stenosis.
IVUS	IVUS enables a physician to detect inside the artery with a camera-like device. IVUS can quantify the percentage of narrowing and give insights into the nature of the plaque.	Some artifacts that occur during imaging causes erroneous results; e.g. ring-down artifact, nurd. The real three-dimensional geometry can hardly be obtained. IVUS is normally applied to a short segment of the vessel to minimize complications in the catheterization procedure, and it is almost impossible to image every branch of the coronary tree in order to recover the complete shape.
OCT	Provides accurate measurement of the structures in the vasculature than IVUS. Images contain broad dynamic range and high resolution. It can be used to determine the morphology of detected plaques.	The real three-dimensional geometry can hardly be obtained. OCT is normally applied to a short segment of the vessel to minimize complications in the catheterization procedure, and it is almost impossible to image every branch of the coronary tree in order to recover the complete shape.
FFR	Provides accurate measurements of the stenosis based on the functional significance.	The pressure wire used for the FFR is costly.

APPENDIX B: PSEUDO CODE OF SKELETON PATH TRACKER

Skeleton Path Tracker (seedPoint)

```
BEGIN
    skeletonPointArray []
    taggedPointArray[]
    candidateKeyArray[]
    candidateKeyDensityArray[]
    trackingStatus ←1
    kpCount, taggedCount, candidateCount, candidateDensityCount ←0
    currentSeedPoint ← seedPoint
    skeletonPointArray[kpCount] ← currntSeedPoint
    WHILE (trackingStatus ==1)
      FOR EACH 8 neighbors of currentSeedPoint
        IF (pixelValue == 255 && notVisited && notTagged) THEN
          skeletonPointArray[++kpCount] ← neighborPoint
          candidateKeyArray[candidateCount++] ← neighborPoint
        END IF
      END FOR
      IF (candidateCount == 0) THEN
        taggedPointArray [++taggedCount] ←currentSeedPoint
        trackingStatus ←0
      ELSE IF (candidateCount == 1) THEN
```

```
    taggedPointArray [++taggedCount]← currentSeedPoint
    currentSeedPoint ← candidateKeyArray[0]
    re-set candidateKeyArray
  ELSE
    FOR EACH candidateKey point in candidateKeyArray
      count ←0
      FOR EACH 8 neighbors of candidateKey point in candidateKeyArray[]
        IF (pixelValue == 255 && notTagged && !currnetSeedPoint) THEN
          count++
          candidateKeyDensityArray [candidateKeyDensityCount++] ← count
        END IF
      END FOR
    END FOR
  max ←0;
  maxIndex ←0;
  FOR (n ← 0; n< candidateCount)
    IF(max<= candidateKeyDensityArray[n]) THEN
      max ← candidateKeyDensityArray[n]
      maxIndex ← n
    END IF
  END FOR
  taggedPointArray [++taggedCount]← currentSeedPoint
  FOR(n ← 0; n< candidateCount)
```

```
            IF( n!= maxIndex) THEN

               taggedPointArray [++taggedCount] ←candidateKeyArray[n]

            END IF

         END FOR

         currentSeedPoint ← candidateKeyArray[maxIndex]

         re-set candidateKeyArray

      END WHILE

END
```

Note:

notVisited indicates that the pixel point is not exists in skeletonPointArray[] and **notTagged** indicates that the pixel point is not exists in taggedPointArrayp[].

Following section elaborates the execution steps of Skeleton Path Tracker algorithm by using a sample skeleton image.

Example:

Following Figure A depicts a sample skeleton image and seed point is given as [5,2]. Arrow head in the Figure A indicates the tracking direction. Table A enlists the steps of the proposed Skeleton Path Tracker algorithm and each column in the table represents the values, which are manipulated in accordance with the execution steps.

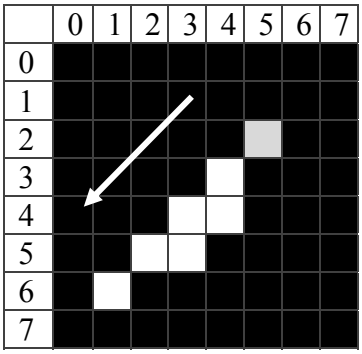

Figure A – Sample skeleton image

Skeleton Point Array	[5,2]	[4,3]	[3,4]	[4,4]	[2,5]	[3,5]	[1,6]

Tagged Point Array	[5,2]	[4,3]	[4,4]	[3,4]	[3,5]	[2,5]	[1,6]

Table A: Steps of the proposed Skeleton Path Tracker algorithm

Iterations	**Iteration 1**	**Iteration 2**	**Iteration 3**	**Iteration 4**	**Iteration 5**
Current seed point	[5,2]	[4,3]	[3,4]	[2,5]	[1,6]
White colored 8 Neighbors	[4,3]	[5,2][3,4] [4,4]	[4,3] [4,4] [2,5] [3,5]	[3,4] [3,5] [1,6]	[2,5]
Key Found status	0	1,0,0	1,1,0,0	1,1,0	1
Tagged status	0	1,0,0	1,1,0,0	1,1,0	1
Add to Skeleton Point array	[4,3]	[3,4] [4,4]	[2,5] [3,5]	[1,6]	-
Selected Candidate Key Points	[4,3]	[3,4] [4,4]	[2,5] [3,5]	[1,6]	-
Selected Candidate Key count	1	2	2	1	0
Case Number	2	3	3	2	1
End tracking	No	No	No	No	Yes
Candidate Density count	-	3,2	2,1	-	
Maximum density value	-	3	2	-	
Maximum density index	-	0	0	-	
Tagged → current seed point and non-maximum density Candidate Key points	[5,2]	[4,3], [4,4]	[3,4][3,5]	[2,5]	[1,6]
Next seed point → maximum indexed Candidate Key point	[4,3]	[3,4]	[2,5]	[1,6]	-

Following diagrams visually illustrate the skeleton path tracking progress according to the iterations. Gray colored pixel depicts the seed point. Yellow colored pixels represent the tracked key points. Orange colored pixels represent the tagged candidate pixels. Arrow head in each diagram indicates the tracking direction.

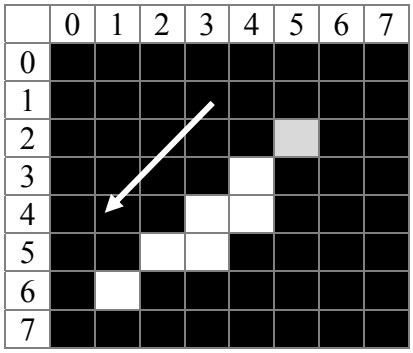

Iteration 1

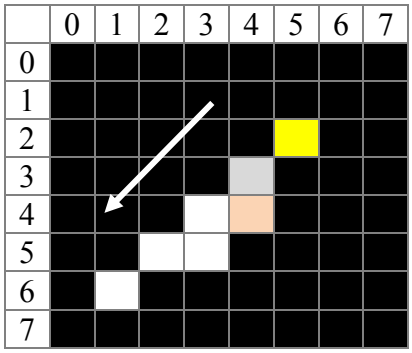

Iteration 2

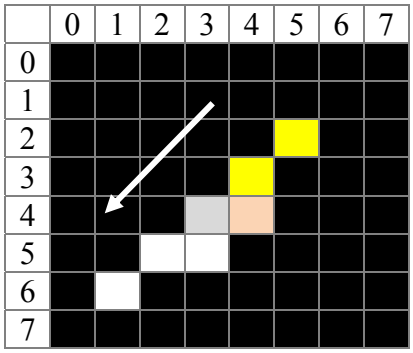

Iteration 3

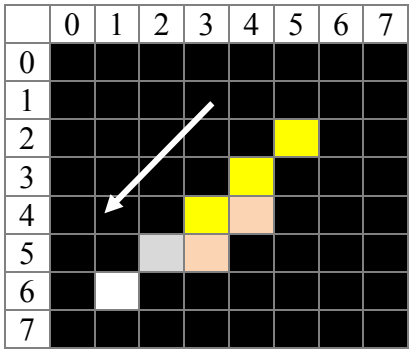

Iteration 4

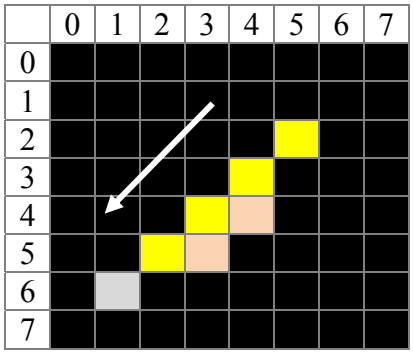

Iteration 5

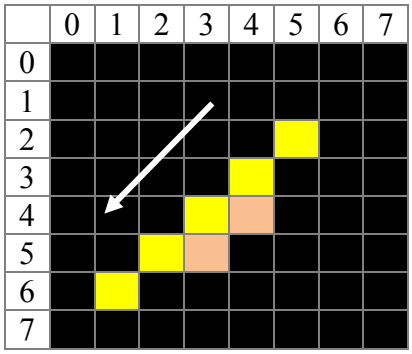

End of tracking

APPENDIX C: VISUAL ILLUSTRATIONS OF PROCESSING STEPS

The visual illustrations of the processing steps of the proposed methodology have been presented in this section. A sample CCA of RCA recorded under LAO cranial view has been selected and it consists of 10 frames to be processed.

Original frames ($f_0(x,y)$) of the selected video

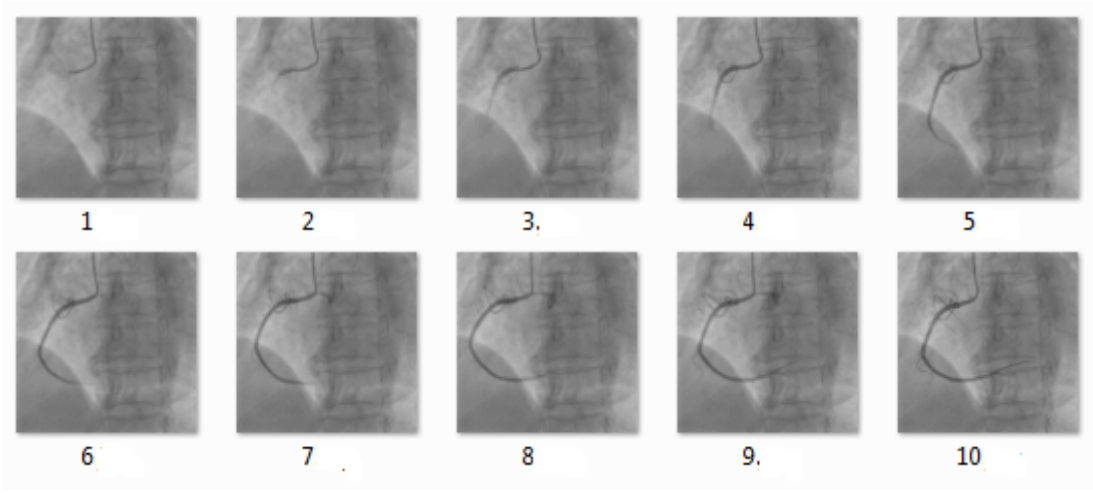

Enhanced Frames ($f_3(x,y)$)

Following are the uniformly illuminated normalized frames.

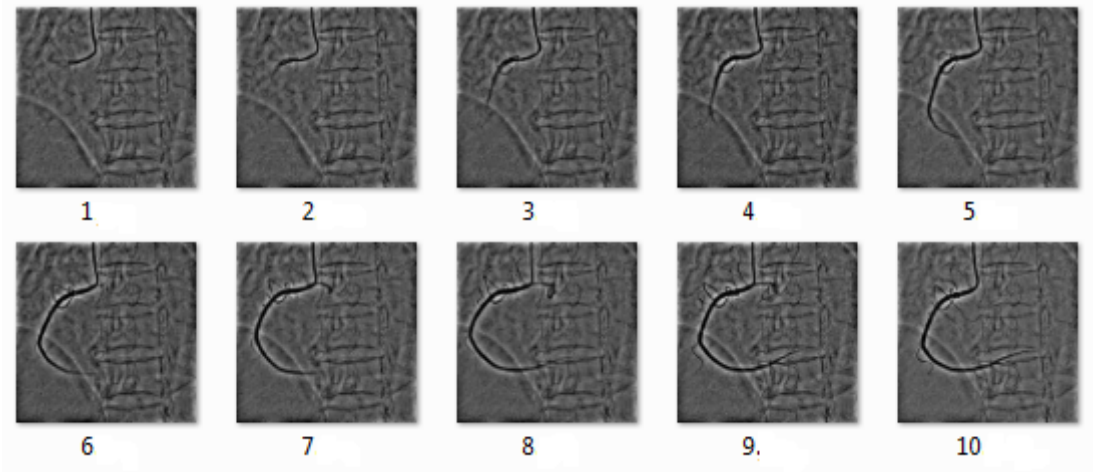

Aligned Frames ($f_4(x,y)$)

Following set of frames can be obtained after reduction of global motion from the enhanced frames.

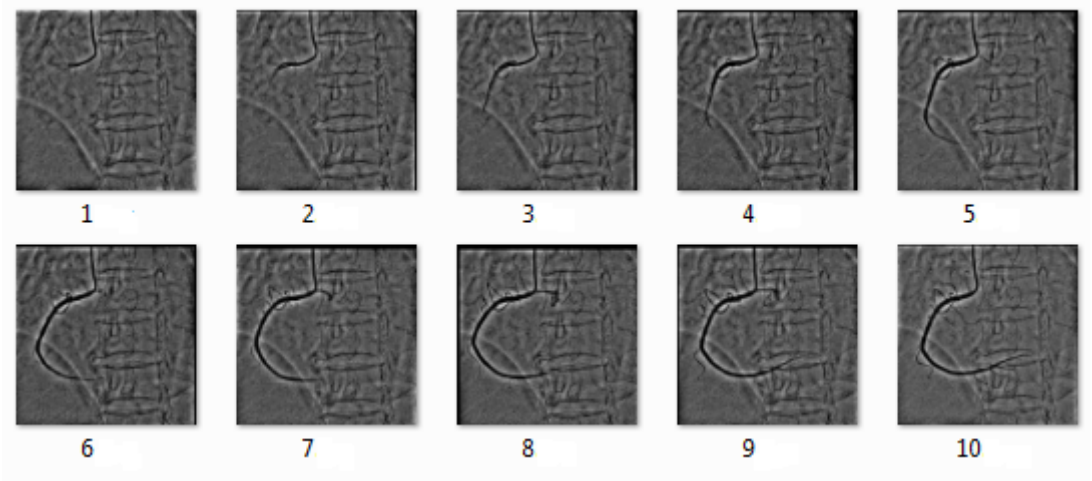

Background subtraction ($f_5(x,y)$)

Following set of frames can be obtained after subtracting the created mask image from each and every aligned frame. As a consequence of the operation the foreground area has been emphasized.

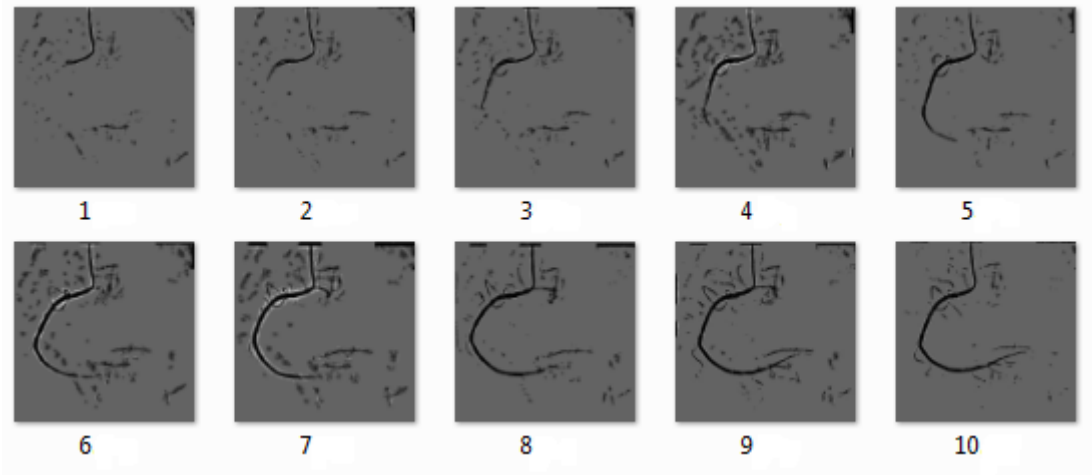

Foreground enhanced frames ($f_6(x,y)$)

Application of Frangi's vessel enhancement filter emphasizes the tubular structures of the CCAs and can be used to determine the vesselness feature of the frames.

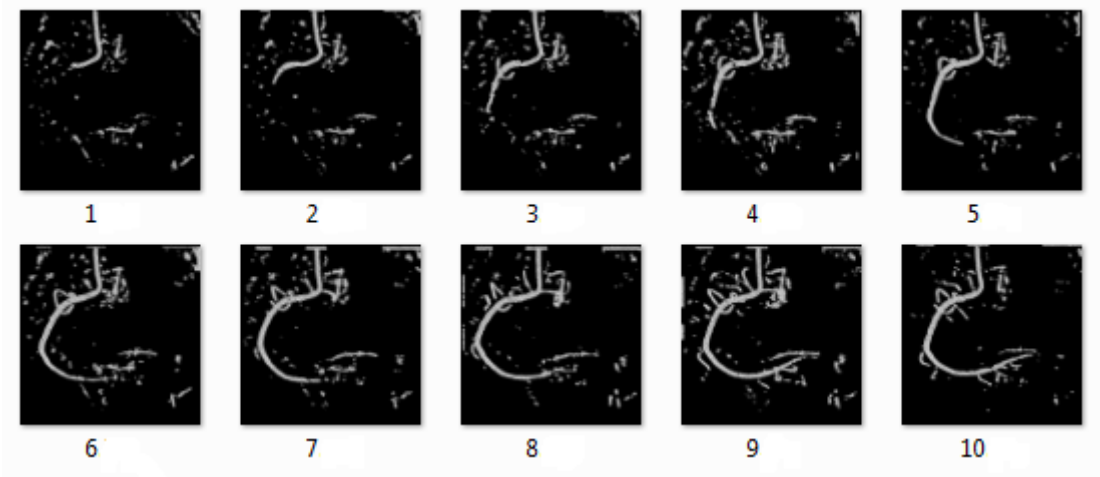

Overlapped and normalized frames ($f_7(x,y)$)

Following frames are obtained as a result of application of structure filling and normalization operations. These operations improve the special coherence of the vessel structures and represent them with uniform intensity.

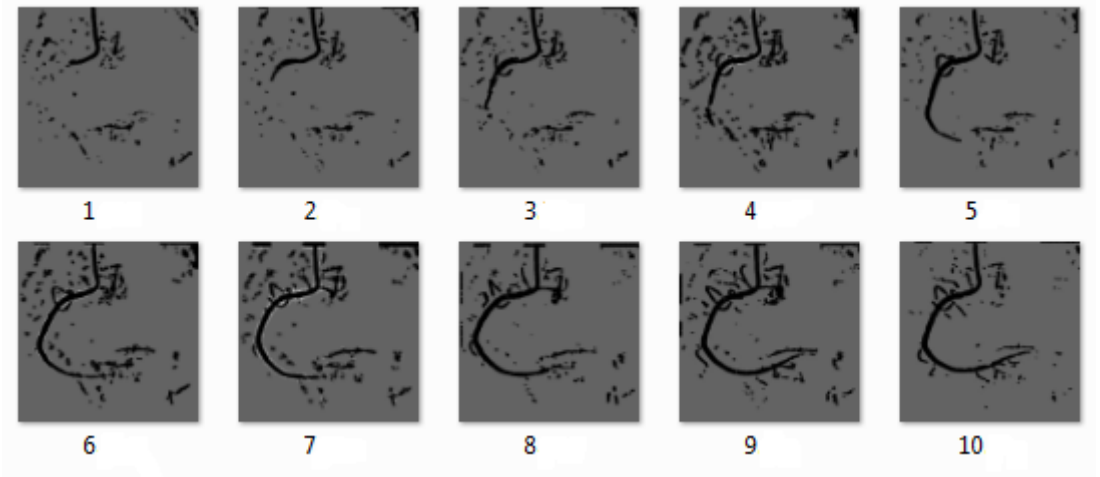

Foreground extracted frames ($f_8(x,y)$)

Following frames provide visual illustrations to emphasize the segmentation results of the processed CCA.

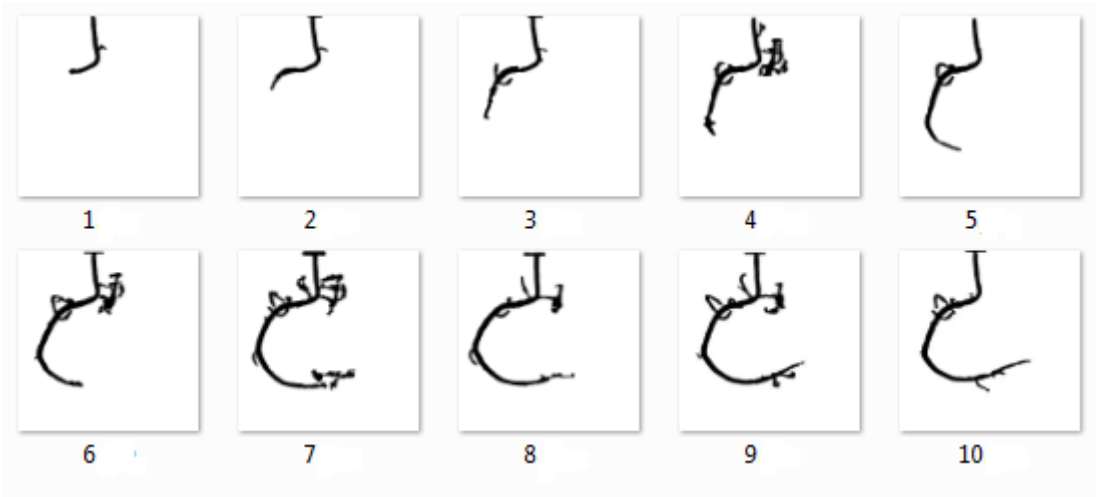

Vessel isolation ($f_9(x,y)$)

The root arterial segments of the RCA selected to be isolated have been depicted in the frames.

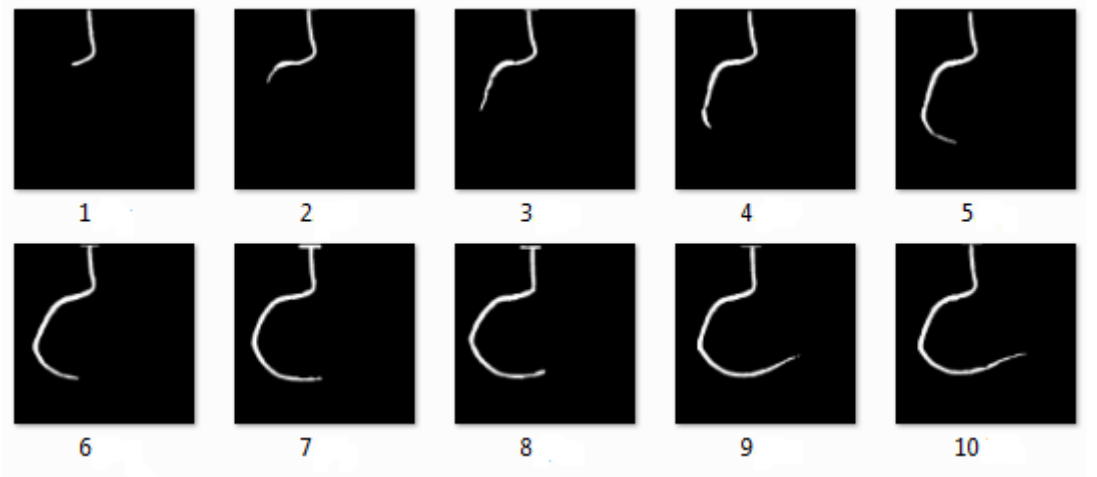

Skeleton ($f_s(x,y)$)

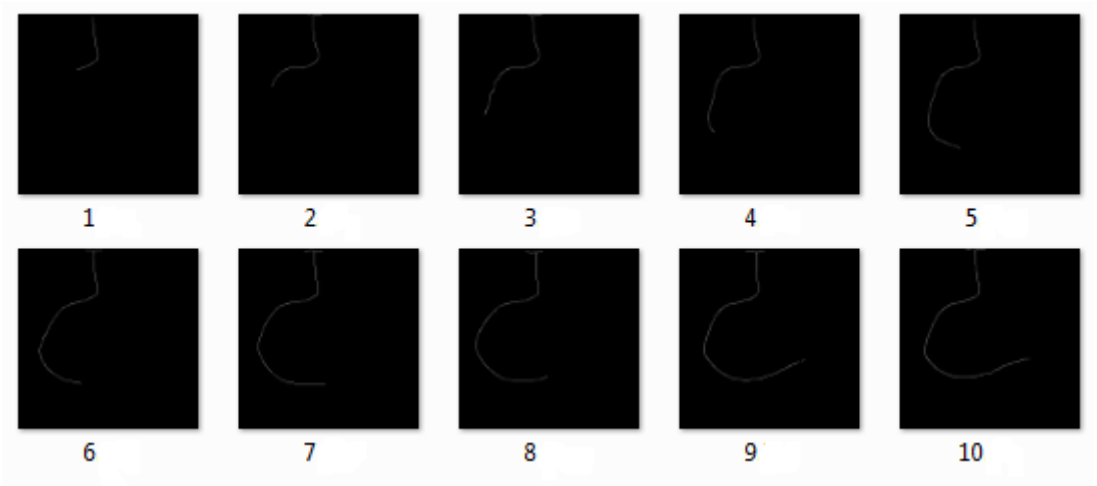

APPENDIX D: RESULTS OF CLINICAL FEASIBILITY ANALYSIS OF PROPOSED METHOD

Following table enlists the results of the clinical feasibility analysis of the proposed method. Selected CCA are listed in CCA case ID column and the English letter of each case indicates the name of the diagnosed CA. Hence, 'R' indicates the RCA, 'L' indicates LCA and 'C' indicates the CX artery. Subjective analysis results are directly extracted from the clinical reports, which belong to these patient cases and objective analysis results are computed by the quantitative coronary analysis method proposed in this study. Severity level of both subjective results and objective results are determined according to the criteria mentioned in section 6.4.2.

CCA case ID	Subjective Analysis Result	Severity Level	Objective Analysis Result	Severity Level	Stenosis Location
3883R	90	Severe	79.18	Severe	Mid
4233R	90	Severe	57.47	Moderate	Proximal
4538R	99	Total Occlusion	75.60	Severe	Mid
4585R	70	Moderate	74.19	Moderate	Mid long lesion
4782R	90	Severe	60.00	Moderate	Proximal mid long lesion
4837R	40	Minimal	65.20	Moderate	Diffuse disease
5088R	90	Severe	57.29	Moderate	Proximal
5339R	95	Severe	79.83	Severe	Proximal
5371R	50	Moderate	44.19	Minimal	Proximal
5438R	70	Moderate	59.36	Moderate	Mid
5713R	99	Total Occlusion	72.33	Moderate	Mid

CCA case ID	Subjective Analysis Result	Severity Level	Objective Analysis Result	Severity Level	Stenosis Location
4234L	99	Total Occlusion	54.98	Moderate	Mid culprit lesion
4585L	40	Minimal	38.90	Minimal	Mid
4645L	90	Severe	66.80	Moderate	Proximal
4646L	40	Minimal	62.49	Moderate	Proximal
5084L	99	Total Occlusion	71.15	Moderate	Mid
5088L	90	Severe	20.00	Minimal	Proximal
5106L	90	Severe	64.09	Moderate	Proximal
5233L	70	Moderate	65.00	Moderate	Proximal
5328L	80	Severe	88.55	Severe	Mid
5339L	70	Moderate	35.71	Minimal	After d1
5371L	40	Minimal	33.67	Minimal	Proximal
5438L	99	Total Occlusion	54.70	Moderate	Proximal
5473L	90	Severe	82.00	Severe	Proximal
5556L	50	Moderate	68.60	Moderate	Proximal
4233C	70	Moderate	30.28	Minimal	Proximal
4434C	70	Moderate	49.53	Minimal	Obtuse marginal
4645C	70	Moderate	52.60	Moderate	Proximal
4646C	65	Moderate	55.87	Moderate	Ostial
4650C	70	Moderate	78.25	Severe	Proximal
4969C	60	Moderate	56.69	Moderate	Proximal

CCA case ID	Subjective Analysis Result	Severity Level	Objective Analysis Result	Severity Level	Stenosis Location
5067C	45	Minimal	50.42	Moderate	Proximal
5556C	50	Moderate	52.30	Moderate	Proximal

APPENDIX E: PUBLICATIONS BASED ON THIS RESEARCH STUDY

Peer Reviewed Journal Article

K. A. S. H. Kulathilake, L. Ranthunga, G. Constantine, and N. A. Abdulla, “Hierarchical region based template matching technique for global motion reduction of coronary cineangiograms,” *Int. J. Comput. Theory Eng*., 7(2), pp. 156–161, 2014.

Kulathilake, K.A.S.H., Ranthunga, L., Constantine, G., Abdullah, "Visual alignment of arteries in coronary cine-angiogram using global motion stabilization approach." in J. National Science Foundation, 45(1), pp.41–51, 2017

Book Chapter

K. A. S. H. Kulathilake, L. Ranathunga, G. R. Constantine, and N. A. Abdullah, “Reduction of motion disturbances in coronary cineangiograms through template matching,” in *Future Information Technology*, J. J. (Jong H. Park, Y. Pan, C.-S. Kim, and Y. Yang, Eds. Springer Berlin Heidelberg, 2014, pp. 267–273.

IEEE Indexed Conference Publications

K. A. S. H. Kulathilake, L. Ranathunga, G. R. Constantine, and N. A. Abdullah, “Region growing segmentation method for extracting vessel structures from coronary cine-angiograms,” in *Moratuwa Engineering Research Conference (MERCon)*, 2015, pp. 142–147.

K. A. S. H. Kulathilake, L. Ranathunga, G. R. Constantine, and N. A. Abdullah, “A segmentation method for extraction of main arteries from Coronary Cine-Angiograms,” in *2015 Fifteenth International Conference on Advances in ICT for Emerging Regions (ICTer)*, 2015, pp. 9–15.

K. A. S. H. Kulathilake, L. Ranathunga, G. R. Constantine, and N. A. Abdullah, “Computing lumen diameter of coronary arteries using segmented vessel's geometry and line tracking,” in *2016 International Conference on Information Science (ICIS)*, 2016, pp. 109–115.

K. A. S. H. Kulathilake, L. Ranathunga, G. R. Constantine, and N. A. Abdullah, "A technique for quantitative coronary analysis of cine-angiograms using segmentation and vessel path tracking", i*n 2016 International Conference on Advances in ICT for Emerging Regions (ICTer)*, 2016. pp.87-95.